Universities of Glasgow and Strathclyde
Department of Naval Architecture and Marine Engineering

CROSS-FLOW AROUND AND STABILITY OF MULTIPLE CIRCULAR CYLINDERS

By
XINGYUAN ZHAO

A thesis presented in fulfillment of the requirements for the degree of
Doctor of Philosophy

Declaration

This thesis is the result of the author's original research. It has been composed by the author and has not been previously submitted for examination which has lead to the award of a degree.

Xingyuan Zhao

Signature: Date:

Summary

In recent years, as the offshore industry moved towards deeper waters, there has been a concerted effort to investigate both theoretically and experimentally the response of a cluster of vertically tensioned risers in ocean currents. It is believed a loss of stability of riser system once the current exceeds a certain critical value can lead to riser clashing.

The turbulent cross flow past multiple circular cylinders at Reynolds number Re = 10^4 is simulated by using FLUENT with a $k-\omega$ SST turbulence model. Position-related fluid forces under wake shielding effect have been obtained. The influence of spacing on fluid forces and relative flow patterns was also been identified and discussed.

Five flow patterns for two cylinders in cross-flow, in tandem or staggered arrangements, are identified. Generally, the downstream cylinder experiences a significant drag reduction for tandem arrangement, and also a non-zero time-averaged lift force for staggered arrangement. The bistable and hysteresis features of flow around two tandem cylinders are observed.

It is found the drag reduction is the result of fluctuating incident flow and the time-averaged lift is due to the asymmetry of the same. The latter is also related to the asymmetric separation points around the downstream cylinder. The change of stagnation point, as a result of the fluctuating incident velocity, is strongly associated with the periodical fluid forces.

For three in-line cylinders in cross flow, the drag coefficient of the third cylinder is largely influenced by the spacings between the cylinders, as a result of the cascading shielding effects of the two upstream cylinders, while the third cylinder only influences the drag coefficients of the upstream two when they are near the critical spacing. It is also found when the first two cylinders are widely spaced, the third

cylinder experiences a reduced vortex shedding frequency.

Based on numerical results and the experimental data, a stability analysis model for two elastically supported cylinders is set up and applied for various aspects. It is found that for a cylinder located in the wake of an upstream one, there can be multiple stable/unstable equilibrium positions. There exists a critical reduced velocity, above which there will be no equilibrium positions, indicating a likely clashing between the two cylinders once the critical velocity is exceeded.

The tandem arrangement is identified as the worst situation for the clashing onset. It is revealed both the diameter and the stiffness ratios have significant impact on the riser clashing onset condition. The drag amplification, caused by VIV, can significantly change the riser clashing onset condition computed from the forces of stationary cylinders.

Acknowledgements

First of all, I would like to express my deepest appreciation to my supervisor, Professor Shan Huang for all his great support, constant guidance, consistent encourage and confidence in me throughout the course of my Ph.D. work. His help in financial support to me is gratefully acknowledged.

I would like to show to my gratitude to Mr. Qiuxin Gao for his selfless and continue support towards my CFD simulations. He was my second supervisor actually.

I would also like to thank my colleagues in the Department of Naval Architecture & Marine Engineering. Working with them made my life in Glasgow much meaningful.

Many thanks to my parents and my sisters. Without their encouragement and support, I would not have got through the hard time.

Table of Contents

List of Figures

List of Tables

Nomenclature

The following nomenclature is used throughout the thesis unless otherwise specifically mentioned.

a	mass parameter of the upstream cylinder ($= \frac{m_1}{\frac{\pi}{4}\rho D_1^2}$)
C_D, C_L	drag and lift coefficients non-dimensionalised with free stream velocity (= $F_{D,L}/0.5\rho V^2 D$)
$\overline{C}_D$, $\overline{C}_L$	drag and lift coefficients defined by the local wake velocity (= $F_{D,L}/0.5\rho U^2 D$)
C_L'	r.m.s. lift coefficient
C_m	added mass coefficient
C_p	pressure coefficient ($= p / 0.5\rho D U^2$)
C_{pb}	base pressure
C_{pF}	pressure coefficient at the extreme front point of a cylinder
C_{pS}	pressure coefficient at stagnation point
D	diameter of the cylinder
d_u, d_d, d_t	distances from the cylinder centre to upstream, downstream and transverse boundary, respectively
F_x, F_y	fluid forces in x and y directions
F_D, F_L	fluid drag and lift forces
I	turbulence intensity
k	turbulent kinetic energy per unit mass
k_1, k_x, k_y	spring stiffness
L	centre to centre spacing between two cylinders
L/D, T/D	longitudinal and transverse pitch ratios between two cylinders, respectively

m	mass of cylinder per unit length
p	static pressure
P/D	centre-to-centre pitch ratio
R_D	diameter ratio ($= D_2 / D_1$)
Re	Reynolds number
R_{kx}, R_{ky}	stiffness ratio ($= k_x$,k_y / k_1)
St	Strouhal number
t	time
T	vortex shedding period
t^*	time interval ($= \Delta t U_0 / D$)
$\vec{u}$	velocity vector
u, v	x-component and y-component of velocity vector
U	wake velocity
U_0	reference velocity
U_c	Critical in-flow velocity
U_R	reduced velocity ($= \frac{2\pi V}{\omega_1 D_1}$)
V	free stream flow velocity
(x, y)	co-ordinates; the position of the downstream cylinder
x_s , y_s	original position of the downstream cylinder
X,Y	non-dimensionalised co-ordinates $X=x/D$, $Y=y/D$
y^+	dimensionless distance to the wall ($= \rho u_\tau y / \mu$)
α	incidence angle of two staggered cylinder relative to free stream
ϕ	general fluid flow variable; or polar angle of a circular cylinder
ϕ_S	stagnation angle
λ	eigenvalue; or a parameter for continuation analysis
μ	dynamic viscosity of the fluid
μ_t	eddy viscosity
ρ	density of the fluid

τ	non-dimensional time variable, ($=\omega_1 t$)
ω	specific dissipation rate
ω_1	natural frequency of the upstream cylinder ($=\sqrt{\frac{k_1}{m_1 + C_{m1}\frac{\pi}{4}\rho D_1^2}}$)
Subscript 1,2,3	first, second and third cylinder, from upstream to downstream

CFD	Computational Fluid Dynamics
CV	control volume used in FVM
DNS	Direct Numerical Simulation
FPSO	Floating Production, Storage and Offloading
FVM	Finite Difference Method
IFP	Institut Francais du Petrole
LES	Large Eddy Simulation
PISO	Pressure Implicit with Splitting of Operators
PRESTO	Pressure Staggering Option
RANS	Reynolds Averaged Navier-Stokes
R&D	Research and Development
SCR	Steel Catenary Risers
SIMPLE	Semi Implicit Method for Pressure Linked Equations
SIMPLEC	SIMPLE-Consistent
SST	Shear Stress Transport (Menter's $k-\omega$ turbulence model)
STD	STandard Deviation
TLP	Tension Leg Platforms
VIV	Vortex-Induced Vibration
WEC	World Energy Council

1 Introduction

The continuous increase in world's hydrocarbon demand and the finite nature of the proven reserves paved way to its exploration and production from onshore to offshore. As more and more offshore shallow water reserves had been discovered and developed, the extraction of hydrocarbons moved to deeper water depths in excess of 1000 meters. As a result of these deep water developments, the production systems towards the extraction of hydrocarbons are being deployed at greater water depths.

Several crucial components of the offshore installations like risers, mooring lines, umbilicals, cables and pipelines can be classified broadly as slender marine structures (Halse 1997). These marine structures are characterised by the bluff nature of their cross sections and hence can be termed bluff bodies. The phenomenon of flow separation around bluff bodies and shedding of vortices into the wake of the body causes the high frequency inline and transverse forces. The inline forces are called drag forces and the transverse forces are referred to as lift forces.

The Morison equation states that the total hydrodynamic force acting on a body due to a flow can be divided into two components, namely inertia force and drag force (Newman 1977). It can be seen from this equation that the form or shape of the body has a significant effect on the hydrodynamic forces acting on it. The effect of the form is quantified as hydrodynamic coefficients or drag and inertia coefficients. By virtue of its shape, a circular cross section provides properties like low hydrodynamic coefficients, high buckling strength and high strength against internal and external pressures that are quite favourable with regard to marine applications. Almost every marine structure like risers, mooring chains, umbilicals, cables, pipelines, piles, jack up legs, bracings etc are of circular cross section.

As offshore production moves to deeper water the structures become very long to cater the increased depth. The wave motion decays exponentially with water

depth and ocean currents gradually dominate the environmental loads (Halse 1997). As a consequence the oscillatory drag and lift forces and the VIV due to a steady flow will become the dominating dynamic response. Hence drag reduction and VIV suppression of these structures becomes interesting topics for investigations. Since it is found to be very difficult to determine the hydrodynamic coefficients of the bodies analytically, the coefficients presently used for the industrial designs are mainly derived from experimental results. In this regard the advent of Computational Fluid Dynamics, or CFD, as a major numerical tool to solve complex flow problems can lead us towards realistic results.

1.1 Deep water oil and gas developments

If the ten years from 1993-2003 is considered, over 70% of the reserves from the new discoveries of oil and condensates are located offshore with half in deepwater zones (around 1000 metres) (IFP 2005). Over the same period, 60% of gas discoveries were located offshore, with two thirds in deepwater. Of the 14 giant oil fields and 23 giant gas fields found between 1999 and 2003, most were offshore mainly in deepwater. Table 1-1 shows the giant oil fields discovered during the 1999-2003 period and the significance of deepwater developments.

Table 1-1 Giant oil field discovered between 1999 and 2003 (IFP 2005).

Country	Field	Location	Year of discovery	Reserves in Mbbl
Nigeria	Erha	Deep offshore	1999	500
Nigeria	Akpo	Deep offshore	2000	590
Nigeria	Bonga Southwest	Deep offshore	2001	500
Kazakhstan	Kashagan	Offshore	2000	10 000
China	Penglai 19-3	Offshore	1999	800
Malaysia	Kikeh 1	Deep offshore	2002	530
Brazil	Jubarte	Deep offshore	2001	539
Brazil	Cachalote	Deep offshore	2002	800
Brazil	1-ESS-121	Deep offshore	2003	660
Brazil	1-ESS-130	Deep offshore	2003	628
Brazil	1-ESS-123	Deep offshore	2003	560
Iran	Azadegan	Onshore	1999	5 000
Saudi Arabia	Niban 2	Onshore	1999	1 800
Iran	Kushk 1	Onshore	2001	1 407

It is estimated that over 60% of the 3.6 million barrels of new oil production will simply offset the loss from depletion of existing fields such as the North Sea or the giant Burgan field in Kuwait (Rubin & Buchanan 2006). Figure 1-1 shows the expected trend of global oil demand and supply. The increase in net global crude supply for the rest of the decade is predicted to come from non conventional sources like deep water and oil sands.

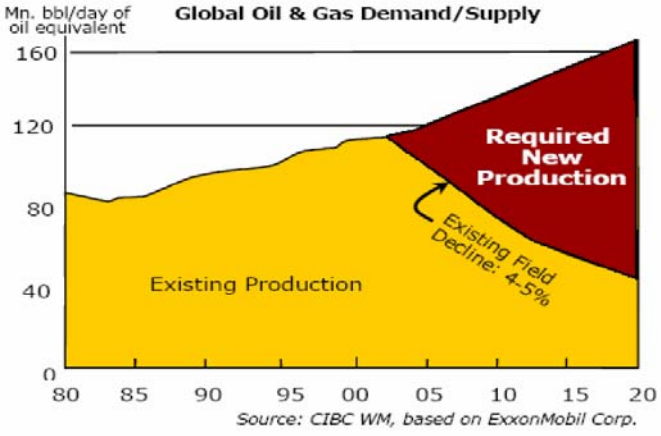

Figure 1-1 Global oil & gas demand and supply (Rubin and Buchanan 2006)

The greatest production depth of 300 meters in 1978 increased to 1800 meters by 1998. Sedimentary areas lying in over 200 meters of water represent nearly 55 million km² of sedimentary basins or four times the conventional offshore surface area (WEC 2001). Deep offshore conditions present certain characteristics like high pressures, low temperatures, large water depth range, the constant presence of ocean currents, etc, that are radically different from those typifying conventional offshore operations. The realisation that the conventional offshore solutions could not be applied at greater water depths leads to the development of new concepts. The various offshore platforms used presently are shown in Figure 1-2.

The next possible target depth of the industry is 3000 meters. The transition from deep offshore to ultra deep offshore will require higher allocations of R&D resources since it will not be possible to extrapolate from existing solutions beyond a certain limit and new ones will have to be found and proven as appropriate and

reliable.

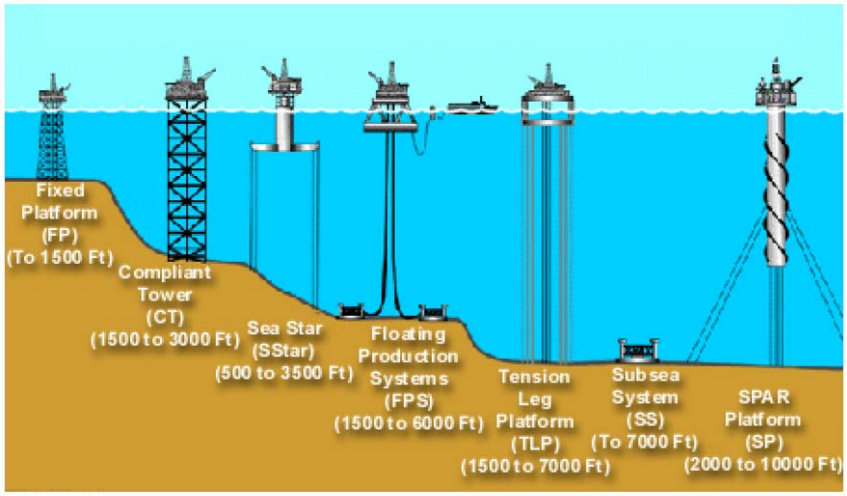

Figure 1-2 Offshore platforms (WEC 2001)

1.2 Marine risers

A riser system is essentially conductor pipes connecting floaters on the surface and the wellheads at the seabed (Bai 2009). A typical riser system is composed of conduit or riser body, interface with floater and wellhead, components and auxiliary. The functions performed by a riser system include production, injection, drilling, export, import, gas lift, completion and workover. Types of risers normally requested for deep-water fields include steel catenary risers (SCRs), top-tensioned risers (TTRs), hybrid and flexible risers.

An SCR is a single pipe suspended from the surface support facilities in a catenary shape and laying down to the seabed and either continuing directly into the horizontal flow-line or connected mechanically to the horizontal flow-line. In the last ten years this production has been greatly improved with FPSO (Floating Production, Storage and Offloading). For deep-water and even the ultra-deep water, the riser designs pose a significant challenge due to the weight of conventional SCR systems. Innovations in riser configuration and materials are needed.

In order to avoid buckling under self weight and to avoid excessive bending stresses under lateral wave, current and vortex shedding loads, rigid risers are tensioned at top from the platform (Barltrop 1998). Top tensioned risers consist of a vertical column made of several pipes used for transporting the fluids or providing some mechanical stiffness to the structure. The platforms associated with this type of risers are Tensioned Leg Platforms (TLPs) (Figure 1-3) and Spars. Deep water TLPs are mainly found in the Gulf of Mexico, but there are also some in west of Africa and off the coast of Brazil. The Spar production option has similar advantages to a TLP and may allow some oil storage. It is currently receiving considerable attention both in the Gulf of Mexico and West of Shetlands.

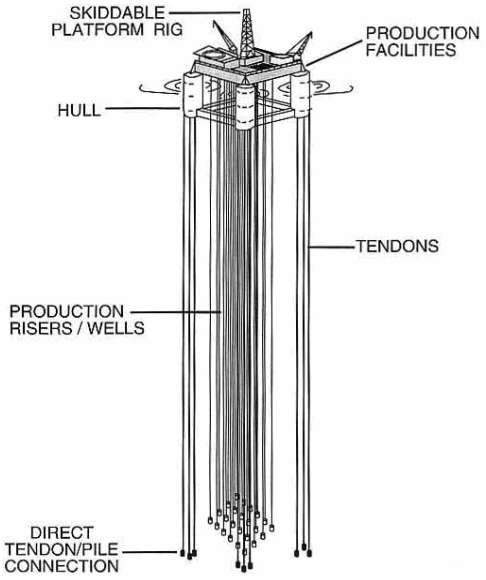

Figure 1-3 Schematic diagram of a tensioned leg platform.

Top tensioned risers for spars and TLPs are arranged in clusters of (near) vertical riser arrays. The number of individual risers in an array may be 20 or more, which may consist of different risers applied for production, drilling, workover, export, etc. Due to the small space available for the high number of risers, the clearances among individual risers are limited. Therefore the problem of riser clashing can happen to tensioned risers of a TLP or a spar located in deep waters.

1.3 Wake-induced riser clashing

Although the relative motion between individual risers is influenced by many factors, such as waves and motions of the floating hulls, it is known that currents play an important role. This is particularly so for applications in deep-waters, West of Shetland and West Africa, where strong currents are observed across the entire water column and the wave effect becomes less important as water depth becomes greater.

For the top tensioned vertical riser system in a current, the vortex-induced vibration (VIV) was and still is a primary design concern which has been under extensive investigation since the early days of offshore oil and gas exploration. As the industry moves into ever deeper waters, an additional problem of the riser system emerges, i.e. the interference between individual risers in the riser cluster in strong ocean currents as the riser lateral deflections are likely to be large and the risers are prone to wake-induced clashing.

The hydrodynamic interaction between a cluster of cylinders in a uniform current is dependent upon many factors such as the relative positions of these cylinders, Reynolds number and oncoming flow turbulence level. Among these the relative positions of these cylinders may be the most important, as the time averaged mean static force, which varies depending upon the cylinder's location in the wake, may cause fluid-elastic instability with ensuing large amplitude vibration (Wu et al. 2002).

According to Wu et al. (2001), for two cylinders with one placed in the wake of another, the downstream cylinder is subjected to non-zero mean static drag and lift forces. In this rather complicated non-linear wake force field, the downstream cylinder can have more than just one equilibrium position. Some of these equilibrium positions are stable while others are unstable. In general, the downstream cylinder will be situated at one of the stable equilibria, and if it is at an unstable equilibrium position it tends to move away from the position and converge towards a stable position under any small disturbances. As the flow velocity increases, however, it is possible that no equilibrium positions exist in the wake for the downstream cylinder.

In this case, it will move about in the wake and it is very likely that the two cylinders will collide with each other.

1.4 Aims of the thesis

The overall aim of this thesis is towards obtaining a thorough understanding of the position-related fluid forces on multiple circular cylinders in a cross flow, and, based upon the forces, developing a practical model to predict the stability of a riser cluster. The study on fluid forces is via numerical simulation of flow around multiple circular cylinders.

Specific objectives include:

i. To validate a numerical model capable of simulating flow around circular cylinders in subcritical flow regime.
ii. To calculate the fluid forces on two circular cylinders in tandem and staggered arrangement, and study the effect of spacing on forces.
iii. To study the flow patterns when two cylinders are closely spaced, and the nature of drag reduction and existence of mean lift on the downstream cylinder.
iv. To calculate the fluid forces on three circular cylinders and analyse the spacing effects.
v. To set up a practical model to analyse the stability of risers.
vi. To extend current study to more general situations, such as different risers and VIV effect.

2 Literature review

2.1 Flow around one circular cylinder

2.1.1 Flow separation and Karman vortex street

In a viscous flow the particles in the thin boundary layer close to the surface will lose parts of their kinetic energy due to friction and may have too little energy to meet the increased pressure field or adverse pressure gradient on the downstream half of the body. Hence a boundary layer separation will result as shown in Figure 2-1. At the separation point the flow from ahead and behind will meet in a stagnation point and advance in a different direction. This will give rise to a vortex that will feed on the energy loss in the wake due to boundary layer separation. The vortices are then convected away by flow velocity and together with other vortices form Karman vortex street.

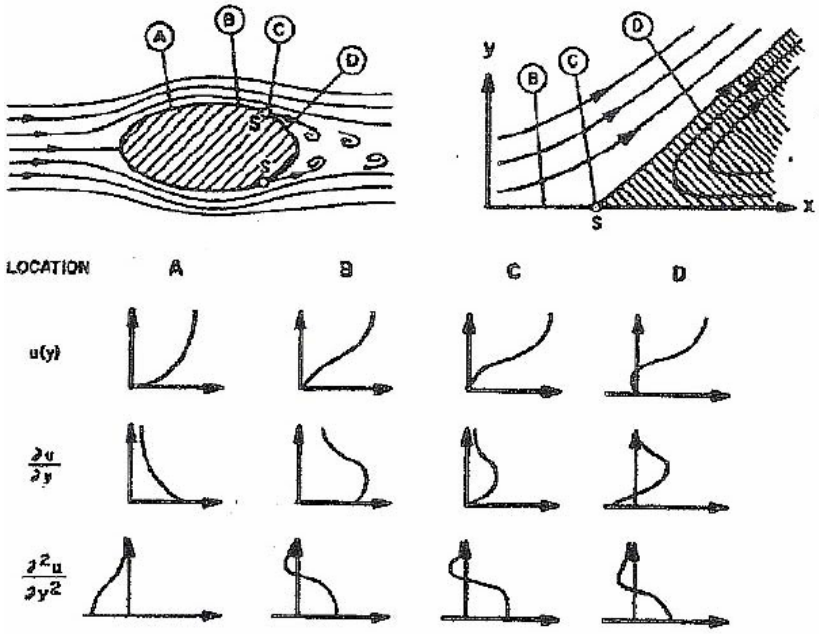

Figure 2-1 Viscous flow around a bluff body (Halse 1997).

When a fluid flows around a circular cylinder like marine riser, the flow will separate from the surface of the cylinder except at very low velocities and form vortices that are convected downstream by the flow velocity. A characteristic vortex street often referred to as a Von Karman Street is formed in the wake of the cylinder. On a fixed cylinder a linear relation is found between the vortex shedding frequency and the flow velocity (Halse 1997). The relation is expressed mathematically as

$$f_s = \frac{S_t V}{D} \tag{2.1}$$

where f_s is the vortex shedding frequency, V is the incoming flow velocity, D is the diameter of the cylinder and St is the proportionality constant called as the Strouhal number. The relationship was established in 1878 by Strouhal and later has been called as the Strouhal relation.

In 1879 Lord Rayleigh confirmed the Strouhal relation but found that the string was actually vibrating in a direction transverse to the flow direction. In 1908 Benard(1908) related the tone to the vortex formation and the existence of a vortex street. In 1912 Von Karman found then a symmetrically staggered vortex arrangement is stable for one explicit ratio of the vortex street width (h) and distance between two adjacent vortices (l) as given below.

$$\frac{h}{l} = \frac{1}{\pi}\cosh^{-1}\left(\sqrt{2}\right) = 0.2805 \tag{2.2}$$

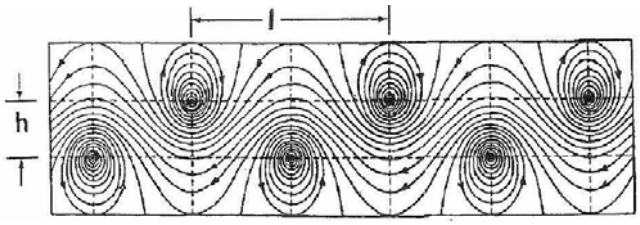

Figure 2-2 Karman Vortex Street (Blevins 1990).

This arrangement is later referred to as Von Karman Street and is shown in Figure 2-2.

2.1.2 Flow regimes for steady flow around a fixed cylinder

For the flow around circular cylinders, whether or not separation will occur and the position of the separation point is Reynolds number dependent. For a circular cylinder the Reynolds number is given as

$$Re = \frac{\rho VD}{\mu} \tag{2.3}$$

where Re is the Reynolds number, ρ is the density of the fluid, V is the characteristic flow velocity, D is the diameter of the cylinder and μ is the dynamic viscosity of the fluid. Figure 2-3 shows main characteristics of six different flow regimes around a smooth cylinder.

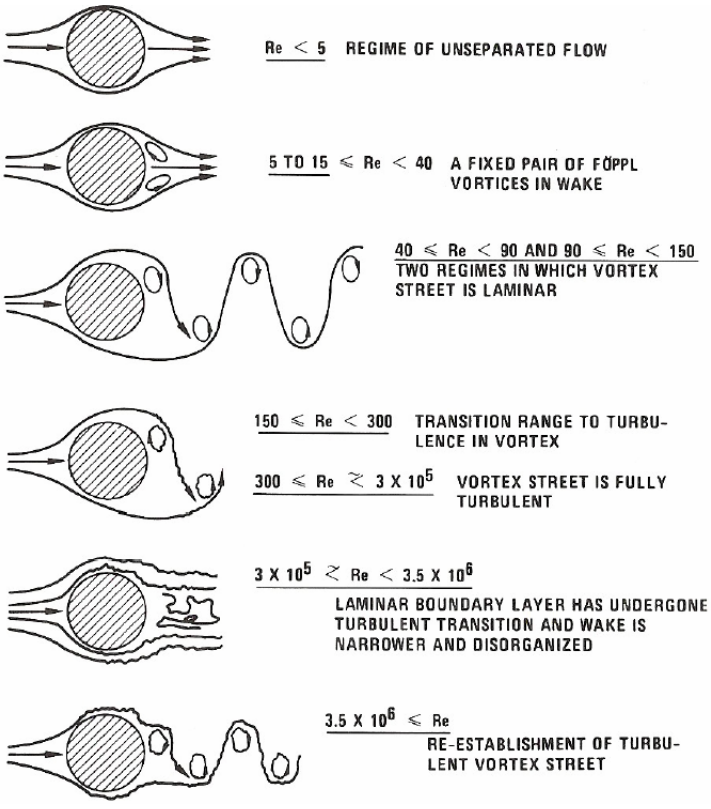

Figure 2-3 Flow regimes around a cylinder (Blevins 1990).

For Re < 5, the flow is laminar and follows the cylinder contours. For 5 ≤ Re ≤

45 the boundary layer separates on each side of stagnation point. The two separated shear layers meet at an increasing distance behind the cylinder enclosing a pair of symmetrical standing vortices. For Re above 50 to 60 wavy characteristics of the wake and alternate shedding of vortices takes place. The laminar vortex shedding forms the Karman's vortex street and this is continued till a Re of 150. As Re increases further, one of the vortices break away and a laminar periodic wake of staggered vortices of opposite sign is formed. Between Re = 150 and 300 the wake becomes turbulent although boundary layer on the cylinder remains laminar (Blevins 1990).

The Re range $300 < Re < 1.5\times10^5$ is called subcritical. In this range the wake is turbulent but boundary layer is laminar and separates at 80^o. The fully developed Karman Street is characterised by a constant Strouhal number of 0.20. In the transitional or critical range, 1.5×10^5 to 3.5×10^6, the separation point moves backwards from an angle of 80^o to an angle of 140^o causing a decrease of wake width and drag coefficient from 1.2 to 0.3. In this range the flow undergoes at first a laminar separation at 100^o and reattaches the cylinder wall, forming an attached separation bubble, before separating downstream at 140^o. No regular vortex shedding is observed in this regime. In the supercritical regime, for $Re > 3.5\times10^6$, the separation bubble gradually disappears and fully turbulent separation occurs at 110^o, the wake width increases and drag coefficient reaches a stable value of 0.54 and turbulent vortex shedding provides a quasi constant Strouhal Number of 0.30 (Blevins 1990).

The vortex shedding frequency is usually found from the Strouhal relation. The Strouhal number is a function of Reynolds number and to a lesser extent surface roughness and free stream turbulence (Blevins 1990). Figure 2-4 shows the variation of Strouhal number with Re. For low Re, *St* increases with Re and exhibits a constant value of 0.20 in the subcritical regime. In the critical regime a broad banded spectrum is found for a smooth cylinder. In supercritical regime a constant value of 0.30 is established.

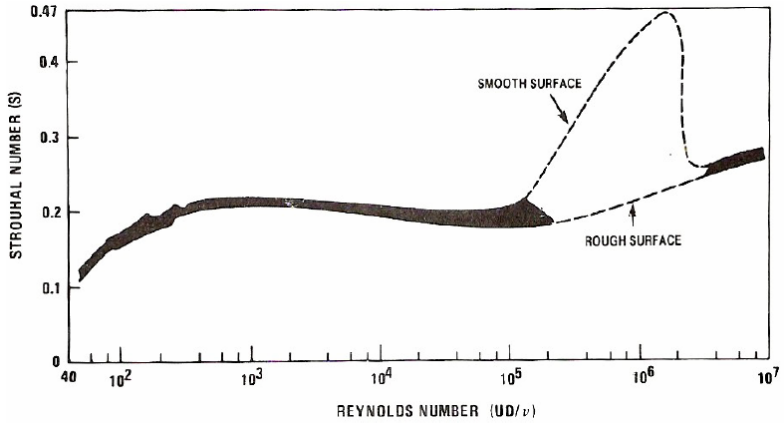

Figure 2-4 Strouhal number with Re (Blevins 1990).

2.1.3 Fluid forces

The alternate shedding of vortices from the either side of the surface of a circular cylinder at significantly high Re results in a periodic pressure field surrounding the structure as illustrated in Figure 2-5. Consequently oscillating forces occur both in line and cross flow to the incoming flow direction. These forces are called vortex induced forces or flow induced forces and the inline and cross flow forces are called drag and lift respectively (Blevins 1990).

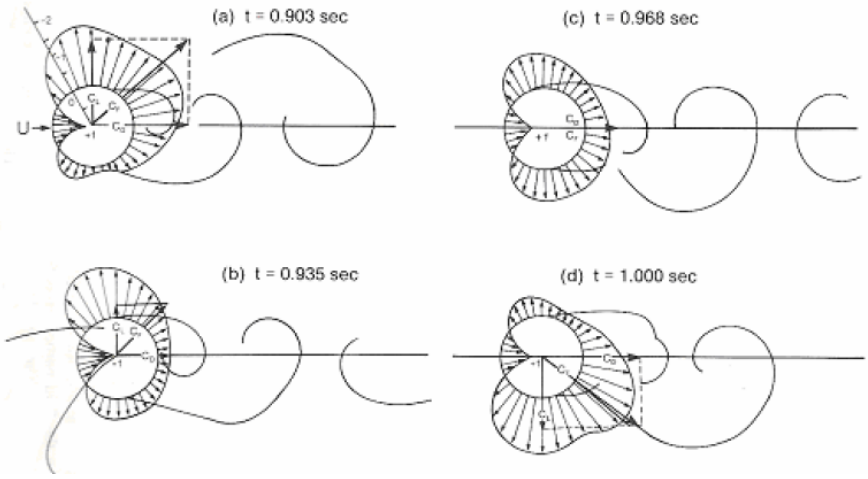

Figure 2-5 Pressure distribution in half a vortex shedding period (Blevins 1990).

The time histories of the oscillating drag and lift forces are given in Figure 2-6. It can be observed that the transverse force component oscillates at the frequency of vortex shedding with a zero mean whereas the inline component oscillates at twice the frequency of vortex shedding with a nonzero mean. The amplitude of lift or transverse force is also observed to be greater than that of the drag or inline force (Sumer & Fredsoe 1997).

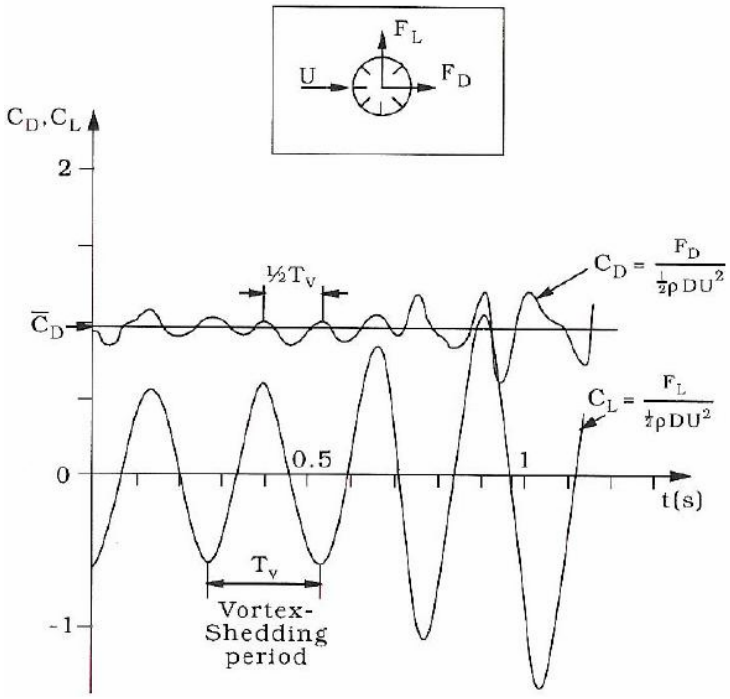

Figure 2-6 Oscillating drag and lift forces (Sumer & Fredsoe 1997).

The drag coefficient C_D and lift coefficient C_L are defined as

$$C_D = \frac{F_D}{\frac{1}{2}\rho DV^2} \tag{2.4}$$

$$C_L = \frac{F_L}{\frac{1}{2}\rho DV^2} \tag{2.5}$$

where $\frac{1}{2}\rho DV^2$ is the dynamic pressure head. For a smooth circular cylinder the

mean drag coefficient is a function of Re and is shown in Figure 2-7. It can be observed that C_D is practically constant at 1.2 throughout the subcritical range (300 to 3×10^5) followed by dropping to a value of 0.30 due to a phenomenon called the drag crisis in the critical regime and attains a constant value of 0.50 in the supercritical regime.

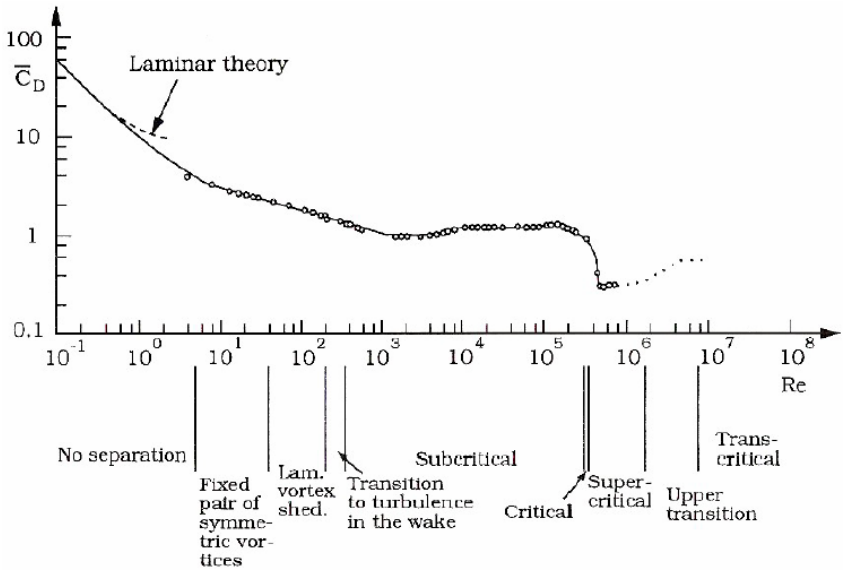

Figure 2-7 Drag coefficient of a smooth cylinder as a function of Reynolds number (Sumer and Fredsoe 1997).

The mean drag force acting on a cylinder in a steady flow can be resolved into two components, one from pressure and other from friction or viscosity. The pressure drag or form drag is the inline component of the mean resultant force due to pressure acting on the cylinder while friction or viscous drag is the inline component of the mean resultant force due to friction (Sumer and Fredsoe, 1997). The contribution of friction drag to total drag force is less than 2-3 % for the range of Re encountered in practice. The pressure at the rear side of the cylinder is always negative due to separation in contrast to the fore and aft symmetry given by potential theory. Pressure drag is due to the fore and aft asymmetry of pressure distribution.

For circular cylinder flow the lift has zero mean value. The r.m.s. (root-mean-square) lift coefficient C_L' is used to measure the oscillating lift force. A vast amount of

quantitative data has been reported and numerous compilation graphs on the variation of lift-related coefficients with Reynolds number have been presented. Despite these efforts, there has been no real consensus on $C_L'(\mathrm{Re})$. As shown in Figure 2-8.

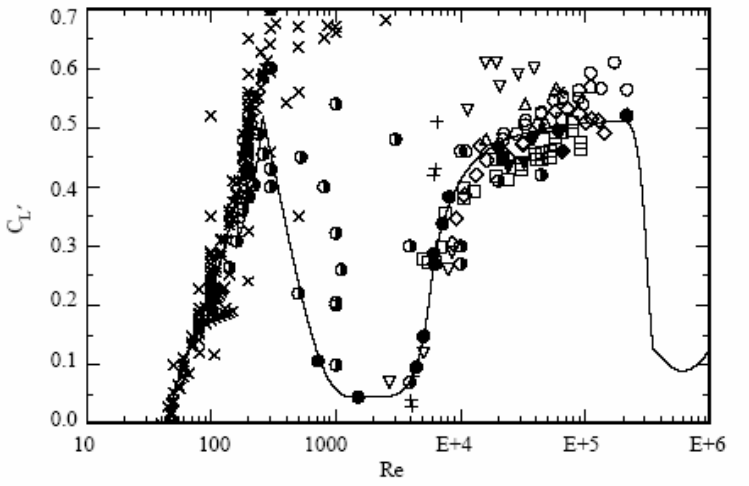

Figure 2-8 r.m.s lift coefficient versus Reynolds number (Norberg 2003).

2.2 Flow around two circular cylinders

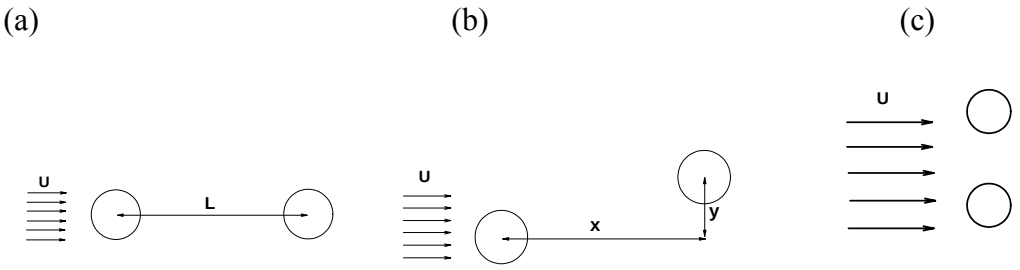

Figure 2-9 Configuration of two circular cylinders.

Basically there are three types arrangements for two identical circular cylinders, as shown in Figure 2-9: tandem (a), staggered (b) and side-by-side (c) arrangements. As the main concern of this thesis is the wake effect of the upstream cylinder on the downstream one, only case (a) and (b) are considered. The tandem arrangement is

often measured by the centre to centre spacing L or the spacing ratio L/D.

Generally, there are two notations for staggered configurations of two circular cylinders of equal diameters in a steady cross-flow. One is by the centre-to-centre pitch ratio, P/D, and the incidence angle, α, see Figure 2-10(a); the other is by the longitudinal and transverse pitch ratios, L/D and T/D, respectively, see Figure 2-10(b). In the thesis, similar with the L/D-T/D system, the positions of the cylinders are defined by Cartesian coordinate system, with the origin located at the centre of upstream cylinder and x-axis parallel to the free stream direction, i.e. Figure 2-10(b). In this way it is more convenient to extend to the case of three cylinders flow. For staggered arrangement, both the upstream and the downstream cylinders are designated an inner side and an outer side, according to their relative positions and the direction of free stream.

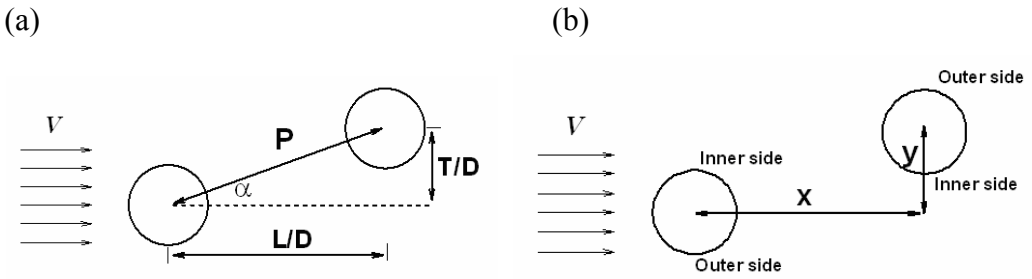

Figure 2-10 Notation for two staggered circular cylinders.

Turbulent flow past two circular cylinders represents a very complicated flow phenomenon. Excellent summaries of this problem have been compiled in review articles by Zdravkovich (1977; 1987; 1997). A number of high-quality experimental investigations of the fluid dynamics for two cylinders flow in subcritical regime can be found in the literature, for example: Price (1976), Zdravkovich & Pridden (1977), Kiya et al. (1980), Igarashi (1981; 1984), Price & Paidoussis (1984), Ljungkrona et al. (1991), Zhang & Melbourne (1992), Gu & Sun (1999), and Sumner et al. (2000; 2005).

2.2.1 Flow patterns

The complexity of the two cylinders flow arises from the interaction of four separated free shear layers, two Karman vortex formation and shedding processes, and interactions between the two Karman vortex streets (Sumner et al. 2005). Zdravkovich(1987) classified the fluid behaviour of two cylinders flow into four types of interference, based on the location of the downstream cylinder with respect to the upstream one, as shown in Figure 2-11:

- Proximity interference, P, which takes place when the cylinders are close to each other, but none of them is submerged in the wake of another.
- Wake interference, W, which takes place when one cylinder is near to or submerged into the wake of the other. Tandem arrangement is a special case of wake interference.
- Combination of proximity and wake interference, P+W.
- Finally, there is a substantial region where the interference is negligible. The flow around each cylinder in that region is effectively identical to that around a single cylinder.

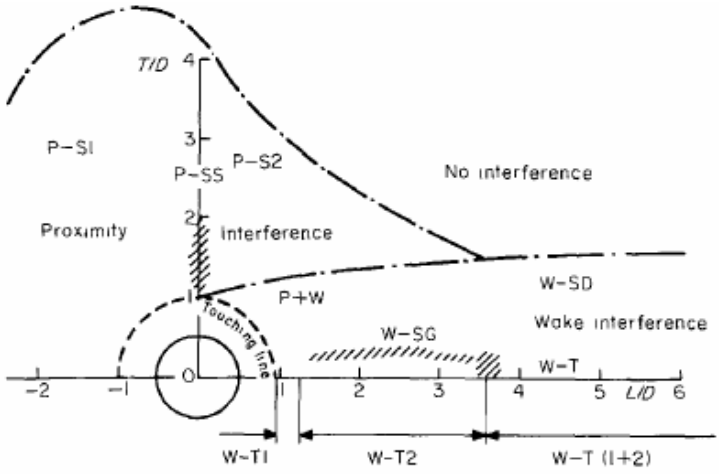

Figure 2-11 Flow patterns of two cylinders in cross flow, after Zdravkovich (1987).

The above four types can be simplified as two basic ones: wake interference and proximity interference. Gu and Sun (1999) extended this classification to three

different types, namely wake interference, shear layer interference, and neighbourhood interference. However, their work was limited to small and intermediate spacing ratios. Recently Sumner et al.(2000) conducted more extensive flow visualization and PIV experiments within the low subcritical regime (Re = 850–1900) and revealed a much wider range of flow patterns for the staggered configuration. Nine distinct patterns were identified which are illustrated in Figure 2-12 and Figure 2-13. These flow patterns can broadly be grouped into three categories: single bluff-body flow patterns (Figure 2-12a-c), flow patterns at small angles of incidence (Figure 2-12d-f), and flow patterns at large angles of incidence (Figure 2-12g-i). The flow patterns were also summarised by Akbari & Price (2005).

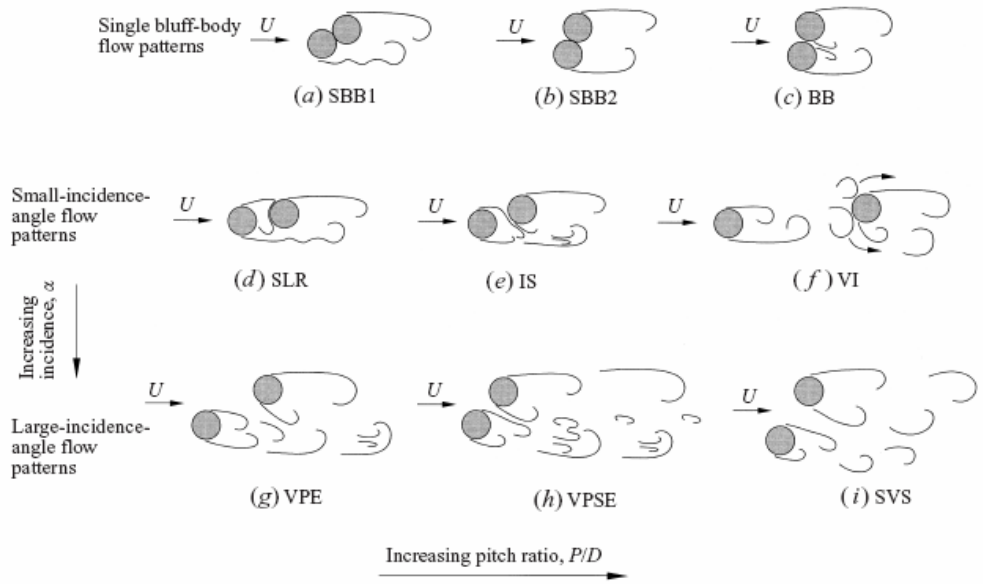

Figure 2-12 Overview of flow patterns for two staggered circular cylinders of equal diameter in steady cross-flow, in the low subcritical regime, based on Sumner et al. (2000).

According to Sumner et al.(2000), when the two cylinders are located very close to each other, the flow pattern resembles that of a single bluff body. The near wake region of the cylinder pair contains two free shear layers that alternately shed Karman vortices at the same frequency, much like that observed for a single, isolated circular cylinder. When the cylinders are in contact, two types of single bluff-body behaviour could be distinguished, designated SBB1 and SBB2 for the incidence

angle less than and greater than 45 degree, respectively. A third single bluff-body flow pattern (BB) is seen at very small pitch ratios (<1.25) and high angles of incidence, with the added effect of base bleed, as shown in Figure 2-12 and Figure 2-13.

Designation	Full name	Occurrence	Key features
SBB1	Single bluff-body, type 1	$P/D = 1.0$ to 1.125 $\alpha = 0°$ to 45°	Instabilities in the shear layer from the upstream cylinder
SBB2	Single bluff-body, type 2	$P/D = 1.0$ to 1.125 $\alpha = 45°$ to 90°	Single, low-frequency Kármán vortex shedding process
BB	Base-bleed	$P/D = 1.125$ to 1.25 $\alpha = 45°$ to 90°	Weak gap flow of variable deflection angle and a single vortex street
SLR	Shear layer reattachment	$P/D = 1.125$ to 4.0 $\alpha = 0°$ to 20°	Reattachment of the inner shear layer from the upstream cylinder
IS	Induced separation	$P/D = 1.125$ to 3.0 $\alpha = 10°$ to 30°	Narrow gap flow induces separation and vorticity generation on the inner surface of the downstream cylinder
VPE	Vortex pairing and enveloping	$P/D = 1.25$ to 3.5 $\alpha = 20°$ to 45°	Pairing of gap vortices and enveloping of the pair by a Kármán vortex from the outer shear layer of the upstream cylinder
VPSE	Vortex pairing, splitting and enveloping	$P/D = 1.25$ to 4.0 $\alpha = 20°$ to 90°	As above, but with incomplete enveloping of the gap vortex pair
SVS	Synchronized vortex shedding	$P/D = 1.5$ to 5.0 $\alpha = 15°$ to 90°	Anti-phase synchronization of gap Kármán vortex shedding
VI	Vortex impingement	$P/D = 3.0$ to 5.0 $\alpha = 0°$ to 20°	Impingement of Kármán vortices from the upstream cylinder onto the downstream cylinder

Figure 2-13 Specification of the flow patterns in Figure 2-12, after Sumner et al. (2000).

Sumner et al. (2000) also identified three flow patterns for small angles of incidence. For very small pitch ratios, P/D < 3.0, and at small angles of incidence, $\alpha < 10^\circ$ to 20°, the shear layer reattachment flow pattern (SLR) is observed, in which the shear layer originating from the upstream cylinder reattaches on the outer side of the downstream cylinder, effectively preventing flow through the gap between the cylinders. At slightly greater angles of incidence, from 10° to 30°, shear layer reattachment can no longer be maintained. The shear layer from the inner side of the upstream cylinder is deflected into the gap between the cylinders. This shear layer rolls up in the gap and induces a separation of the flow from the downstream cylinder. This flow pattern is referred as induced separation (IS). At larger pitch ratios and small angles of incidence, the Karman vortices from the upstream cylinder are

formed completely and impinge upon the downstream one, hence the vortex impingement flow pattern arises (VI).

For larger angles of incidence, vortex shedding occurs from both cylinders. Sumner et al. (2000) reported that, the most commonly observed flow pattern is synchronized vortex shedding (SVS). The vortices shedding from the two sides of the gap synchronized, resulting in two adjacent, anti-phase Karman vortex streets. The vortex pairing and enveloping flow pattern (VPE) was reported for smaller pitch ratios. There is a counter-rotating vortex pair structure at the gap exit, which is then enveloped by a Kaman vortex from the outer shear layer of the upstream cylinder. When the enveloping process was not complete, it involves splitting of the vortex pair, resulting in vortex pairing, splitting and enveloping flow pattern (VPSE).

Approximate boundaries for the above nine distinct flow patterns are shown in Figure 2-14. For detail, the readers are referred to Sumner et al.(2000).

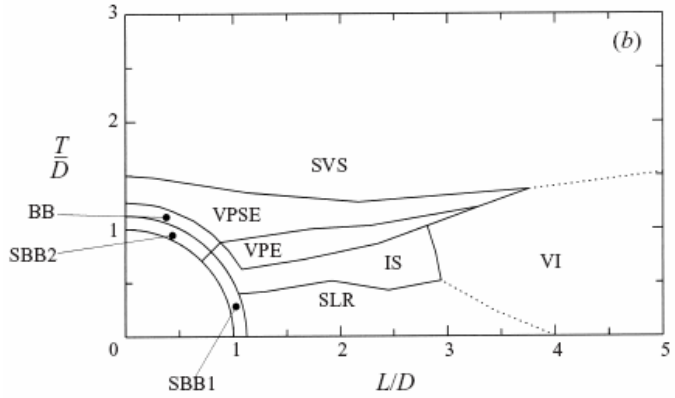

Figure 2-14 Flow pattern boundaries for two staggered cylinders in steady cross-flow, after Sumner et al.(2000).

2.2.2 Fluid forces

As a special case, flow around two tandem circular cylinders has been well studied. Zdravkovich (1987) compiled all the drag coefficient data into a single plot of C_{D1}

(upstream cylinder) and C_{D2} (downstream cylinder) in terms of spacing ratio and Reynolds number, as shown in Figure 2-15. It can be seen the most prominent feature is a discontinuous jump in C_{D1} and C_{D2} at $3 < L/D < 4$. There is a negligible Re effect on C_{D1} curves but a strong effect on C_{D2} curves. For $L/D < 2$, C_{D2} is negative, and acts as a thrust force. For $L/D > 3.5$, C_{D2} becomes positive.

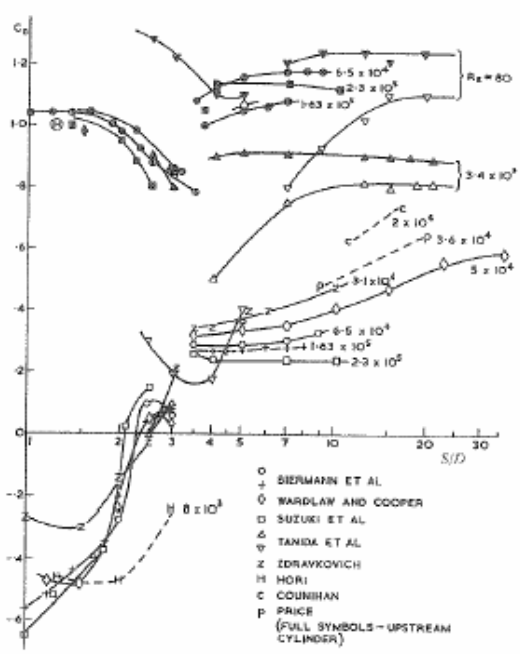

Figure 2-15 Drag coefficients on two tandem cylinders in term of spacing ratio S/D and Re, after Zdravkovich (1997).

A map of the static force coefficients for two circular cylinders of equal diameter subjected to cross-flow in the subcritical Reynolds number regime, which was furnished by Zdravkovich (1987), is shown in Figure 2-16. Contours of constant static drag and lift coefficients are plotted in the L/D versus T/D plane.

The upstream cylinder experiences positive lift directed outward for $\alpha > 40^{\circ}$ and a relatively small decrease in drag and a significant increase in Strouhal number. There is a region of negative lift directed towards the gap when the two cylinders are close to each other, at small angle of incidence.

For the downstream cylinder, when 1.1 < L/D < 3.5 and T/D = 0.2, the strong gap flow between the cylinders induces a significant inner lift force (Zdravkovich 1977), which suddenly disappears for T/D < 0.2 as the gap flow ceases. When L/D > 2.8 and T/D > 0.4, the outer lift force is produced by the displacement of the fully formed wake of the upstream cylinder by the flow around the downstream cylinder. The outer lift reaches a maximum value near the edge of the wake boundary when T/D > 0.4and diminishes gradually to zero when the tandem arrangement is reached.

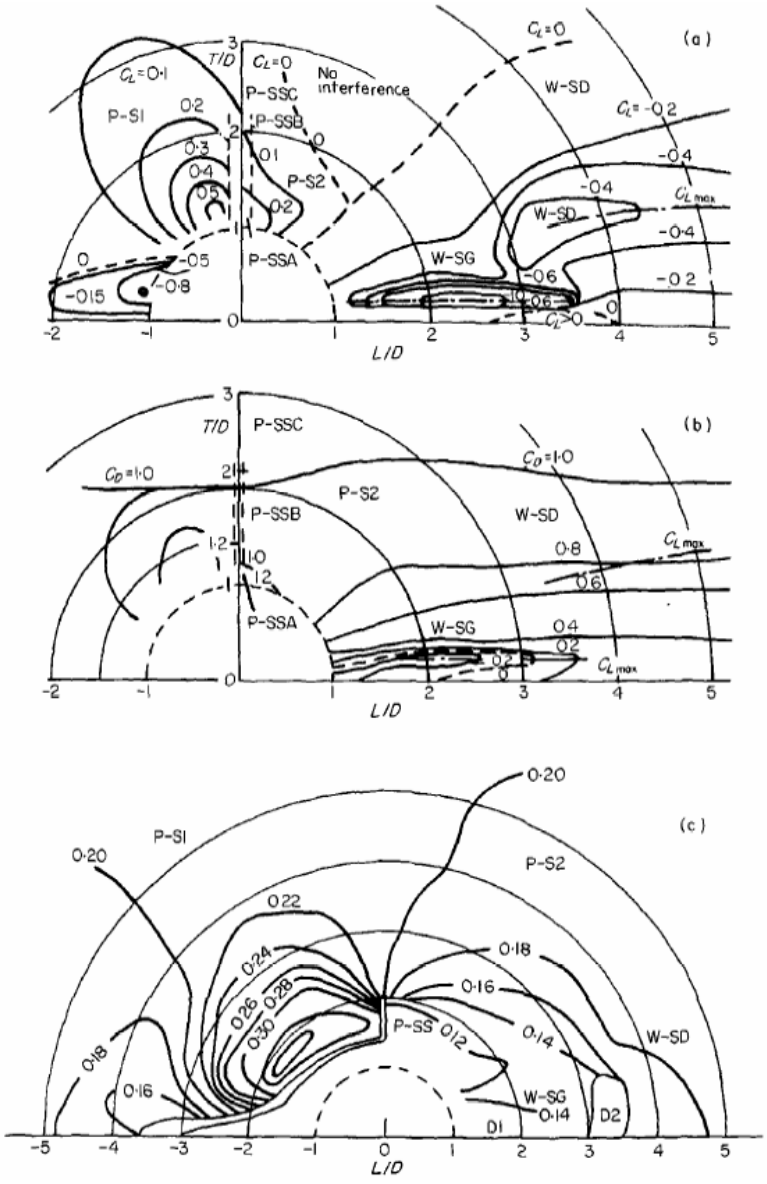

Figure 2-16 Force coefficients and Strouhal number for two circular cylinders: (a) lift coefficient; (b) drag coefficients; (c) Strouhal number, after Zdravkovich (1987).

Figure 2-16 shows the variation of the lift, drag, and Strouhal number. The inner and outer lift forces are always directed towards the axis of the upstream wake. The deflected near wake behind the downstream cylinder produces a minimum drag force at the same staggered arrangements where the inner lift force is maximum. In contrast, the outer lift maximum has no effect on the drag force or Strouhal number.

A number of different explanations for the origin of the outer lift force have been provided in the literature, which were summarized and assessed by Price (1976) and Ting et al. (1998). Maekawa (1964) attributed the lift force to a buoyancy-like effect as the static pressure distribution in the wake is at its minimum at the center of the wake. However, by integrating the static pressure around the cylinder's surface, Best and Cook (1967) concluded that only 30 percent of the lift force could be attributed to buoyancy.

Mair and Maull (1971) suggested a resolved drag model. This model is based upon the observation that due to the entrainment of fluid into the wake, the flow velocity at the downstream cylinder is directed towards the wake centerline; hence, the lift force experienced by the downstream cylinder would be a resolved component of the drag force. However, it was shown by Price (1976) that this amount is still far from sufficient to account for the total lift force.

Rawlins (1974) ascribed the lift force to circulation. Owing to the variation of turbulence and velocity across the wake of the windward cylinder, the upper and lower boundary layers of the leeward cylinder feed different amounts of vorticity into their associated shear layers. Applying Kelvin's circulation theorem, Rawlins concluded that a circulation around the cylinder is built up until the vorticity discharging rates from the two boundary layers are equal. A lift force can then be calculated which is proportional to the drag gradient across the wake. Price showed that the result predicted by this method is still some 30 percent lower than the measured one.

2.3 Flow around three circular cylinders

According to Zdravkovich (1987), three cylinders can be arranged into three categories: (a) all three cylinders aligned and oriented from in-line to side-by-side arrangements; (b) regular triangular arrangement where all cylinders are spaced equidistantly; and (c) distorted triangular cluster, composed of all other possible arrangements, except (a) and (b).

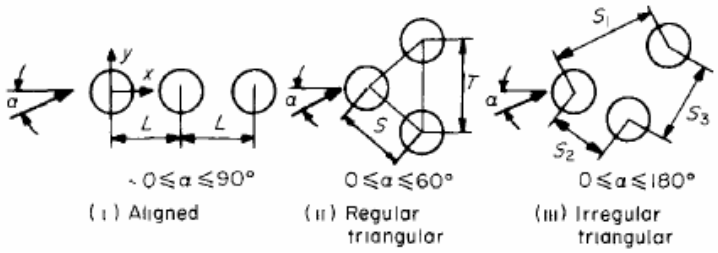

Figure 2-17 Classification of three-pipe clusters after Zdravcovich (1987).

The addition of a third cylinder to a tandem arrangement of two, produces a new kind of flow which differs from both the flow behind the first two cylinders. Early pressure distribution measurements show that the flow around the first two cylinders was almost unaffected by the addition of the third and fourth cylinder. The pressure distributions around the third and fourth cylinders were similar, and might be taken as typical for any additional number of cylinders aligned in a column (Zdravkovich (1987).

A systematic investigation of the flow around three in-line cylinders has been carried out by Igarashi (Igarashi & Suzuki 1984; Igarashi 1986) in the subcritical state of flow. Figure 2-18 shows the pressure drag coefficients for all three pipes and Strouhal numbers measured behind the third one. Three flow patterns can be identified. When the cylinders are very close, they act like a single cylinder. The flow pattern changes with the formation of vortices in the gap between the second and third cylinder, which results in distinct jumps in the drag of the last two cylinders and a fall in the Strouhal number. At L/D = 3.5 vortices form behind the first cylinder and the drag of the third cylinder decreases slightly and Strouhal number increases

considerably. The hysteresis phenomenon can be observed when the flow pattern changes. A hysteresis phenomenon means the flow pattern persists longer when inceasing (labelled A and B) or decreasing (labelled C and D) the spacing between the cylinders. The hysteresis produced an apparent overlap of the two flow patterns for certain spacing although only one flow pattern exists at a time.

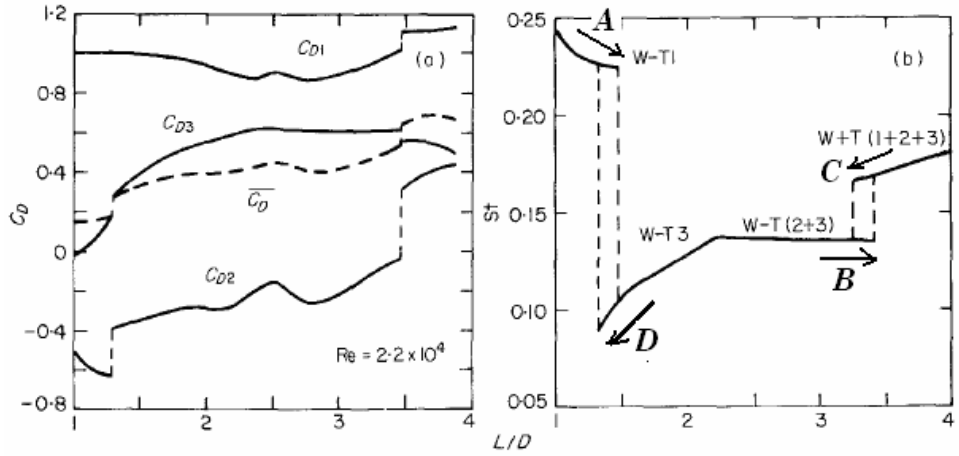

Figure 2-18 Effect of spacing on flow around three in-line circular cylinders: (a) drag coefficient ($\mathrm{Re}=2.2\times10^4$); (b) Strouhal number ($\mathrm{Re}=2.7\times10^4$), after Igarashi and Suzuki (1984).

Dalton & Szabo (1977) measured the drag component of force exerted on each of three aligned cylinder in the range $0^\circ<\alpha<90^\circ$, as shown in Figure 2-19. It is evident that the variation of the drag coefficient of the third cylinder is considerably different from that behind the second cylinder. there is an increase in C_{D3} in comparison to C_{D2}, but C_{D3} is always less than C_{D1}.

2.4 Numerical simulations of flow around multiple cylinders

Flow around a cylinder with circular section is a widely studied phenomenon since this problem is of interest with respect to many technical applications. The simulation of this flow is considered a classic benchmark problem for evaluating numerical methods, such as Tutar & Holdo (2001), Rocchi & Zasso (2002),

Richmond-Bryant (2003) and Holloway et al. (2004).

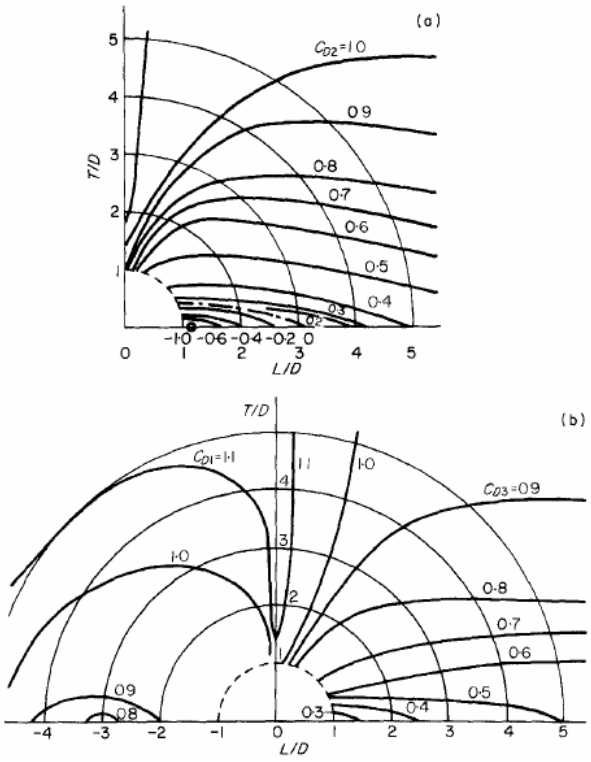

Figure 2-19 Measured drag coefficient on the three aligned pipes in tandem, staggered and side-by-side arrangements at $\mathrm{Re} = 6.7 \times 10^4$. (a) Second cylinder; (b) third cylinder, after Zdravcovich (1987) adapted from Dalton and Szabo (1977).

Flow around multiple cylinders has been studied primarily from an experimental approach, and mostly at high subcritical Reynolds numbers, since they are more commonly found in industrial applications. Because of the complexity of the flow, numerical work on two cylinders flow is limited and often for low Reynolds numbers Re < 200, for example: Li et al. (1991) developed a finite element program to simulate flow past two tandem circular cylinders at Re = 100; Slaouti and Stansby (1992) applied the random vortex method to study flow around multiple circular cylinders at a Reynolds number of 200; and Meneghini et al. (2001) investigated two tandem circular cylinders in a cross flow with the Reynolds number ranged from 100 to 200. Nevertheless, there are some numerical researches on flow around two cylinders at higher Reynolds numbers recently.

Mittal et al. (1997) employed a stabilized element formulation to study incompressible flow past a pair of cylinders at Re = 100 and 1000, in tandem and staggered arrangement. For tandem arrangement two cases of L = 2.5D and 5.5D were studied while for staggered arrangement the spacings were x = 5.5D and y = 0.7D. In all cases, when the flow becomes unsteady, the downstream cylinder, which lies in the wake of the upstream one, experiences very large unsteady forces that may lead to wake-induced flutter. The Strouhal numbers for both cylinders have the same value.

Jester & Kallinderis (2003) performed a comprehensive numerical investigation of incompressible flow about fixed cylinder pairs for Re = 80 and 1000. A second order Streamline Upwind Petrov–Galerkin projection scheme is used along with routines for interactive steering and dynamic meshing to solve the 2-D incompressible Navier–Stokes equations efficiently on a large number of different configurations. Qualitative and quantitative comparisons with published experimental data were made which show the ability of their numerical method to capture complex, unsteady flow features. Experimentally observed flow physics such as hysteresis effect and bistable phenomenon in tandem arrangements were reproduced. Furthermore, an extensive series of staggered simulations were performed.

Akbari & Price (2005) carried out numerical simulations of the flow patterns around two staggered circular cylinders in cross-flow at Re = 800. The unsteady two-dimensional Navier–Stokes equations were solved using a numerical vortex method. Detailed numerical results for the flow patterns for different arrangements of the cylinders were presented and compared with existing experimental data. Five distinct flow regimes, depending on the geometrical arrangement of the cylinders, were identified in the simulations.

Recently Kitagawa & Ohta (2008) performed three-dimensional fluid computations to investigate the flows around two circular cylinders in tandem arrangements at a subcritical Reynolds number, $Re = 2.2\times10^4$. The center-to-center space between the cylinders was varied from twice the cylinder diameter to five times. Special attention

was paid to the characteristics of the vortices shed from the upstream cylinder such as the convection, the impingement onto the downstream cylinder and the interaction with the vortices from the downstream cylinder. The effects of the vortices from the upstream cylinder on the fluid-dynamic forces acting on the downstream cylinder were discussed. With the 3-D simulation, the fluid forces and the characteristics of the vortices in the study showed agreement with the experimental data.

Numerical work on flow around more than two cylinders is considerably limited and only for low Reynolds numbers. For example, Lam et al. (2003) investigated the flow around four cylinders in a square configuration with a spacing ratio of 4 and at a Reynolds number of 200. Several distinct flow patterns were observed. Liang et al. (2009) numerically studied the effect of tube spacing on the vortex shedding characteristics and fluctuating forces on an inline cylinder array up to six cylinders. The examined Reynolds number is 100 and the flow is laminar.

2.5 Stability of elastically supported cylinders with wake interference

The above reviews are all for stationary cylinder(s). For a riser cluster, which can be simplified as elastically supported cylinders, the flow field becomes significantly more complicated because of the interaction of the fluid flow and the cylinders' motion. To engineers, unfortunately this is more likely the case of reality.

According to Price (1995), the possibility exists for riser vibrations induced by the flowing fluid via one or more of the following: (i) buffeting of the body due to turbulence, (ii) resonance with a flow periodicity (vortex shedding), and (iii) fluidelastic instability. The last can cause riser clashing with large amplitude vibration.

For a riser cluster or elastically mounted cylinders the fluidelastic instability is mainly associated with the position-related fluid forces (Wu et al. 2001; Blevins 2005). For two staggered cylinders in cross flow, the downstream cylinder is carried aft by its drag and toward the wake centreline by its lift. The upstream cylinder has

larger streamwise displacement owing to the higher drag, which results in smaller spacing between the cylinders than the initial. The change of relative positions of the cylinders consequently leads to the change of fluid forces on the downstream cylinder. Therefore the system is non-linear. Wake-induced fluidelastic instability can occur at certain velocity of the current.

The work on wake-induced fluidelastic instability of a riser cluster or multiple cylinders involves basically two parts: the prediction of fluid forces and the establishment of the stability analysis model.

Huse (1993) described a simple calculation procedure based on wake and momentum considerations, for predicting the current force on each individual cylinder in an array of cylinders. He then used this procedure for calculating the static deflection of each riser in the riser system of TLPs, and determining necessary spacing to prevent the risers from colliding with each other.

Considering two cylinders, with one in the wake of the upstream cylinder, Huse (1993) calculated the wake velocity deficit based on Schlichting (1979) as follows:

$$u = U_0 \exp(-0.639(y/b)^2) \tag{2.6}$$

$$U_0 = V(C_{D1}D_1 / x_s)^{1/2} \tag{2.7}$$

$$b = 0.25(C_{D1}D_1 x_s)^{1/2} \tag{2.8}$$

$$x_s = x_v + x \tag{2.9}$$

$$x_v = 4D_1 / C_{D1} \tag{2.10}$$

where u is the wake velocity deficit at a position (x, y) (where the downstream cylinder situates) in the wake and U_0 is the maximum wake velocity deficit the wake centreline; V is the free stream velocity; C_{D1}, D_1 are the drag coefficient and diameter of the upstream cylinder, respectively; b is the half width of the wake; x_v is the distance from virtual source to the cylinder which is used to modify the result when x is not large enough.

The current force on the downstream cylinder can now be calculated as

$$F = 0.5\rho D_2 C_{D2}(V-u)^2 \tag{2.11}$$

where C_{D2}, D_2 are the drag coefficient and diameter of the downstream cylinder. The RMS averaged value over the downstream cylinder diameter is used by Huse (1993) for the wake velocity deficit *u* in the above formula, considering *u* varies over the space occupied by the downstream cylinder.

Wu et al. (2001; 2002; 2003) investigated the mean lift and drag forces on a cylinder placed in the wake of another upstream cylinder and the influence of these forces on the stability of the downstream cylinder. The forces were predicted based upon a free streamline model and the utilisation of some available experimental data. The stability of the downstream cylinder's equilibrium position was then analysed by finding eigenvalues of the linearised equation of motion. It is found that under the influence of these forces the equilibrium position can become unstable depending upon the value of the mass parameter.

Blevins (2005) produced a simple model for the steady lift and drag on a cylinder that is in the wake of another cylinder using theoretically based equation forms fitted to data. The resultant expressions have good agreement with the data for axial spacing more than about two diameters. The model was applied to static response and dynamic stability of elastically mounted cylinders. Equations were given for mean position of the downstream cylinder, critical velocities for onset of instabilities, and clashing with the upstream cylinder.

Numerical simulations of elastic cylinders in cross flows are feasible only for the low values of the Reynolds number, due to the large computational power required for these kinds of applications. Mittal and Kumar (2001) employed a stabilized finite element formulation to study flow-induced oscillations of a pair of cylinders in tandem arrangement placed in uniform incompressible flow. The computations were carried out at Re = 100.

2.6 Concluding remarks

Flow around multiple circular cylinders has been well studied experimentally. For one cylinder flow, there are six different flow regimes based on the Reynolds number. The hydrodynamic characteristics for each flow regime are different. The drag coefficient and Strouhal number are constant throughout the subcritical range, which is commonly found in engineering practice. Flow around two cylinders displays complexity in flow patterns and fluid forces. There are as many as nine flow patterns found by Sumner et al.(2000). Generally, the downstream cylinder experiences a reduced drag force for tandem arrangement and also a non-zero mean lift force for staggered arrangement. Flow around three cylinders is less systematically investigated. For three in-line cylinders, the vortex shedding from and fluid forces on the third cylinder is different from those for the second one, as a result of cascading shielding effect by the two upstream cylinders.

While numerical simulations are widely applied on flow around one circular cylinder for various Reynolds numbers, those on two cylinders flow are limited and often for low Reynolds numbers and those on three cylinders are even more limited. Flow physics such as flow patterns can be observed numerically and fluid forces can be obtained with reasonable accuracy. A systematic study of spacing effect for various arrangements at subcritical Reynolds number, and the nature of drag reduction and existence of mean lift force for staggered arrangement, still remain to be investigated numerically.

For elastically mounted multiple cylinders, the wake-induced fluidelastic instability can lead to cylinder clashing. The fluidelastic instability is mainly associated with the position-related fluid forces. Relative work involves basically two parts: the fluid forces prediction and the stability analysis. Several analysis models are found in literature with good performance. Nonetheless, a thorough understanding of the hydrodynamic characteristics of multiple cylinders in cross flow is necessary and desirable.

3 Mathematical model

3.1 Basic equations

3.1.1 Fluids and flows

Fluids are substances that cannot resist external shear forces; even the smallest force causes deformation of a fluid particle. Fluids are composed of molecules that collide with one another and solid objects. However, the continuum assumption considers fluids to be continuous, rather than discrete. Consequently, properties such as density, pressure, temperature, and velocity are taken to be well-defined at infinitely small points, and are assumed to vary continuously from one point to another. Although significant differences exist between liquids and gases, both types of fluids obey the same laws of motion. The most important properties of fluids are density and viscosity (Versteeg & Malalasekera 2007).

All fluids are compressible to some extent. The changes in pressure or temperature will result in changes in density (mass per unit volume). However, in many situations the changes in density are negligible. In this case the fluid density may be assumed constant and the flow can be modelled as an incompressible flow. Incompressibility is a property of the flow, rather than of the fluid.

The viscosity of a fluid is a measure of its resistance to shear deformations. It is due to interaction between fluid molecules. As the temperature increases, the viscosities of all liquids decrease, while the viscosities of all gases increase.

The Reynolds number can be used to evaluate whether viscous or inviscid equations are appropriate to the problem. High Reynolds numbers indicate that the inertial forces are more significant than the viscous (friction) forces. Therefore, the flow may be assumed to be an inviscid flow, an approximation in which the viscous term is

neglected, compared to inertial terms. This idea can work fairly well when the Reynolds number is high. However, certain problems such as those involving solid boundaries may require that the viscosity be included. Viscosity often cannot be neglected near solid boundaries because the no-slip condition can generate a thin region of large strain rate (known as Boundary layer) which enhances the effect of even a small amount of viscosity, and thus generating vorticity.

When the flow velocity is very small, the fluid is very viscous or the geometric dimensions are very small (i.e. when the Reynolds number is small), the inertial force plays a minor role and can be neglected. The flow is then called creeping (Stokes) flow.

As the velocity is increased, and thus the Re, inertia becomes important but each fluid particle follows a smooth trajectory, the flow is laminar. Viscosity effects still dominate and are able to damp out a disturbance. Further increase in velocity may lead to instability that produces a more random type of flow called turbulence. Turbulent flows are unsteady, irregular, nonlinear and are characterized by the formation of eddies. At high velocities the Reynolds number is very high and viscous and turbulence effects are important in a small region near the walls, i.e. in the boundary layer.

3.1.2 Laws of fluid motion

The governing equations of fluid flow represent mathematical statements of the conservation laws of physics, i.e. the mass and the momentum conservation. The Navier–Stokes equations describe the motion of fluid substances. These equations arise from applying Newton's second law to fluid motion. The fluid will be regarded as a continuum and the behaviour of the fluid will be described in terms of macroscopic properties, such as velocity, pressure, density and temperature, and their space and time derivatives.

The conservative (or divergence) form of the governing equations of the

time-dependent two dimensional fluid flow of an incompressible Newtonian fluid is:

Continuity $$\mathrm{div}(\vec{u}) = 0 \tag{3.1}$$

x-momentum $$\rho\frac{\partial u}{\partial t} + \rho\mathrm{div}(u\vec{u}) = -\frac{\partial p}{\partial x} + \mathrm{div}(\mu\mathrm{grad}u) + S_x \tag{3.2}$$

y-momentum $$\rho\frac{\partial v}{\partial t} + \rho\mathrm{div}(v\vec{u}) = -\frac{\partial p}{\partial y} + \mathrm{div}(\mu\mathrm{grad}v) + S_y \tag{3.3}$$

where t is time, p is static pressure, u and v are x-component and y-component of velocity vector $\vec{u}$, respectively, and S_x and S_y are source terms. The compressibility is not considered here.

It is clear from equation (3.1) and (3.3) that there are significant commonalities between these equations. The general conservative form of all fluid flow equations for the variable ϕ can be written as the following form:

$$\rho\frac{\partial \phi}{\partial t} + \rho\mathrm{div}(\phi\vec{u}) = \mathrm{div}(\mu\mathrm{grad}\phi) + S_\phi \tag{3.4}$$

Equation (3.4) is the so-called transport equation for property ϕ. In words,

Rate of increase of ϕ of fluid element + Net rate of flow of ϕ out of fluid element (convection) = Rate of increase of ϕ due to diffusion + Rate of increase of ϕ due to sources.

3.2 Turbulence modelling

Most flows encountered in practice are turbulent. In contrast to laminar flow problems, numerical simulation of turbulent flows cannot be carried out by simply discretizing the governing equations and solving them in certain grid. This is caused by the fact that turbulence is essentially three dimensional and contains many length

scales simultaneously. With increasing Reynolds number the length scales of the smallest eddies in the flow become smaller and smaller. Consequently, the amount of computational ressources necessary to describe all the length scales that occur, increases with the Reynolds number. Even the largest supercomputer do not have (yet) the required speed and memory capacity to handle this amount of data, except for turbulent flow with relative low Re.

3.2.1 General remarks

In order to compute all significant structures (motions) of a turbulent flow, the domain on which the computation is performed must be at least as large as the largest eddy, and the grid must be as fine as the smallest eddy. Computational methods to simulate turbulent flows:

- Direct Numerical Simulation (DNS)
- Large Eddy Simulation (LES)
- Reynolds Averaged Navier-Stokes Models (RANS)

Direct Numerical Simulation

The most accurate approach to turbulence simulation is to solve the N-S equations without averaging. This so-called direct simulation does not assume any modelling. It discretizes and solves N-S equations on a grid sufficiently fine for resolving all motions occurring in the turbulent flow (Gushchin et al. 2002). The computed flow field obtained is similar to a laboratory experiment. The characteristic length scale for the smallest eddies is given by the Kolmogorov scale η. The relation between η and the length scale L of the largest eddies is given by (Yokokawa et al. 2002):

$$\frac{L}{\eta} = (\mathrm{Re}_L)^{\frac{3}{4}} \tag{3.5}$$

where Re_L is the Reynolds number with respect to characteristic length L. If the dimensions of the mean flow field are of the order L^3 and the sizes h of the grid elements are about equal to η, then the number of elements needed to discretize the flow field is

$$n_{elem} = (\mathrm{Re}_L)^{\frac{9}{4}} \tag{3.6}$$

In industrial applications such as aerodynamic investigations of automobiles or aircraft, typical Reynolds numbers are 10^6 and above. Hence, solving these types of problems properly using DNS would require over 10^{13} grid points. Neither existing parallel computers nor computers of the near future can supply the storage space or the necessary CPU performance demanded by such a simulation.

Large Eddy Simulation

Only the large eddies (or resolvable scale motions) are calculated, whereas the small eddies (subgrid-scale motions) are modelled by a closure assumption (Breuer 1998; Catalano et al. 2003).

The flow dependent large eddies are directly affected by the boundary conditions. They are therefore the most difficult ones to model. LES avoids this problem by explicit computation of these motions. Since the small eddies dissipate energy from the large ones, a so-called subgrid-scale (SGS) model is needed that takes into account this physical energy cascade process. The sizes of the grid elements, and thereby the distinction between large and small eddies, has to be chosen to be small enough for the unresolved subgrid-scale motions to behave statistically in a nearly isotropic manner. If this is the case, the SGS motions can be modelled independently of the flow geometry.

Reynolds (Ensemble) Averaging

In Reynolds averaging, the solution variables in the instantaneous (exact) Navier-Stokes equations are decomposed into the mean (ensemble averaged or time-averaged) and fluctuating components. For any scalar quantity:

$$\phi_i = \overline{\phi_i} + \phi_i' \tag{3.7}$$

where ϕ denotes a scalar such as velocity, pressure, energy, or species concentration. Substituting expressions of this form for the flow variables into the instantaneous continuity and momentum equations and taking a time (or ensemble) average yields the ensemble-averaged momentum equations. They have the same general form as the instantaneous Navier-Stokes equations, with the velocities and other solution variables now representing ensemble-averaged (or time-averaged) values, except that additional terms now appear that represent the effects of turbulence, i.e. the Reynolds stresses, $-\rho\overline{u_i' u_j'}$. They must be modelled in order to close the equations.

There are four turbulence models (FLUENT Inc. 2003):

- Spalart-Allmaras model
- k-ε model
- k-ω model
- Reynolds stress model

In the case of the Spalart-Allmaras model, only one additional transport equation (representing turbulent viscosity) is solved. In the case of the k-ε and k-ω models, two additional transport equations (for the turbulence kinetic energy, k, and either the turbulence dissipation rate, ε, or the specific dissipation rate, ω) are solved. The Reynolds Stress Model (RSM), is to solve transport equations for each of the terms in the Reynolds stress tensor. An additional scale-determining equation (normally for ε) is also required. This means that five additional transport equations are required in 2D flows and seven additional transport equations must be solved in 3D, which

cost more computational resource (FLUENT Inc. 2003).

When attention is drawn to industrial applications, DNS method is unfeasible as the associated grid resolution would cause prohibitive computational expenses. The simulation of engineering turbulent flows is thus restricted to turbulence-modelling practices based on Reynolds-averaged Navier–Stokes (RANS) equations and large eddy simulation (LES). In the framework of RANS, all aspects of turbulence are modelled, which enhances the numerical efficiency at the expense of a strong model dependency. As opposed to the RANS approach, a major portion of the turbulent scales is numerically resolved within LES. The primary advantage of LES is the reduced influence of the turbulence model, which significantly increases the computational effort in comparison to RANS. Recently developed explicit algebraic stress models revealed remarkable improvements of the RANS methodology for several steady flows at low computational costs, which motivates their investigation in unsteady turbulent bluff-body flows (Lubcke et al. 2001).

3.2.2 Menter $k-\omega$ SST turbulence model

Flows in the laminar regime are completely described be the equations (3.1)-(3.3). Many, if not most, flows of engineering significance are turbulent. In this regime the velocity and all other flow properties vary in a random and chaotic way (Versteeg & Malalasekera 2007).

In Reynolds averaging, the solution variables in the instantaneous (exact) Navier-Stokes equations are decomposed into the mean (ensemble averaged or time-averaged) and fluctuating components. For the velocity components and pressure:

$$u_i = U_i + u_i' \tag{3.8}$$

$$p_i = P_i + p_i' \tag{3.9}$$

where U_i and $u_i^{'}$ denote the mean and fluctuating velocity, and P and p' are mean and fluctuating pressure.

Substituting expressions of this form for the flow variables into the instantaneous continuity and momentum equations and taking a time average yields the ensemble-averaged momentum equations. They can be written in Cartesian tensor form as:

$$\frac{\partial U_i}{\partial x_i} = 0 \tag{3.10}$$

$$\rho \frac{\partial U_i}{\partial t} + \rho \frac{\partial}{\partial x_j}\left(U_i U_j\right) = -\frac{\partial P}{\partial x_i} + \mu \frac{\partial^2 U_i}{\partial^2 x_j} + \frac{\partial}{\partial x_j}\left(-\rho \overline{u_i^{'} u_j^{'}}\right) \tag{3.11}$$

Equations (3.10) and (3.11) are called Reynolds-averaged Navier-Stokes (RANS) equations. They have the same general form as the instantaneous Navier-Stokes equations (3.1)-(3.3), with the velocities and pressure now representing time-averaged values. But the process of time averaging has introduced a new term, which involves products of fluctuating velocities and associated with convective momentum transfer due to turbulent eddies. The Reynolds stresses, $-\rho \overline{u_i^{'} u_j^{'}}$, must be modelled to close equation (3.11). A common method employs the Boussinesq hypothesis to relate the Reynolds stresses to the mean velocity gradients:

$$-\rho \overline{u_i^{'} u_j^{'}} = \mu_t \left(\frac{\partial U_i}{\partial x_j} + \frac{\partial U_j}{\partial x_i} \right) - \frac{2}{3} \rho k \delta_{ij} \tag{3.12}$$

where $k = \frac{1}{2} \sum \overline{u_i^{'2}}$ is the turbulent kinetic energy per unit mass.

Based on Boussinesq hypothesis, the $k - \varepsilon$ turbulence model is the most widely used and validated turbulence model. It has achieved notable success in calculating a wide range of flows with industrial engineering applications. Menter (1994) noted

that the results of $k-\varepsilon$ model are much less sensitive to the assumed values in the free stream, but its near wall performance is unsatisfactory for boundary layers with adverse pressure gradients. This led him to suggest a hybrid model using (i) a transformation of the $k-\varepsilon$ model into $k-\omega$ model in the near wall region and (ii) the standard $k-\varepsilon$ model in the fully turbulent region far from the wall (Versteeg & Malalasekera 2007). This was called shear stress transport (SST) model. The turbulence kinetic k and the specific dissipation rate ω are obtained from the following transport equations:

$$\rho\frac{\partial k}{\partial t}+\rho\frac{\partial}{\partial x_j}\left(kU_j\right)=\frac{\partial}{\partial x_j}\left[\left(\mu+\frac{\mu_t}{\sigma_k}\right)\frac{\partial k}{\partial x_j}\right]+G_k-\beta^*\rho k\omega \tag{3.13}$$

$$\rho\frac{\partial \omega}{\partial t}+\rho\frac{\partial}{\partial x_j}\left(\omega U_j\right)=\frac{\partial}{\partial x_j}\left[\left(\mu+\frac{\mu_t}{\sigma_\omega}\right)\frac{\partial \omega}{\partial x_j}\right]+\alpha\frac{\omega}{k}G_k-\beta\rho\omega^2+(1-F_1)D_\omega \tag{3.14}$$

Where $G_k=2\mu_t S_{ij}S_{ij}$ is the rate of production of turbulent kinetic energy with

$$S_{ij}=\frac{1}{2}\left(\frac{\partial U_i}{\partial x_j}+\frac{\partial U_j}{\partial x_i}\right) \tag{3.15}$$

$$D_\omega=\frac{2\rho}{\sigma_{\omega 2}\omega}\frac{\partial k}{\partial x_j}\frac{\partial \omega}{\partial x_j} \tag{3.16}$$

$$F_1=\tanh\left\{\min\left[\max\left(\frac{\sqrt{k}}{\beta^*\omega y},\frac{500\mu}{\rho y^2\omega}\right),\frac{4\rho k}{\sigma_{\omega 2}D_\omega^+ y^2}\right]\right\}^2 \tag{3.17}$$

where *y* is the distance to the next surface and

$$D_\omega^+=\max\left(D_\omega,10^{-20}\right) \tag{3.18}$$

The eddy viscosity is defined as

$$\mu_t=\frac{a_1\rho k}{\max(a_1\omega,SF_2)} \tag{3.19}$$

where $S = \sqrt{2S_{ij}S_{ij}}$, $a_1 = \text{constant}$ and F_2 is a blending function, which restricts the limiter to the wall layer computed by

$$F_2 = \tanh\left[\max\left(\frac{2\sqrt{k}}{\beta^* \omega y}, \frac{500\mu}{\rho y^2 \omega}\right)\right]^2 \tag{3.20}$$

Numerical instabilities may be caused by differences in the computed values of the eddy viscosity with the standard $k-\varepsilon$ model in the far field and the transformed $k-\omega$ model near the wall. Blending functions are used to achieve a smooth transition between the two models. The coefficients of the SST model, σ_k, σ_ω, α and β, are a linear combination of the corresponding coefficients of original $k-\omega$ model and standard $k-\varepsilon$ model:

$$C = F_1 C_1 + (1 - F_1) C_2 \tag{3.21}$$

The constants used in the SST model equations are

$$\sigma_{k1} = 1.176 \quad \sigma_{\omega 1} = 2.0 \quad \alpha_1 = 0.553 \quad \beta_1 = 0.075 \quad a_1 = 0.31$$

$$\sigma_{k2} = 1.0 \quad \sigma_{\omega 2} = 1.17 \quad \alpha_2 = 0.44 \quad \beta_2 = 0.083 \quad \beta^* = 0.09$$

For the detail of $k-\omega$ SST model, readers are referred to Versteeg & Malalasekera (2007) and FLUENT Guide (2003).

Boundary conditions

For the two dimensional flow around cylinders the following boundary conditions are applied:

- On the inlet: complete specification of all velocity components and distribution of k and ω must be given.
- On the outlet: set gradient of all velocity components, k and ω to zero in the

flow direction and specify the static pressure.

- On symmetry boundary: for all the variables ϕ, $\partial\phi/\partial n = 0$.

On solid walls:

Due to the complexity of flow around cylinders, in the current simulation the viscosity-affected near wall region is completely resolved all the way to the viscous sublayer. The no-slip condition is applied and the value of turbulence kinetic energy *k* at the wall is set to zero. According to FLUENT, the value of ω at the smooth wall is specified as

$$\omega_{\mathrm{w}} = \frac{\rho(u^*)^2}{\mu}\omega^+ \tag{3.22}$$

where

$$u^* = y^* = \frac{\rho C_\mu^{1/4} k^{1/2} y}{\mu} \tag{3.23}$$

in the viscous sublayer, where $C_\mu = 0.09$ is a constant and *y* is the distance to the nearest wall. The asymptotic value of ω^+ in the laminar sublayer is given by

$$\omega^+ = \min\left(2500, \frac{6}{\beta^*(y^+)^2}\right) \tag{3.24}$$

where $y^+ = \rho u_\tau y/\mu$ is the dimensionless distance to the wall.

3.3 Numerical method

In the past there have been two approaches in science and engineering: the experimental and the theoretical. With the invention of the computer a new approach

has appeared: the numerical simulation.

Computational Fluid Dynamics (CFD) is the analysis of systems involving fluid flow, heat transfer and associated phenomena such as chemical reactions by means of computer-based simulation. Nowadays expensive experiments are increasingly replaced by computer simulations. Moreover, simulation enables the examination of processes that cannot be experimentally tested.

This thesis uses a commercial software FLUENT to simulate flow around multiple cylinders. FLUENT is based on the finite volume method, which is a method for representing and evaluating partial differential equations in the form of algebraic equations. Similar to the finite difference method, values are calculated at discrete places on a meshed geometry. 'Finite volume' refers to the small volume surrounding each node point on a mesh. In the finite volume method, volume integrals in a partial differential equation that contain a divergence term are converted to surface integrals, using the divergence theorem.

3.3.1 Integral form of basic equations

Equation (3.4) is used as starting point in the finite volume method. By setting ϕ equal to 1, u and v, we obtain the partial differential equations for mass and momentum equations. The key step of the finite volume method is the integration of equation (3.4) over a control volume CV:

$$\rho\int_{CV}\frac{\partial\phi}{\partial t}dV+\rho\int_{\mathrm{CV}}\mathrm{div}(\phi\vec{u})dV=\int_{CV}\mathrm{div}(\mu\mathrm{grad}\phi)dV+\int_{CV}S_{\phi}dV \tag{3.25}$$

By using Gauss's divergence theorem:

$$\int_{\mathrm{CV}}\mathrm{div}(\vec{a})dV=\int_{S}n\cdot\vec{a}dS \tag{3.26}$$

The volume integrals in the second term on the left hand side, the convective term, and in the diffusion term (on the right hand side) in equation (3.25) are rewritten as integrals over the bounding surface of the control volume:

$$\rho\int_{CV}\frac{\partial\phi}{\partial t}dV+\rho\int_{S}\vec{n}\cdot(\phi\vec{u})dS=\int_{S}\vec{n}\cdot(\mu\text{grad}\phi)dS+\int_{CV}S_{\phi}dV \tag{3.27}$$

3.3.2 Discretization

The Finite Volume Method (Versteeg & Malalasekera 2007) begins with the integral form of the equation (3.27). The domain is subdivided into a finite number of small control volumes (CV) by a grid which defines the CV boundaries, not the computational nodes.

To obtain an algebraic equation for each CV, the surface and volume integrals need to be approximated using quadrature formulae. For the volume integrals the simplest approximation is the midpoint rule:

$$\int_{CV}qdV=\overline{q}\text{Vol(CV)}=q_{P}\text{Vol(CV)} \tag{3.28}$$

where $\overline{q}$ is the mean value and q_P the value of q at the CV center. This approximation is exact if q is either constant or varies linearly within the CV; otherwise is of second order.

The surface integral on CV boundary is the sum of integrals over the faces:

$$\int_{S}f\cdot\vec{n}dS=\sum_{k}\int_{S_k}fdS \tag{3.29}$$

where $f=\rho\vec{n}\cdot(\phi\vec{u})$ or $\vec{n}\cdot(\mu\text{grad}\phi)$.

To calculate the surface integrals, we need the value of ϕ and its gradient normal to

the cell face at some location on the CV surface. They have to be expressed in terms of nodal values by interpolation, such as upwind differencing scheme and central difference scheme.

3.3.3 Solution of linear equation systems

By summing all the approximated integrals we produce an algebraic equation at each control volume:

$$A_P\phi_P + \sum_l A_l\phi_l = Q_P \tag{3.30}$$

where the index l runs over the neighbour nodes involved, and the system of equations for the whole domain has the matrix form

$$[A] \cdot [\phi] = [Q] \tag{3.31}$$

The matrix A is always sparse.

There are mainly two types of methods for solving the system of linear algebraic equations, i.e. direct method and iterative method.

Iterative methods are based on the repeated application of a relatively simple algorithm leading to a (eventual) convergence after a (sometimes large) number of repetitions. The total number of operations, typically on the order of N per iteration cycle, cannot be predicted in advance. It is not possible to guarantee convergence unless the system of equations satisfies strict criteria. The main advantage of iterative methods is that only non-zero coefficients need to be stored.

In an iterative method one guesses a solution and uses the equation to systematically improve it. If each iteration is cheap and the number of iterations is small, an iterative solver may cost less than a direct method. In CFD problems this is usually

the case.

When using iterative solvers, it is important to know when to quit. The most common convergence criteria are based on the difference between two successive iterates. The procedure is stopped when this difference is less than a pre-selected value.

3.3.4 Unsteady problems: Time discretization

For the unsteady (initial value) problem we rewrite the conservation equation in the form

$$\rho\frac{\partial\phi}{\partial t} = -\mathrm{div}(\rho\phi\vec{u}) + \mathrm{div}(\mu\,\mathrm{grad}\,\phi) + S_\phi = f((t,\phi(t)),\phi(t_0)) = \phi^0 \tag{3.32}$$

The convective, diffusive and source terms represented by $f(t,\phi(t))$ are discretized using finite volume method. For time integration we can use similar methods than for initial value problems in ODE.

$$\int_{t_n}^{t_{n+1}} \frac{\partial\rho\phi}{\partial t}dt = \rho(\phi^{n+1} - \phi^n) = \int_{t_n}^{t_{n+1}} f(t,\phi(t))dt \tag{3.33}$$

Two types of methods for time integration are

(i) explicit method ($\phi^{n+1} = \phi^n + f(t_n,\phi^n)\cdot\Delta t$) (3.34)

(ii) implicit method ($\phi^{n+1} = \phi^n + f(t_{n+1},\phi^{n+1})\cdot\Delta t$) (3.35)

For the explicit method, solution values at time t_{n+1} are computed from the values of f at time t_n, i.e. all fluxes and source terms are evaluated using known values at time t_n. It is easy to program and parallelize and needs few numbers of operations per time step, but demands strong conditions on the time step for stability. For

implicit method, f is evaluated at time t_{n+1}, i.e. all fluxes and source terms are evaluated in terms of the unknown variable values at the new time t_{n+1}. It is always stable and much larger time step is possible, but every time step requires the solution of a system of equations so more number of operations. This causes difficulty to program and parallelize.

3.3.5 Coupling of pressure and velocity

Transport equations for each velocity component (momentum equation) can be derived from the general transport equation by replacing ϕ by u, v and w. The velocity field must also satisfy the continuity equation.

The convective terms of the momentum equation are non-linear. All three equation are coupled because every velocity component appears in each momentum equation and the continuity equation. The most complex issue to be solved is the role played by the pressure. It appears in both moment equations but there is no equation for the pressure.

If the flow is compressible, the continuity equation may be used as a transport equation for density and the energy equation for the temperature. The pressure may then be obtained from the density and temperature by using the equation of state $p = p(\rho, t)$. If the flow is incompressible, the density is constant and not related with the pressure. In this case coupling between pressure and velocity introduces a constraint on the solution of the flow field: if the correct pressure field is applied in the momentum equation the resulting velocity field should satisfy continuity.

There are several algorithms for pressure-velocity coupling, such as, SIMPLE, SIMPLEC and PISO. The main steps of SIMPLE algorithm are:

(i) An approximation of the velocity field is obtained by solving the momentum equation. The pressure gradient term is calculated using the pressure distribution

from the previous iteration or an initial guess.
(ii) The pressure equation is formulated and solved in order to obtain the new pressure distribution.
(iii) Velocities are corrected and a new set of conservative fluxes is calculated.

3.4 Concluding remarks

In this chapter the basic equations governing the fluid flow and the numerical methods are introduced. The Navier-Stokes equations describe the motion of fluid substances. As most flows encountered in practice are turbulent, turbulence modelling is essential for numerical simulation. Basically there are three methods, DNS, LES and RANS, of which the RANS method has been widely used and makes a balance between computation efficiency and accuracy. The $k-\omega$ SST model is introduced as a RANS model.

The numerical simulations used in this thesis are via a commercial software FLUENT, which is based on the finite volume method (FVM). In FVM, volume integrals in a partial differential equation that contain a divergence term are converted to surface integrals, using the divergence theorem. The discretization of the integral form of the governing equations and solution of linear equation system are simply introduced in this chapter. For the detail of FVM, the readers are referred to the relative textbooks (Versteeg & Malalasekera 2007).

4 Flow around a circular cylinder

4.1 Introduction

The uniform cross-flow around a circular cylinder is a classical example of bluff body flow. Although the configuration is simple, the flow is characterised by very rich and complex physical phenomena for the subcritical Reynolds number studied in this work: thin and attached laminar boundary layers in the front part of the cylinder, separating shear layers, development of instabilities along these layers that lead to transition, as well as small scale streamwise and spanwise vortices in the turbulent wake that interact with large scale Karman vortices. A comprehensive review of the flow characteristics for a wide range of Reynolds numbers is given by Williamson (1996).

4.2 Numerical model

Two-dimensional uniform flow past a circular cylinder is computed using a commercial software FLUENT. The flow in the wake of a cylinder is turbulent in the subcritical flow regime, so a turbulence model is needed. The $k-\omega$ SST model is selected here, for its good behaviour in adverse pressure gradients and separating flow.

Unless otherwise noted, The Reynolds number for the simulations is 10^4, which is in the subcritical range. It is believed that the hydrodynamic characteristics of a single circular cylinder, such as the vortex shedding frequency, the separation points, the shear layers and the wake structures, are similar in the region of subcritical Reynolds number (Zdravkovich 1997; Gu & Sun 1999). Therefore, if an understanding of flow with Re = 10^4 is obtained, it is reasonable to suggest that it represents some valuable information about the flow around multiple cylinder in the region of subcritical

Reynolds number. This Reynolds number is selected because it is in the subcritical region and is not too demanding on computer resource for simulation.

A segregated, unsteady solver has been selected for simulations. The flow is considered incompressible. A Second order implicit formulation is selected for temporal discretization. A second order upwind scheme has been used for solving momentum equations with standard pressure interpolation scheme, and SIMPLE algorithm is employed for pressure velocity coupling. The simulation settings in FLUENT are summarised in Table 4-1.

Table 4-1 Simulation settings.

Settings	Choice
Solver	Segregated
Temporal discretisation	2^{nd}-order Implicit
Pressure	Standard
Momentum equations	2^{nd}-order Upwind
Pressure-velocity coupling	SIMPLE
Turbulence model	$k-\omega$ SST

4.2.1 Computational domain and boundary conditions

The flow field around a cylinder is modelled in two dimensional flow with the axis of cylinder perpendicular to the direction of flow. The cylinder is modelled as a circle with a diameter D = 0.2m and a square flow domain is created around the cylinder (Figure 4-1). Inlet (upstream), upper and lower boundaries have been extended in the lateral interaction so that the effects due to the cylinder presence have been assumed to be negligible at these boundaries. The domain has been also extended long enough downstream to eliminate the far field effects on the near wake and to produce full development of the vortex street. The actual geometric size of the computational domain, namely d_u, d_d and d_t in Figure 4-1, will be discussed later.

A Cartesian coordinate system, where the x-axis is aligned with the incoming flow direction (streamwise direction), the y-axis is perpendicular to the plane containing the streamwise and spanwise direction (z-axis), is used to describe the flow. The origin of the coordinate system is located on the cylinder's axis. For the convenience of describing the point around the cylinder surface, a polar system is also used here, with the polar axis directed towards the front point as shown in Figure 4-1.

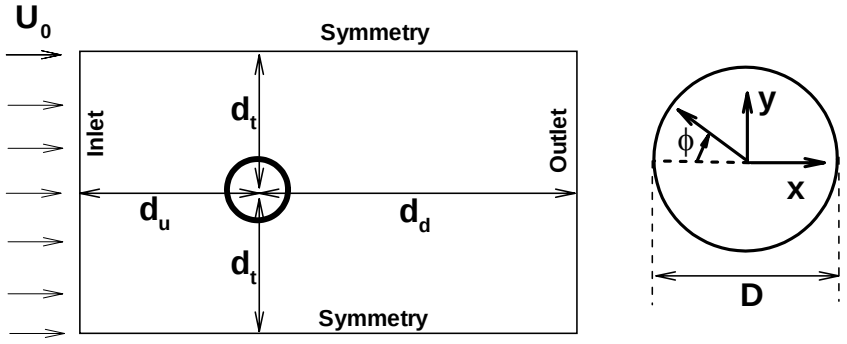

Figure 4-1 Schematic of computation domain and coordinate system.

The boundary conditions used for all simulations are as follows:

i. Inlet: uniform flow at the inlet, which is normal to the boundary, is specified, namely, $u = u_0$, $v = 0$. Low turbulence intensity, I = 0.6%, and a turbulence viscosity ratio, $r_\mu = 1$, are assumed.

ii. Outlet: free outflow condition is imposed. An average static pressure over the entire outlet boundary is assumed, which is 0.0 Pa in all simulations.

iii. Lateral boundaries: the symmetry boundary condition is used where the normal velocity at the boundary is zero and the scalar variable gradients normal to the boundary are also zero.

iv. The cylinder surface: in this case the no slip boundary condition is applied. Meaning that the fluid velocity at the wall has a zero value.

In order to facilitate meshing, the domain is subdivided into nine parts using two longitudinal lines and two transverse lines, with curves near the cylinder, as shown in Figure 4-2. The zone surrounding the cylinder is meshed with O type structured

quadrilateral grids and will be taken extra care for the boundary layer. The outer subdomains are all quadrilateral spaces and easy to be meshed with structured grids. The mesh is denser near the cylinder by design and stretches out with a growth factor of approximately 1.06 in most instances and less than 1.0 in all cases. The same strategy was also used by Yong & Ooi (2004).

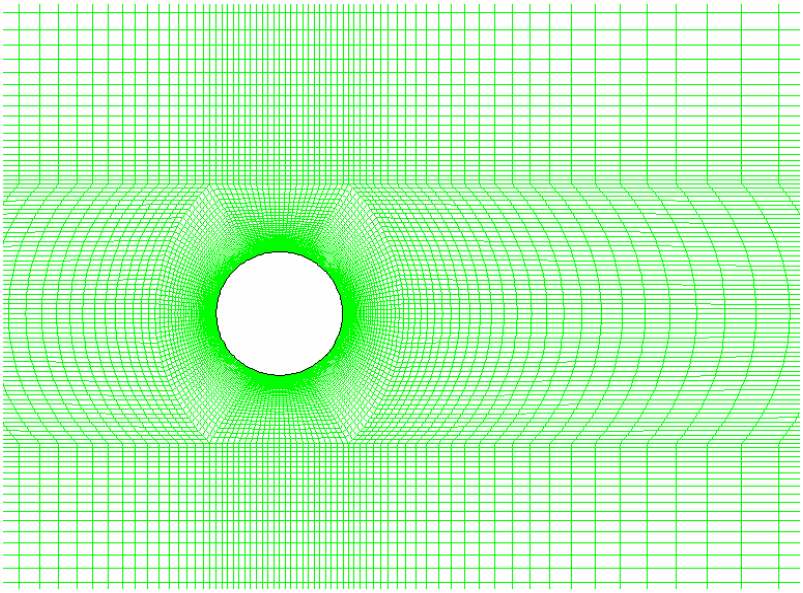

Figure 4-2 Computational mesh around the cylinder.

As the very first step of any CFD simulation, determining computation domain and drawing mesh are extremely important on computing convergence and accuracy. Generally, large domain and fine enough mesh always produce better results, whereas in the meantime, consume more computation resource and time. So a good balance should be determined between the two sides primarily.

According to ideal fluid model of flow around a circular cylinder, when the upstream distance $d_u > 10D$, the local velocity at the inlet is within 0.25% difference from the free stream flow velocity (Table 4-2). This suggests the distance from the cylinder to inlet boundary needs to be around 10D, although the viscous flow around a cylinder is much different from the ideal one.

Table 4-2 The difference between the velocity at the inlet and the free stream velocity versus d_u, based on potential flow model.

d_u	5D	7.5D	10D	15D
$\Delta u = D^2 / 4d_u^2$	0.01	0.0044	0.0025	0.0011

To find out suitable distances, several cases are computed. Starting from a large enough domain, with $d_u = 20D$, $d_d = 40D$ and $d_t = 15D$, the distances are decreased respectively. For computing the wake behind the cylinder, the downstream distance, d_d, is at least 25D. For all cases, the grids in the boundary layers are the same. The results are shown in Table 4-3. It can be seen that the domain with $d_u = 15D$, $d_d = 25D$ and $d_t = 10D$ is optimal in its accuracy and reduction of CPU time and will be used thereafter.

Table 4-3 Drag coefficient and Strouhal number for different computational domains.

d_u	d_t	d_d	C_D	St
20D	15D	40D	1.25	0.229
20D	15D	25D	1.25	0.229
20D	10D	25D	1.26	0.229
15D	10D	25D	1.26	0.229
10D	10D	25D	1.29	0.231

4.2.2 Near-wall treatment

Mesh in the boundary layer, especially the height of the wall-adjacent cells is highlighted here as the preliminary simulations showed that it had significant influence on the computing results.

The wall function approach does not need a very fine dicretization in the vicinity of a no-slip surface, and it makes simulations with boundaries more feasible, in terms of

computational resources. However, this approach has been questioned by Launder (1984) and Rodi (1997), because the law of the wall is invalid where the flow is separated. For the laminar separation flow studied in this thesis, the best treatment is to use a sufficiently fine mesh to resolve the near wall flow with no-slip condition, as shown in Figure 4-3.

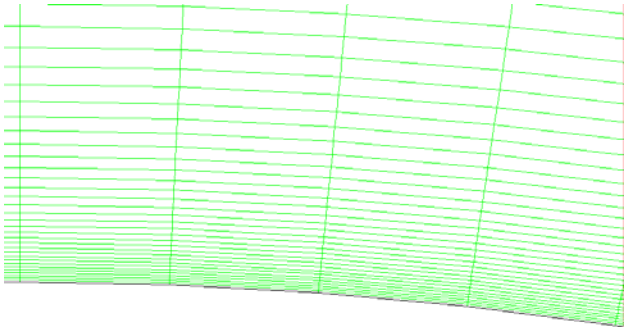

Figure 4-3 Close view of the mesh near the cylinder's surface.

The viscous sublayer is fully resolved in all simulations. To accomplish this, it is necessary to place at least 5 cells within $y^+ = \rho u_\tau y/\mu < 7$ in the near wall region and to have $y^+ < 1$ for the first cell (Fluent Guide and Holloway et al. (2004)), where y^+ denotes the dimensionless distance to the wall.

Table 4-4 Mesh convergence for the first cell height.

Mesh	First cell height ($\times 10^{-4} D$)	y^+	C_D	St
A	10	0.94	1.30	0.230
B	5	0.52	1.26	0.229
C	2.5	0.26	1.25	0.229
D	1.5	0.15	1.25	0.229

Four meshes A, B, C and D are created to study the convergence of the first cell height. Mesh A is created such that $y+$ is less than one for Reynolds number 10^4 and for mesh B, C and D the first cell height is successively decreased based on mesh A.

All cases are computed with $k-\omega$ SST turbulence model and second order discretization at Re = 10^4 and the results are shown in Table 4-4. Note the value of y^+ here is the maximum around the cylinder.

As shown in Table 4-4, mesh A, corresponding to y^+ = 0.94, is nearly convergent, which agrees with the conclusion in literature, the requirement to have $y^+ < 1$ for the first cell to simulate the flow around the circular cylinder in subcritical regime. Based on the results here, the near-wall cell needs to be even smaller to ensure fully convergence. This can be demonstrated by the relationship between y^+ and the first cell height, as shown in Figure 4-4. y^+ is linear with the first cell height up to $5\times10^{-4}D$, i.e. mesh B, while the same linear relationship does not exist for mesh A (the first cell height is $10\times10^{-4}D$). This suggests that the requirement for the first cell height is to have $y^+ < 0.5$ rather than 1.

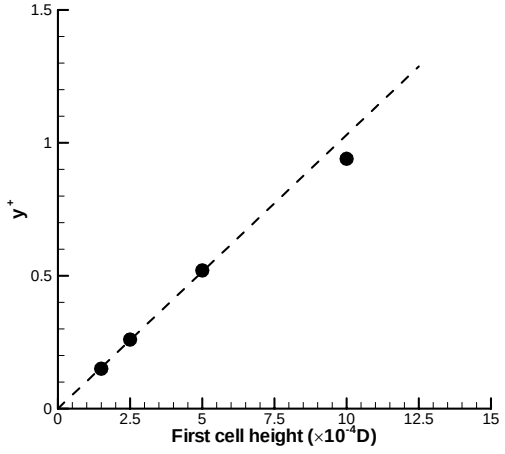

Figure 4-4 Relationship between y^+ and the first cell height.

The following simulations will be based on the mesh C, with first cell height 0.025%D, at which the mesh is fully convergent for the first cell height.

4.2.3 Mesh independence

Mesh independence means that the converged solution obtained from a CFD

calculation is independent of the grid density. Increasing the number of cells in one region or throughout the entire domain for a grid-independent CFD model would not (ideally) change the flow-field solution and integrated quantities. In practice, grid independence is indicated when further mesh refinement yields only insignificant changes in the numerical solution.

Mesh independence is tested with higher density meshes in both the radial and circumferential directions, while keeping the first cell height 0.025%D. A refinement factor of $\sqrt{2}$ is applied to both the inner and outer subdomains which leads to nearly doubling the number of cells. The aforementioned numerical approach is then employed to compute the flow with each mesh. The results are given in Table 4-5.

Table 4-5 Mesh independence investigation.

Mesh	First cell height $(\times 10^{-4})$	Number of cells	C_D	St
C	2.5D	24880	1.25	0.229
CP	2.5D	48140	1.25	0.232
CPP	2.5D	105080	1.25	0.232

As shown in Table 4-5, the resulted drag coefficients and Strouhal numbers have no appreciable change among the three successively finer meshes, i.e. mesh C, CP and CPP, which suggests mesh C is a convergent one in terms of the drag force and vortex shedding frequency.

4.2.4 Time stepping

For flow around a circular cylinder, the dimensionless vortex shedding period is often expressed as

$$\frac{TU_0}{D} = \frac{1}{St}.$$

With St = 0.23 here, the dimensionless vortex shedding period is about 4.35. The

dimensionless time step size ($\Delta tU_0 / D$) is firstly selected as about 1% of this period, then further reduced to compute the flow around a circular cylinder at $\mathrm{Re} = 10^4$ based on mesh C, as shown in Table 4-6.

Table 4-6 Numerical results for different time step sizes.

Dimensionless time step size	C_D	St
0.05	1.20	0.227
0.025	1.24	0.229
0.0125	1.25	0.229
0.005	1.25	0.229

When the dimensionless time step size ($\Delta tU_0 / D$) is 0.025, i.e. 0.57% of the vortex shedding period, the computation is convergent in terms of drag force and vortex shedding frequency, which has no appreciable changes by using the smaller time step sizes.

It is well known that the time step size is proportional to the cell size. This is confirmed here, as shown in Table 4-7. For mesh C (24880 grids), the convergent time step size is 0.025, while it is at least 0.005 for a finer mesh CPP (105080 grids). This indicates the time step size needs to be smaller for finer meshes to achieve convergent simulations.

Table 4-7 Comparison of time step sizes between mesh C and CPP.

Dimensionless time step size	Mesh C		Mesh CPP	
	C_D	St	C_D	St
0.05	1.20	0.227		
0.025	1.24	0.229	1.17	0.227
0.0125	1.25	0.229	1.22	0.231
0.005	1.25	0.229	1.25	0.232

4.3 Simulation results and discussions

4.3.1 Fluid forces and vortex shedding frequency

Figure 4-5 presents an example of the drag (C_D) and lift (C_L) coefficients histories. For C_L, there is hardly any oscillation until the dimensionless time 40, it then starts to oscillate with increasing amplitude. After $tU_0 / D = 110$, the fluctuation of C_L becomes a periodic signal, indicating the alternating vortex shedding state is fully developed. At the same time, the fluctuation of C_D also becomes steady.

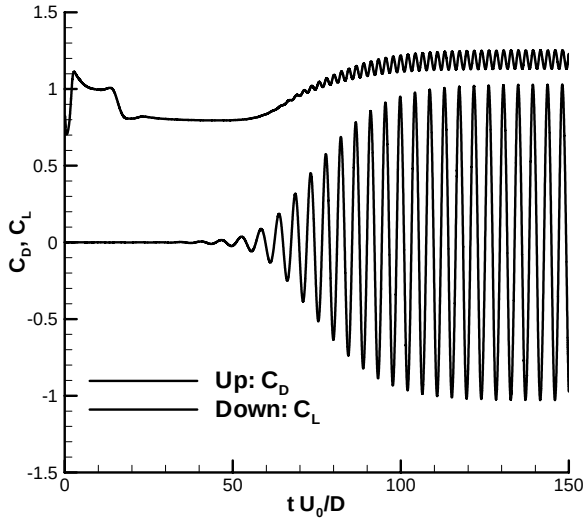

Figure 4-5 Drag and lift coefficients histories.

The time-averaged CD is 1.19 here, matching the well known drag coefficient of a circular cylinder in cross-flow within subcritical flow regime, which is 1.2. The value is a little below that reported before, because the turbulence equations are discretized with first order formula here, instead of second order upwind formula before. The lift force has a zero time-averaged value. The amplitude of fluctuating lift, which is significantly larger than the fluctuating drag, is often measured as r.m.s. lift coefficient $C_{L'}$. Norberg (2003) summarised the presented experimental data, for example, West & Apelt (1993) and Szepessy & Bearman (1992), and found the value of $C_{L'}$ is well

scattered in subcritical regime, mostly in the range of 0.4 - 0.6. The r.m.s. lift coefficient in Figure 4-5 is found to be 0.48, within the experimental results.

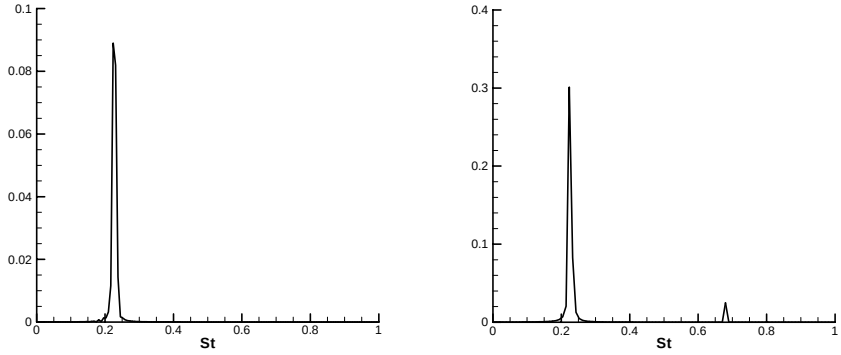

Figure 4-6 Power spectra of lift coefficient and y-component velocity at x = 2D, y = 0. Left: lift coefficient; Right: velocity.

The Strouhal number St is predicted by using a power spectrum of the lift force history (Figure 4-5), as well the y-component velocity at a point in the near wake region (x =2D, y = 0 here), as shown in Figure 4-6. Both show one dominant peak, corresponding to the same frequency at St = 0.23. This value is higher than that summarised by Norberg (2003), which is about 0.2 in subcritical flow regime. West & Apelt (1993) reported St = 0.195 at a similar Reynolds number and Cantwell & Coles (1983) presented St = 0.179 at Re = 1.4×10^5. In comparison, the current simulation gives a slightly higher value of the vortex shedding frequency.

4.3.2 Pressure and velocity around the cylinder

Shown in Figure 4-7 are the pressure coefficient distributions varying in one cycle of the vortex shedding, with an equal time interval of one tenth of the period. Stable stagnation point and stagnation pressure can be seen in the whole period. The pressure on the upper and lower sides oscillates in remarkable amplitude, as a result of alternative vortex forming and shedding. Interestingly the pressure distributions in the first half (0.0T – 0.4T) and those in the second half (0.5T – 0.9T) are arranged in

mirror symmetry with respect to the cylinder's centre line. This indicates the vortex forming and shedding on each side is highly similar.

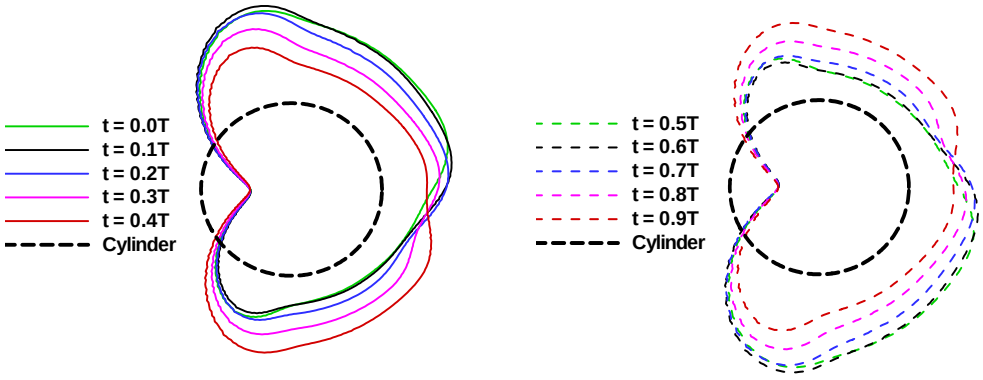

Figure 4-7 Pressure distributions around the cylinder varying in a period: the line outside the circle represents negative pressure and the inner line represents positive pressure.

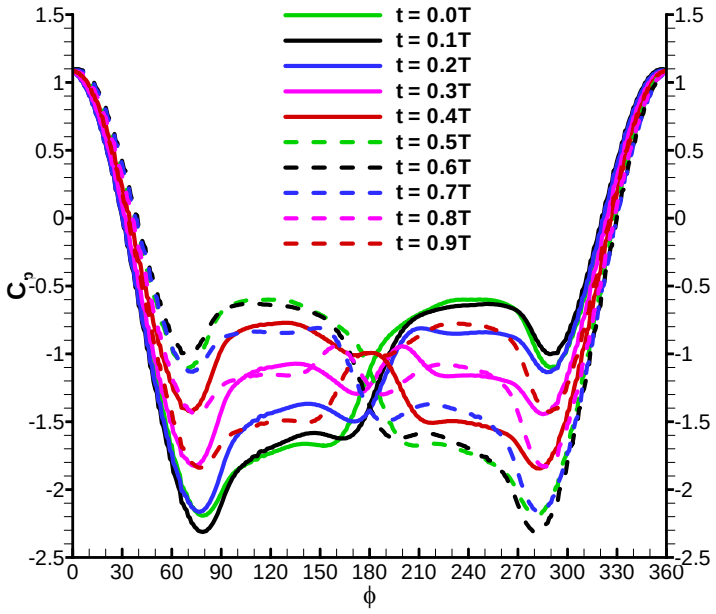

Figure 4-8 Pressure distributions around the cylinder varying in a vortex shedding period.

Shown in Figure 4-8 are the pressure distributions around the cylinder surface at ten instants in a cycle of vortex shedding in $\phi - C_p$ coordinate system. Note the stagnation pressure here is slightly over 1, because the gauge pressure at the flow outlet is set as zero in current simulation. It is seen that the pressure coefficient at the extreme aft point changes with time regularly in a small range from –1.4 to -1, and the averaged value, i.e. the base pressure $C_{pb} = -1.22$. Moreover, the pressure coefficient on the rear surface at certain instant always varies around the base pressure, and its deviations from the base pressure for the upper and lower sides are nearly opposite. One can expect the contribution of the pressure on the rear surface of the cylinder on its drag force is nearly constant, and that on lift force is significant.

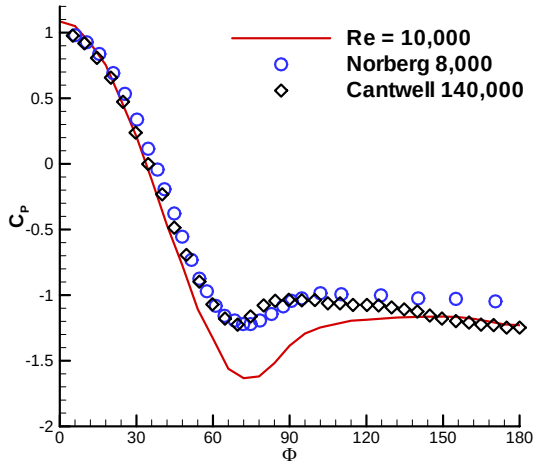

Figure 4-9 Mean pressure distribution around the cylinder.

The results in terms of the time-averaged pressure coefficient (C_p) distribution around the cylinder is compared with the experimental data in Figure 4-9. Only upper half of the cylinder is shown here, as the time-averaged value is symmetrical with respect to the flow centre line. It is seen that the time-averaged pressure on the upstream cylinder part ($\phi < 60^\circ$) agrees well with that by Norberg (2002) and Cantwell & Coles (1983). On the downstream part ($\phi > 120^\circ$), current result also agrees with the experimental data. The base pressure $C_{pb} = -1.22$, close to that reported by Cantwell & Coles (1983), witch is -1.237. However, on the middle part

of the cylinder, where the boundary layer separation takes place, the calculated time-averaged pressure coefficient deviates from the experimental results. This may be due to the current $k-\omega$ SST model is not good enough to simulate the flow separation accurately, though it has improved a lot from other RANS models (see Tutar & Holdo 2001 and Holloway et al. 2004).

The separation point, defined by Norberg (2002) as the angular position of local maximum for $dC_p/d\phi$, is not easy to be identified in Figure 4-9. Alternatively the velocity vector field is used to locate the separation point, as illustrated in Figure 4-10, where the reverse velocity in the boundary layer occurs. The separation point is oscillatory and its position varies between 85^o to 95^o in a vortex shedding period. The time-averaged separation angle is 90^o, while Norberg (2002) reported $\phi_s = 80^o$ for the same Reynolds number $\mathrm{Re} = 10^4$ in the experiment.

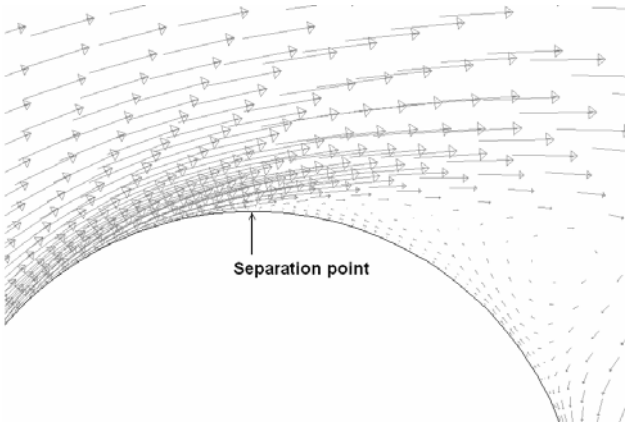

Figure 4-10 Velocity vector field near the separation point.

4.3.3 Time-averaged velocity in the wake

The mean streamwise velocity distribution along the wake centreline agrees with the experimental results by Norberg (1998) and Cantwell & Coles (1983), as shown in Figure 4-11. To study the influence of mesh resolution on simulation results, two different meshes, i.e. mesh C (24880 cells) and mesh CP (48140 cells), are investigated. It can be seen that the coarser mesh C produces an unphysical result of

mean streamwise velocity, which decreases in the far wake. This indicates fine mesh in the wake region is needed to simulate the wake flow. The reason may be due to the numerical diffusion, which has been produced less in the finer mesh system.

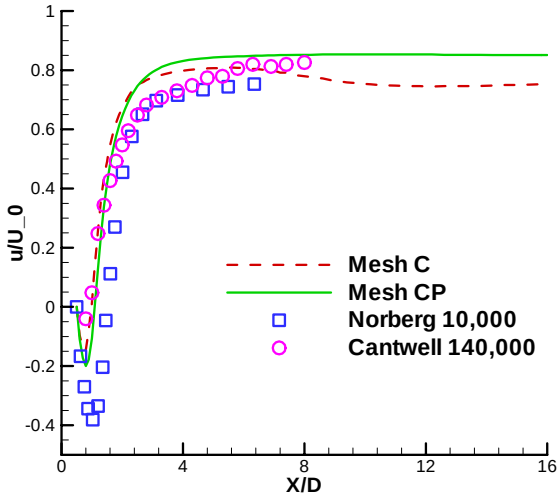

Figure 4-11 Mean streamwise velocity distribution along the wake centreline.

The mean streamwise velocity distribution gives the information about the time-averaged recirculation length behind the cylinder. The wake closure length, or the vortex formation length, which is defined as the streamwise length of the adverse velocity zone (Norberg 1998), is 1.1D for current simulation, while Norberg (1998) reported 1.5D for Re = 10^4 and in the results by Cantwell & Coles it is about 0.9D for Re = 1.4×10^5. Norberg (1998) also reported the maximum reverse velocity U_m = -0.38U_0 at L = 1.04D, while current simulation predicts U_m = -0.20U_0 at L = 0.9D. The difference suggests current model is capable of obtaining the physical characters but the accuracy is insufficient in the near wake. This may again be due to the turbulence modelling in the near wake, which is probably one of the most difficult problems in fluid mechanics.

The velocity distributions across the wake at the cross sections x = 2D, 4D and 8D based upon mesh CP are shown in Figure 4-12. The experimental data by Cantwell & Coles (1983) are also included for comparison. It can be seen that a generally good agreement is obtained except for those near the wake centreline. The comparison is

increasingly better as x/D increases.

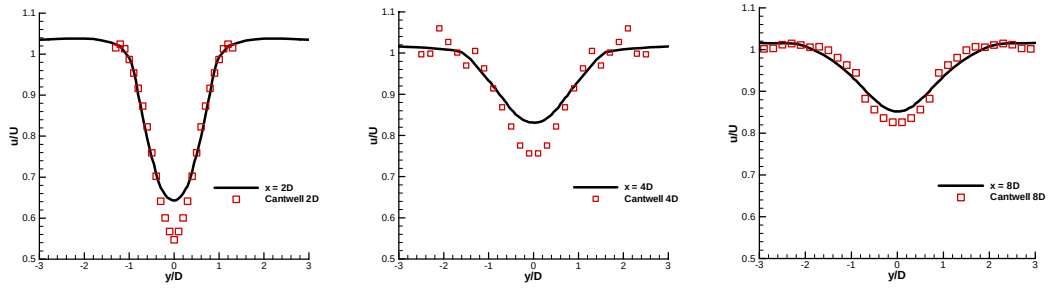

Figure 4-12 Mean streamwise velocity across the wake.

4.3.4 Time-varying velocity history in the wake

Shown in Figure 4-13 to Figure 4-15 are the velocity histories of both streamwise component, u, and transverse component, v, at nine points in near and far wake. The experimental data by Cantwell & Coles (1983) are also included for comparison. It can be seen that the varying trend of either the velocity component of the current simulation is similar with that of the experimental results, while the amplitudes are significantly higher. The reason possibly lies in the following two aspects.

Firstly, in the subcritical flow regime, the boundary layer all along the cylinder surface remains laminar up to and after the separation point and becomes turbulent somewhere in the free shear layer region. The simulations, however, have to be carried out with a turbulence model. The transition is therefore not simulated in the numerical model as it assumes an all turbulent flow in the domain (Tutar & Holdo 2001).

Secondly, approximating flow at this Reynolds number with two-dimensional simulation does not take into account 3-D effects which are present. The small scale streamwise and spanwise vortices in the turbulent wake that interact with large scale Karman vortices are ignored in 2-D simulation.

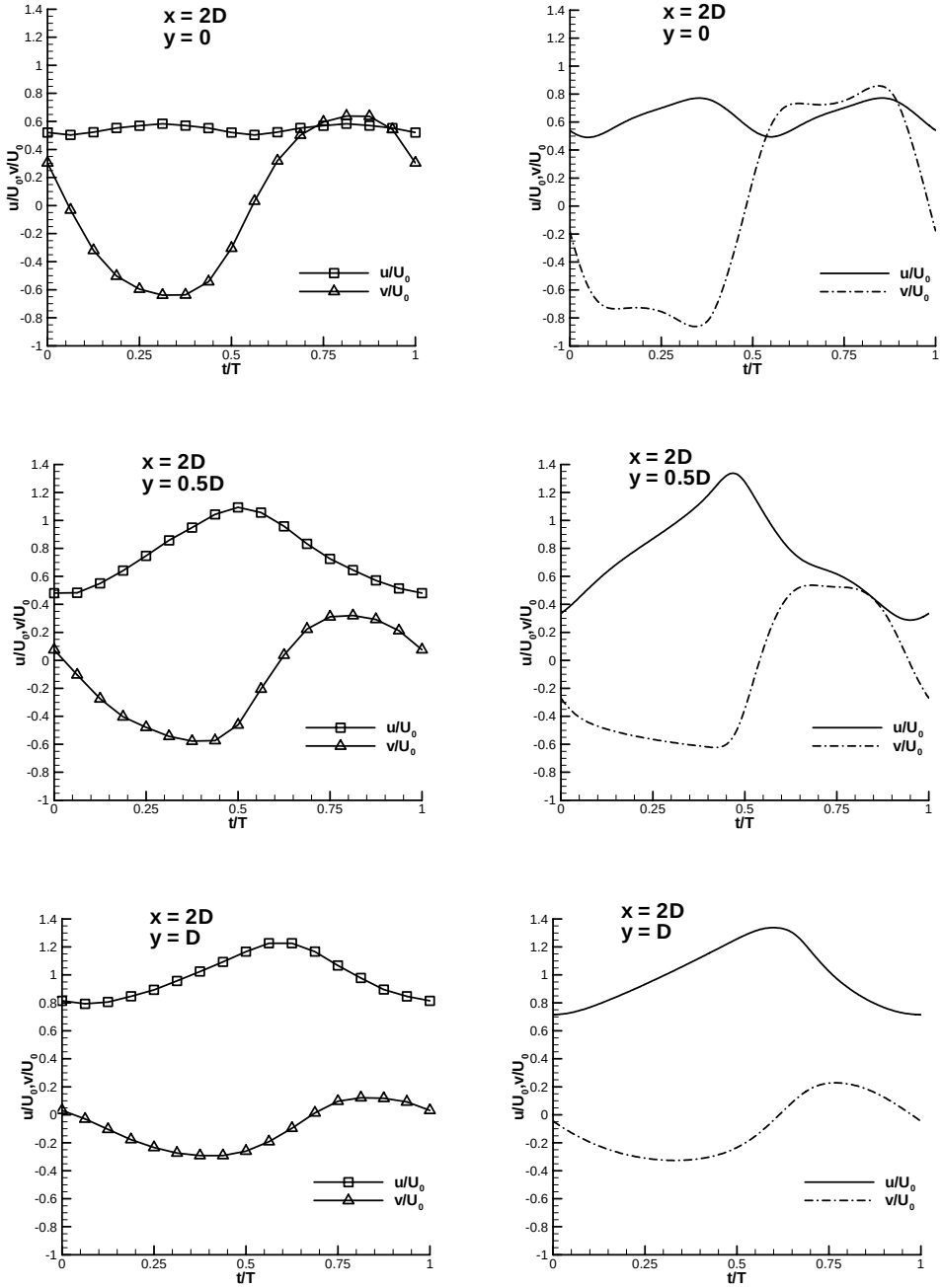

Figure 4-13 Velocity history at x=2D, y=0, 0.5D, D, respectively. Left: experimental data by Cantwell & Coles (1983); Right: Numerical results.

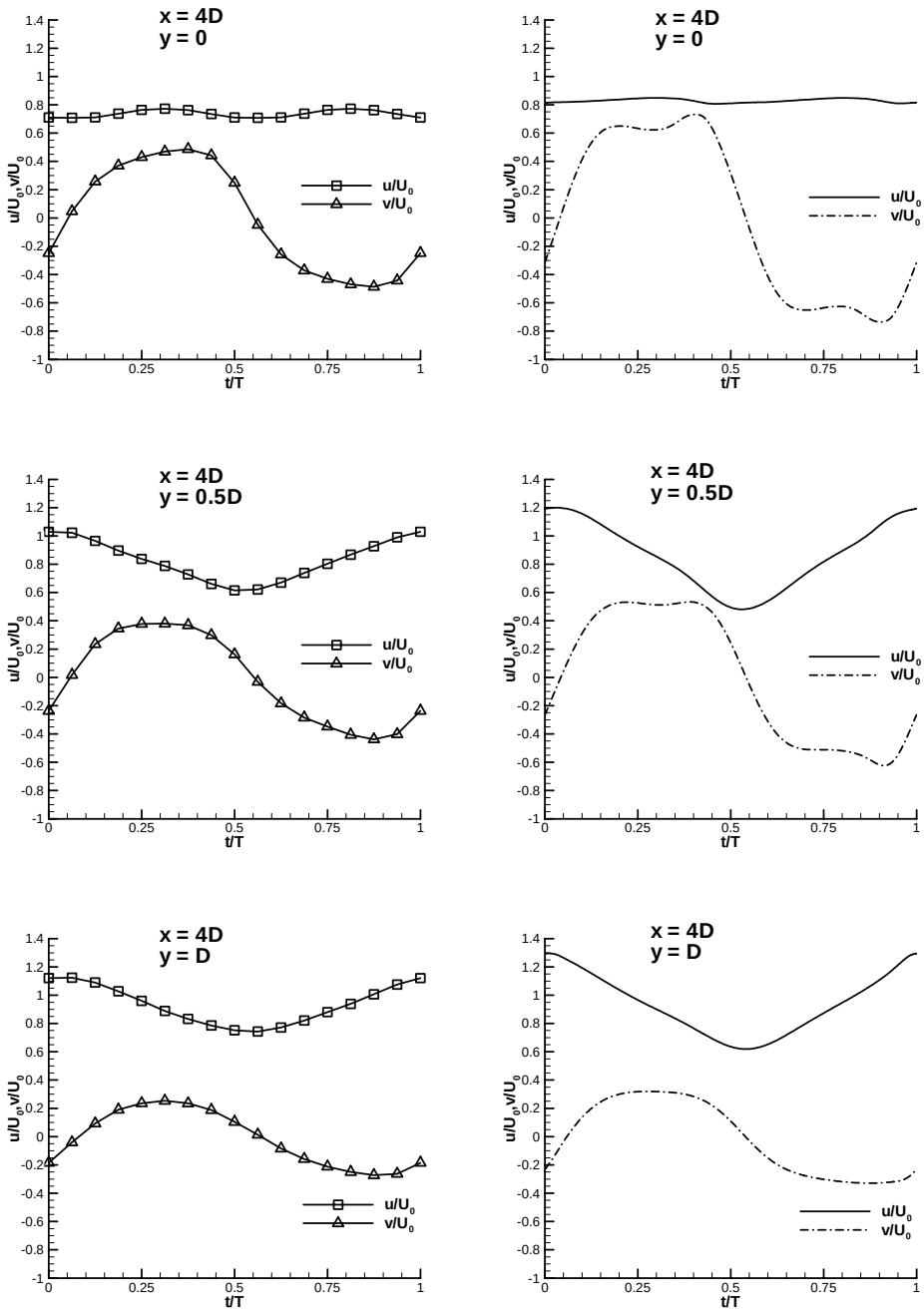

Figure 4-14 Velocity history at x=4D, y=0, 0.5D, D, respectively. Left: experimental data by Cantwell & Coles (1983); Right: Numerical results.

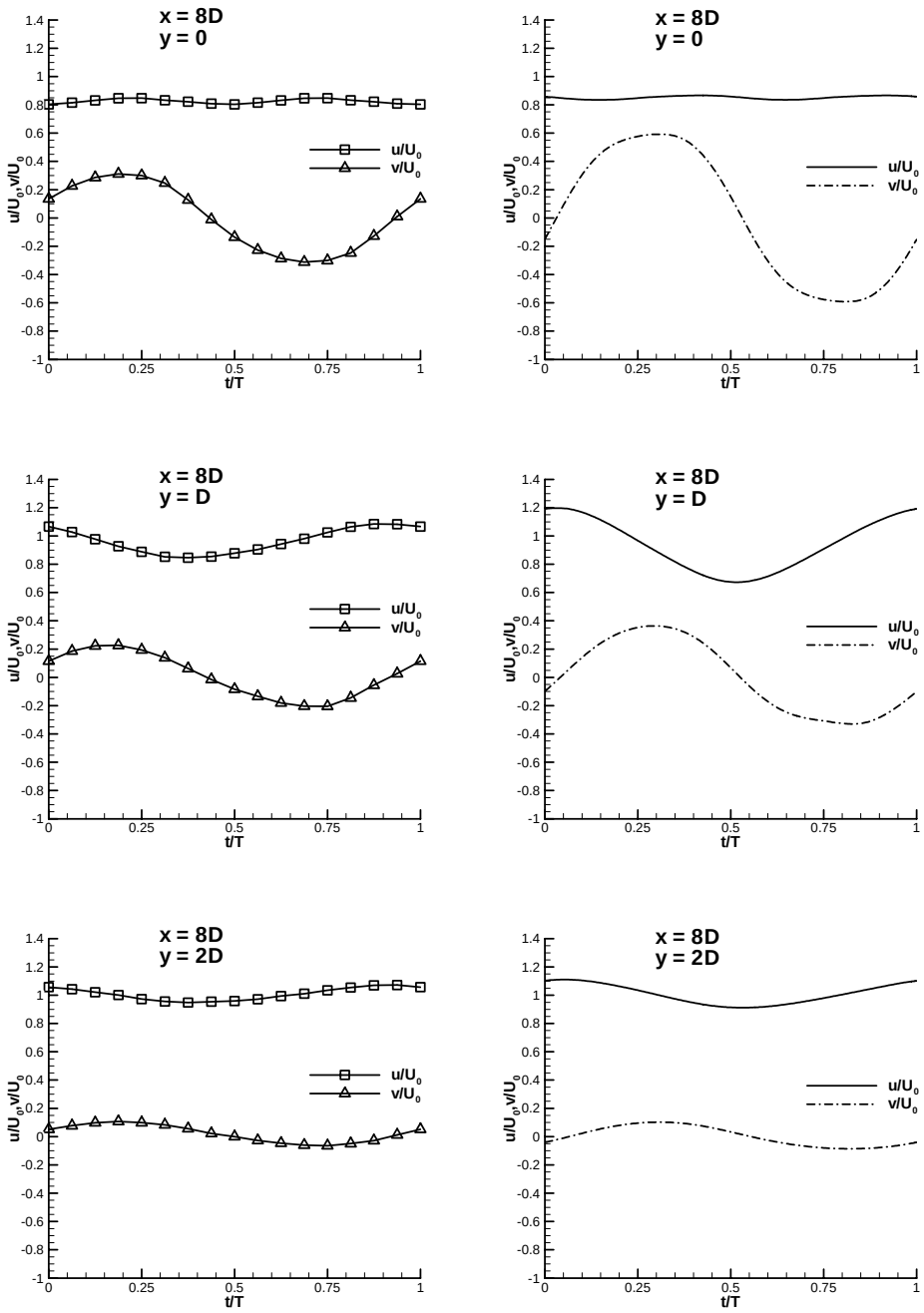

Figure 4-15 Velocity history at x=8D, y=0, D, 2D, respectively. Left: experimental data by Cantwell & Coles (1983); Right: Numerical results.

4.4 Concluding remarks

The turbulent cross flow past a circular cylinder at Reynolds number Re = 10^4 was

simulated in this chapter by using a commercial CFD software FLUENT with a $k-\omega$ SST model. The computational domain and mesh independence were carefully checked to ensure a convergent simulation. The near wall zone is using sufficiently fine mesh to simulate the separation flow. It is found the requirement for the first cell height is to have $y^+ < 0.5$. The convergent non-dimensional time step size is 0.025 for a typical mesh used in most simulations, while it should be even smaller for a finer mesh.

All the simulation results are compared with existed experimental data. The time-averaged drag coefficient C_D is found to be 1.19, and r.m.s. lift coefficient $C_{L'}$ 0.48, which agree well with the experimental results. The computed Stouhal number St = 0.23 is slightly above the value reported in literature. The time-averaged velocity distributions in the wake also agree with experimental results.

It is also shown that despite proper resolution of the flow physics, discrepancies still exist between the computational and experimental results. The separation point is overestimated and the pressure distribution near it deviates from the experimental results. The time-varying velocities have similar trends with that of the experimental results, while the amplitudes are higher.

It must be noted that approximating flow at this Reynolds number with 2-D, eddy-viscosity model simulation ignores the 3-D effects which are present and the model is for fully developed turbulent flow. However, as pointed out by Mittal et al. (1997), the flow simulation can give excellent insight into the underlying physical phenomena present in real applications. The numerical approach will continue to be adopted to simulate flow around multiple cylinders in the following chapters.

5 Two cylinders flow: tandem arrangement

5.1 Introduction

The chapter will investigate the hydrodynamic characteristics of two tandem circular cylinders in uniform flow, while the staggered case will be tackled in the following chapter. The important parameters for the tandem arrangement are free stream velocity V, the diameter of the cylinders D and their centre to centre spacing L.

Turbulent flow past two circular cylinders in tandem represents a very complicated flow phenomenon. There are three flow patterns for such kind of flow according to Zdravkovich (1987).

- The first flow pattern is observed when two cylinders are in contact or in extremely close proximity. The shear layers separating from the upstream cylinder completely engulf the downstream cylinder. Thus, the two cylinders essentially behave as an extended bluff body.
- The second flow pattern is observed when L/D is within a medium range in which a separation bubble is formed behind the upstream cylinder and is captured by the downstream cylinder. Vortex shedding is observed behind the downstream cylinder but not from the upstream cylinder. A steady circulation region consisting of a pair of counter-rotating vortices exists in the gap.
- The third flow pattern is observed for a larger L/D in which vortex shedding occurs from both cylinders. The wake behind the downstream cylinder is called binary, because each vortex is formed by the combination of one vortex shed from the upstream cylinder and another by the downstream cylinder.

In this chapter the flow around two tandem circular cylinders with the spacing L from 1.5D to 8D is simulated. All cases presented use a Reynolds number of 10^4 and

a turbulence model of $k-\omega$ SST, as in the last chapter.

The inflow and outflow boundaries are situated to allow at least 15 diameters between the inflow boundary and the upstream cylinder and 25 diameters between the outflow boundary and the downstream cylinder. The lateral boundaries are situated to allow at least 10 diameters distance to the closest cylinder. The mesh in the boundary layer for each cylinder is identical with that used in the last chapter, while the mesh between the two cylinders is determined by considering the results in 4.2.3 and 4.3.3, i.e. the density of the mesh behind the upstream cylinder is as good as or finer than mesh CP. An example of the case L = 4D is shown in Figure 5-1.

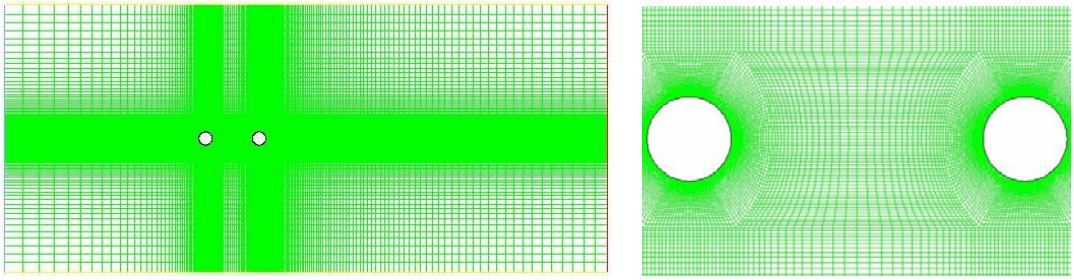

Figure 5-1 Computational mesh around two tandem cylinders. Left: the whole domain; Right: close view of the region between two cylinders.

5.2 Fluid forces

5.2.1 Drag and lift force history

Figure 5-2 shows typical lift and drag force coefficients histories for a downstream cylinder, L = 8D here. The lift force is zero when numerical iteration began, with no vortices shedding. Then it gradually fluctuates with the formation of the vortices, and finally a periodic state is achieved, by which the calculation is considered convergent. When the lift force converges, so does the drag force accordingly.

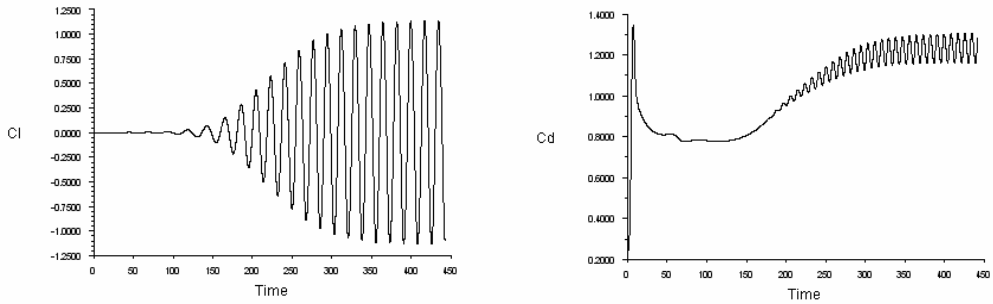

Figure 5-2 Typical lift and drag forces histories for the downstream cylinder, L = 8D.

Figure 5-3 to Figure 5-6 show the time variation in drag and lift coefficients of the upstream and downstream cylinder at L = 2D, 4D, 6D and 8D, respectively. These data are gathered when steady periodic states were achieved, after at least 30 periods of computing. The dash-dot line denotes the force coefficient for the upstream cylinder, while the solid line denotes that for the downstream cylinder. All the force coefficients are based on the free stream velocity.

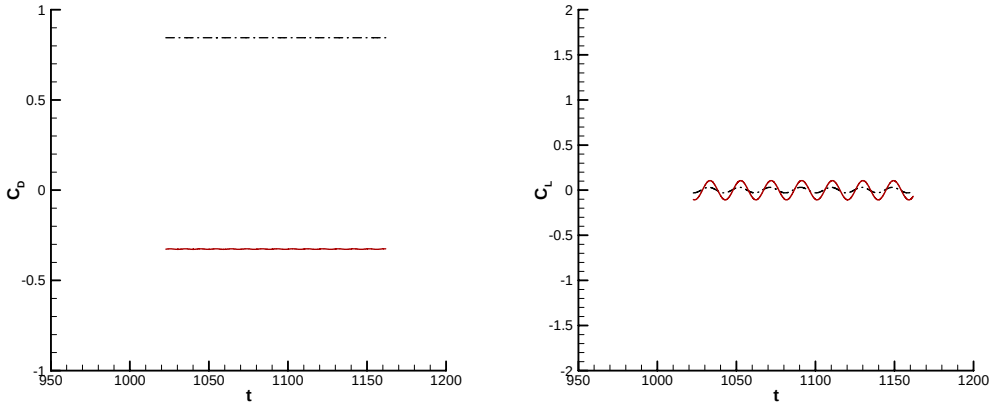

Figure 5-3 Drag and lift coefficients history of the upstream and downstream cylinder, L = 2D: Dash-dot line: upstream cylinder; Solid line: downstream cylinder.

At L = 2D, the drag force coefficient for the upstream cylinder, C_{D1}, is around 0.84, much less than that of the one cylinder flow. This means the pressure behind the upstream cylinder is less negative in the presence of the downstream one. C_{D2} is about –0.33, which is caused by the negative pressure region between the two

cylinders, as shown in Figure 5-12. The fluctuations of the drag force coefficients for both cylinders are negligible, and that for the lift force coefficients is also very small. No alternating vortices are shed from the upstream cylinder and the flow between the two cylinders is relatively steady. Although there are vortices shed from the downstream cylinder, the vortex formation length is larger compared to that of the one cylinder flow or the two vortex street flow patterns, as shown in Figure 5-10. This indicates the vortex shedding has insignificant effect on the downstream cylinder.

At L = 4D, 6D and 8D, the flow is in two vortex streets pattern. The force coefficients for both cylinders fluctuate along with the vortices shedding. The amplitudes of the fluctuations for the upstream cylinder are smaller than those for the downstream cylinder, for the force fluctuation of the downstream cylinder is induced by the alternate vortex shedding from itself, as well as by the impingement of vortices from the upstream cylinder. With increasing the spacing between the two cylinders, the amplitudes of the force coefficients for the downstream cylinder decrease, as the result of the decline in the impinging vortices. At the same time, those for the upstream cylinder keep nearly identical, which indicates the existence of the downstream cylinder hardly has any effect on the upstream one, as long as the flow is in two vortex streets pattern.

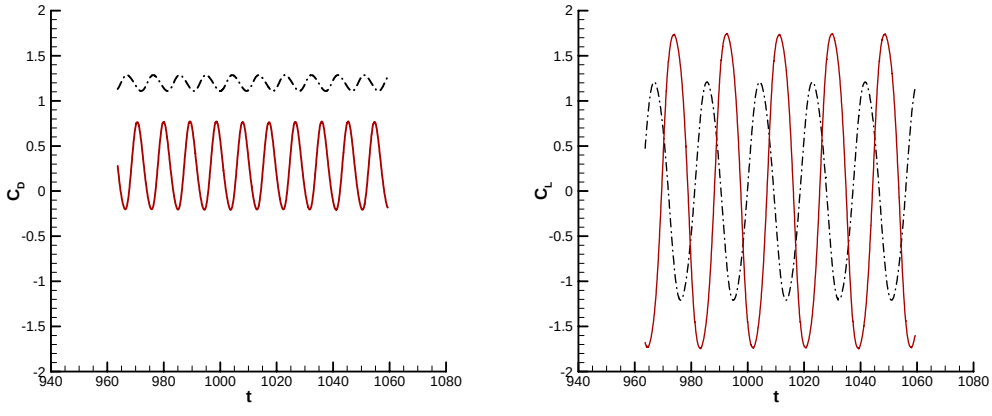

Figure 5-4 Drag and lift coefficients history of the upstream and downstream cylinder, L = 4D: Dash-dot line: upstream cylinder; Solid line: downstream cylinder.

The force coefficients of the downstream cylinder are very regular at L = 4D, become not so regular at L = 6D, and show significant irregularity at L = 8D. This indicates that, at L = 4D, the flow around the downstream cylinder is dominated by the impinging vortices coming from the upstream. As the spacing increases, the flow around the downstream cylinder is influenced by the impinging vortices, with decreasing intensity, as well as the vortices shed from itself. The interaction between these two types of vortices is also an important factor for the drag and lift on the downstream cylinder.

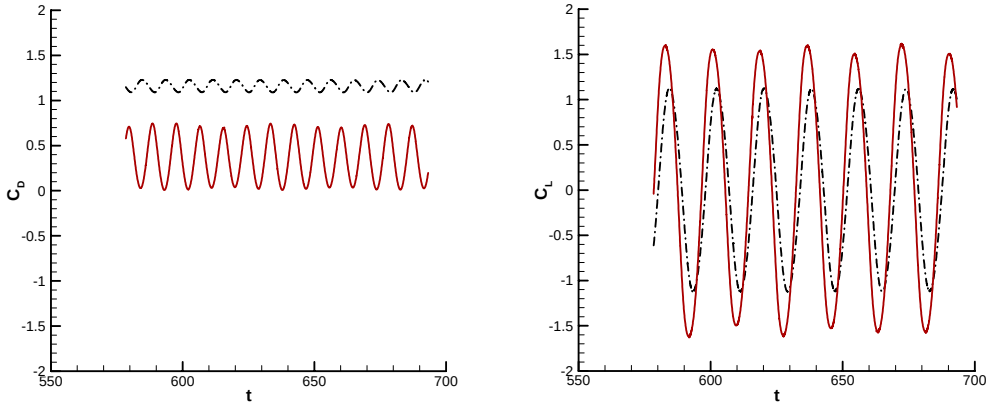

Figure 5-5 Drag and lift coefficients history of the upstream and downstream cylinder, L = 6D: Dash-dot line: upstream cylinder; Solid line: downstream cylinder.

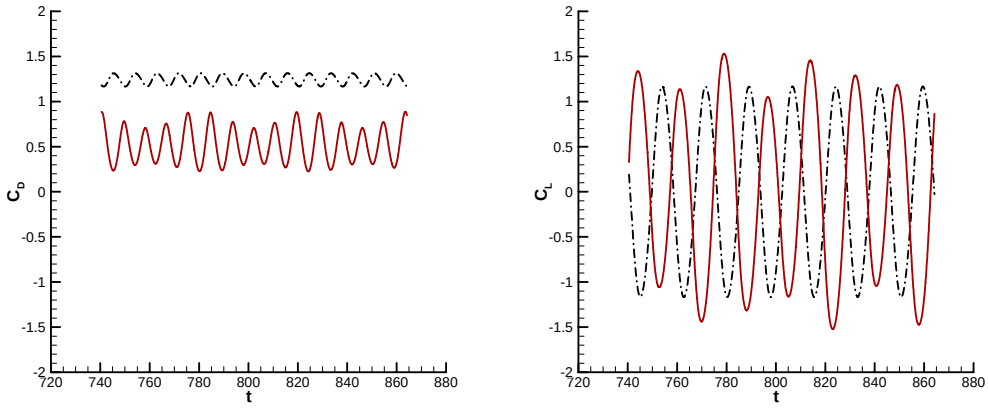

Figure 5-6 Drag and lift coefficients history of the upstream and downstream cylinder, L = 8D: Dash-dot line: upstream cylinder; Solid line: downstream cylinder.

5.2.2 Vortices shedding frequency

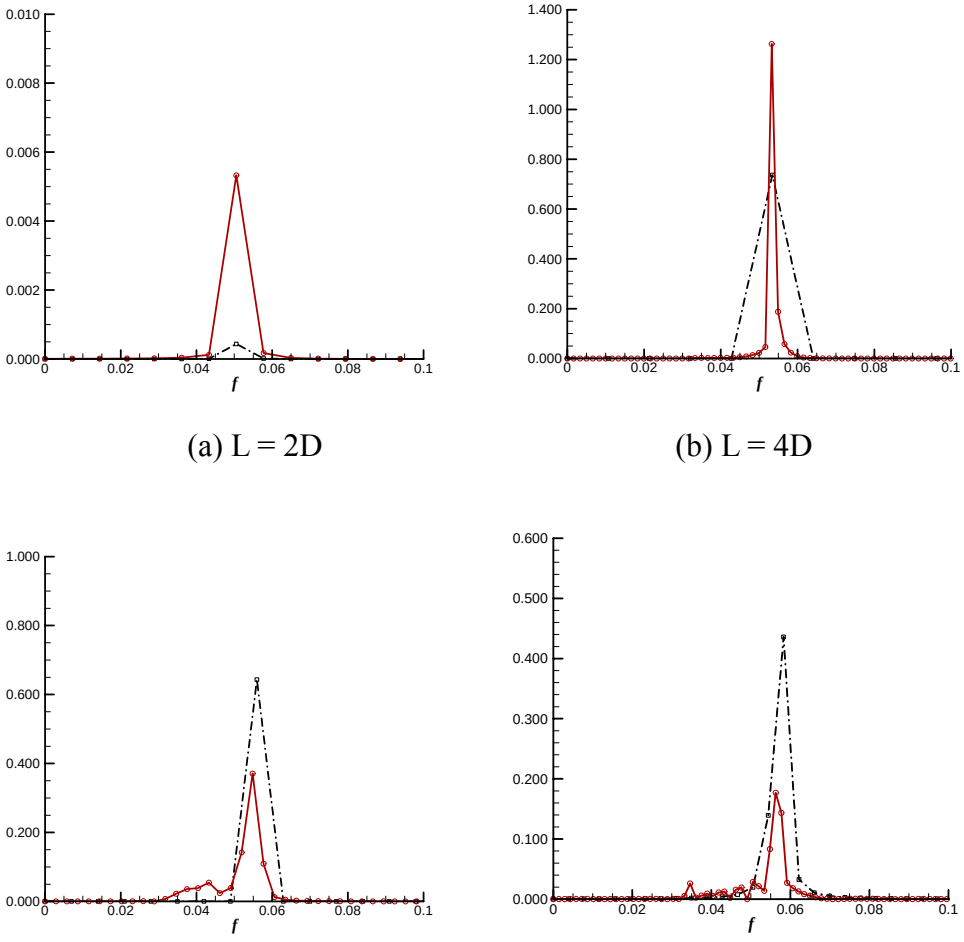

(a) L = 2D (b) L = 4D

(c) L = 6D (d) L = 8D

Figure 5-7 Power spectra of lift coefficients of the upstream and downstream cylinder. Dash-dot line: upstream cylinder; Solid line: downstream cylinder.

Figure 5-7 shows the power spectra of the lift force of upstream and downstream cylinders, at L = 2D, 4D, 6D and 8D. For small cylinder spacing, the dominant frequencies of vortex shedding from both cylinders are coincident with each other. This indicates the frequency of the vortex shedding from the downstream cylinder is strongly influenced by that from the upstream one, even though the average incident flow velocity to the downstream cylinder is much reduced due to the wake shielding. With increase of the distance, the upstream influence becomes less strong, as there is

a small peak frequency shift and more frequencies appear (L = 6D and 8D).

The Strouhal number, St = f D/U, obtained from the dominant frequencies and the free stream velocity, is around 0.22. This value is slightly above those presented in literatures (Kiya et al. 1980; Ljungkrona et al. 1991).

While the peak frequencies of the C_L fluctuations of both cylinders are almost same, it is inferred that there is a phase shift between the C_L fluctuations which may correlate with L/D (Kitagawa & Ohta 2008). Alam and Zhou (2007) also investigated the phase shift, or phase lag, and suggested

$$\varphi = 2.44\pi S_t (L_c - L_c^*) + 2\pi \tag{5.1}$$

Where φ is the phase lag and $L_c = L/D$ is the normalized cylinder center-to-center spacing and L_c^* is the critical spacing defined as the minimum L_c at which the upstream cylinder could shed vortices in the gap between the cylinders. Alam and Zhou claimed this relationship agrees well with experimental data previously reported.

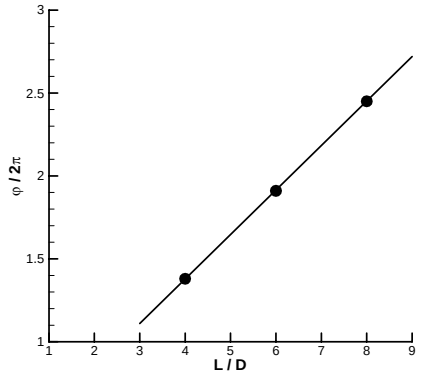

Figure 5-8 Phase shift of fluctuating lift of the cylinders.

Symbol: present study; line: equation by Alam and Zhou.

From Figure 5-10 and Figure 5-6, the phase lag for L=4D is $\varphi = 1.38 \times 2\pi$. With $S_t = 0.22$ it can be calculated $L_c^* = 2.582$ here. The phase lag values of present study for L = 4D, 6D and 8D are plotted in Figure 5-8, together with the result of the

above equation. Current result agrees well with the relationship proposed by Alam and Zhou.

With the phase lag value, the nondimensional mean convection speed of the vortices shed from the upstream cylinder can be estimated as (Kitagawa & Ohta 2008)

$$u_{con} = \frac{2\pi}{\varphi} S_t L_c \,. \tag{5.2}$$

The calculated u_{con} values are 0.64, 0.69 and 0.72 for L_c = 4, 6, and 8, respectively.

5.2.3 Mean force coefficients

Table 5-1 summarizes the time-averaged drag and lift coefficients for L = 2D, 4D, 6D and 8D, from Figure 5-3 to Figure 5-6, while in Table 5-2 are the STD values of those force coefficients. Note the average lift forces are non-zero for some cases, which suggest the error level of the current simulation is about 2%.

When the flow is in reattachment pattern, which is indicated by L = 2D, the drag force of the upstream cylinder decreases significantly (C_{D1} = 0.84), compared to that of the one cylinder flow (1.20), while the downstream cylinder has a negative drag. This shows that the negative pressure zone (Figure 5-12) between the two cylinders has heavy impact on the downstream cylinder. The STD values of force coefficients are also quite small.

Table 5-1 Time averaged drag and lift forces coefficients.

L	C_{D1}	C_{D2}	C_{L1}	C_{L2}
2	0.84	-0.33	0.00	0.00
4	1.20	0.26	-0.02	0.03
6	1.20	0.39	-0.03	-0.02
8	1.24	0.52	0.00	-0.02

When the flow is in two vortex streets pattern, L = 4D, 6D and 8D here, both the mean forces and the STD values of the upstream cylinder remain relatively constant, while for the downstream cylinder, the average drag increases with the clearance, and the STD values decrease with the clearance. The influence of the downstream cylinder on the upstream one can be ignored as long as the gap between the cylinders is greater than 4D. On the other hand, the wake effect on the downstream cylinder is significant and decreases with the spacing.

Table 5-2 Standard deviation of drag and lift forces coefficients.

L	STD (C_{D1})	STD (C_{D2})	STD (C_{L1})	STD (C_{L2})
2	0.00	0.00	0.02	0.07
4	0.06	0.34	0.85	1.28
6	0.05	0.25	0.81	1.16
8	0.05	0.19	0.83	0.95

Shown in Figure 5-9 are the mean drag coefficients on both cylinders, C_{D1} and C_{D2}, versus the spacing ratio, L/D. Some of the experimental results are also included for comparison. For L < 2.5D, the upstream cylinder has a reduced drag coefficient and the downstream cylinder experiences adverse drag. The drag coefficient of the upstream cylinder decreases with increasing the spacing. The same trend can be observed in the experimental results. Though some literature reported C_{D2} also decreases when increasing the spacing between the two cylinders but still keeping the flow in reattachment pattern (Kitagawa & Ohta 2008), the present results, together with the experimental data shown here, suggest the drag coefficient of the downstream increases with increasing the spacing.

Between L = 2.5D and L = 3D, the drag coefficients for both cylinders have an abrupt jump. C_{D1} is close to that of an isolated cylinder in cross flow while C_{D2} is still far below that.

The exact spacing ratio where the abrupt jump in C_D happens, i.e. the critical spacing ratio, was reported by many other researchers with rather scattered values. It can be seen from Figure 5-9 that it is 3.6 by Igarashi (1981), while the results by Ljungkrona et al. (1991), Moriya et al. (1983) and Zdravkovich & Pridden (1977) show the critical spacing ratio is about 3.0. It is around 2.5 in current simulation. The underestimate is likely due to the current computational model, the three dimensional effects and the difference in Reynolds number.

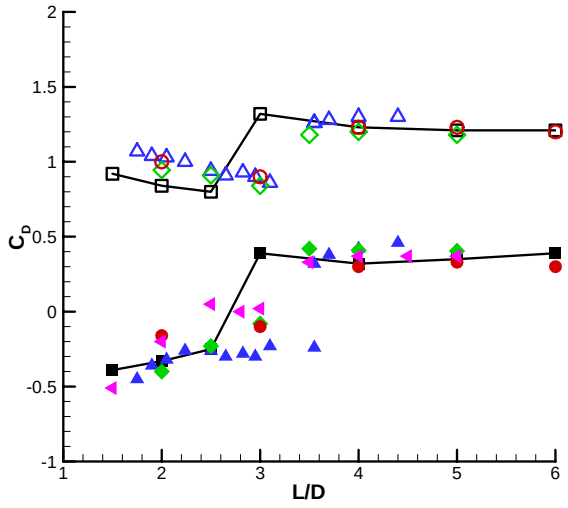

Figure 5-9 Mean drag coefficients on two tandem cylinders. Open symbol: upstream cylinder. Solid symbol: downstream cylinder. Square and line, current study (Re = 10^4); Delta, Igarashi (Re = 3.55×10^4); Diamond, Ljungkrona et al. (Re = 2×10^4); Circle, Moriya et al. (Re = 9×10^4); Left triangle, Zdravkovich and Pridden (Re = 1.2×10^5).

5.3 Flow features

5.3.1 Reattachment and two vortex streets patterns

Figure 5-10 (a) shows an instantaneous contour of vorticity distribution in the case of

L = 2D. Alternating vortex shedding is not observed from the upstream cylinder. The shear layers separated from the upstream cylinder reattach to the downstream one, and two quasi-steady vortices are formed between the cylinders, which was also obtained by Igarashi (1981). However, vortices are alternately formed and shed behind the downstream cylinder. In this shear layer reattachment flow pattern the cylinders act as a single body.

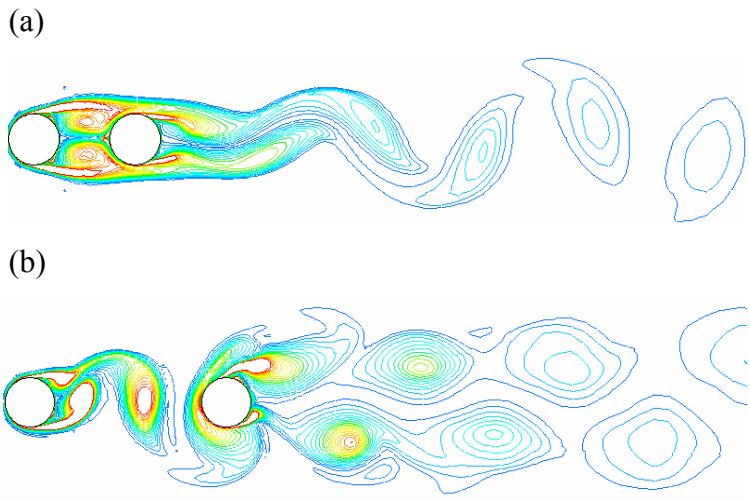

Figure 5-10 Instantaneous contours of vorticity magnitude. (a) L = 2D; (b) L = 4D.

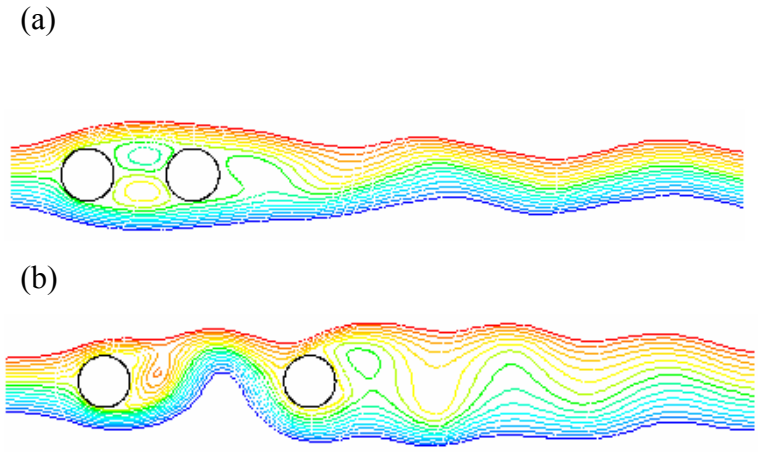

Figure 5-11 Instantaneous contours of stream function. (a) L = 2D; (b) L = 4D.

Increasing the spacing between the two cylinders to 4D, the two vortex streets

pattern is observed, as shown in Figure 5-10 (b). The shear layers from the upstream cylinder do not reattach to the downstream one, and the vortices are alternately shed from the upstream cylinder. The vortices shed from the upstream cylinder rapidly deform as they approach the downstream cylinder. Because of impingement of the vortices from the upstream cylinder on the downstream one, the flow near the downstream cylinder is highly unsteady. The wake behind the downstream cylinder is called a binary vortex street (Williamson 1985), because each vortex is formed by the combination of one vortex from the upstream cylinder and another by the downstream one.

Figure 5-11 shows the instantaneous contours of stream function, L = 2D and 4D, respectively. In part (a), which represents the stream function of the case L = 2D, a steady recirculation region consisting of a pair of counter-rotating vortices exists in the gap. However there is no such a region existed when L = 4D, as shown in part (b), and the flow between the two cylinders is highly unsteady.

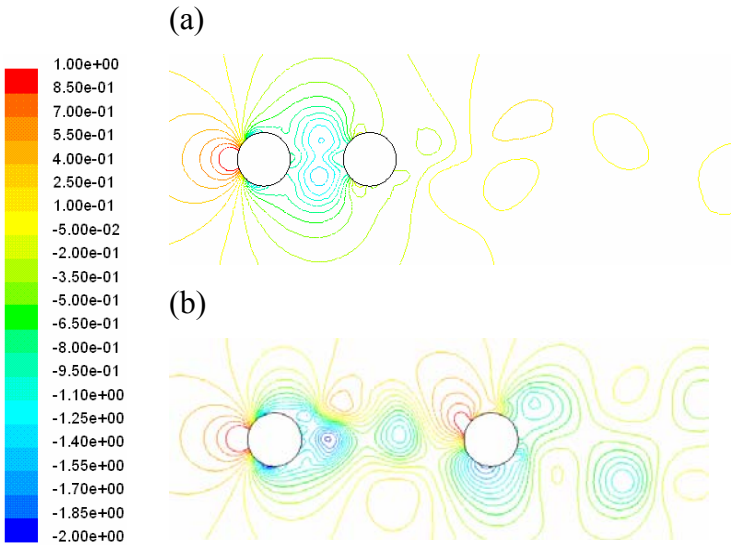

Figure 5-12 Instantaneous contours of static pressure. (a) L = 2D; (b) L = 4D.

The pressure distributions also indicate differences between the two flow patterns, as shown in Figure 5-12. In part (a), there exists a steady negative pressure region between the two cylinders at L = 2D. This significant negative pressure is acted on the front part of the downstream cylinder, resulting in a negative drag on it; on the

contrary, this steady negative pressure zone does not exist when L = 4D. Both positive and negative pressure alternately act on both sides of the downstream cylinder. The fluid forces will be discussed in detail in the following parts.

5.3.2 Bistable and hysteresis features

For certain spacing, the flow can be in either reattachment pattern or two vortex streets pattern, and both states are stable. This phenomenon is called bistable (Zdravkovich 1997). The bistable nature of the flow around two tandem cylinders was also been observed here. It is possible to drive the flow into either the reattachment or two vortex streets patterns by selecting different initial conditions.

Figure 5-10 (a) shows the reattachment flow pattern for the case L = 2D, by directly running the simulation, with two fixed cylinder in cross flow. To achieve the two vortex streets pattern, a steady solution at a larger spacing, say, L = 3D, was first obtained. The flow was in two vortex street pattern in this case. Then using the dynamic mesh technique, the spacing between the two cylinders was slowly decreased to 2D. The flow pattern persisted for any additional time steps, as shown in Figure 5-13.

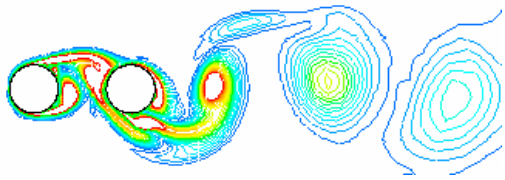

Figure 5-13 Instantaneous contours of vorticity magnitude, L = 2D.

A hysteretic effect is an experimentally observable feature in two cylinders in tandem. It has been summarized by the following quote from Zdravkovich (1984).

One of the two flow patterns persisted longer when the velocity was increased or, at the same velocity when the cylinder was displaced in one direction and the other pattern lasted longer when the opposite conditions were imposed. The hysteresis

produced an apparent overlap of the two flow patterns although only one flow pattern exists at a time.

Using the dynamic mesh, the spacing was increased by moving the downstream cylinder at a velocity of 0.2% of the free stream velocity from the initial L = 1.3D, which was obviously in reattachment pattern, to L = 4D. It was found that this flow pattern persisted until L = 2.7D (Figure 5-14), at which point a rapid transition to the two vortex streets pattern occurs.

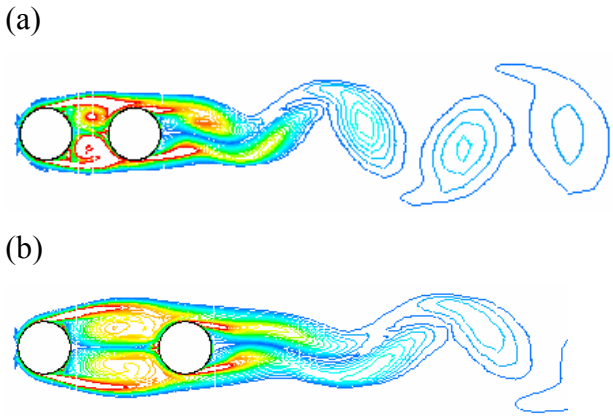

Figure 5-14 Instantaneous contours of vorticity magnitude showing reattachment flow pattern. (a) L = 1.7D; (b) L = 2.7D.

The hysteresis phenomenon can also be observed in Figure 5-15, which shows the drag coefficient on the upstream cylinder and downstream cylinder as a function of the clearance L/D for either an increasing spacing (shown as squares) or decreasing spacing (shown as deltas).

By starting the simulation from the reattachment pattern at L = 1.3D and slowly increasing the spacing to 8D, the reattachment flow pattern persists up to a spacing of 2.7D at which point a sharp increase in drag coefficients for both cylinders, indicating a transition to the two vortex streets pattern occurs.

Similarly, when the spacing was decreased from 4D to 1.3D, the two vortex streets pattern persisted until L = 1.7D, as shown in Figure 5-16. Note in Figure 5-16 (b),

there are not two vortex streets formed behind the upstream cylinder actually, but obviously the shear layers do not reattach the downstream cylinder either. This special flow state causes significant drag on the downstream cylinder, as shown in Figure 5-15. Similar results were also found by Jester & Kallinderis (Jester & Kallinderis 2003).

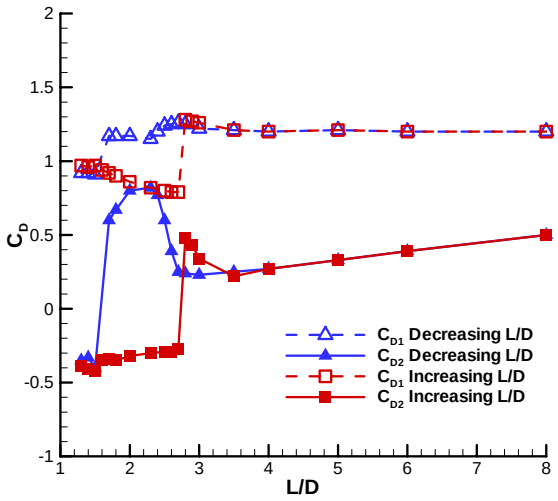

Figure 5-15 Hysteresis of drag coefficients of two tandem cylinders when increasing and decreasing the spacing.

(a)

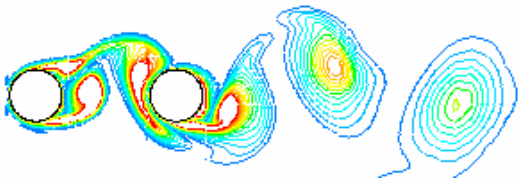

(b)

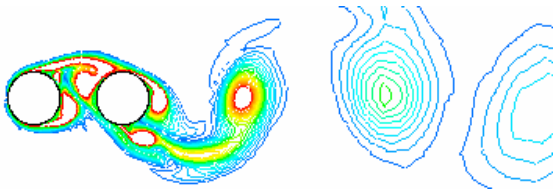

Figure 5-16 Instantaneous contours of vorticity magnitude showing two vortex streets pattern, (a) L = 2.7D; (b) L = 1.7D.

5.4 The wake behind the downstream cylinder

The wake behind the downstream cylinder is very complex because it features intensive turbulence and vortex superposition. Previous work about this can hardly be found, either experimentally or numerically. Huse (1993) calculated the wake velocity by RMS summation of the wake contributions generated by all upstream cylinders, based on wake and momentum considerations.

In this thesis the characteristics on wake centre line behind two tandem cylinders are studied. The time-averaged velocity and the power spectra of the velocity history are presented, which can be of importance for three in-line cylinders flow in Chapter 7. No comparisons are made due to lack of experimental data.

5.4.1 Time-averaged velocity along the wake centre line

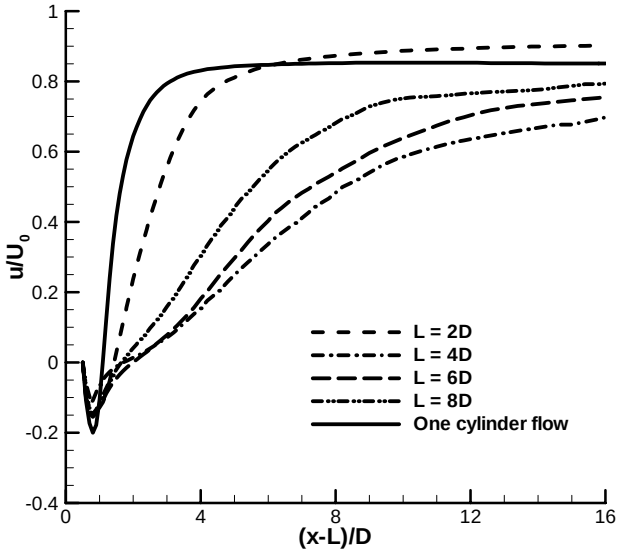

Figure 5-17 Time-averaged streamwise velocity along the wake centre line behind the downstream cylinder.

Shown in Figure 5-17 are the time-averaged streamwise velocity distributions along

the wake centreline behind the downstream cylinder in the case of two tandem cylinders with the spacing L = 2D, 4D, 6D and 8D. The distribution behind an isolated cylinder is also presented for comparison. It can be seen that the increase in the averaged velocity along the wake centreline for tandem arrangement is slower than that for an isolated cylinder flow. This indicates the cascading shielding effects by both the cylinders.

For L = 2D, the flow is in reattachment pattern. The time-averaged recirculation length behind the downstream cylinder is larger than that of an isolated cylinder (see part 4.3.3). The vortex formation length is 1.5D here. Though the average velocity increases slower along the wake centreline, the magnitude is greater than that of an isolated cylinder in the wake further than 6D. This is mainly due to the fact that the vortices generated behind the downstream cylinder are not as strong as those behind an isolated cylinder (Figure 5-10a).

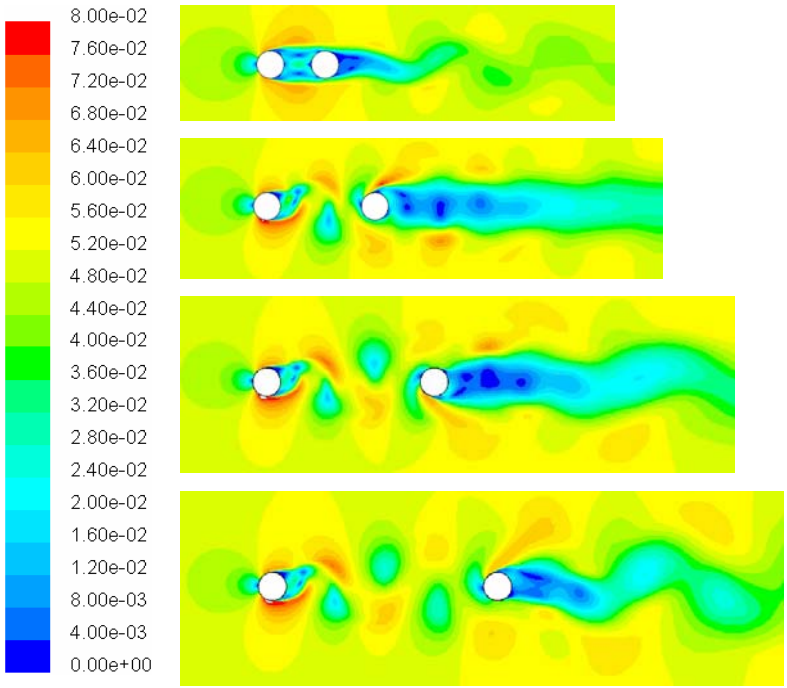

Figure 5-18 Instantaneous velocity magnitude contours of flow around two tandem cylinders. L = 2D, 4D, 6D and 8D, respectively. The free stream velocity V = 0.05 for this figure.

For L = 4D, 6D and 8D, the flow is in two vortex streets pattern. The increase in velocity along the wake centreline downstream is even slower. It can be seen that in this flow pattern, the increase is slower when the spacing between the two cylinders is less. This probably is the result of strong vortex-body interaction when the two cylinders are close.

Figure 5-18 shows the instantaneous velocity contours of flow around two tandem cylinders, L = 2D, 4D, 6D and 8D, respectively. It is evident there is a zone behind the downstream cylinder where the velocity is greatly reduced, which is significantly longer streamwise for two vortex streets flow pattern compared to the reattachment pattern or the flow behind an isolated cylinder.

5.4.2 Wake power spectra analysis

The power spectrum analysis of the downstream cylinder lift history suggests the vortex shedding frequency is almost constant with St = 0.22 for all the spacings investigated between two tandem cylinders. This does not mean the oscillating flow in the wake has the same frequency, as demonstrated by the following wake velocity power spectra analysis.

Shown in Figure 5-19 - Figure 5-22 are wake power spectra density of velocities measured on the wake centreline behind two tandem cylinders with the spacing L = 2D, 4D, 6D and 8D. The measurement points are selected in such a way that they are away from the centre of the downstream cylinder at distances x – L = D, 2D, 4D, 6D and 8D. For comparison, the power spectrum density of the lift force for each configuration is also included.

Figure 5-19 shows the case for L = 2D. It can be seen that the wake along the centreline up to 8D has the same frequency as the lift history, with the non-dimensional frequency St = 0.20. This indicates in reattachment flow pattern the vortex shedding behind the downstream cylinder shares some similarity to the one cylinder flow.

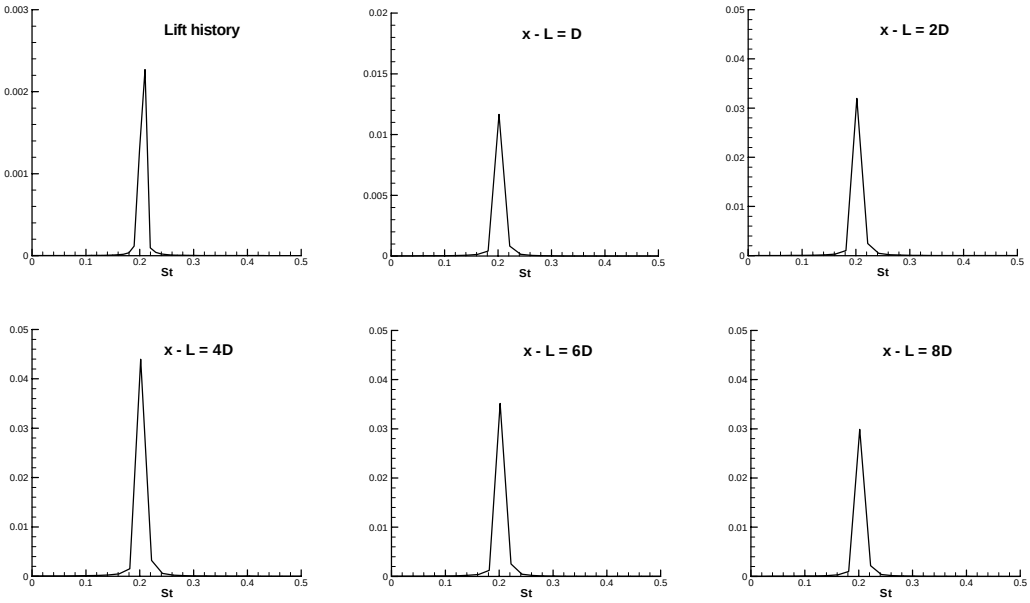

Figure 5-19 Power spectra analysis of lift history and velocities at several points along the wake centre line. L = 2D.

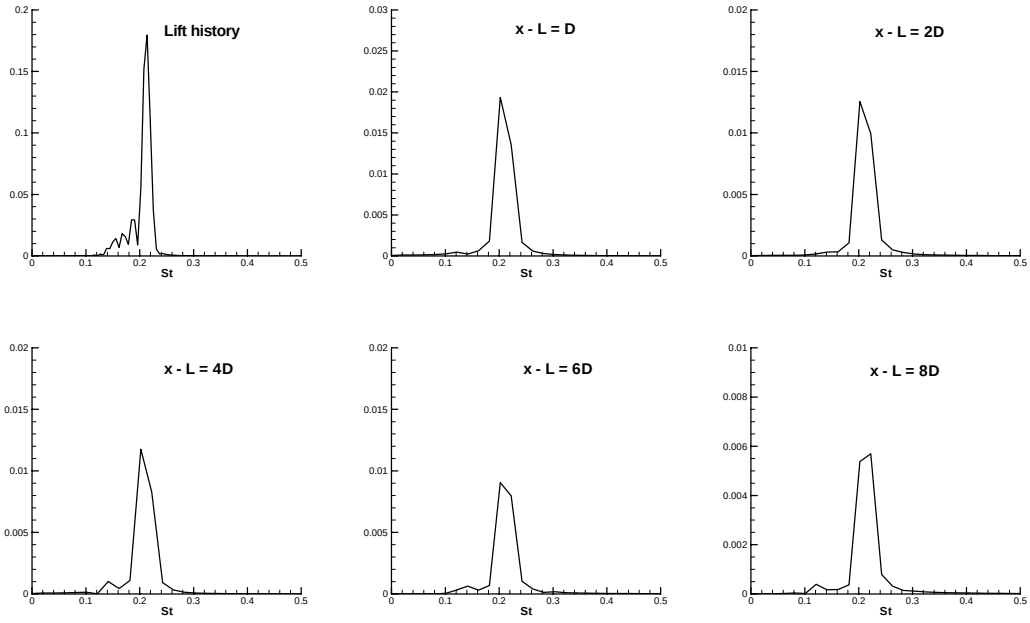

Figure 5-20 Power spectra analysis of lift history and velocities at several points along the wake centre line. L = 4D.

Figure 5-20 shows the case for L = 4D. Again the wake along the centreline up to 8D has the same frequency as the lift history, with St = 0.22. This probably is due to the strong influence of the vortices from the upstream cylinder on the downstream cylinder.

Figure 5-21 shows the case for L = 6D, which is different from the two cases above. The power spectra density of the lift history and the velocity at x – L = D indicate the vortex shedding frequency St = 0.22. At x – L = 2D, there is a significant peak at 0.14 as well as the dominant frequency at 0.22. Further downstream beyond x – L = 4D, the dominant frequency is reduced to around 0.13. This indicates when the two cylinders are spaced at a distance of 6D, the developed wake has a reduced frequency, though the vortex shedding frequency is still dominated by the oncoming vortices.

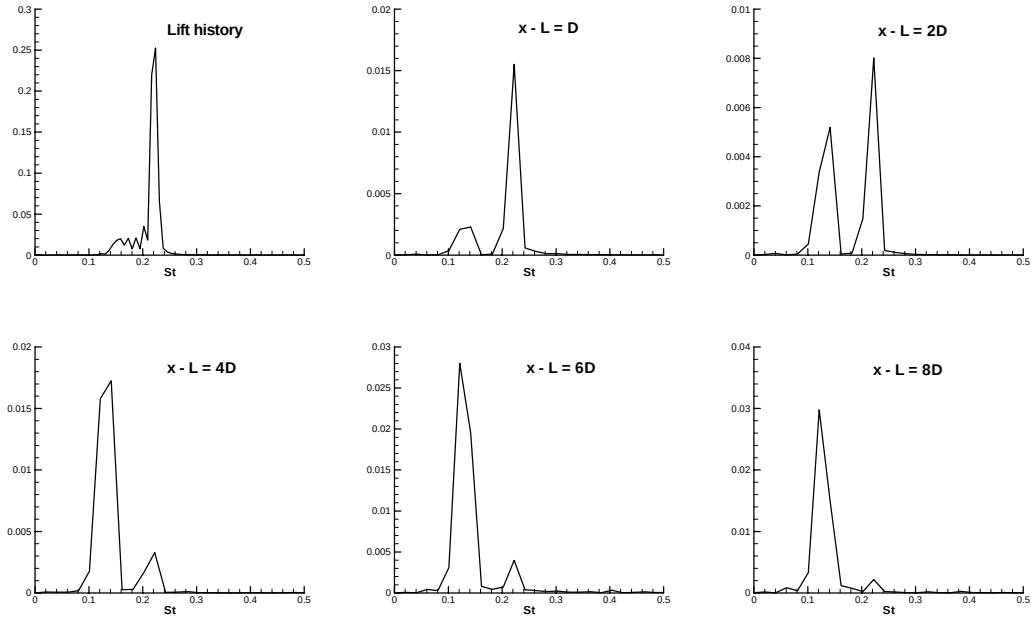

Figure 5-21 Power spectra analysis of lift history and velocities at several points along the wake centre line. L = 6D.

Figure 5-22 shows the case for L = 8D. The power spectra density of the lift history indicates the vortex shedding frequency St = 0.22, but at x-L = D there are two distinct peak frequencies at 0.22 and 0.14 respectively for the velocity, with the

dominate peak at 0.22. As the distance increases, i.e. further downstream, the dominant peak frequency of the velocity shifts to 0.14 with a reduced peak at 0.22. At x-L = 6D, the peak at 0.22 disappears altogether. This may suggest that the wake developed behind the downstream cylinder is mainly controlled by the vortices shed from itself, rather than the impinging vortices from upstream, even though the frequency of the lift is heavily influenced by the impinging vortices.

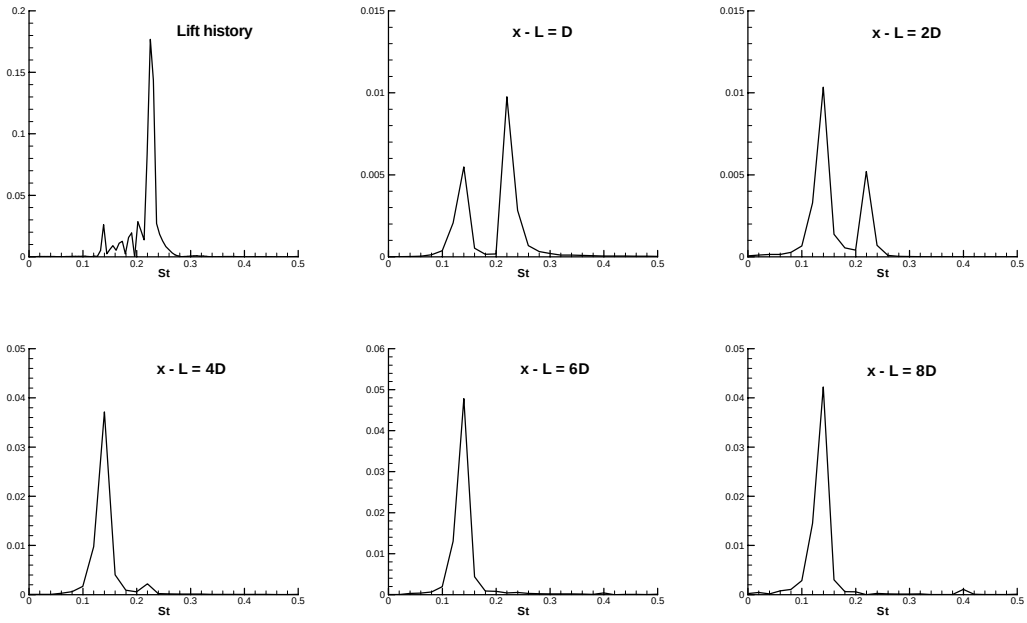

Figure 5-22 Power spectra analysis of lift history and velocities at several points along the wake centre line. L = 8D.

5.5 The cause of fluid forces on the downstream cylinder

The fluid forces on the downstream cylinder show some different characteristics from those on the upstream or an isolated one. To study the time-averaged drag reduction and lift force enhancement, the vortex and pressure fields, velocity vector around the downstream cylinder and their relationships with each other need to be investigated in greater detail.

5.5.1 Vortex impingement

Shown in the following figures are the pressure and vorticity contour and velocity vector varying within a vortex shedding period, for flow around two tandem circular cylinders with the spacing L = 4D. The time-interval between consecutive plots in these figures is one tenth of the period for one complete cycle of vortex shedding in the cylinders' wake. All variables are dimensionless based on the free stream velocity, U and the cylinder diameter, D.

Legend

(a) Vorticity contour

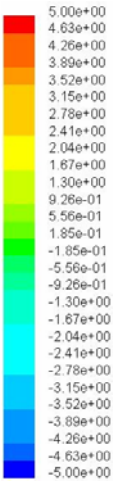

(b) Velocity vector

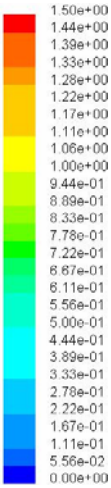

(c) Pressure contour

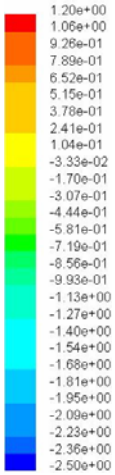

t = 0.0T

(a)

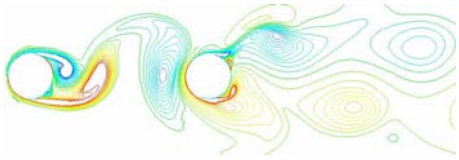

(b)

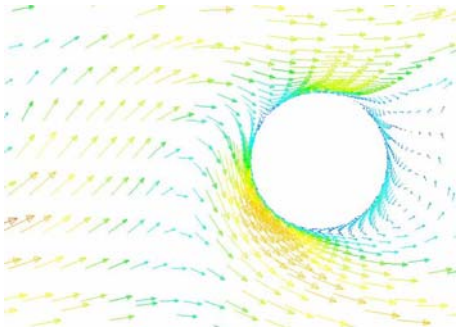

(c)

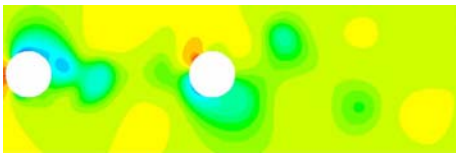

t = 0.1T

(a)

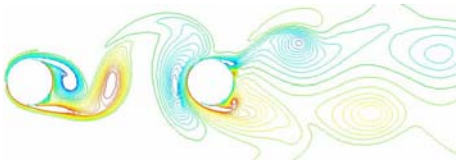

(b)

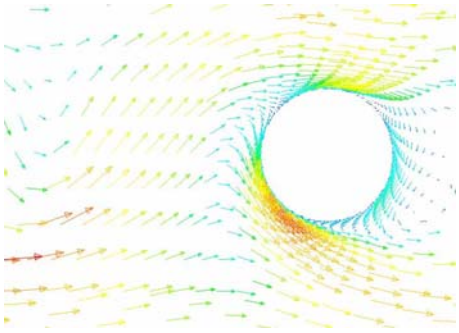

(c)

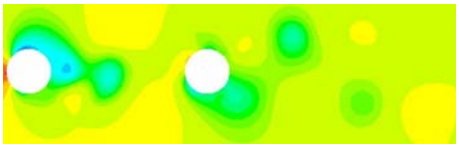

t = 0.2T

(a)

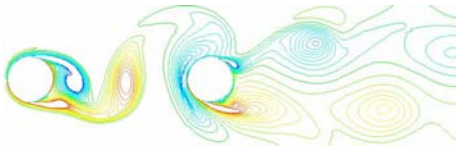

(b)

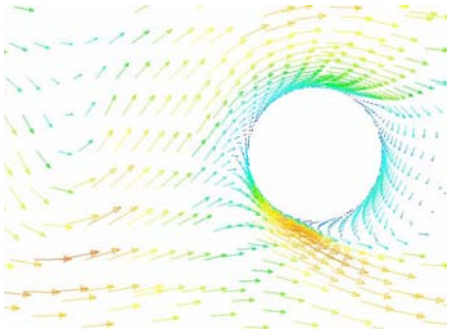

(c)

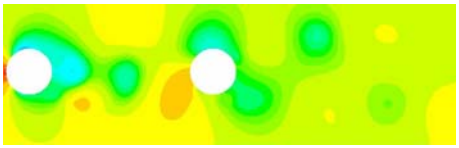

t = 0.3T

(a)

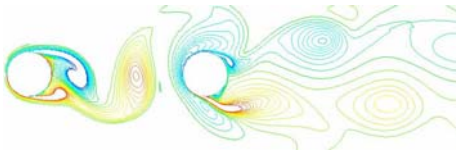

(b)

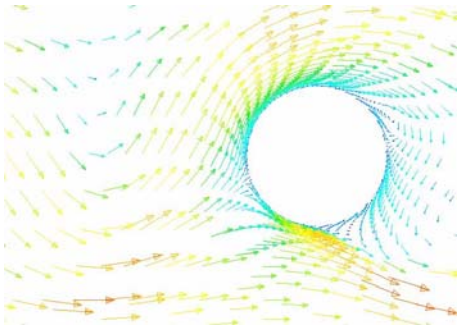

(c)

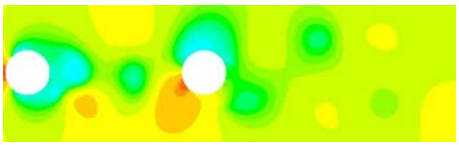

t = 0.4T

(a)

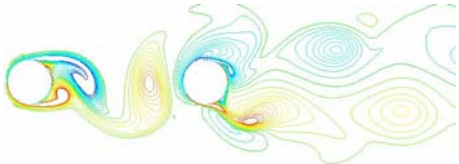

(b)

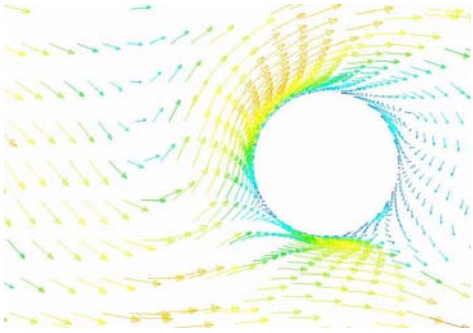

(c)

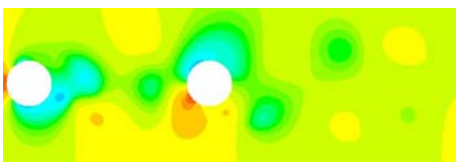

t = 0.5T

(a)

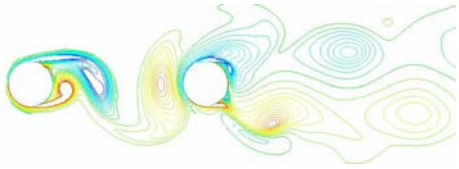

(b)

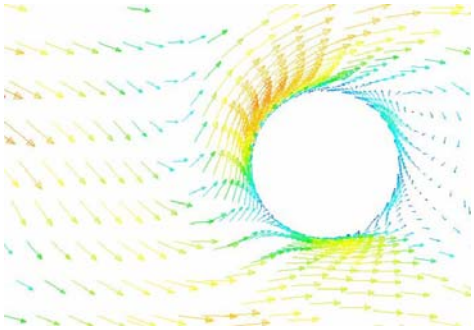

(c)

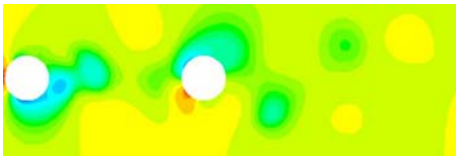

t = 0.6T

(a)

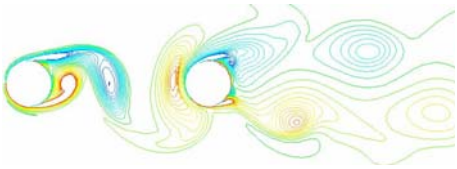

(b)

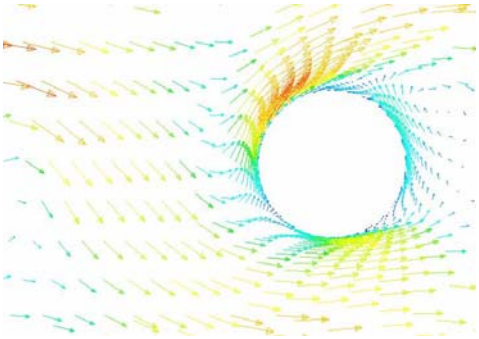

(c)

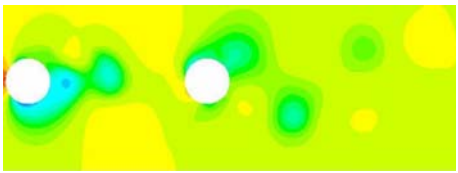

t = 0.7T

(a)

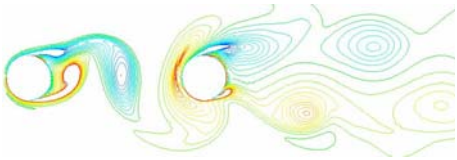

(b)

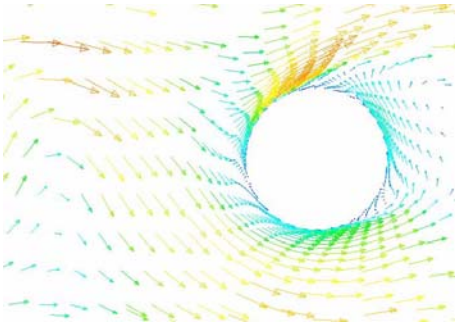

(c)

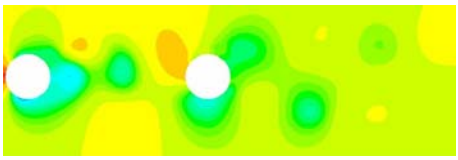

t = 0.8T

(a)

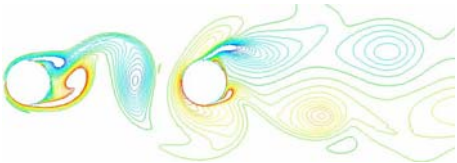

(b)

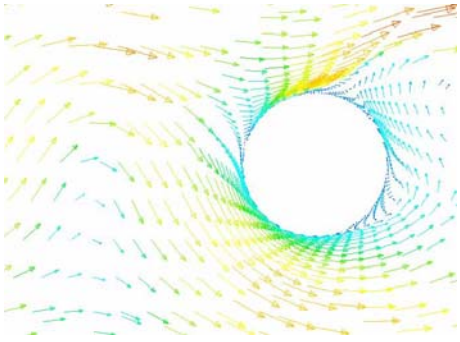

(c)

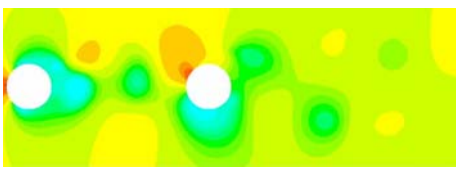

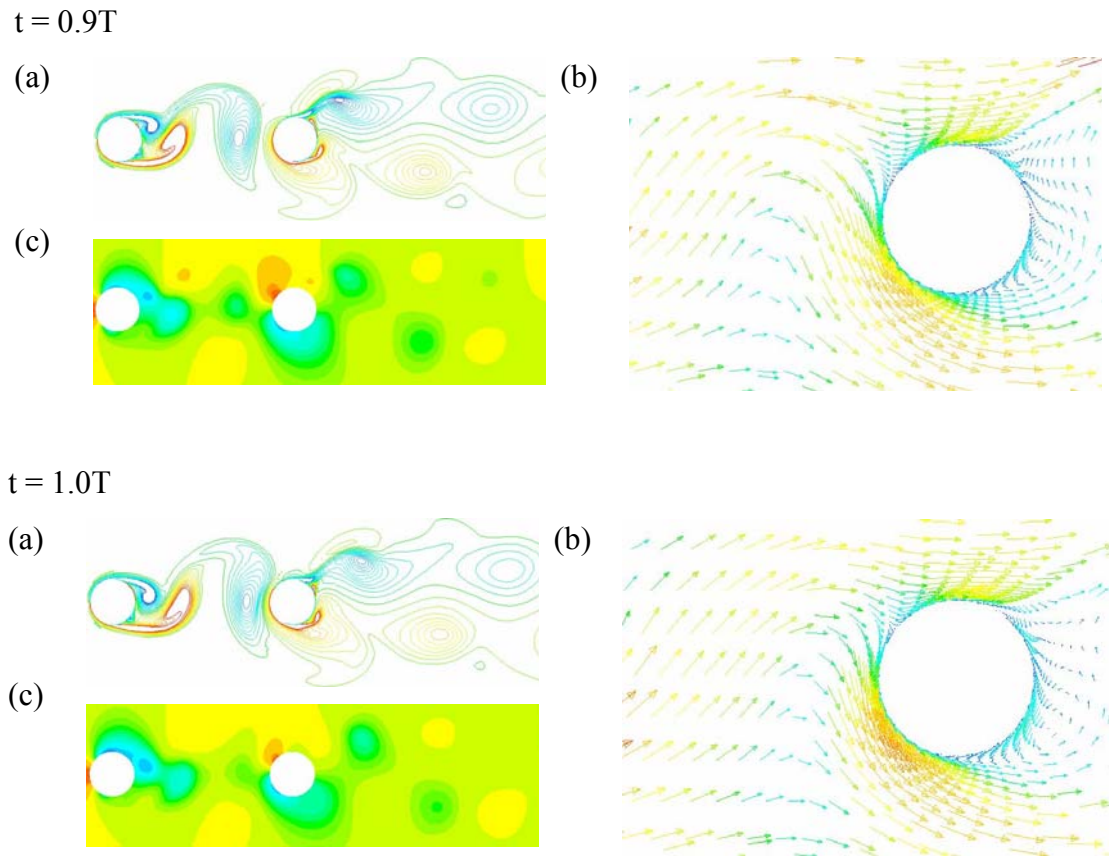

Figure 5-23 Pressure and vorticity contour and velocity vector varying in a vortex shedding period.

The Karman vortex from the upstream cylinder is fully formed, and its impingement on the downstream cylinder is observed, shown in Figure 5-23 0.0T(a)~1.0T(a). As a negative vortex from the upper surface of the upstream cylinder approaches the downstream cylinder (0.0T), it is deformed (0.0T~0.3T) and then splits into two parts (0.4T) upon impingement, the upper part of which merges into the like-sign newly-forming vortex from the upper surface of the downstream cylinder, and the lower part merges into the opposite-sign shedding vortex from the lower side of the downstream cylinder. It is difficult to decide the proportion into which the impinging vortex splits up, but it is observed only a small portion of that merges into the opposite-sign vortex. The same process happens to the positive vortex shedding from the lower side of the upstream cylinder (0.5T~0.9T).

During the process of the like-sign vortices merging by the split upstream vortex and that formed behind the downstream cylinder, it is observed that the upstream vortex dominates the latter. As the split vortex bypass the cylinder, its centre is pushed away from the cylinder axis. It entrains the newly forming, incomplete vortex behind the downstream cylinder and then convects downstream. The centre of the combined vortex is well off the cylinders' centreline, which is different from the vortices shed from the upstream cylinder, or an isolated one, since their centres are more close to the cylinders' centreline.

The upstream vortices' dominance can also be verified by the Strouhal number data measured in the wakes of the upstream and downstream cylinders. Shown in Figure 5-24 are power spectra of velocities of a few points in both wakes, of which those x = 2D and 3D are in the upstream wake, and those x = 5D and 8D are in the downstream wake. The results show the same frequency for all the cases (St = 0.21). This may indicate synchronization between the impingement flow and Karman vortex shedding from the downstream cylinder, analogous to lock-in condition (Rockwell 1998).

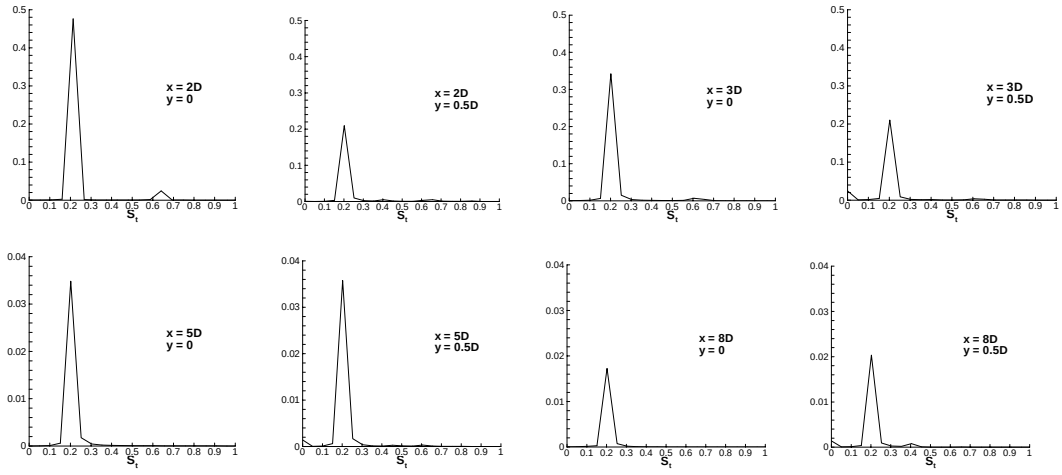

Figure 5-24 Power spectra of velocities of some points in two cylinders' flow field.

The strong effect of the impingement flow on the vortex shedding behind the downstream cylinder is mainly because of the cylinders' tandem arrangement with

L=4D. With increasing the spacing, weaker effect should be expected, as the vortex intensity decreases with convecting downstream.

5.5.2 Velocity vector

Shown in Figure 5-23 0.0T(b)~1.0T(b) are velocity vector plots which depict the magnitudes and orientations of the flow velocities around the downstream cylinder. The first noticeable is the change of stagnation point near the surface of the downstream cylinder. At t = 0.2T, the stagnation point is near the middle part of the front surface of the cylinder, and moves downwards to about minus forty degree at t = 0.3T, 0.4T, 0.5T and 0.6T, then back to the middle point at t = 0.7T. The similar process, with the stagnation point moving upwards and then back, takes place in the other half cycle of the vortex shedding. It is seen from Table 5-3, which shows the actual positions of the stagnation point changing in one cycle of the vortex shedding, that for the most part of a period, the stagnation point is around $\phi = \pm 35^{\circ}$, and highly symmetric at the relative time in both half of the vortex shedding cycle.

Table 5-3 Position of the stagnation point in a period.

t	0.0T	0.1T	0.2T	0.3T	0.4T
ϕ_S (degree)	43	31	-13	-31	-38
t	0.5T	0.6T	0.7T	0.8T	0.9T
ϕ_S (degree)	-43	-29	13	31	38

The reason of the change of the stagnation point is the highly fluctuating velocity in the wake of the upstream cylinder. This can be explained with Figure 5-25, which shows an assumed circular cylinder B lies in the wake of an identical cylinder A. When t = 0.2T, corresponding to t = 0.2T in Figure 5-23, the incident flow upon cylinder B is basically parallel to the free stream, with significantly reduced velocity. Shown in t = 0.5T is the main fluctuating flow acting on the bottom left side of cylinder B, which corresponds to the significant minus degree of the stagnation point

in Table 5-3. With the flow convecting downstream, the incident flow upon cylinder B is parallel again at t = 0.7T. Finally at t = 1.0T, the flow impacts on the top left side of cylinder B, corresponding to the position of the stagnation point, $\phi = 43^{\circ}$.

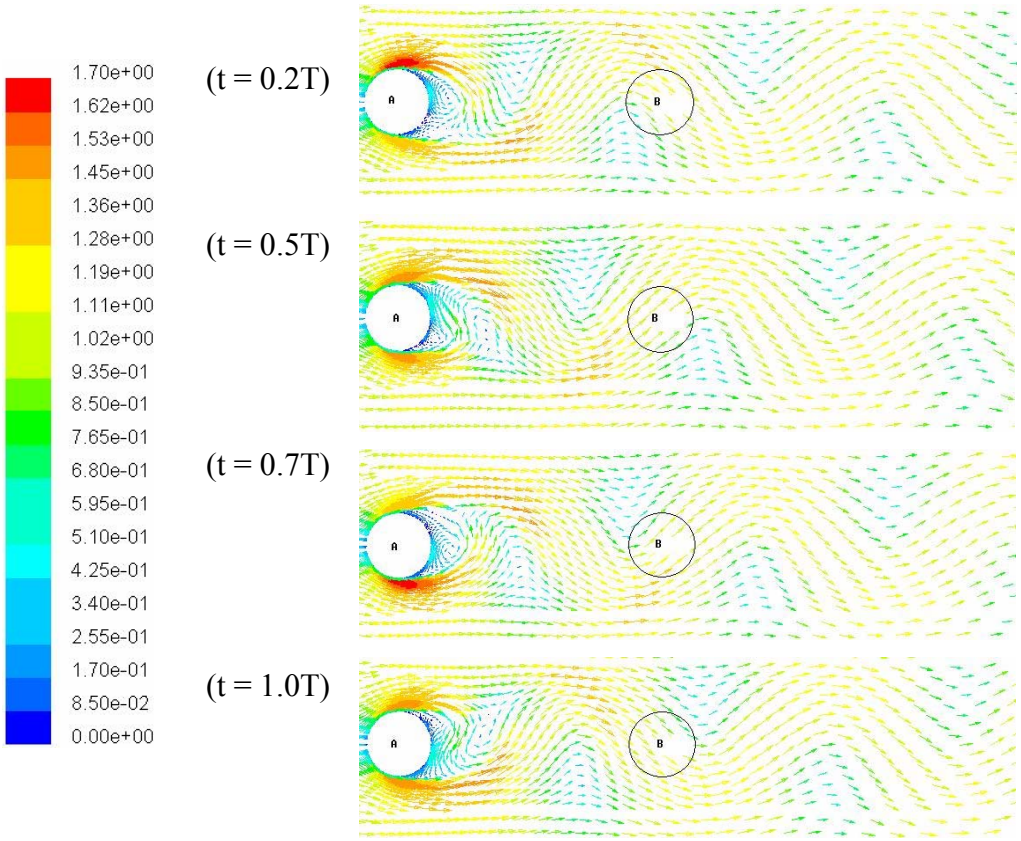

Figure 5-25 Velocity vector of incident flow upon an assumed downstream cylinder.

Another feature in the velocity vector plots is, because of its fluctuation, the flow passes the downstream cylinder 'positively'. It is known that for the upstream cylinder or an isolated cylinder, when the flow approaches it, the velocity magnitude and direction are changed 'negatively', due to the blockage of the cylinder. For the downstream cylinder, taking the case t = 0.1T in Figure 5-23 as an example, the oncoming flow has the potential to go top right, and its most flux does bypass the cylinder in that direction. Nevertheless, there is no significant accelerating flow near the top of the cylinder, with the velocity magnitude still in the vicinity of that of the oncoming flow velocity, which indicates that the flow passes the blockage in a 'positive' way. Even at t = 0.4T, when the fluctuating flow completely impacts on the

bottom left side of the downstream cylinder, the velocity magnitude of the accelerating flow around the cylinder is just slightly greater than that of the oncoming flow.

Shown in Table 5-4 is the change of separation points in a vortex shedding period. Similar to the stagnation point, the separation points in both half of a period are highly symmetrical, and there is an abrupt change at certain times. Different from the stagnation point, whose abrupt change happens at t = 0.2T and 0.7T, that of the separation point happens at t = 0.4T and 0.9T. This delay of change indicates the flow hysteresis in response to the change of the incident flow.

Table 5-4 Separation angle in a period (NE: No Exact separation point detected).

t	0.0T	0.1T	0.2T	0.3T	0.4T
Separation angle (degree)	109	111	114	108	87
	-75	-70	-74	NE	NE
t	0.5T	0.6T	0.7T	0.8T	0.9T
Separation angle (degree)	75	70	74	NE	NE
	-109	-112	-114	-109	-87

The velocity field in the wake of the downstream cylinder shows a difference from that of the upstream or an isolated cylinder, as shown in Figure 5-26. Due to the increased lateral interval of the Karman vortex street, the flow velocity in the near wake of the downstream cylinder is significantly reduced, to about 0.2 times the free stream velocity, and still highly fluctuating due to the Karman vortex street. This effect lasts until 6 diameters distance from the downstream cylinder, where the flow velocity begins to increase and the vortex intensity decreases. This feature of the two cylinders wake will affect the hydrodynamic characteristic of the third cylinder if it is added to this region, which will be discussed in detail in the following chapter.

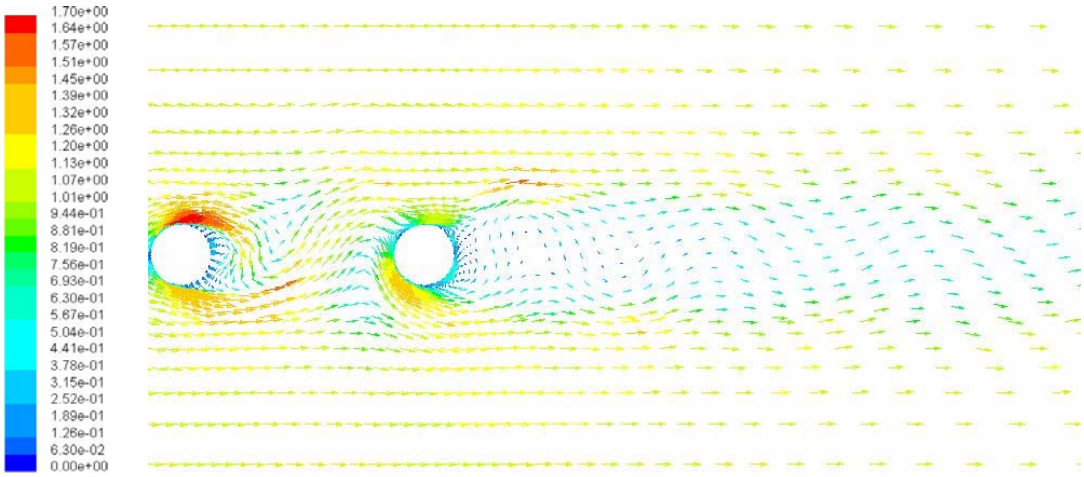

Figure 5-26 Instantaneous velocity vector in the wake of two tandem cylinders.

5.5.3 Pressure distribution

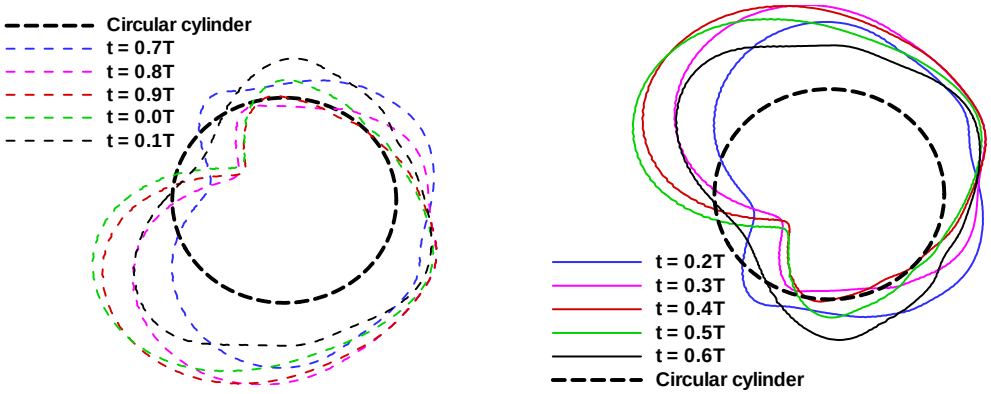

Figure 5-27 Pressure distributions around the downstream cylinder varying in a period: the line outside the circle represents negative pressure and the inner line represents positive pressure.

The pressure distribution around the downstream cylinder, and its integral over the surface, namely the fluid forces, are the main concern of this thesis. Shown in Figure 5-23 0.0T(c)~1.0T(c) are pressure coefficient contours varying in one cycle of vortex shedding. Unlike the pressure distribution around an isolated circular cylinder, or the

upstream cylinder in Figure 5-23, in which the stagnation pressure keeps constant ($C_p \approx 1$) and always acts on the most front point of the cylinder ($\phi = 0^\circ$), the pressure distribution around the downstream cylinder is more complex. Because of the change of stagnation point, the maximum positive pressure impacts on the top and bottom left alternately, and the negative pressure centre exists on the other side, as shown in Figure 5-23 and Figure 5-27.

From the viewpoint of velocity vector, the stagnation point is determined by the direction of incident flow. At the stagnation point, the dynamic pressure totally transfers to static pressure (Figure 5-23 0.0T (b), (c)). On the other side, i.e. bottom left side, there is a negative pressure centre caused by the accelerating flow, thanks to the blockage of the cylinder. At t = 0.1T, there are no specific positive or negative centres, because the fluctuating approaching flow automatically bypasses the cylinder. At t = 0.2T, the stagnation point moves to the bottom left side on which the incident flow acts, and a negative pressure centre exists on the top side of the cylinder due to the accelerating flow. This state lasts until t = 0.6T, when fluctuating approaching flow automatically bypasses the cylinder from the lower side of the cylinder. The above-mentioned process of the pressure on the downstream cylinder surface is repeated in another half cycle of vortex shedding, with the opposite side being influenced by the incident flow.

From the viewpoint of vortex impingement, according to Kitagawa and Ohta (2008), the oncoming vortex shed from the upstream cylinder is likely to induce positive pressure on the same side (upper or lower), and the impinging vortex together with that forming in the wake of the downstream cylinder will induce negative pressure. So is it in Figure 5-23. At t = 0.0T, the oncoming negative vortex induces positive pressure on the top left side, and the split positive vortex causes negative pressure on the lower side. At t = 0.1T, because the negative vortex is impinging on the cylinder and oncoming positive vortex is still too far to influence the pressure on the cylinder, there is no specific positive pressure centre on the surface of the downstream cylinder. On the lower side, the negative pressure is weakened because the positive vortex near the surface is attracted by the impinging negative vortex. This state changes at t

= 0.2T, when the oncoming positive vortex begins to induce positive pressure on the bottom left side of the downstream cylinder and the deformed negative vortex causes negative pressure on the upper side. At the same time, the negative vortex near the lower side continues to drag the positive vortex out so that the pressure on the lower side of the cylinder increases. This state lasts until t = 0.5T. Again, the process is repeated in another half period, with opposite side being influenced by opposite vortices.

For the rear of the downstream cylinder, its pressure is not so low as that of the upstream cylinder, because the split like-sign vortex is not so close to the cylinder's rear due to its inertia after bypassing the cylinder, and the forming like-sign vortex is merged. So the negative pressure on the rear of the cylinder, often induced by the vortices near the cylinder surface, is weakened.

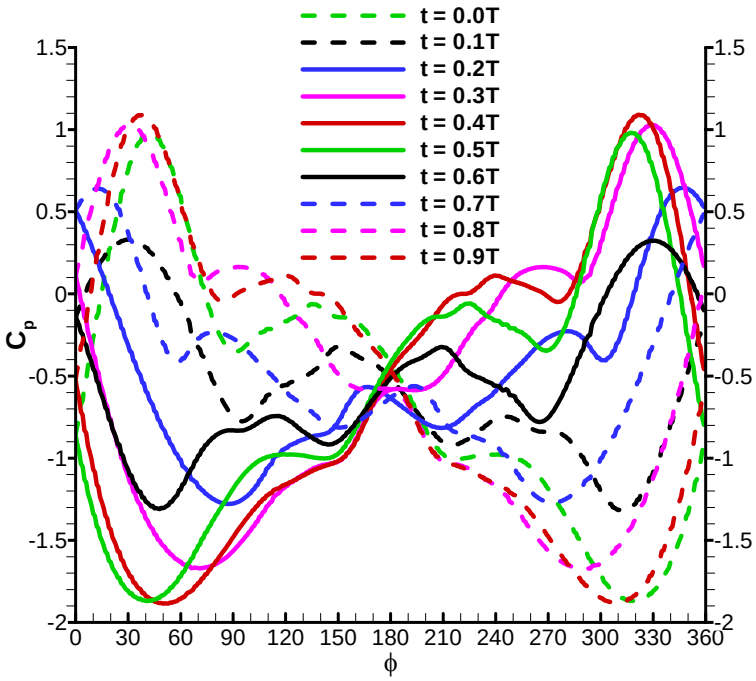

Figure 5-28 Pressure distributions around the downstream cylinder varying in a vortex shedding period.

Shown in Figure 5-28 is the pressure distribution around the downstream cylinder at ten instants in a cycle of vortex shedding. It is seen that the pressure coefficient at the

most rear point changes with time regularly in the range from –0.4 to 0.65, and the averaged value $C_p \approx -0.5$ is much higher than that of an isolated cylinder, which is about –1.2. Moreover, the pressure coefficient on the rear surface at certain instant always varies around the base pressure, and its deviations from the base pressure for the upper and lower sides are nearly opposite. One can expect the contribution of the pressure on the rear surface of the cylinder on its drag force is nearly constant.

For the front of the downstream cylinder, during t = 0.3T~0.5T and t = 0.8T~1.0T, there exist a significant stagnation angle (around $\phi = \pm 35^\circ$), a high stagnation pressure ($C_p \approx 1$) and a low negative pressure on the opposite side ($C_p \approx -1.8$). This causes large variartions in both the drag and lift, as shown in Figure 5-29. The mechanism of the lift force here is significantly different from that of the upstream or an isolated cylinder, whose lift force is caused by the pressure difference of the upper and lower sides of the cylinder, due to the periodically vortex shedding. For the downstream cylinder in the wake, the lift force is additionally caused by the shifting stagnation point on the front of the cylinder, with a resulting force component in the cross flow direction. Therefore, the amplitude of the lift force coefficient of the downstream cylinder is much higher than that of the upstream one (Table 5-2).

At t = 0.1T, 0.2T, 0.6T and 0.7T, the flow is transitional between the two incident directions, therefore the lift forces are smaller.

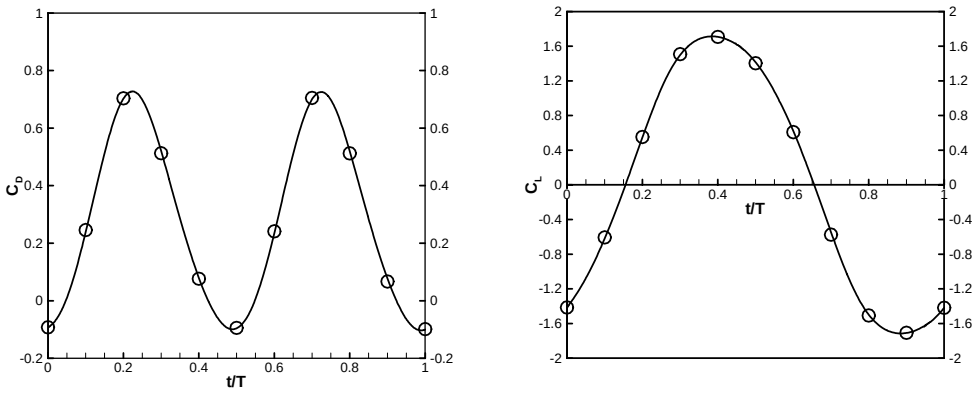

Figure 5-29 Drag and lift force coefficients in a period.

As for the drag force, its variation mainly depends on the pressure on the front surface of the cylinder, since, as mentioned before, the contribution of the rear is nearly constant. At t = 0.0T and 0.5T, the drag force is at its minimum (Figure 5-29), corresponding to the maximum stagnation angle, relative to the most front point F (the green lines in Figure 5-28), while the maximum drag is reached at t = 0.2T and 0.7T, corresponding to the minimum stagnation angle (the blue lines in Figure 5-28). The drag force variation also depends on the variation of the stagnation angle, not the stagnation pressure, since actually it is much higher at t = 0.0T and 0.5T ($C_{pS} = 0.98$) than that at t = 0.2T and 0.7T ($C_{pS} = 0.64$).

Shown in Figure 5-30 is the drag force coefficient and cosine of the relative stagnation angle. The result indicates significant correlation between them, though they are not completely in-phase. The lift force is also notably correlative to the minus sine of the relative stagnation angle, as shown in Figure 5-31. This indicates the periodical change of stagnation point, caused by the fluctuating incident flow, plays a significant role on the variation of the fluid forces on the downstream cylinder.

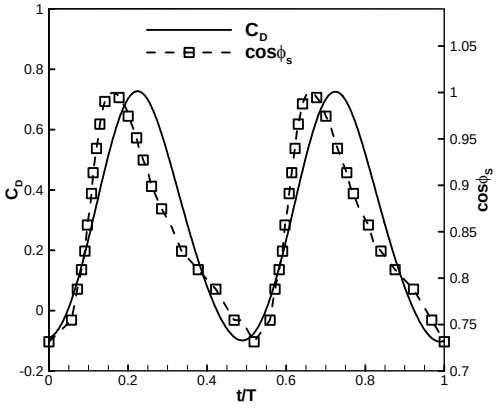

Figure 5-30 Drag force coefficient and cosine of stagnation angle in a period.

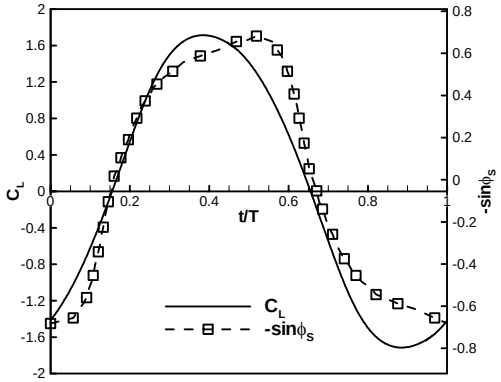

Figure 5-31 Lift force coefficient and minus sine of stagnation angle in a period.

5.5.4 Correlation analysis

The correlation coefficient is used to study the relationship between fluid forces and some other flow variables. The correlation coefficient between two discrete sequences $\{x_n\}$ and $\{y_n\}$ is defined as

$$R = \frac{\sum_n (x_n - \bar{x})(y_n - \bar{y})}{\sqrt{\sum_n (x_n - \bar{x})^2 \sum_n (y_n - \bar{y})^2}} \quad , \tag{5.3}$$

where $\bar{x}$ and $\bar{y}$ are the averaged values of $\{x_n\}$ and $\{y_n\}$, respectively. The correlation coefficient indicates the strength and direction of a linear relationship between two random variables.

Table 5-5 shows the correlation coefficients between drag force and cosine of the stagnation angle, the stagnation pressure, the production of them, and C_{pF}, the pressure coefficient at the most front point. The results reveal that the correlation between the drag force and cosine of the stagnation angle is very strong, while the stagnation pressure, as mentioned before, has moderate minus correlation with the drag force. The stagnation pressure's component on *x* direction ($C_{pS}Cos\phi_S$) is insignificant, which suggests the stagnation pressure, though has its contribution, is not a main influencing factor to drag force.

Surprisingly, the correlation coefficient between the drag force and the pressure at the most front point is as high as 0.99, which is also illustrated in Figure 5-32. This indicates the latter is the main influencing factor to the drag force of the downstream cylinder, considering the contribution of the pressure on the rear of the cylinder is quite constant, as shown in Figure 5-28. Further calculation shows the correlation coefficient between the cosine of stagnation angle and pressure of the most front point is 0.97, indicating the influence of them on the drag force is synchronous, which is also revealed in Figure 5-28, where larger stagnation angle is always corresponding to lower pressure at the most front point, among the ten instant pressure distributions, and vice visa. The variation of the pressure at the most front

point is caused by and synchronised with the variation of the stagnation point.

Table 5-5 Correlation coefficient between drag force and some expressions.

	$Cos\phi_s$	C_{pS}	$C_{pS}Cos\phi_S$	C_{pF}
R_{C_D}	0.940	-0.296	-0.035	0.990

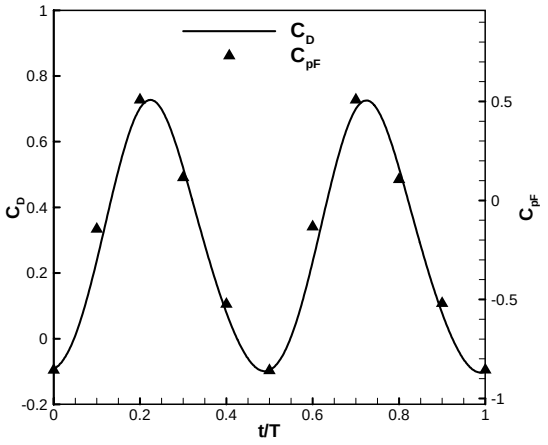

Figure 5-32 Drag force coefficient and pressure coefficient at the most front point in a period.

Table 5-6 shows the correlation coefficient between the lift force and minus sine of stagnation angle, the stagnation pressure, the product of them, and the pressure at the most front point. Again, the link between the stagnation angle and relative lift force is significant, while the stagnation pressure is insignificant. The stagnation pressure's component on $-y$ direction ($C_{pS}(-Sin\phi_s)$) is strongly correlated with the lift force, which indicates it is synchronous with other lift-influenced factors such as the negative pressure on the opposed side of the front of the cylinder, and the pressure difference on the rear. As can be expected, the pressure at the most front point has no link to the lift force, as they are perpendicular to each other.

The significant influence of the stagnation angle on the fluid forces of the downstream cylinder located in the wake of an upstream one is revealed by above

analysis. This does not mean it is the only factor, as the pressure distribution around the rear of the cylinder also plays a role on the forces. But it is simpler to be dealt with, since the pressure distribution on the rear either can be seen as a constant when calculating drag force, or is in-phase with stagnation angle when calculating lift force.

Table 5-6 Correlation coefficient between lift force and some expressions.

	$-Sin\phi_s$	C_{pS}	$C_{pS}(-Sin\phi_s)$	C_{pF}
R_{C_L}	0.967	0.002	0.988	0.001

5.6 Concluding remarks

This chapter investigated uniform flow past two circular cylinders of the same diameter in tandem arrangements at a subcritical Reynolds number Re = 10^4. The centre to centre spacing between the cylinders is from 1.5D to 8D, thus the proximity interference and wake interference are both covered. For $L \le 2.5D$, the reattachment flow pattern is observed. The shear layers separated from both sides of the upstream cylinder reattach onto the downstream cylinder, with a steady recirculation region consisting of a pair of counter-rotating vortices in the gap. For $L > 3D$, vortices are shed not only from the downstream cylinder but also from the upstream cylinder. The drag coefficient of the downstream cylinder experiences a jump when the flow pattern changed. The critical spacing is found to be around 2.5D in the current study.

The bistable and hysteresis features of flow around two tandem cylinders are also observed. With the dynamic mesh technique, it is found for certain spacing around L = 2D, the flow can be either the reattachment or two vortex streets patterns depending upon the initial conditions. By starting the simulation from the reattachment pattern and slowly increasing the spacing, the reattachment flow pattern persists up to a spacing of 2.7D at which point a transition to the two vortex streets pattern occurs. Similarly, when the spacing is decreased, the two vortex streets

pattern persists until L = 1.7D.

The wake behind the downstream cylinder shows some different characteristics from that of an isolated cylinder. The velocity is greatly reduced due to the cascading shielding effects by both cylinders. It is observed that the increase in averaged velocity along the wake centreline for tandem arrangement is slower than that for an isolated cylinder flow. The wake power spectra analysis shows the oscillating flow in the wake behind the downstream cylinder is strongly influenced by its own vortex shedding when $L \geq 6D$.

This chapter also investigated in great detail the main factors influencing the fluid forces of a circular cylinder located in the wake of an upstream one, in tandem arrangement with the spacing L = 4D. The changes of vorticity and velocity in flow field and the pressure distributions around the cylinder in a vortex shedding period are studied in detail to investigate the relationship among them. Then the correlation coefficient is used to analyse the influence of various factors on fluid forces, such as stagnation angle and the pressure at stagnation point and the most front point.

Due to the periodically shed vortices from the upstream cylinder, the flow incident on the downstream cylinder is highly fluctuating. The pressure distribution around the downstream cylinder can be explained in the viewpoint of either vortex impingement or change of incident velocity vector.

It is revealed that the stagnation point, also the point on which the maximum pressure acts, changes periodically on the front of the downstream cylinder, and at the same time varies the pressure distribution on this part of the cylinder significantly. On the rear of the cylinder the pressure distribution is almost a constant.

It is found that the change of the stagnation point, as a result of the fluctuating incident velocity, is strongly associated with the large and periodical variations of the drag and lift forces, while the stagnation pressure is not. The cosine and minus sine of the stagnation angle are highly correlated with the drag and lift force, respectively.

6 Two cylinders flow: Staggered arrangement

6.1 Introduction

The aim of the chapter is to numerically study the flow patterns and fluid forces of two staggered circular cylinders in cross flow, especially the origin of the mean lift force on the downstream cylinder.

Two identical circular cylinders are considered. The upstream cylinder is at x = 0 and y = 0, and the downstream cylinder is at x = 2D, 4D, or 8D, and y = 0.5D, D, or 2D. So the proximity interference, near wake interference and far wake interference are all covered.

The inflow and outflow boundaries are situated to allow at least 15 diameters between the inflow boundary and the upstream cylinder and 20 diameters between the outflow boundary and the downstream cylinder. The lateral boundaries are situated to allow at least 10 diameters distance to the closest cylinder. The meshes in the boundary layers and between the cylinders are in the same way as described in the last chapter.

6.2 Flow patterns

In the last chapter the shear layer reattachment flow pattern was presented for the tandem arrangement with the spacing ratio less than 2.7. As reported in the literature (Zdravkovich 1987; Sumner et al. 2000; Akbari & Price 2005), this flow regime persists for configurations with moderate pitch ratios, 1.1 < P/D < 2, and small angles of incidence, $\alpha < 10^{\circ}$. The distance between the two cylinders is small

enough for the inner shear layer from the upstream cylinder to reattach onto the outer surface of the downstream cylinder. The flow through the gap between the cylinders is small compared to the main flow around the two cylinders. There is only one Karman vortex street in the wake of the cylinder pair.

While increasing the angle of incidence, or moving the downstream cylinder away from the flow axis of the upstream cylinder, i.e. y = 0.5D, D and 2D, shear layer reattachment flow pattern can no longer exist, and several different flow patterns were identified. The flow patterns for two staggered circular cylinders in cross flow were systematically investigated by Sumner et al. (2000) using flow visualization and particle image velocimetry and by Akbari & Price (2005) numerically. Current results are compared with theirs, though the Reynolds numbers in their studies are within the low subcritical regime, Re = 800 to 1900, while $Re = 10^4$ in this thesis.

6.2.1 Shear layer enveloping

When the downstream cylinder is situated at x = 2D and y = 0.5D, as shown in Figure 6-1, it is easier for the inner shear layer from the upstream cylinder to be deflected into the gap between the cylinders. In addition, some of the oncoming mean flow is now permitted to penetrate the gap. Because of the existence of the downstream cylinder, the shear layers from the upstream cylinder do not have sufficient space to roll up before convecting into the wake of the downstream cylinder. The vorticity of the inner shear layer of the upstream cylinder, being constrained between two opposite signed vortices from the outer side of the upstream cylinder and the inner side of the downstream cylinder, soon fade out. The inner shear layer of the downstream cylinder is enveloped by the outer shear layer of the upstream cylinder, before it rolls up completely.

The combined shear layers roll up into an expanded, weakened Karman vortex, while the outer shear layer of the downstream cylinder forms regular Karman vortex almost without interruption. In this flow pattern there is only one Karman vortex street in the wake of the two cylinders, similar to that for one cylinder flow and shear layer

reattachment flow pattern of two tandem cylinders flow, although the vortex street is not as regular as that for a single cylinder.

As an example of the flow pattern, a sequence of vorticity contour plots is presented in Figure 6-1. The time-interval between the successive frames in these figures is $t^* = \Delta t U_0 / D = 1$, corresponding to about one fifth of the period for one complete vortex shedding cycle, assuming the typical Strouhal number value of 0.2 in this case. Figure 6-1(a, b) show the shear layers in the gap between the cylinders form and the inner shear layer from the downstream cylinder is ready to roll up. In Figure 6-1(c, d) it is enveloped by the outer shear layer of the upstream cylinder. Figure 6-1(f-h) show the shedding process of the combined Karman vortex.

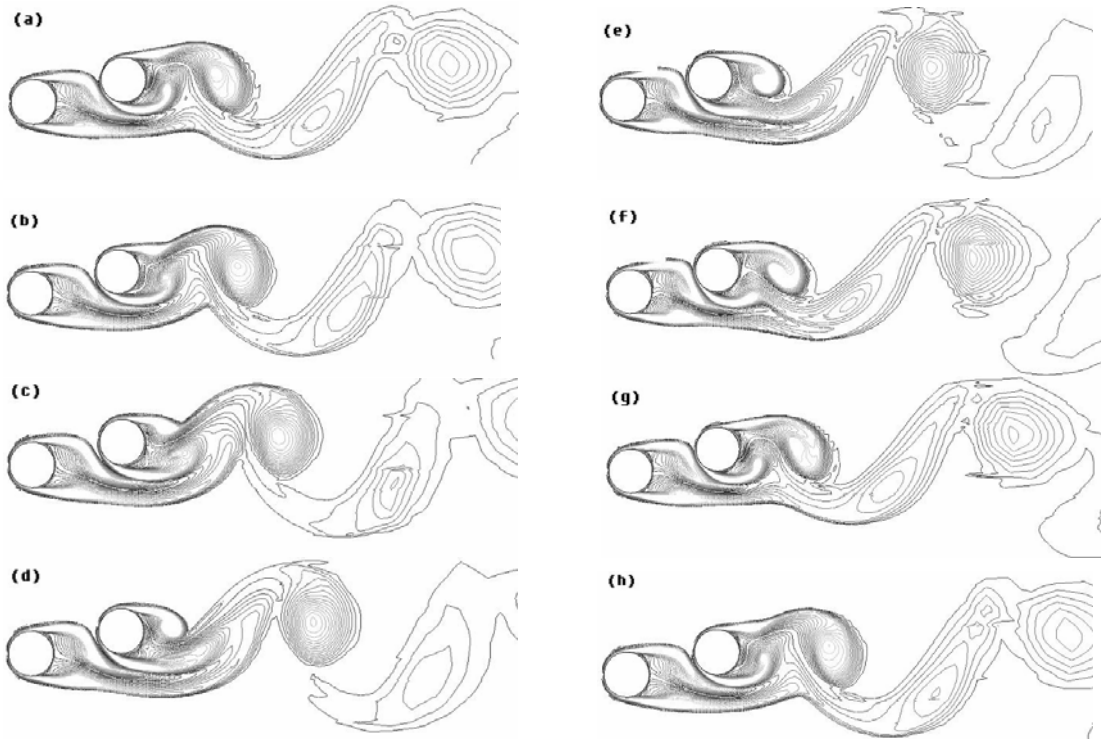

Figure 6-1 Vorticity contour plots for the vortex enveloping flow pattern, x = 2D, y = 0.5D. Equal time-intervals of $t^* = 1$ between consecutive plots (a)-(h).

Sumner et al. (2000) classified the flow of this range as 'induced separation' flow pattern. It was reported that the Karman vortices from the inner shear layer of the upstream cylinder induce a separation of the flow from the inner side of the

downstream cylinder and the induced vorticity production does not involve the formation and roll-up of a free shear layer (Figure 6-2). However, Akbari and Price (2005) offered a different explanation. According to them, this phenomenon does not appear to be really an 'induced' separation, for the separation on the inner surface of the downstream cylinder appears to be due to the impingement of part of the main flow through the gap and its subsequent deflection off the cylinder surface. The latter explanation is confirmed here, as the Karman vortex formation from the inner surface of the downstream cylinder does involve the roll-up of a free shear layer, though it is enveloped simultaneously by the outer shear layer from the upstream cylinder.

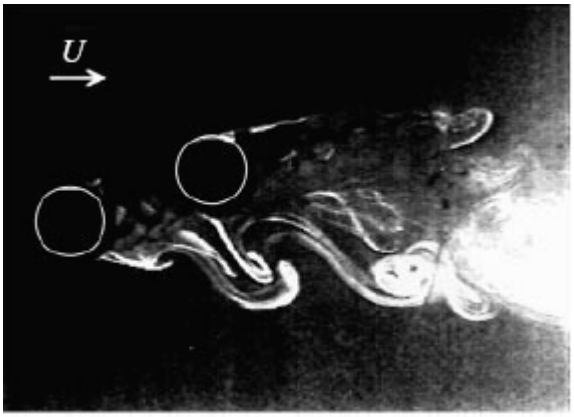

Figure 6-2 Flow visualization of 'induced separation' flow pattern, P/D = 2.0, $\alpha = 20^{\circ}$, Re = 850, after Sumner et al. (2000).

The wake power spectra analysis show, the dominant wake frequency, i.e. Strouhal number, is approximately 0.17 at an arbitrary wake point. Shown in Figure 6-3 is a typical wake power spectrum for which the velocity is sampled at x = 3D and y = 0, in the combined wake of the two cylinders. Sumner et al. (2000) reported that in 'induced separation' flow pattern the frequencies of Karman vortex formation are different for each row and those from the outer shear layer of the downstream cylinder are considerably lower. This is not found here, which possibly means the shear layer enveloping flow pattern is totally different from the 'induced separation' flow pattern identified by Sumner et al., because these two cases are under different Reynolds numbers.

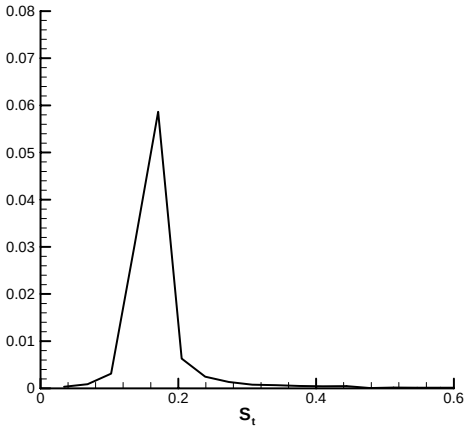

Figure 6-3 Wake power spectrum for x = 2D, y = 0.5D. Velocity measurement at x = 3D and y = 0 as indicated in Figure 2-10.

6.2.2 Vortex pairing and enveloping

When the downstream cylinder is at x = 2D and y = D, the flow pattern is similar to the above-mentioned shear layer enveloping regime. However, this flow involves the formation of vortices from the upstream cylinder and the inner side of the downstream cylinder, though the process is incomplete before they merge into an expanded, weakened composite vortex.

This ‘vortex pairing and enveloping’ flow pattern is identified by Sumner et al. (2000) using flow visualization and particle image velocimetry and by Akbari & Price (2005) numerically. In the near wake region the Karman vortex from the inner side of the downstream cylinder is paired with smaller-scale vortex of opposite sign from the inner shear layer of the upstream cylinder. The counter-rotating vortex pair structure is a distinct feature of this flow pattern. A little further downstream this vortex pair is enveloped by the vortex from the outer shear layer of the upstream cylinder. Again in this flow pattern there is only one Karman vortex street in the wake of the two cylinders.

Shown in Figure 6-4 is a sequence of vorticity contour plots for ‘vortex pairing and

enveloping' flow pattern with x = 2D and y = D. Figure 6-4(a-e) show the process of vortices formation from both sides of the gap and the outer side of the upstream cylinder. Due to the accelerated main flow the vortices are elongated. In Figure 6-4(f) the vortices from both sides of the gap are paired and then been enveloped by the outer shear layer of the upstream cylinder, as shown in Figure 6-4(g-h).

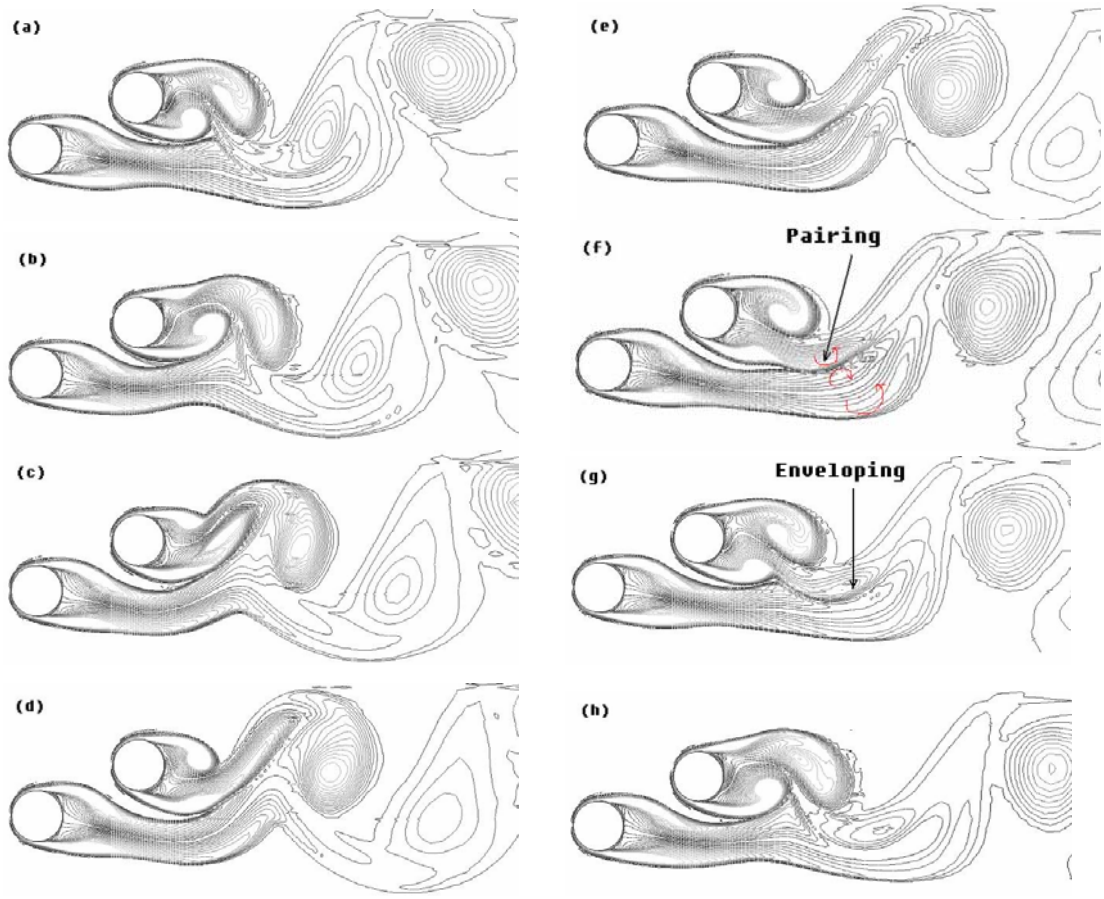

Figure 6-4 Vorticity contour plots for the vortex enveloping flow pattern, x = 2D, y=D. Equal time-intervals of t^* = 1 between the consecutive plots (a) to (h).

Shown in Figure 6-5 are illustrations of the vortex pairing and enveloping flow pattern by Sumner et al. (2000) and Akbari & Price (2005). In the picture of flow visualization by Sumner et al. the process of pairing and enveloping happens further away from the flow centreline of the upstream cylinder, while the numerical result by Akbari & Price shows this process happens near the flow centreline of the upstream cylinder, which resembles the current numerical results. In the results by Akbari &

Price it can be seen that the vortices are elongated too, not only in the process of enveloping, but also in the wake downstream.

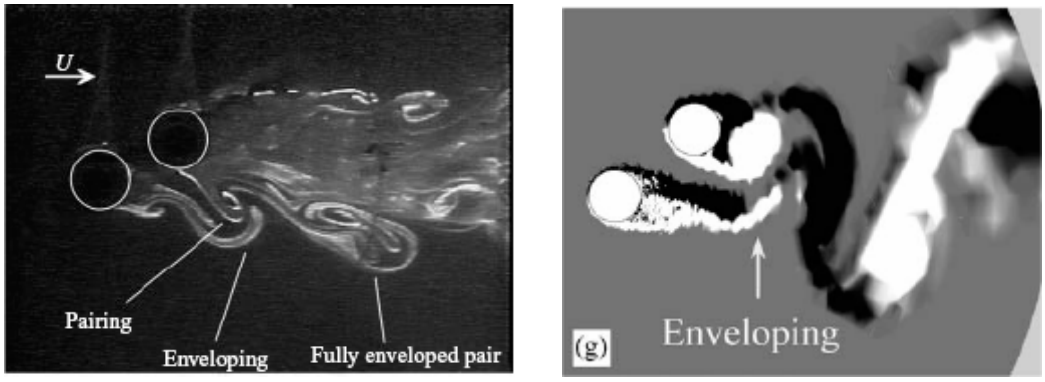

Figure 6-5 Vortex pairing and enveloping flow pattern. Left: flow visualization by Sumner et al. (2000), P/D = 1.5, $\alpha = 30^{\circ}$, *Re* = 850; Right: numerical results by Akbari & Price (2005), P/D = 2.0, $\alpha = 40^{\circ}$, *Re* = 800.

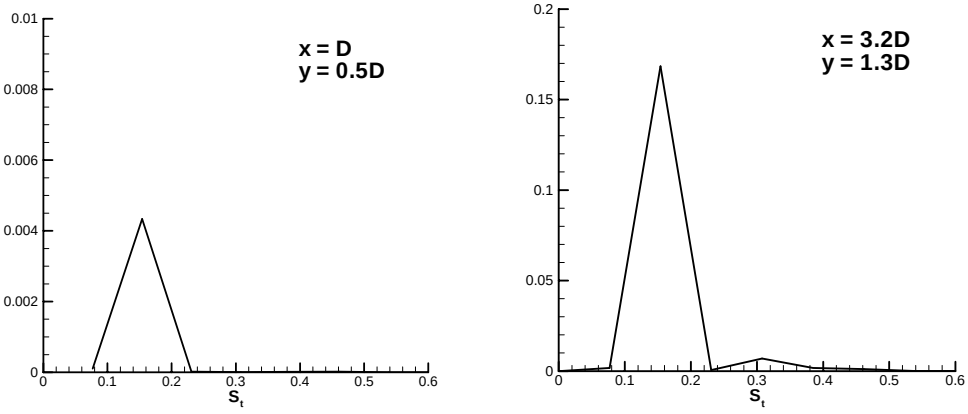

Figure 6-6 Wake power spectra for x = 2D, y = D. The coordinates indicate the points at which the velocities are measured.

The wake power spectra for this flow are measured at x = D, y = 0.5D and x = 3.2D, y = 1.3D, which correspond to the wake of upstream cylinder and the downstream one, respectively, as shown in Figure 6-6. It can be seen a dominant nondimensional frequency St = 0.15 is observed in both figures. Sumner et al. (2000) reported St = 0.14 and Akbari & Price (2005) reported St = 0.19 for this flow pattern. This

considerable discrepancy, as stated by Akbari & Price, may be due to the high sensitivity of the wake power spectra to the exact locations at which the signals are obtained.

6.2.3 Complete vortex shedding

This phenomenon occurs for x = 2D and y = 2D where the downstream cylinder is not immersed in the wake of the upstream cylinder, but the two cylinders are close enough for them to influence the vortex shedding from each other. In this arrangement two distinct Karman vortex streets are seen in the wake of the cylinder pair. Sumner et al. (2000) classified the flow at this range as 'synchronized vortex shedding'. It was reported that within the near field, vortices of opposite sign from opposite sides of the gap, are observed to pair up. Within the combined wake of the pair of cylinders, this results in two adjacent Karman vortex streets that exhibit anti-phase synchronization, as shown in Figure 6-7. In this flow pattern, according to Sumner et al., the two shear layers from the upstream cylinder and the inner shear layer of the downstream cylinder shed vortices at the same frequency, while lower-frequency happens at the outer shear layer of the downstream one only.

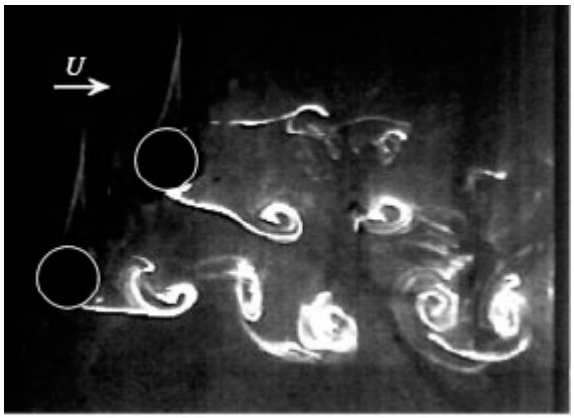

Figure 6-7 Flow visualization of 'synchronized vortex shedding' flow pattern, P/D = 2.5, $\alpha = 50^{\circ}$, Re = 900, after Sumner et al. (2000).

The same features can be found from the results of the current simulation, as shown

in Figure 6-8. The vortex streets from both cylinders are highly synchronized, as the counter-rotating vortex pairs arranged transversely are regularly laid within the near wake. However, Akbari & Price (2005) carefully checked their numerical results and concluded that this vortex pairing occurs only during some instances, and that there is no synchronization of vortex shedding between the two cylinders.

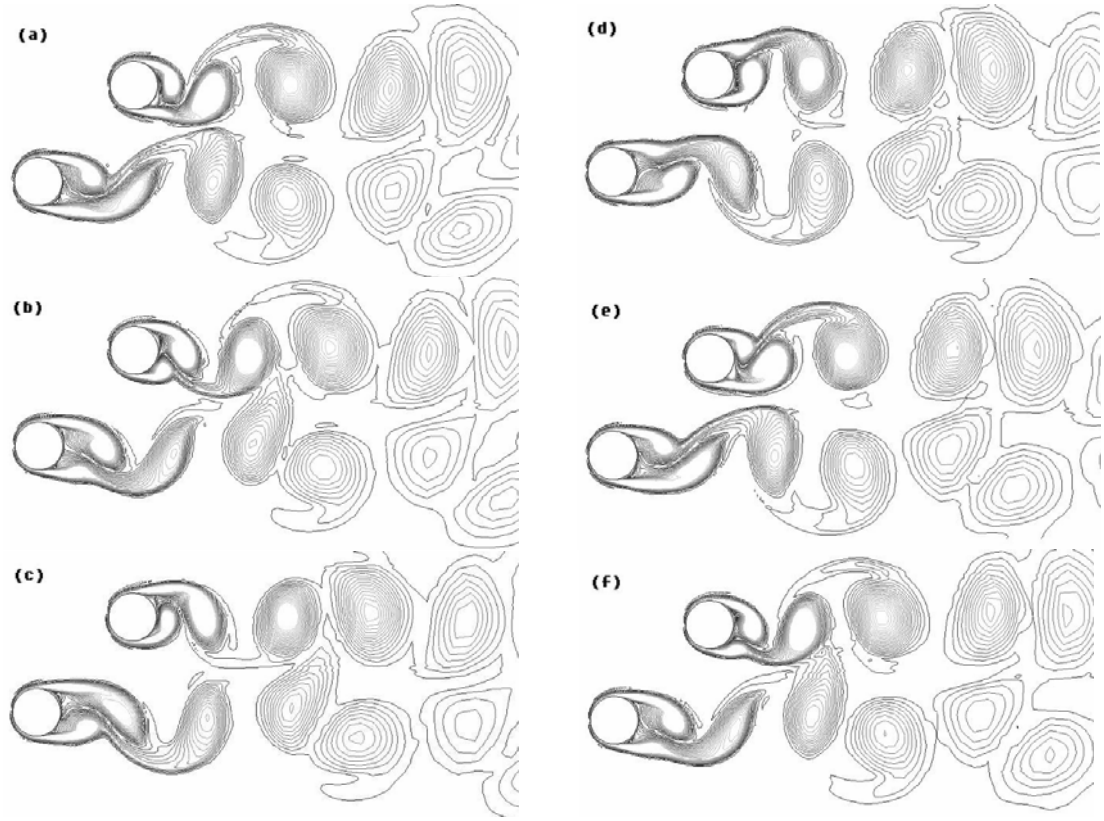

Figure 6-8 Vorticity contour plots for the complete vortex shedding flow pattern, x = 2D, y = 2D. Equal time-intervals of t^* = 1 between consecutive plots (a)-(f).

Wake power spectra are analysed to study the frequencies of the shear layers. Shown in Figure 6-9 are power spectra for four points, i.e. x = D, y = -0.5D and x = D, y = 0.5D, corresponding to the outer and inner shear layer of the upstream cylinder, respectively; x = 3D, y = 1.5D and x = D, y = 2.5D, corresponding to the outer and inner shear layer of the downstream cylinder, respectively. It can be seen that the frequency of vortex shedding from the two shear layers of the same cylinder is always the same. The Strouhal number for the upstream cylinder is St = 0.23, while that for the downstream cylinder is St = 0.21. This suggests no synchronization

between the vortices of the two cylinders, but the frequencies are close enough so that the synchronization-like condition happens when the two Karman vortex streets are in certain phases. There is also a peak at St = 0.23 in the power spectra for the downstream cylinder, which indicates the influence of the upstream cylinder on the vortex shedding of the downstream one. Akbari & Price (2005) computed a case in this range and the Strouhal numbers for the upstream and downstream cylinders were found to be St = 0.22 and 0.2, respectively, which is similar to current simulation.

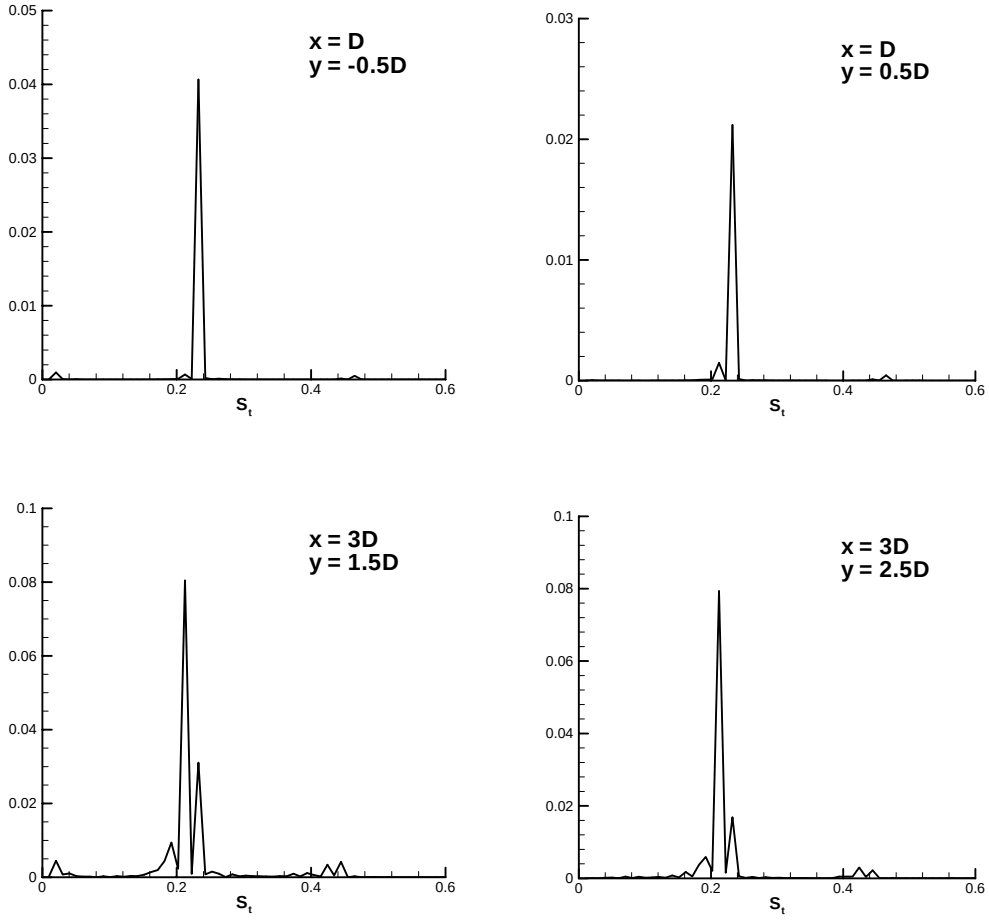

Figure 6-9 Wake power spectra of several points behind the upstream and downstream cylinder for x = 2D, y = 2D. The coordinates indicate the points at which the velocities are measured.

Actually, by computing this case for a little more time from Figure 6-8, the vorticity contour is like Figure 6-10(a), which indicates the vortices shedding from the two

cylinders are not in phase. In Figure 6-10(b) the vortices are involved in complex interaction in the near wake, and the phenomenon of synchronization completely disappears. This again suggests the so called 'synchronized vortex shedding' flow pattern does not exist in the current simulation and the flow is in a complete vortex shedding mode for the two cylinders while has complex vortices interaction in the near wake.

(a) (b)

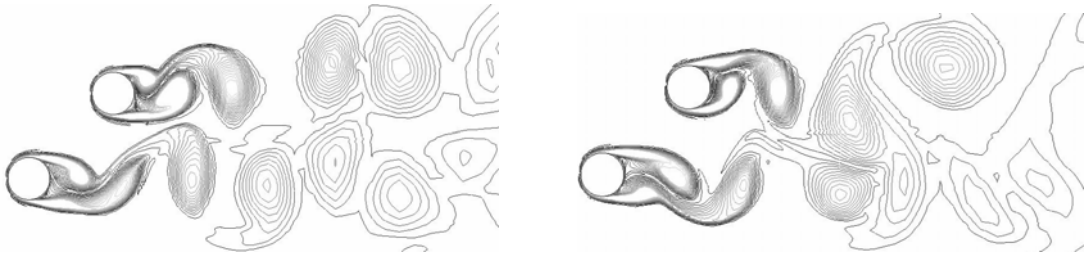

Figure 6-10 Vorticity contour plots for two instances, x = 2D, y=2D.

6.3 Fluid forces

6.3.1 Drag and lift forces history

Shown in Figure 6-11 are drag and lift coefficients time histories for both cylinders when the downstream one is located at x = 2D and y = 0.5D, D and 2D. The solid lines denote those for the downstream cylinder, and the dashed lines for the upstream one. These data were gathered when steady periodic states were achieved, after at least 30 periods computing.

For x = 2D and y = 0.5D, the amplitudes of both drag and lift coefficients of the upstream cylinder are very small, which indicates that in the 'shear layer enveloping' flow pattern, the flow around the upstream cylinder is quite steady, and no vortex shedding happens behind it. For the downstream cylinder, the amplitudes of both drag and lift coefficients are significant. The periodic vortex shedding causes the

fluctuation of the lift force, as well as the drag force. The fluctuation of the drag force may also be due to the fact that the gap flow between the two cylinders changes the direction of the oncoming flow to the downstream cylinder, which is towards the flow centre line of the upstream cylinder. This can also explain the existence of the time-averaged lift force of the downstream cylinder, which possibly is a part of resolved drag force.

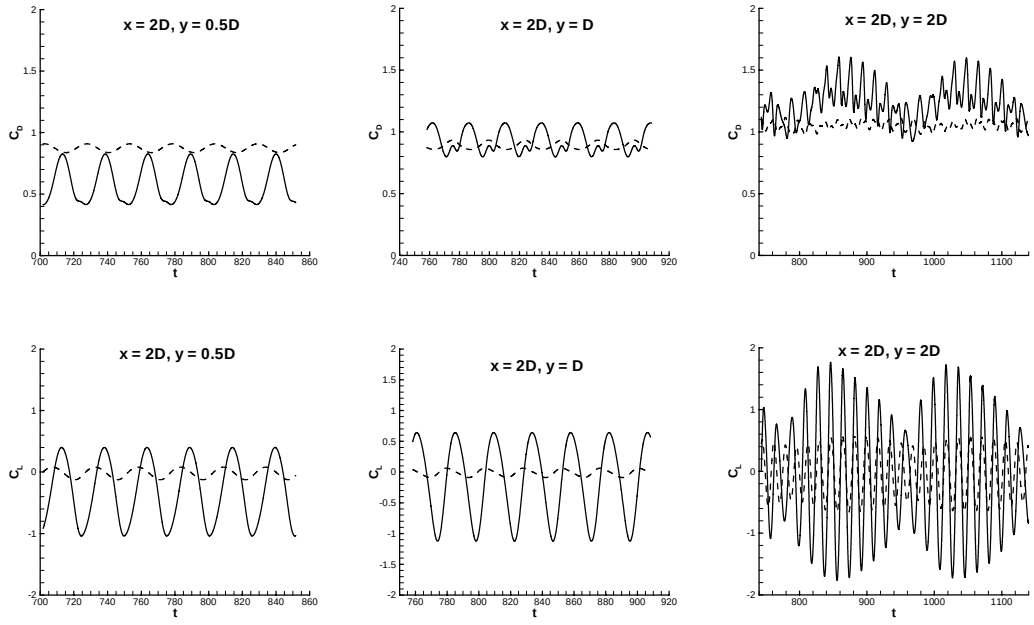

Figure 6-11 Drag and lift forces histories, the downstream cylinder is at x=2D, y=0.5D, D and 2D, respectively. Solid line: downstream cylinder; Dashed line: upstream cylinder.

For x = 2D and y = D, the force coefficients are similar to the above, except the averaged drag coefficient of the downstream cylinder increases significantly, which can be expected because the shielding effect of the upstream cylinder is weakened as the downstream one move outwards. The amplitudes of both drag and lift coefficients of the upstream cylinder are still very small. This suggests though there are vortices forming behind the upstream cylinder, they are too far from the cylinder surface to significantly influence the pressure distribution around it.

The force coefficients become very complex for x = 2D and y = 2D. The lift coefficient history of the downstream cylinder depicts a phenomenon of interference effect, which can be explained that the vortex shedding from the downstream cylinder is at the nondimensional frequency St = 0.21, while modulated by the vortices from the upstream one at St = 0.23 (Figure 6-9). Surprisingly, the lift coefficient history of the upstream cylinder also displays the interference effect feature, which indicates in this arrangement the upstream cylinder is also influenced by the downstream one, though complete Karman vortex street formed behind the former.

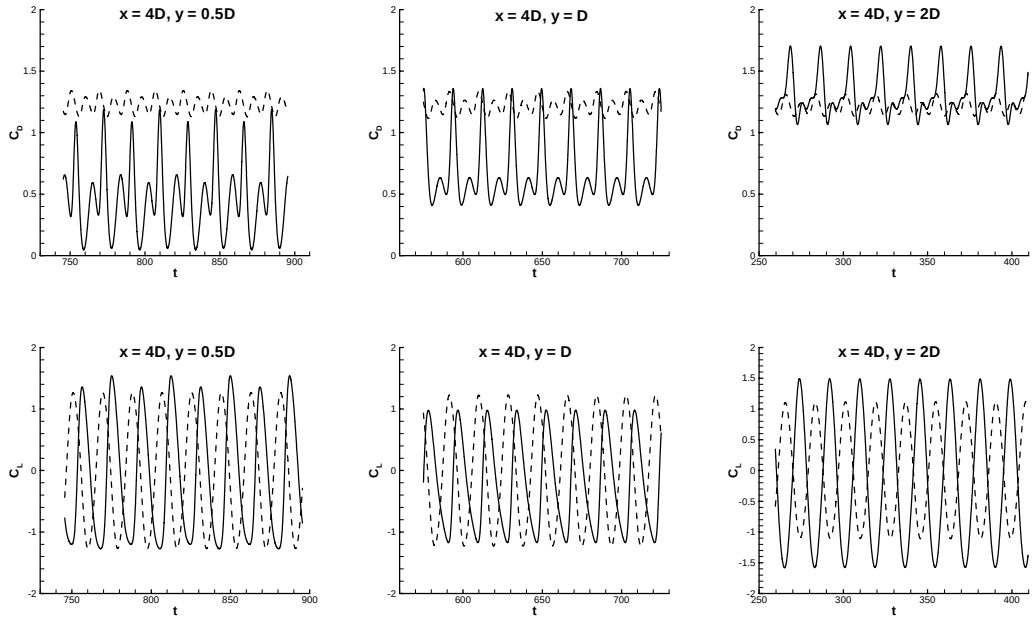

Figure 6-12 Drag and lift forces histories, the downstream cylinder is at x=4D, y=0.5D, D and 2D, respectively. Solid line: downstream cylinder; Dashed line: upstream cylinder.

When x = 4D, the flow is in the vortex impingement regime, so the hydrodynamic loading of the downstream cylinder is the result of vortex-body interaction while the loading for the upstream cylinder can be treated as an isolated one. The averaged drag force coefficient of the downstream cylinder increases when the lateral distance is increased from 0.5D to 2D, while the variation amplitude of the drag force

decreases, indicating a weakening effect of the wake.

Abnormally, the amplitude of the lift coefficient of the downstream cylinder is larger than that of the upstream cylinder for the case x = 4D and y = 2D, which is possibly because the downstream cylinder is actually out of the wake of the upstream one in this arrangement, and the oncoming flow velocity is larger than that of the free stream. The drag force of the downstream cylinder is also larger than that of the upstream one for the same reason.

For x = 8D, the influence of the downstream cylinder on the upstream one can be neglected, as shown by the drag and lift coefficients histories in Figure 6-13. The averaged drag coefficient of the downstream cylinder increases significantly when moving it outward the wake, while its amplitude keeps in a similar range. This is different from the cases x = 4D, which indicates at this cross section at x = 8D, the flow around the downstream cylinder is dominated by the local oncoming flow, while less significantly influenced by the vortices from the upstream cylinder.

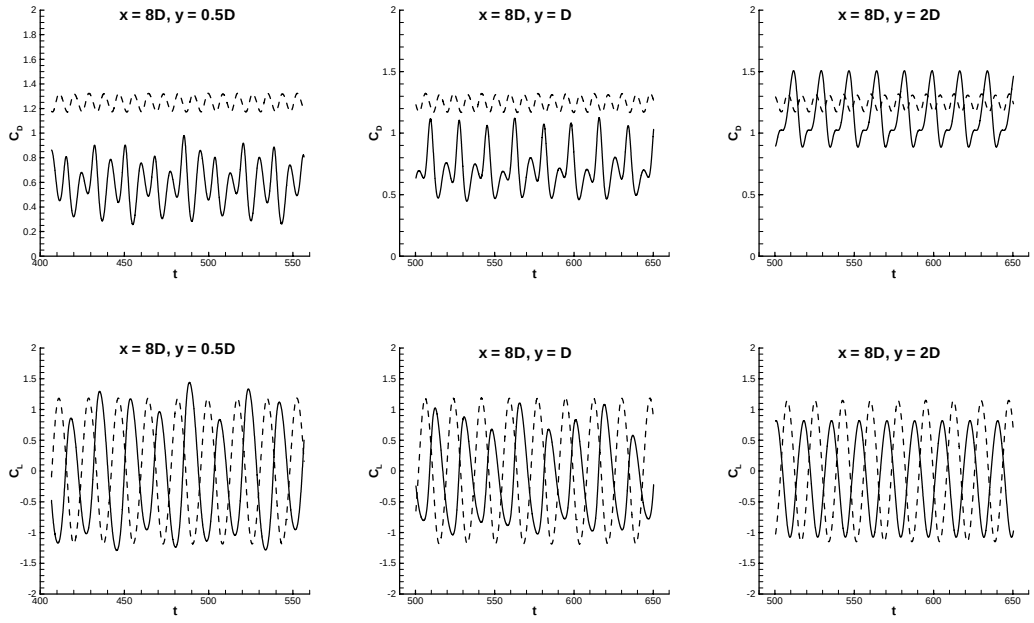

Figure 6-13 Drag and lift forces histories, the downstream cylinder is at x=8D, y=0.5D, D and 2D, respectively. Solid line: downstream cylinder; Dashed line: upstream cylinder.

The fluctuation of the lift force of the downstream cylinder becomes more consistent when increasing the lateral spacing. The unstable amplitudes for y = 0.5D and y = D also indicates the oncoming vortices have certain but not essential effect on the downstream cylinder.

6.3.2 Vortex shedding frequency

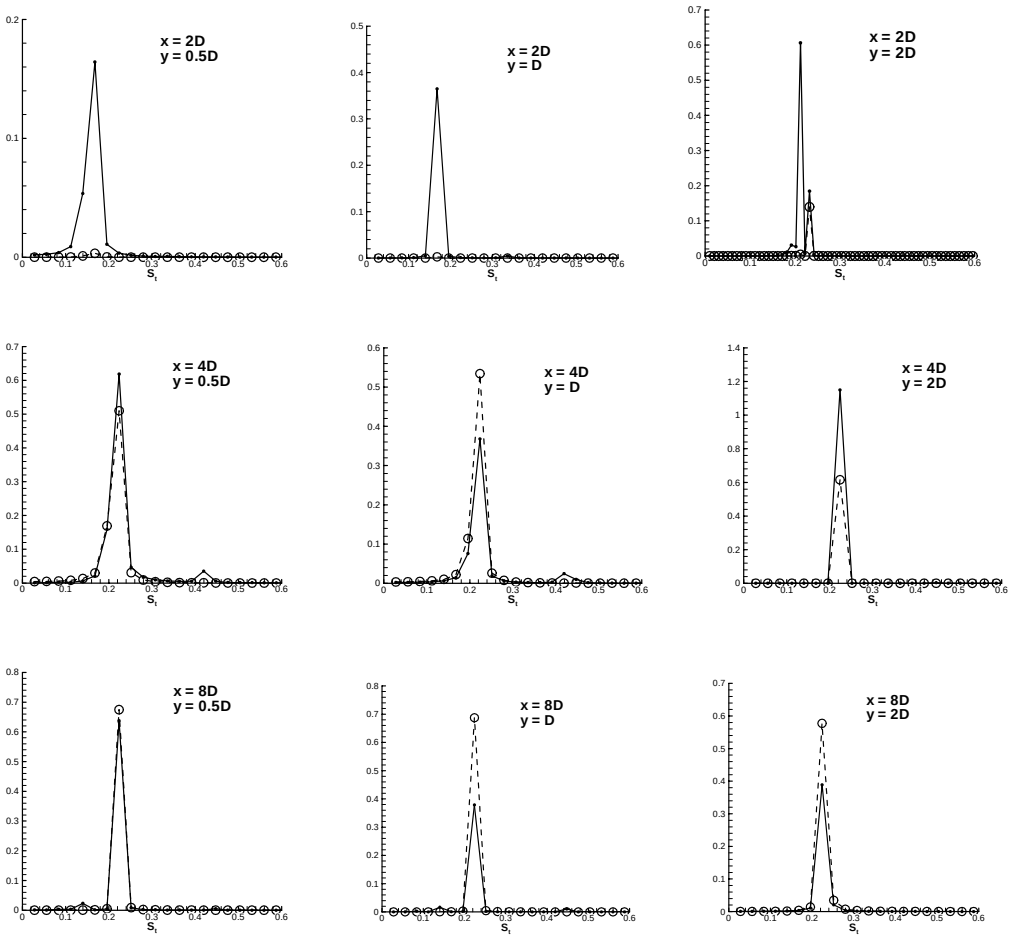

Figure 6-14 Power spectra of lift coefficients of the upstream and downstream cylinders. Circle and dashed line: upstream cylinder; Solid line: downstream cylinder.

The Strouhal number, St, was obtained from the power spectrum of the lift force history of the downstream cylinder, as shown in Figure 6-14. Nine configurations, x

= 2D, 4D or 8D, and y = 0.5D, D or 2D, are presented. The power spectra for the upstream cylinder are also shown here. For x = 2D, St = 0.16, 0.17 and 0.21 for y = 0.5D, D or 2D, respectively, which agree with the results from wake power spectra in chapter 6.2. At x = 2D and y = 2D, the power spectrum of the lift history of the upstream cylinder indicates its dominant frequency is 0.23, which suggests the complete vortex shedding flow pattern is a special case. This is the only exception of all cases, where both cylinders share the same dominant frequency. At x = 4D and x = 8D, the dominant frequencies for both cylinders, and therefore the Strouhal numbers, are found to be 0.21-0.22. This indicates the strong 'lock-in' state for two staggered cylinders in cross flow.

Table 6-1 summarised the strouhal numbers for all the nine staggered cases. Comparing with those from Zdravkovich (1987), current simulation overestimated a little, especially for smaller spacings. Nevertheless, the results here reflect similar trends, i.e. smaller Strouhal numbers for the proximity interference and a value around 0.2 for the wake interference.

Table 6-1 Strouhal number of the downstream cylinder for flow around two staggered circular cylinders.

x/D	y/D	St	St from Zdravkovich (1987) Re= 1.58×10^4
2	0.5	0.16	0.14
	1	0.17	0.14
	2	0.21	0.16
4	0.5	0.21	0.17
	1	0.21	0.18
	2	0.22	0.20
8	0.5	0.22	0.20
	1	0.21	0.20
	2	0.22	0.20

6.3.3 Mean force coefficients

Shown in Table 6-2 are the mean drag and lift coefficients of both cylinders for the cases computed in this thesis. For comparison, the results of the tandem arrangement, i.e. y = 0, are also shown here. C_{D1} and C_{L1} denote the drag and lift coefficients of the upstream cylinder, while C_{D2} and C_{L2} for the downstream cylinder.

Table 6-2 Time average of drag and lift coefficients.

x/D	y/D	C_{D1}	C_{D2}	C_{L1}	C_{L2}
2	0	0.84	-0.33	0.00	0.00
	0.5	0.87	0.58	-0.02	-0.32
	1	0.89	0.93	-0.01	-0.18
	2	1.05	1.25	-0.03	-0.09
4	0	1.20	0.26	-0.02	0.00
	0.5	1.23	0.47	-0.01	-0.09
	1	1.22	0.69	-0.01	-0.18
	2	1.21	1.31	-0.01	-0.12
8	0	1.24	0.52	0.00	-0.02
	0.5	1.25	0.59	-0.01	-0.04
	1	1.24	0.71	0.02	-0.10
	2	1.24	1.15	-0.01	-0.09

For the upstream cylinder, the mean lift force is close to zero for all the cases, and the drag coefficient is close to that of an isolated circular cylinder in cross flow, except for x = 2D, where proximity interference between the two cylinder happens (Zdravkovich(1987). At x = 2D, the drag coefficient is almost constant (C_{D1} = 0.84 - 0.89) for y = 0, 0.5D and D, where the flow is in shear layer reattachment, shear layer enveloping and vortex enveloping flow patterns. At x = 2D and y = 2D where complete vortex shedding happens, C_{D1} = 1.05, which indicate the upstream cylinder is less influenced by the downstream one at this arrangement, though its vortex shedding frequency is still influenced (Figure 6-9). The results suggest the influence

of the downstream cylinder on the upstream one has to be considered when the two cylinders are close enough, while upstream cylinder can be treated as an isolated one once the impingement flow pattern happens.

For the downstream cylinder, the drag coefficient increases when the lateral spacing, y, increases, which also is shown in Figure 6-15. The lift coefficient of the downstream cylinder is at its maximum when x = 2D and y = 0.5D. For x = 4D and 8D, the maximum lift occurs around y = D. This agrees with the result given by Zdravkovich and Pridden (1977). Quantitatively, the lift coefficients from current simulations are significantly undervalued comparing with experimental results, only about half of the experimental data for x = 4D (Figure 6-16), which suggests this 2-D $k-\omega$ SST model is not sufficient to predict lift forces, though is quite good for drag forces.

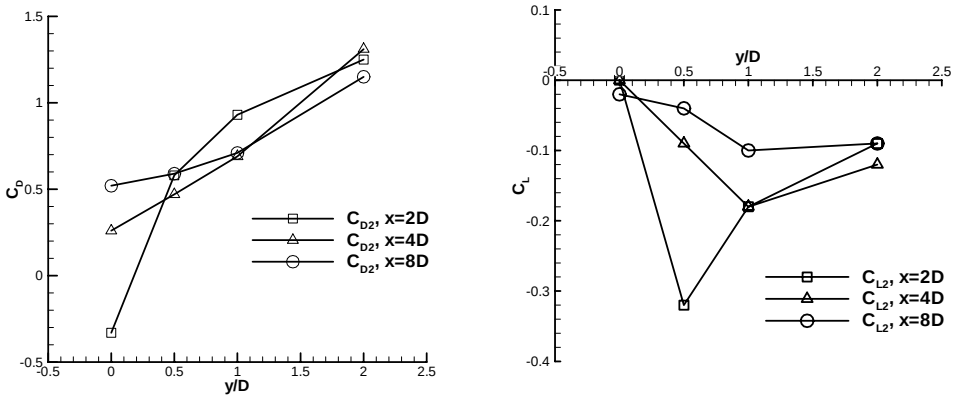

Figure 6-15 Drag and lift force coefficients of the downstream cylinder.

Table 6-3 summarised the standard deviation of the force coefficients. Again, the results for the tandem arrangement, i.e. y = 0, are also presented here for comparison. For the upstream cylinder, it can be seen that standard deviation of the drag coefficient is very small for all configurations, close to that of an isolated circular cylinder. As the downstream cylinder moves downstream, the standard deviation of the lift coefficient of the upstream cylinder is also close to that of a single cylinder in cross flow. This again suggests the downstream cylinder hardly have any influence

on the upstream one, except when they are very close (L = 2D), at which the standard deviation of the lift coefficient of the upstream cylinder is significantly reduced. This is possibly due to the incomplete vortex formation behind the upstream cylinder. It is interesting to notice that when x = 2D and y = 2D, STD(C_{L1}) = 0.39, far below that of a single cylinder. This indicates that for this configuration, though complete vortex street is formed behind the upstream cylinder, the influence of the downstream cylinder on its hydrodynamics is still significant.

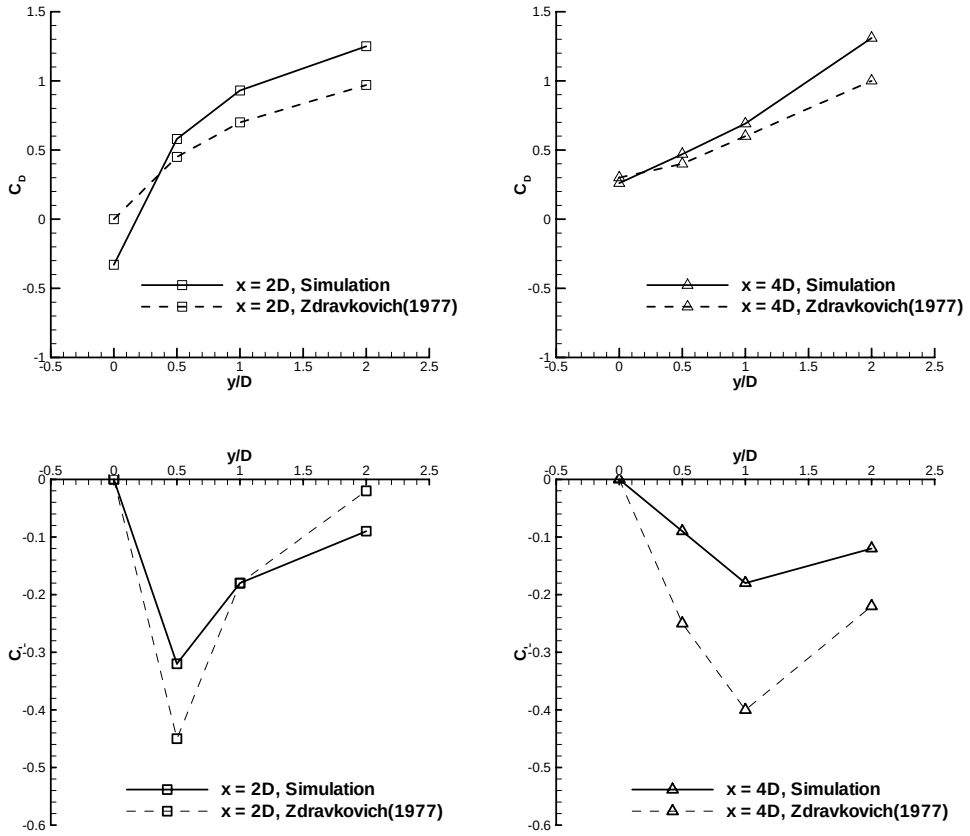

Figure 6-16 Comparison of force coefficients between results of current simulation (Re = 10^4) and those by Zdravkovich (1977) (Re = 6.1×10^4).

For the downstream cylinder, the standard deviations of the force coefficients are more complex. At x = 2D, its values for both coefficients increase while moving the downstream cylinder away from the wake centre line of the upstream one, which is understandable considering the weakening shielding effect of the upstream cylinder.

Table 6-3 Standard deviation of drag and lift forces.

x/D	y/D	STD (C_{D1})	STD (C_{D2})	STD (C_{L1})	STD (C_{L2})
2	0	0.00	0.00	0.02	0.07
	0.5	0.03	0.07	0.15	0.51
	1	0.03	0.09	0.05	0.61
	2	0.03	0.15	0.39	1.00
4	0	0.06	0.34	0.85	1.28
	0.5	0.06	0.30	0.90	0.98
	1	0.06	0.28	0.87	0.75
	2	0.05	0.17	0.77	1.09
8	0	0.05	0.19	0.83	0.95
	0.5	0.05	0.16	0.83	0.81
	1	0.05	0.17	0.83	0.63
	2	0.05	0.20	0.81	0.66

The standard deviation of drag coefficient of the upstream cylinder at x = 4D decreases from 0.34 to 0.17 when increasing the lateral spacing from 0 to 2D, while that of the lift coefficient decreases from a significant value STD(C_{L2}) = 1.28 to 0.75 at y = D, which indicates the influence of the oncoming vortices on the downstream cylinder weakens. At y = 2D, STD(C_{L1}) = 1.09, together with the significant value at x = 2D and y = 2D, it can be inferred that the reason is the higher oncoming flow velocity at this lateral clearance.

At x = 8D standard deviations of the force coefficients are quite stable except that of the lift coefficient is a little higher in the range from y = 0 to y = D. This suggests the influence of the vortices from the upstream cylinder on the downstream one is insignificant in the far wake.

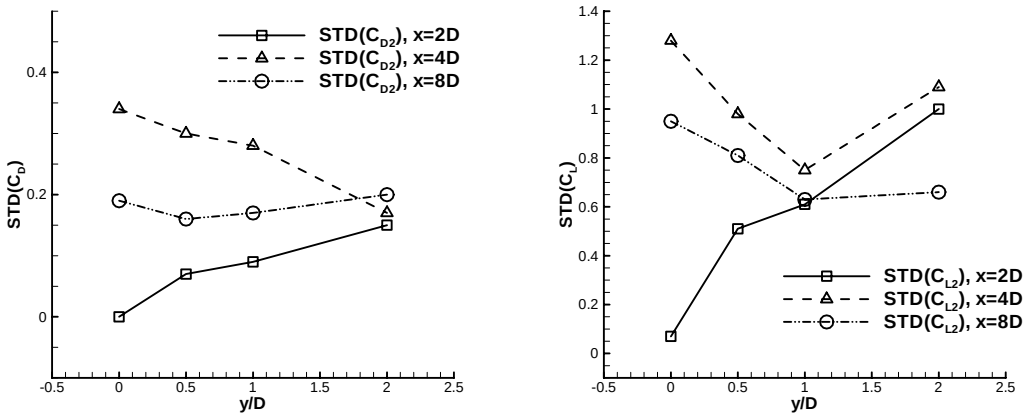

Figure 6-17 Standard deviation of drag and lift coefficients of the downstream cylinder.

6.4 The cause of fluid forces on the downstream cylinder

6.4.1 Vortex impingement

Shown in the following figures are the pressure and vorticity contours and velocity vectors varying in a vortex shedding period, for flow around two staggered circular cylinders with the downstream cylinder at x = 4D and y = D. The time-interval between consecutive plots in these figures is one tenth of the period for one complete cycle of vortex shedding in the cylinders' wake. All variables are dimensionless based on the free stream velocity, V, and the cylinder diameter, D.

This configuration is similar to that described in the last chapter for the tandem arrangement with L = 4D, where two rows of vortices from the upstream cylinder impinge on the downstream one. However for the staggered arrangement x = 4D and y = D here, only one row of vortices impinges directly on the downstream cylinder, as shown in Figure 6-18 0.0T(a)~1.0T(a).

Legend

(a) Vorticity contour

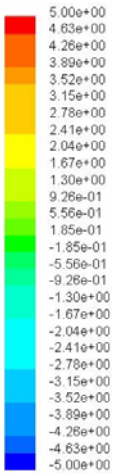

(b) Velocity vector

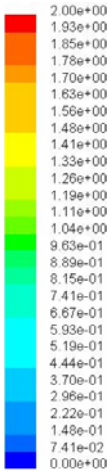

(c) Pressure contour

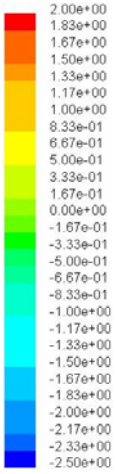

t = 0.0T

(a)

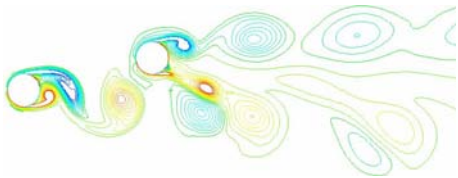

(b)

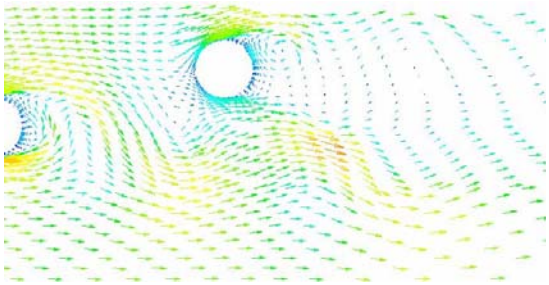

(c)

t = 0.1T

(a)

(b)

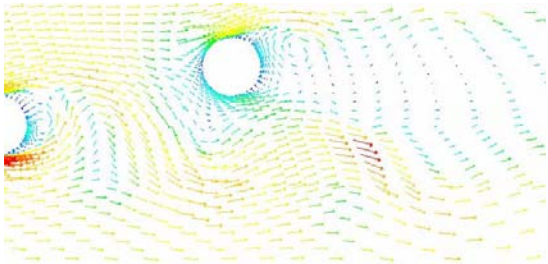

(c)

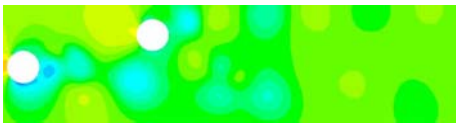

t = 0.2T

(a)

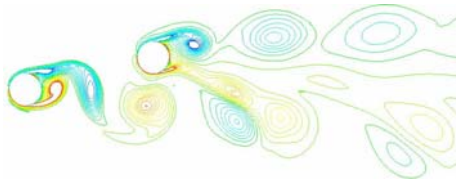

(b)

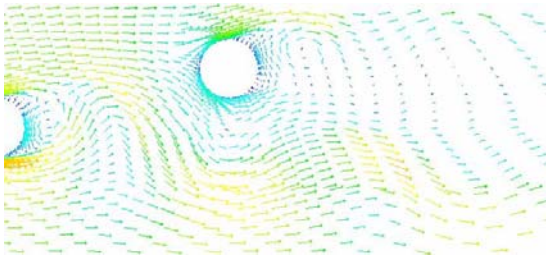

(c)

t = 0.3T

(a)

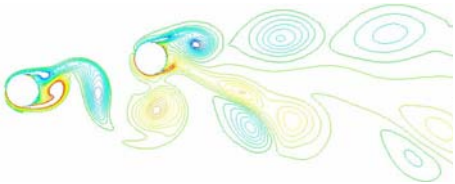

(b)

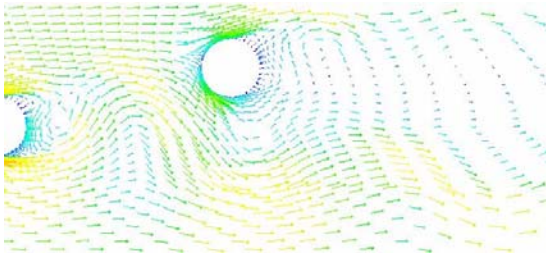

(c)

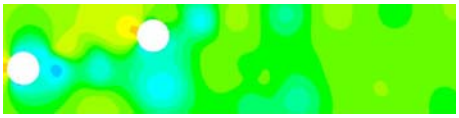

t = 0.4T

(a)

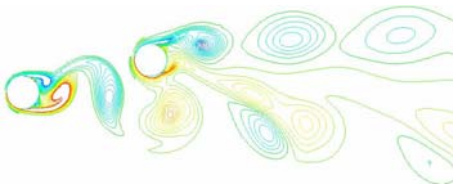

(b)

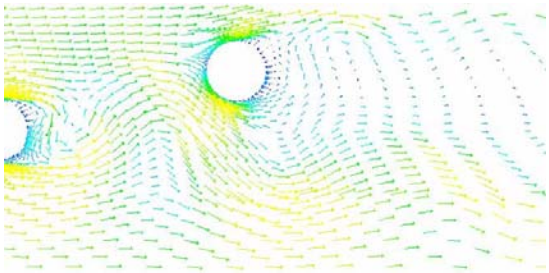

(c)

t = 0.5T

(a)

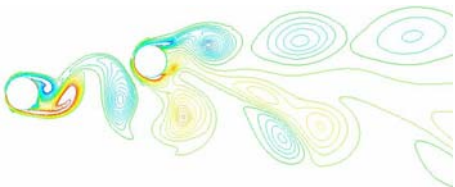

(b)

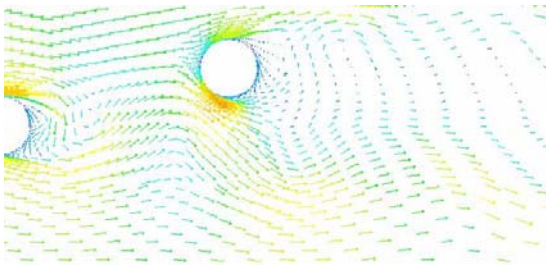

(c)

t = 0.6T

(a)

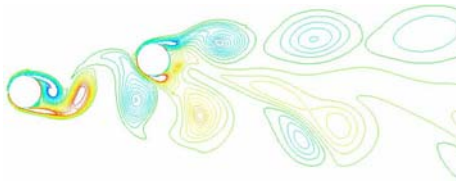

(b)

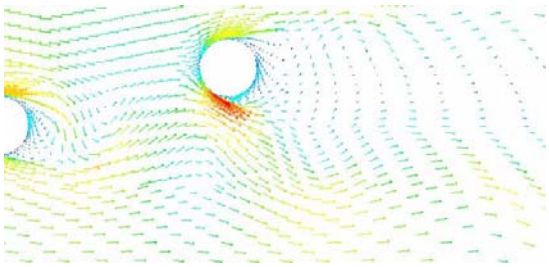

(c)

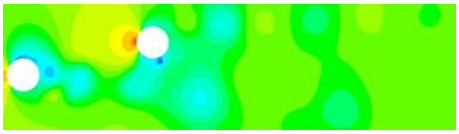

t = 0.7T

(a)

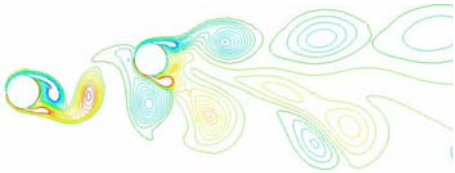

(b)

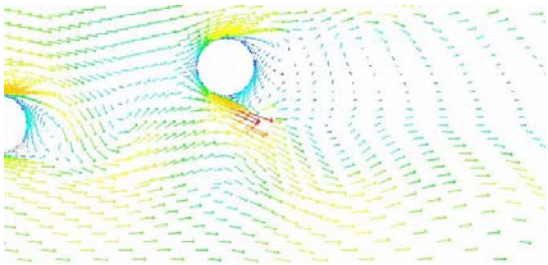

(c)

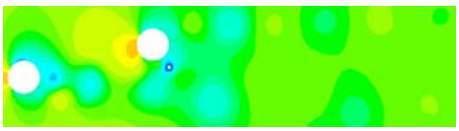

t = 0.8T

(a)

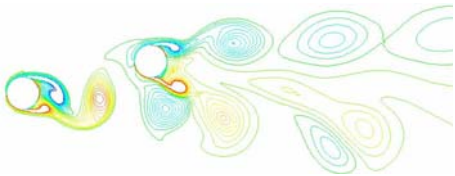

(b)

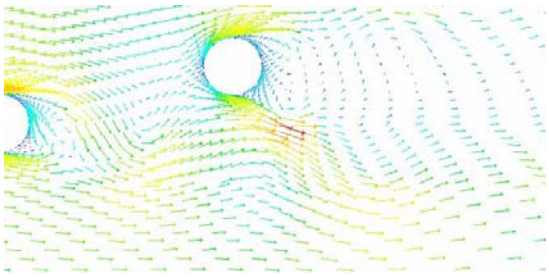

(c)

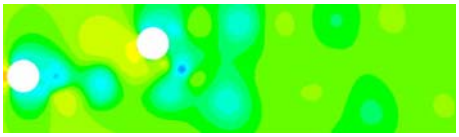

t = 0.9T

(a)

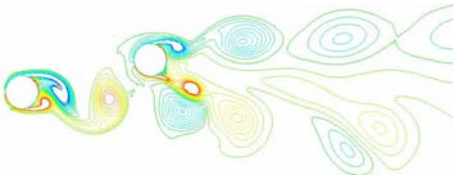

(b)

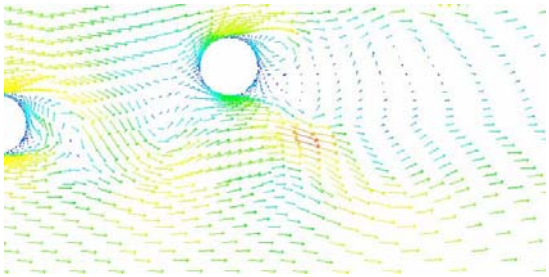

(c)

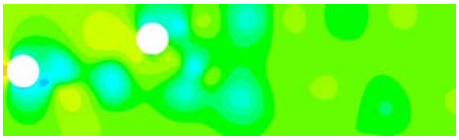

t = 1.0T

(a)

(b)

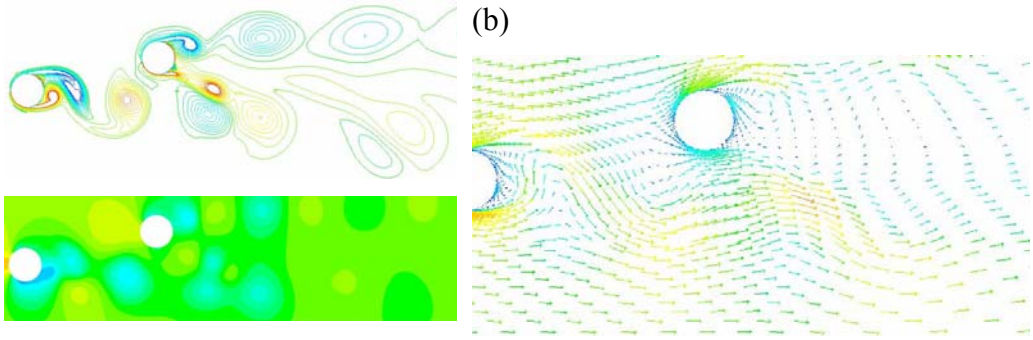

(c)

Figure 6-18 Pressure and vorticity contour and velocity vector varying in a vortex shedding period.

The Karman vortex shed from the outer shear layer of the upstream cylinder (the positive vortex here) remains intact as it approaches the downstream cylinder. When it passes the downstream cylinder, the vortex becomes a little distorted and connects the newly forming like-sign vortex from the inner side of the downstream cylinder (Figure 6-18 0.0T~0.6T). As the negative vortex from the inner surface of the upstream cylinder approaches the downstream cylinder (0.5T), it is deformed (0.6T~0.7T) and then splits into two parts (0.8T~0.9T) upon impingement, the outer part of which merges into the like-sign newly-forming vortex from the outer surface of the downstream cylinder, and the inner part merges into the opposite-sign shedding vortex from the inner side of the downstream cylinder. In contrast to the tandem arrangement, it is observed here only a small portion of split vortex merges into the like-sign vortex. Sumner (2000) schematically described this process, as shown in Figure 6-19, in which the newly-forming vortex on the inner side of the downstream cylinder is considered as induced vorticity by the impinging opposite-sign vortex.

During the merging process of the split upstream vortex (labelled B in Figure 6-19) and that formed behind the downstream cylinder (C) and previously shed outer Karman vortex (A), it is found that the centre of the combined vortex is well off the upstream cylinder' centreline (Figure 6-18). This transverse movement of vortex may

be a result of votex-body interaction.

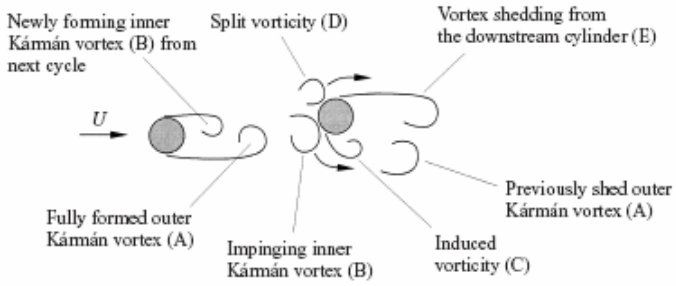

Figure 6-19 The vortex impingement flow pattern for two staggered circular cylinders in cross flow, after Sumner et al. (2000).

The vortex impingement flow pattern is of practical importance because the vortex-body interaction will cause large changes in the time-dependent pressure forces on the downstream cylinder (Sumner et al. 2000), which is important in the study of flow-induced vibrations of multiple cylinders.

6.4.2 Velocity vector

Shown in Figure 6-18 0.0T(b)~1.0T(b) are velocity vector plots which depict the magnitudes and orientations of the flow velocities around the downstream cylinder. It can be seen that the oncoming flow acts on the downstream cylinder in various directions and so the stagnation point shifts within the front surface of it. Shown in Table 6-4 are the actual positions of the stagnation point in one cycle of the vortex shedding. The position variation for this staggered configuration is significantly smaller compared with those for the tandem arrangement. For example in the tanden case with L = 4D, for the most part of a period the stagnation point varies in the range $\phi = \pm 35^{\circ}$, while in Table 3-4 it varies between $\phi = \pm 15^{\circ}$. The reason is that In tandem case, both the positive and negative vortices contribute to the variation, while in the staggered case, it is mainly from one row of vortices.

Another feature in the positions of the stagnation point here is, those in the first half

period and in the second half are asymmetric, while for tandem case described in last chapter, stagnation points are highly symmetric in both half of the vortex shedding cycle. Furthermore, it has a positive angle in most time, and the mean angle of stagnation point among these ten instances is 2.8^{o}. This mean value is actually underestimated here, which will be discussed in the following part. Similarly, Price (1976) reported the average stagnation angle was 5.8^{o} for x = 6D and y = D.

Table 6-4 Position of the stagnation point on the downstream cylinder in a period, x = 4D and y = D.

t	0.0T	0.1T	0.2T	0.3T	0.4T
ϕ_S (degree)	1	8	13	15	15
t	0.5T	0.6T	0.7T	0.8T	0.9T
ϕ_S (degree)	10	3	-8	-17	-12

It is also observed that, the fluctuating flow behind the upstream cylinder has a significant offset after it passes the downstream cylinder. This can be illustrated by Figure 6-20. For a single cylinder flow, the fluctuating flow in the wake convects directly downstream, i.e. along the wake centre line (a). If another cylinder is added on one side of this line while still in the wake, the fluctuating flow cannot maintain its trajectory due to the blockage of the downstream cylinder, therefore the main flow is pushed away to another side, and an offset δy is found (Figure 6-20 b), as shown in Figure 6-18 0.0T(b)-1.0T(b).

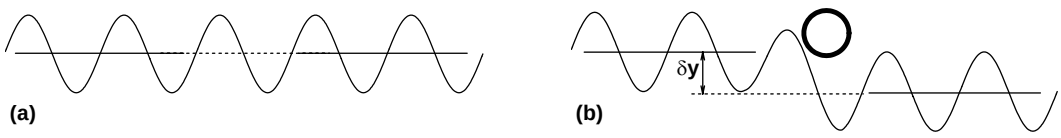

Figure 6-20 Illustration of fluctuating flow in the wake of a circular cylinder, (a): free wake; (b): after adding a downstream staggered cylinder.

As mentioned in the last chapter, the reason of the change of the stagnation point is

the highly fluctuating flow in the wake of the upstream cylinder. If the oncoming flow is symmetric with respect to the centre line of the downstream cylinder, symmetric stagnation points around it should be expected, which is not the case here. It is found through careful observation that the oncoming flow to the downstream cylinder is actually asymmetric due to its transverse offset. In Figure 6-20 (b), the oncoming flows toward the wake centre and that outward the wake centre are different; the amplitude of the former is A/2 + δy, while that of the latter is A/2 - δy. As a result of this difference the fluid acting on the downstream cylinder toward the wake centre is likely to be more and to last longer than the outward flow. This possibly is the reason of the existence of the asymmetric stagnation points. In some literatures this phenomenon was called entrainment of fluid into the wake (Mair & Maull 1971; Price 1976).

Table 6-5 Separation angle in a period of the downstream cylinder for x = 4D and y = D.

T		0.0T	0.1T	0.2T	0.3T	0.4T
Separation angle (degree)	Outer	85	85	87	89	91
	Inner	-108	-112	-115	-112	-80
T		0.5T	0.6T	0.7T	0.8T	0.9T
Separation angle (degree)	Outer	92	91	89	87	87
	Inner	-74	-74	-79	-89	-98

Shown in Table 6-5 is the change of separation point of the downstream cylinder in a vortex shedding period. Similar to the stagnation point, the separation points in both half of a period are asymmetric here. It can be seen that the separation point on the outer side is relatively stable, from 85^o to 92^o, while that on the inner side covers a wide range, -74^o to -115^o. Furthermore, the mean separation angle on the inner side is higher than that on the outer side, -94.1^o and 88.3^o, respectively. Price (1976) reported the separation angles on the inner side and outer side are -94^o and 85^o, respectively, for the case x = 6D and y = D, Re = 6.36×10^4. Together with the fact of positive stagnation angle and larger inner separation angle, the flow around the

downstream cylinder is asymmetric. This obviously will influence the pressure distribution around it, which will be discussed in the following part.

6.4.3 Pressure distribution

Pressure distribution around the downstream cylinder, and its integral over the surface, namely most part of the fluid forces, is the main concern of this thesis. Shown in Figure 6-18 0.0T(c)~1.0T(c) are pressure coefficient contours varying in one cycle of vortex shedding. Unlike the pressure distribution around the downstream cylinder in tandem arrangement, as shown in (5.5.3), where the pressure is symmetric with respect to the cylinder's centre line in both half of a full vortex shedding period, the pressure distribution around the downstream cylinder in staggered arrangement is more complex. The pressure distributions in both half of a period are remarkably asymmetric, as shown in Figure 6-21. This feature of asymmetry will give rise to a time-averaged lift force on the downstream cylinder.

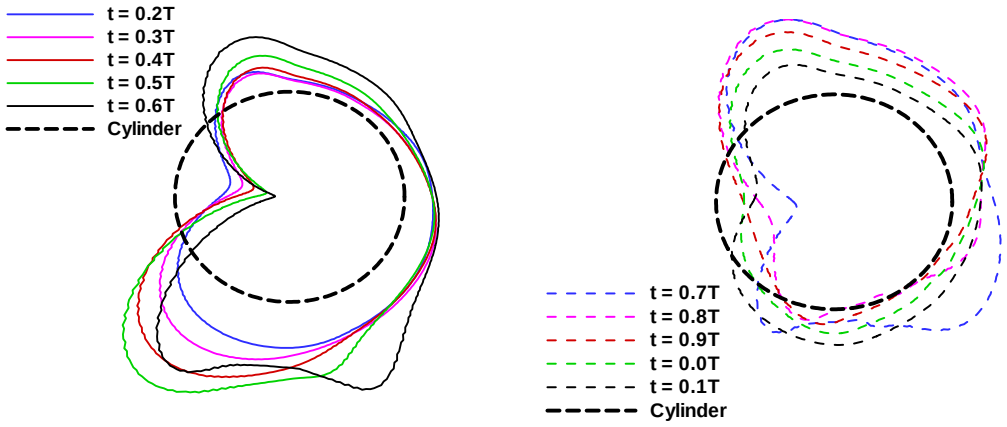

Figure 6-21 Pressure distribution around the downstream cylinder varying in a period: the line outside the circle represents negative pressure and the inner line represents positive pressure.

From the viewpoint of vortex impingement, the asymmetry of pressure distribution is a result of the fact that only one row of vortices from the upstream cylinder impinges

the downstream one. In Figure 6-18 the vortex from the inner side of the upstream cylinder is transversely closer to the downstream cylinder, and split into two parts during the process of impingement, while that from the outer side only deforms a little when it passes the downstream cylinder. Though quantitatively the vortex-body interaction is not clear, the asymmetry of pressure distribution around the downstream cylinder can be expected.

As mentioned before, the fluid acting on the downstream cylinder is toward the wake centre in most time of a period. This will likely cause more stagnation pressure on the outer side and more negative pressure on the inner side, as shown in Figure 6-21. The negative pressure at t = 0.4T, 0.5T and 0.6T on the inner side is significant among all distributions. Furthermore, this negative pressure covers more area on the inner side, as a result of further separation point on the same side. Therefore the total pressure on the inner side is lower than that on the outer side.

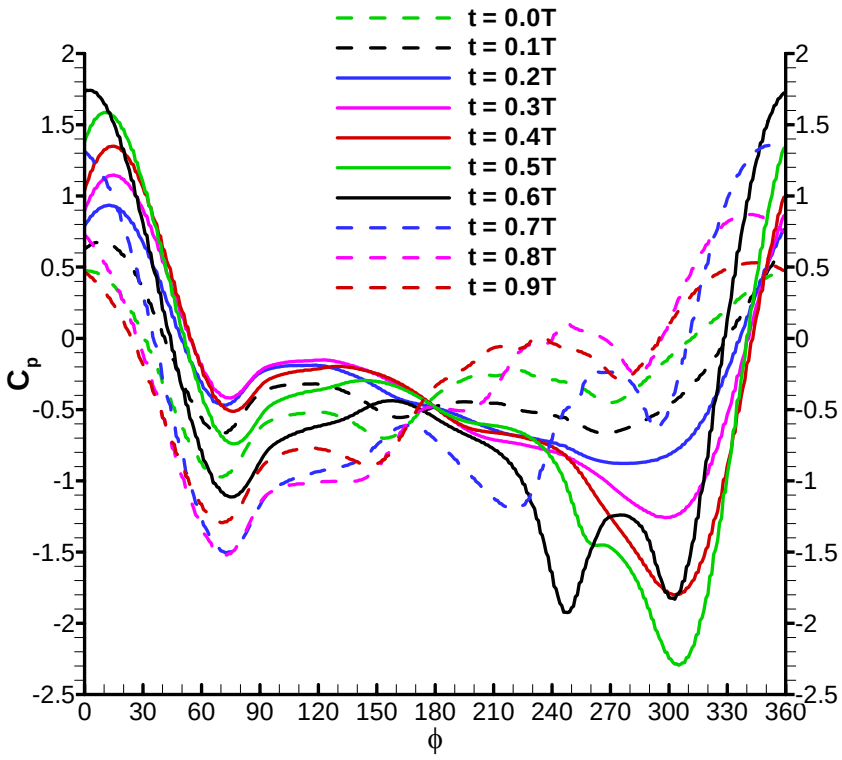

Figure 6-22 Pressure distribution around the downstream cylinder varying in a period.

Shown in Figure 6-22 are the pressure distributions around the downstream cylinder at ten instants in a cycle of vortex shedding. The stagnation point, where the maximum pressure exists, shifts around the extreme front point of the downstream cylinder, and the stagnation pressure changes in a remarkable range. Despite of the shift of stagnation point, it is seen that the pressure at the extreme aft end is relatively stable, with the base pressure $C_{pb} \approx -0.5$. Moreover, the pressure coefficient at most instants always varies around the base pressure for $\phi = 150^\circ \sim 210^\circ$. One can expect the contribution of the pressure on the rear surface of the cylinder, about a quarter of the total area, to its time-averaged lift force is insignificant.

What contributes more to the average lift force is the pressure distributions on the inner and outer surface, i.e. around $\phi = \pm 90^\circ$. The separation points are also in these regions. It can be seen from Figure 6-22 that the distributions on the outer surface are in the manner of those for flow around an isolated cylinder, while on the inner surface, the distributions are disorderly, indicating the main influence of the wake on the downstream cylinder impacts on the inner side of it.

Shown in Figure 6-23 is the time-averaged pressure distribution around the downstream cylinder. The exact average stagnation angle, where the maximum pressure acts on the downstream cylinder, is 6.5°, and is similar to that reported by Price (1976). Some characteristics of asymmetry can be found in Figure 6-23. Firstly, the positions of zero pressure are at $\phi = 42^\circ$ and -30° on the outer and inner surface, respectively. Secondly, the maximum negative pressure happens at $\phi = 74^\circ$ on the outer surface and $\phi = -62^\circ$ on the inner surface. Thirdly, the pressure coefficients are $C_p = -0.57$ and -0.70 at $\phi = 90^\circ$ and -90°, respectively. Furthermore, increasing of pressure from the maximum negative to base pressure is relatively smooth on the inner side, due to the further and scattered separation points. All above factors will cause the time-averaged lift force directed towards the wake centre line.

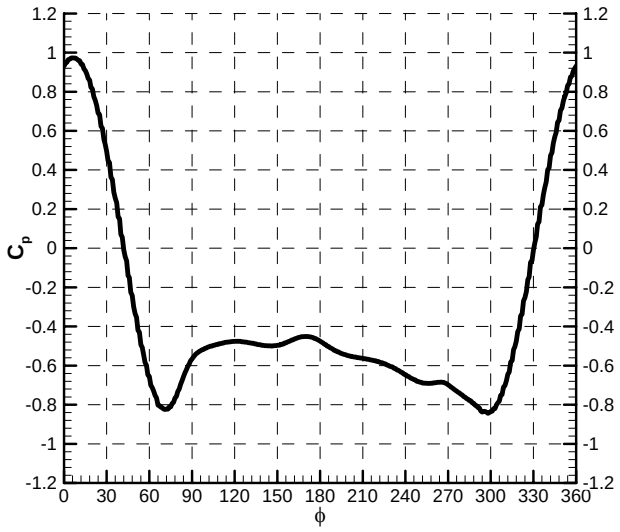

Figure 6-23 Time-averaged pressure distribution around the downstream cylinder.

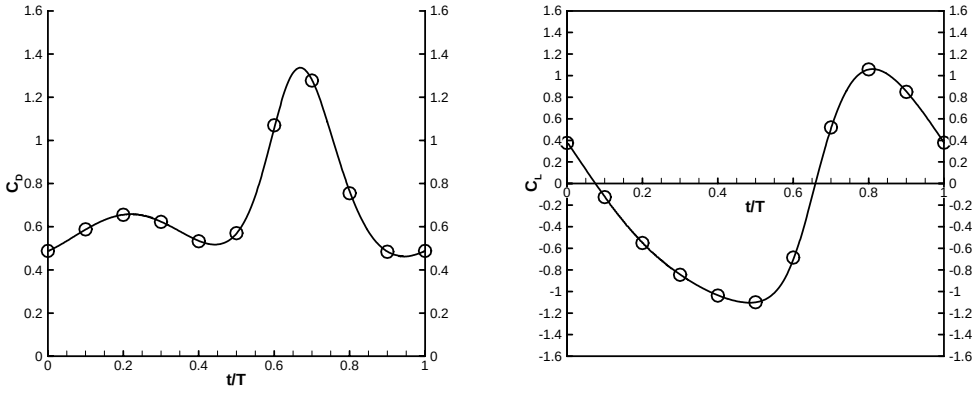

Figure 6-24 Drag and lift force coefficients varying in a period.

Shown in Figure 6-24 are drag and lift coefficients histories for the downstream cylinder in a vortex shedding period. The drag coefficient is around 0.6 for most of the time and a significant rise at t = 0.7T is found. It can be seen from Figure 6-22 this is because the pressure distribution on the rear of the cylinder is not point symmetric with respect to $\phi = 180^\circ$ and $C_p = -0.5$ at t = 0.7T, and results in much lower base pressure. The reason for this asymmetry is not clear but it displays the complexity of this flow. The lift coefficient history shows a significant feature, that

the cylinder experiences negative lift longer than positive lift. The proportions are 58% and 42%, respectively. To the best of the author's knowledge, this is not reported in literatures. This feature correlates with the longer positive stagnation angle in Table 6-4 and entrainment of fluid into the wake.

6.4.4 Correlation analysis

Table 6-6 shows the correlation coefficients between drag force and cosine of the stagnation angle, the stagnation pressure, the production of them, and C_{pF}, the pressure coefficient at the extreme front point. The results reveal that the correlation between the drag force and these expressions is not very strong, just around 0.6, while for tandem arrangement L = 4D, the drag force of the downstream cylinder is significantly correlated with the stagnation pressure's component on *x* direction ($C_{pS}Cos\phi_S$) and the pressure at the extreme front point (C_{pF}). This suggests the other influence on the drag force is not synchronous with these expressions, so none of them is representative. For example, none of these expressions reflects the abrupt rise of drag at t = 0.7T in Figure 6-24. The asymmetry of the flow around the downstream cylinder, especially that of the separation point, obviously affects the pressure distribution around it, and therefore the drag force.

Table 6-6 Correlation coefficients between drag force and some expressions.

	$Cos\phi_s$	C_{pS}	$C_{pS}Cos\phi_S$	C_{pF}
R_{C_D}	0.282	0.549	0.561	0.670

Table 6-7 shows the correlation coefficients between the lift force and minus sine of stagnation angle ($-Sin\phi_s$), the stagnation pressure C_{pS}, the product of them ($C_{pS}(-Sin\phi_s)$), and the pressure at the extreme front point C_{pF}. Similar to tandem case, the stagnation angle and the stagnation pressure's component on –*y* direction ($C_{pS}(-Sin\phi_s)$) are strongly correlated with the lift force, which indicates they are

synchronous with other lift-influenced factors such as the negative pressure on the opposed side of the front of the cylinder, and the pressure difference on the rear.

Table 6-7 Correlation coefficient between lift force and some expressions.

	$-Sin\phi_s$	C_{pS}	$C_{pS}(-Sin\phi_s)$	C_{pF}
R_{C_L}	0.919	-0.63	0.953	-0.519

6.5 Concluding remarks

This chapter investigated uniform flow past two circular cylinders of the same diameter in staggered arrangement at a subcritical Reynolds number Re = 10^4. The the downstream cylinder is at x = 2D, 4D, or 8D, and y = 0.5D, D, or 2D. So the proximity interference, near wake interference and far wake interference are all covered. Some flow patterns are identified and compared to those by Sumner et al. (2000) and Akbari and Price (2005).

The 'shear layer enveloping' pattern is observed when the downstream cylinder is situated at x = 2D and y = 0.5D. The inner shear layer from the upstream cylinder is deflected into the gap between the cylinders and soon fades out, being constrained between two opposite sign vortices from the outer side of the upstream cylinder and the inner side of the downstream cylinder. The inner shear layer of the downstream cylinder is enveloped by the outer shear layer of the upstream cylinder, before it rolls up into an expanded, weakened Karman vortex. The gap flow causes significant time-averaged lift force on the downstream cylinder.

The 'vortex pairing and enveloping' flow pattern is identified when the downstream cylinder is at x = 2D and y = D. The flow pattern is similar to the above-mentioned shear layer enveloping regime. However, in the near wake region the Karman vortex from the inner side of the downstream cylinder is paired with smaller-scale vortex of opposite sign from the inner shear layer of the upstream cylinder. A little further

downstream this vortex pair is enveloped by the vortex from the outer shear layer of the upstream cylinder. A reduced vortex shedding frequency St = 0.15 is observed for this flow pattern.

For x = 2D and y = 2D where the downstream cylinder is not immersed in the wake of the upstream cylinder, but the two cylinders are close enough for them to influence the vortex shedding from each other, the 'complete vortex shedding' flow pattern is observed. In this arrangement two distinct Karman vortex streets are seen in the wake of the cylinder pair. The Strouhal number for the upstream cylinder is St = 0.23, while that for the downstream cylinder is St = 0.21. As a result the force coefficient histories of the downstream cylinder depict a phenomenon of interference effect. Surprisingly, the force coefficient histories of the upstream cylinder also display the wave group feature, which indicates in this arrangement the upstream cylinder is still influenced by the downstream one.

The 'vortex impingement' flow pattern occurs when the downstream cylinder is immersed in the wake of the upstream cylinder with larger spacing, for example, x = 4D and y = D. The inner vortices from the upstream cylinder impinge on the downstream cylinder and split into two parts, the outer part of which merges into the like-sign newly-forming vortex from the outer surface of the downstream cylinder, and the inner part merges into the opposite-sign shedding vortex from the inner side of the downstream cylinder, before entrained by the outer Karman vortices from the upstream cylinder. In the vortex impingement pattern, the hydrodynamics of the downstream cylinder are results of vortex-body interaction while those for the upstream cylinder can be treated as an isolated one. The Strouhal numbers for both cylinders are found to be around 0.22, which indicates the strong 'lock-in' state for this flow pattern.

The case for x = 4D and y = D is carefully examined to investigate the origin of the time-averaged lift force. The changes of vorticity and velocity in flow field and the pressure distributions around the cylinder in a vortex shedding period are studied in detail to investigate the relationship among them. Then the correlation coefficient is

used to analyse the influence of various factors on fluid forces, such as stagnation angle and the pressure at stagnation point and the extreme front point.

Due to the periodically shed vortices from the upstream cylinder, the flow incident on the downstream cylinder is highly fluctuating. It is also observed that, the fluctuating flow behind the upstream cylinder has a significant offset after it passes the downstream cylinder. This introduces asymmetrical instantaneous stagnation points in a vortex shedding period. Furthermore, the stagnation point exists on the outer side of the downstream cylinder longer than on the inner side. This not only causes more stagnation pressure on the outer side, but also more negative pressure on the inner side, which obviously contribute to the time-averaged lift force.

Similar to the stagnation point, the separation points on both sides of the downstream cylinder are asymmetrical. The average separation angle on the inner side is higher than that on the outer side, being -94.1^{o} and 88.3^{o}, respectively. This again causes more negative pressure on the inner side. Together with the facts of outward stagnation angle and higher separation angle on the inner side, the flow around the downstream cylinder is highly asymmetric, which introduces a significant time-averaged lift force.

It is found that the change of the stagnation point, as a result of the fluctuating incident velocity, is strongly associated with the periodical variation of lift force, but not with the drag force. This suggests the asymmetry of separation points is also a significant influencing factor to the forces. The influences of stagnation point and separation point are synchronous on lift force but not on drag force.

7 Three cylinders flow: in-line arrangement

According to Zdravkovich (1987), three cylinders can be arranged into three categories: (a) all three cylinders aligned and oriented from in-line to side-by-side arrangements; (b) regular triangular arrangement where all cylinders are spaced equidistantly; and (c) irregular triangular arrangements, composed of all other possible arrangements, except (a) and (b).

Among various arrangements three aligned cylinders with in-line arrangement (Figure 7-1) represents a special case and will be studied in detail in this chapter. Zdravkovich (1987) pointed out that the addition of a third cylinder to a tandem arrangement of two, produces a new kind of flow which differs from both the flows behind the first two cylinders. The drag force measured by Igarashi & Suzuki (1984) and Dalton & Szabo (1977) indicated that the variation of the drag coefficient on the third cylinder is considerably different from that of the second cylinder. It was evident in Chapter 5 that when two cylinders are in tandem arrangement, the downstream cylinder experiences most drag reduction and the wake shielding effect is most remarkable, which also suggests the flow around three in-line cylinders is worth studying.

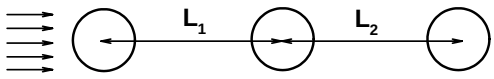

Figure 7-1 Three in-line circular cylinders in cross flow.

Though some of the experimental study about this arrangement can be found in the literature, the numerical simulation of flow around three in-line cylinders is very rare. To the author's knowledge, no one has studied the effect of various unequal spacing between the cylinders ($L_1 \neq L_2$) on the flow characteristics. This chapter will study

the influence of the third cylinder on the flow around first two; the spacing between the second and third cylinders, L_2, on the third cylinder with fixed L_1; and the spacing between the first and second cylinder, L_1, on the third cylinder with fixed L_2.

Flow around three in-line circular cylinders is simulated with the spacing L_1 from 1.5D to 8D, and L_2 from 1.5D to 12D. All cases presented use a Reynolds number of 10^4 and a turbulence model of k-w SST, as in the previous chapters. The domain, mesh and boundary conditions are all tackled in the same way described in the two-cylinder case.

7.1 Equal spacing $L_1 = L_2$

7.1.1 Vorticity contours and flow patterns

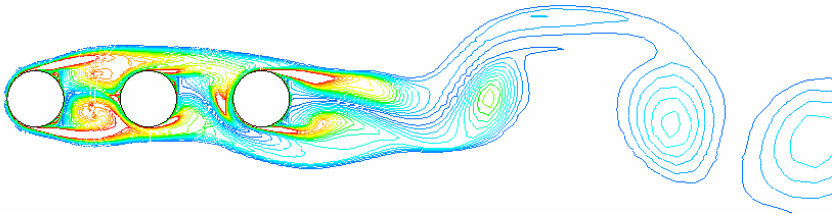

Figure 7-2 Vorticity contours of flow around three circular cylinders with equal spacing L = 2D.

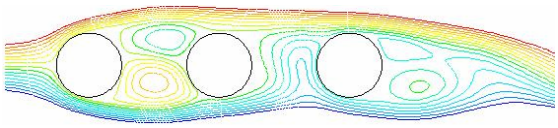

Figure 7-3 Stream function of flow around three circular cylinders with equal spacing L = 2D.

Figure 7-2 shows instantaneous contours of vorticity distribution for the case L = 2D. Vortex shedding is not observed from the upstream two cylinders. The shear layers separated from the first cylinder reattach to the second one, and two quasi-steady

vortices are formed between the cylinders, which is similar to the flow around two tandem cylinders with L = 2D. A steady recirculation region consisting of a pair of counter-rotating vortices exists in the first gap, as shown in Figure 7-3, which shows the stream function of this flow. However, no steady recirculation region is formed in the second gap. This region is alternately disturbed by the outer flow on both sides. This is mainly due to the fact that more turbulence is generated when the flow past the second gap, compared to the first one. Vortices are alternately formed on and shed from the third cylinder. Similar to the tandem flow case, the vortex formation length in current arrangement is much longer than that of an isolated cylinder.

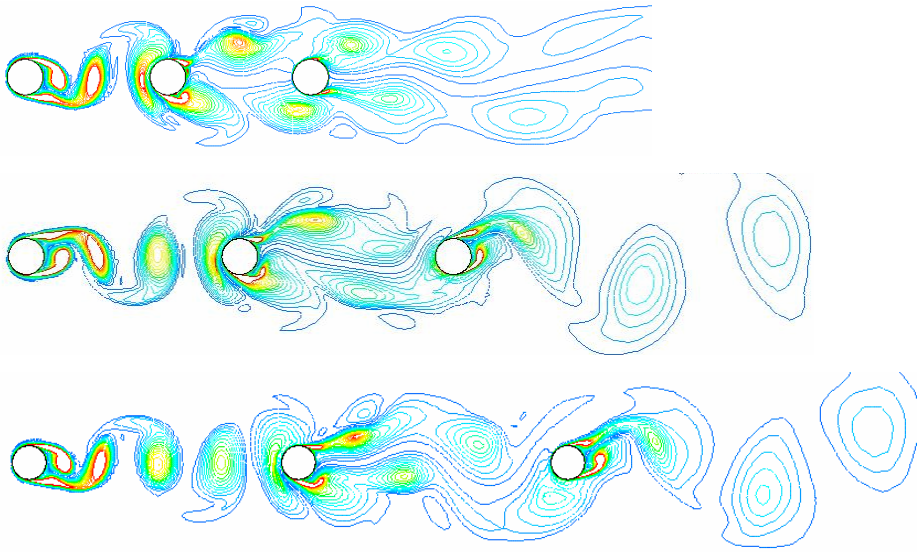

Figure 7-4 Vorticity contours of flow around three circular cylinders with equal spacing, L = 4D, 6D and 8D.

Figure 7-4 shows instantaneous contours of vorticity distribution for the cases L = 4D, 6D and 8D, respectively. In these configurations the two vortex streets pattern is observed behind every cylinder. The shear layers from the first cylinder rolls up into Karman vortex streets, and the vortices alternately impinge on the second cylinder. As a result the vortex streets behind the second cylinder have an increased transverse displacement and impinge on the third cylinder with greater attack angle. It is interesting that at L = 4D the vortices from the third cylinder are shed at similar frequency of those behind the second one, while at L = 6D and 8D the frequency of

the vortices behind the third cylinder is much lower. This will be studied in detail in the following part.

7.1.2 Pressure distributions and drag coefficients

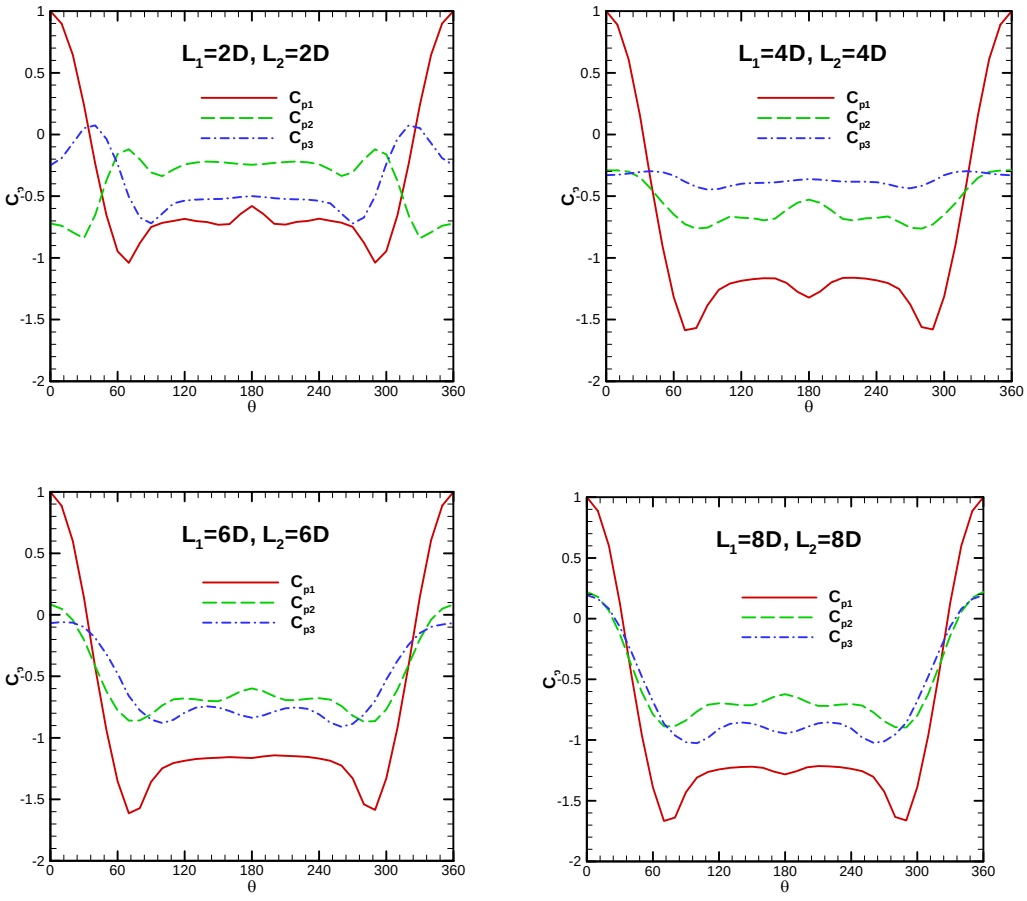

Figure 7-5 Time-average pressure distribution around three cylinders of various spacing.

The time-averaged pressure distributions around the cylinders at L = 2D, 4D, 6D and 8D are shown in Figure 7-5. When the third cylinder is situated in the far wake of the second cylinder, i.e. L = 6D and 8D, the pressure distribution around the third cylinder resembles that around the second one, with a lower base pressure. However, when the cylinders are closely arranged, the pressure distribution around the third

cylinder is much different from those around the first two. At L = 2D, the third cylinder has higher stagnation pressure and lower base pressure, compared to the second cylinder. At L = 4D, the last two cylinders have similar stagnation pressure but the base pressure of the third cylinder is much higher than the second one's. Actually the averaged pressure around the third cylinder is nearly constant. This may be because the oncoming flow to the third cylinder is much weakened by the cascading shielding effect of the upstream two cylinders (Figure 5-18).

The difference of the pressure distributions between the second and third cylinders at L = 2D is highlighted here. Shown in Figure 7-6 is the instantaneous pressure contour of this configuration. It can be seen that the first gap is a significant negative pressure zone, as a result of the steady recirculation region. Typically the pressure coefficient in this region is nearly -1.0. However, the pressure in the second gap is much higher due to non-existence of such a recirculation region. This again demonstrates the difference of flow patterns in both gaps. Behind the third cylinder the pressure drops a lot because of periodic vortex formation and shedding. Therefore the third cylinder will experience positive drag while the second cylinder has an adverse drag.

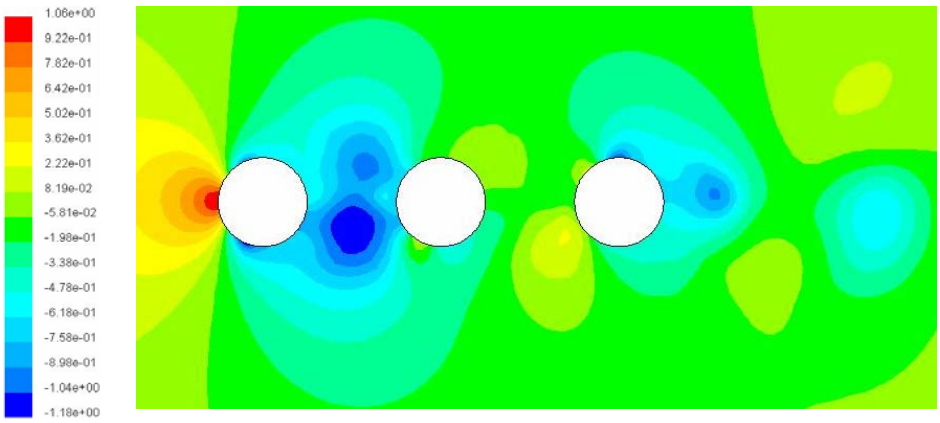

Figure 7-6 Instantaneous pressure coefficient contour of flow around three in-line circular cylinders, L = 2D.

Figure 7-7 shows the drag coefficients of three circular cylinders with in-line arrangement under various spacing. The data of the upstream two cylinders in

two-cylinder case are also included to investigate the influence of the third cylinder on the upstream two. It is found that the variation of the drag coefficients of the first two cylinders with the spacing basically coincides with those results in the two-cylinder flow case, except that the critical spacing, where the flow pattern changes from shear layer reattachment to two vortex streets, decreases by about 0.5D. The existence of the third cylinder makes the reattachment flow pattern sustain in shorter spacing. The influence of third cylinder is mainly limited within L < 4D.

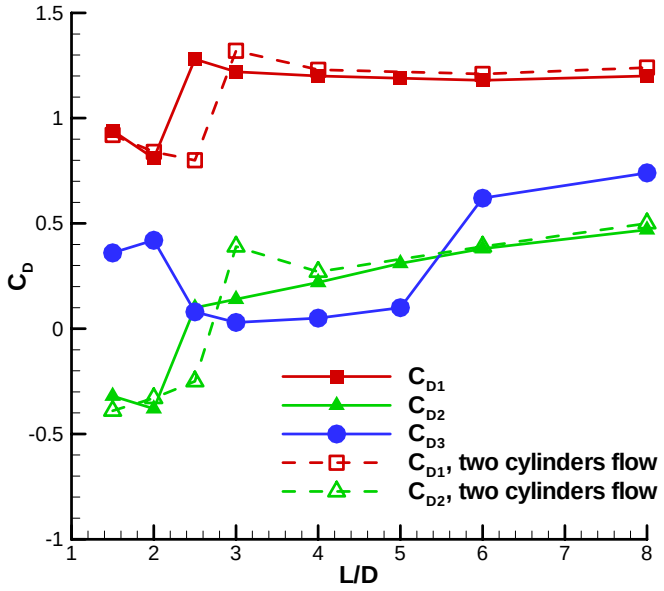

Figure 7-7 Drag force coefficients of three in-line circular cylinders with the distance L between them, in comparison to two-cylinder case.

As for the drag coefficient of the third cylinder concerned, its variation with the spacing is quite different from both upstream cylinders. When the flow around the first two cylinders is in reattachment pattern, the drag coefficient of the third cylinder $C_{D3} \approx 0.4$ is much higher than that of the second one ($C_{D2} \approx -0.35$), but still less than that of the first cylinder ($C_{D3} \approx 0.85$). The positive drag for the third cylinder has been analysed above. When the reattachment pattern is broken, but the third cylinder is still in the near wake behind the second one, i.e. L = 2.5D to 5D, C_{D3}

drops rapidly to nearly zero, and is less than C_{D2} in this range. As seen above, the pressure distribution around the third cylinder is nearly constant, which leads to little drag acting on it. As the third cylinder locates in far wake, the drag coefficient is again greater than C_{D2}, as a result of lower base pressure in comparison with that of the second cylinder.

7.1.3 Vortex shedding frequency

The Strouhal number, St, is obtained from the power spectrum of the lift force history of the third cylinder, as shown in Figure 7-8. Eight configurations, where drag coefficients are computed and shown above, are presented. At L = 1.5D and 2D, the dominant frequencies are about $St = 0.1$, with small peaks at the multiple-harmonics, 0.3 and 0.2 respectively. The dominant frequency increases to about 0.2 with some small peaks, when the third cylinder is in the near wake of the second cylinder. With increasing the spacing, the sub-harmonic peak at $St = 0.1$ becomes significant. Finally then L = 6D and 8D, only one dominant frequency, $St = 0.13$, is found.

Figure 7-9 summarised the Strouhal numbers obtained above. Its variation with the spacing indicates a strong correlation with that of the drag coefficient of the third cylinder. When the flow around the upstream two cylinder changes from reattachment pattern to two vortex streets pattern, the Strouhal number jumps from 0.1 to 0.2, corresponding to the drop of drag on the third cylinder. Similarly, when the spacing between the cylinder changes from 5D to 6D, the Strouhal number decrease to 0.13, corresponding to the increase in C_{D3}. This reduced St may link to the frequency of incident flow to the third cylinder. When the distance between the first two cylinders is large enough, possibly 5D, as shown in Figure 7-9, the dominated wake frequency is greatly reduced, as analysed in 5.4.2.

The results are compared with those from those by Igarashi & Suzuki (1984), as shown in Figure 7-9. The current simulation overestimated slightly, especially for $2.5D < L < 4D$. Nevertheless, the results here reflect similar trends.

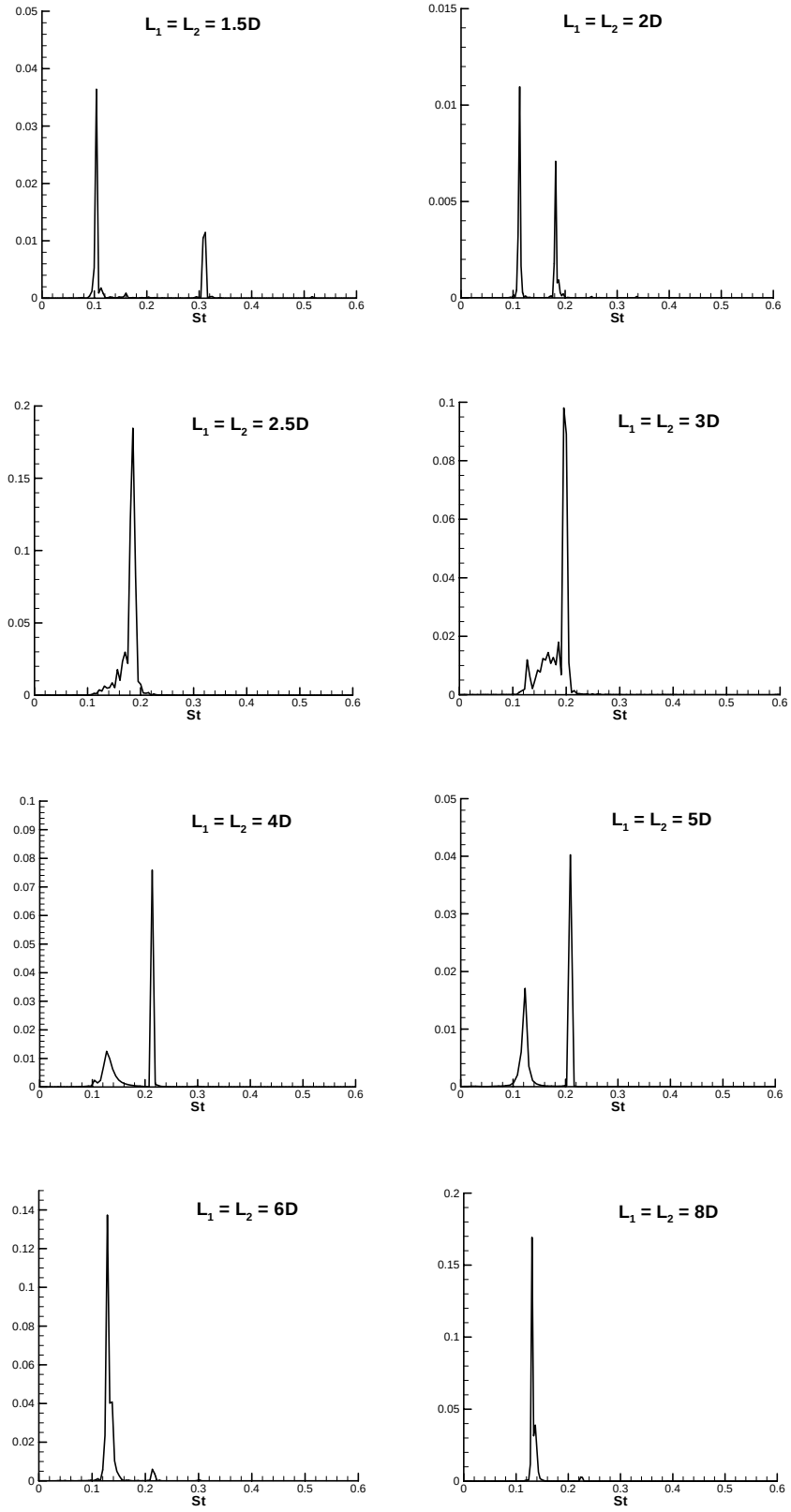

Figure 7-8 Power spectra of the lift force history of the third cylinder under various arrangements.

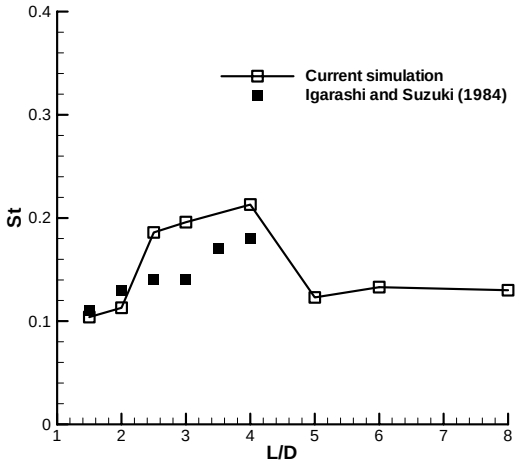

Figure 7-9 Strouhal number of flow around three in-line circular cylinders with the distance L between them.

7.2 The influence of L_2 on the third cylinder

7.2.1 L_1 = 2D

The influence of spacing L_2 on the characteristics of the third cylinder is approached by keeping the upstream two cylinders fixed with L_1 = 2D, while moving the third cylinder along the wake centre line. Five cases, L_2 = 2D, 4D, 6D, 8D and 12D, are modelled. The drag coefficients of all three cylinders are shown in Figure 7-10. The drag coefficients of the upstream two cylinders are unaffected in all cases, which indicates the flow pattern of the first two cylinders is relatively stable when L_1 = 2D. Of course the conclusion that there is no influence of the third cylinder on the upstream two cannot be drawn, as only a few cases are modelled here.

The drag coefficient of the third cylinder in the wake of two cylinders with 2 diameters apart is significant, not only much greater than that of the second cylinder, but comparable to that of the first one. As mentioned above, $C_{D3} = 0.4$ when L_1 = L_2 = 2D. Increasing L_2 to 4D, the drag coefficient of the third cylinder increases to

near 1, which is unexpected as it is even more than that of the first cylinder. From L_2 = 6D, C_{D3} is less than but slowly approaches C_{D1} with increasing L_2.

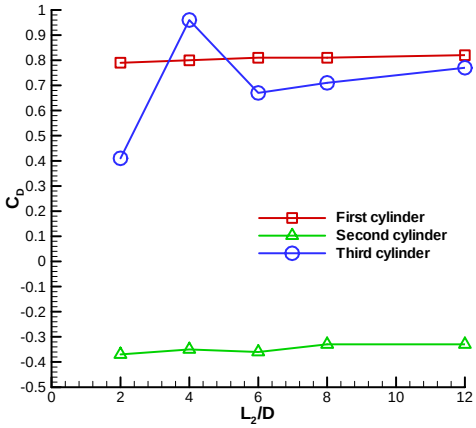

Figure 7-10 Drag coefficient of the third cylinder versus L_2 while L_1 = 2D.

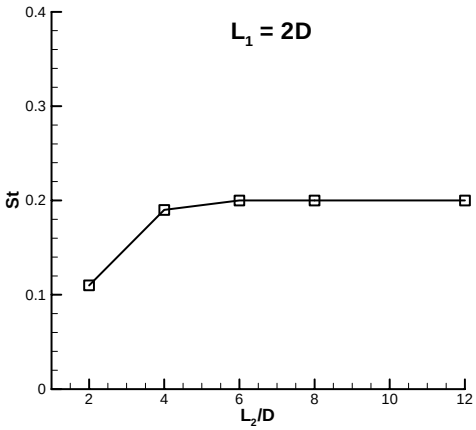

Figure 7-11 Strouhal number for flow around three in-line cylinders versus L_2 while L_1 = 2D.

Shown in Figure 7-11 is the Strouhal number varying with L_2, corresponding to the above cases. It can be seen that the Strouhal number is 0.2 for all cases except for L_2 = 2D, at which no vortices shed from the second cylinder. The shear layers envelope the third cylinder and merge those newly formed ones, then roll up into Karman vortices, as shown in Figure 7-12. The reduced vortex shedding frequency may

correlate with this flow pattern. When the spacing between the second and third cylinders increases to 4D, vortices shed from the second cylinder and impinge upon the third cylinder. The frequency of vortex shedding from the third cylinder is dominated by the impinged vortices which, as seen in chapter 4, have a frequency of 0.2.

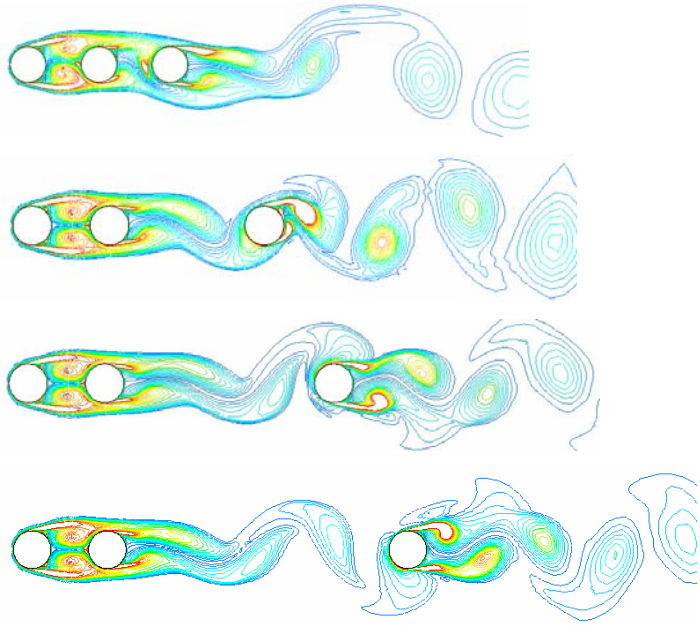

Figure 7-12 Contours of vorticity magnitude, L_1 = 2D, L_2 = 2D, 4D, 6D and 8D, respectively.

7.2.2 L_1 = 4D

When L_1 = 4D, the vortices from the first cylinder impinge on the second one and two vortex streets form behind the second cylinder. A third cylinder added into the wake of the second cylinder will also be impinged by the vortices. Thus the characteristics of the flow around the third cylinder may display different features from those of L_1 = 2D.

The drag coefficient of the cylinders varying with L_2 is shown in Figure 7-13. As expected, those of the upstream cylinders are not affected, except that C_{D2} slightly

increases when L_2 = 2D. Surprisingly C_{D3} does not change when L_2 increases from 2D to 4D, similar with the equal-spaced case described in 7.1.2. This suggests the shielding effect of near wake is very strong. C_{D3} gradually increases when further increasing L_2, but the values are much less than those for L_1 = 2D. The trend of C_{D3} varying with L_2 resembles that of the downstream cylinder of two tandem cylinders flow.

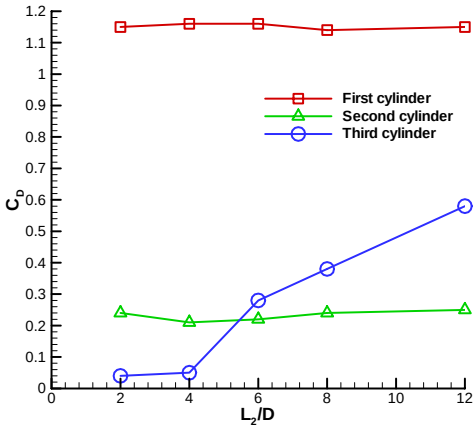

Figure 7-13 Drag coefficient of the third cylinder versus L_2 while L_1 = 4D.

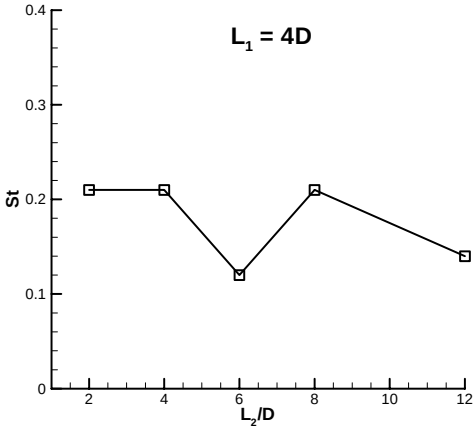

Figure 7-14 Strouhal number for flow around three in-line cylinders versus L_2 while L_1 = 4D.

Strouhal numbers for these cases are shown in Figure 7-14. St = 0.21 when L_2 = 2D,

4D and 8D, and 0.12 and 0.14 when L_2 = 6D and 12D, respectively. It seems that the trend is very random. However, it is found from the power spectrum of lift force of the third cylinder when L_2 = 8D that at this configuration there is a significant peak at $St = 0.11$, as well as the dominant frequency $St = 0.21$. This indicates the vortex shedding frequency of the third cylinder has a tendency to decrease when it moves into far wake.

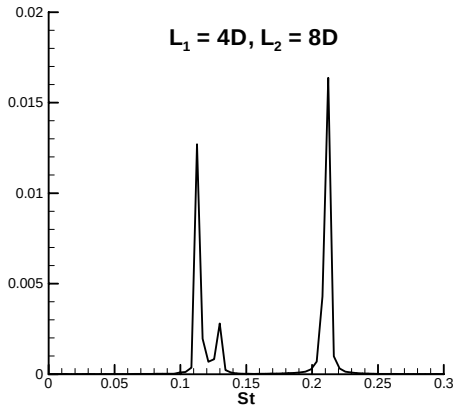

Figure 7-15 Power spectrum of lift history of the third cylinder, L_1 = 4D, L_2 = 8D.

The change of vortex shedding frequency can be observed through the vorticity contours, as shown in Figure 7-16. The spacing between the successive vortices indicates the relative amplitude of the frequencies. The vortices shedding from the second cylinder for all the cases here is in a similar frequency, which is about 0.22 as computed in Chapter 5. The vortices shedding from the third cylinder have different frequencies for the cases shown here. At L_2 = 2D and 4D, the frequency is similar with that behind the second cylinder, while at L_2 = 6D and 8D, the frequency of the vortices shedding from the third cylinder is much lower.

7.2.3 L_1 = 8D

When L_1 = 8D, the second cylinder is situated in the far wake of the first cylinder. The fully developed vortices from the first cylinder impinge on the second one and a

combined wake forms behind the second cylinder. A third cylinder added into the wake of the second cylinder will also be impinged by the vortices. Thus the characteristics of the flow around the third cylinder may display different features from those of L_1 = 2D and 4D.

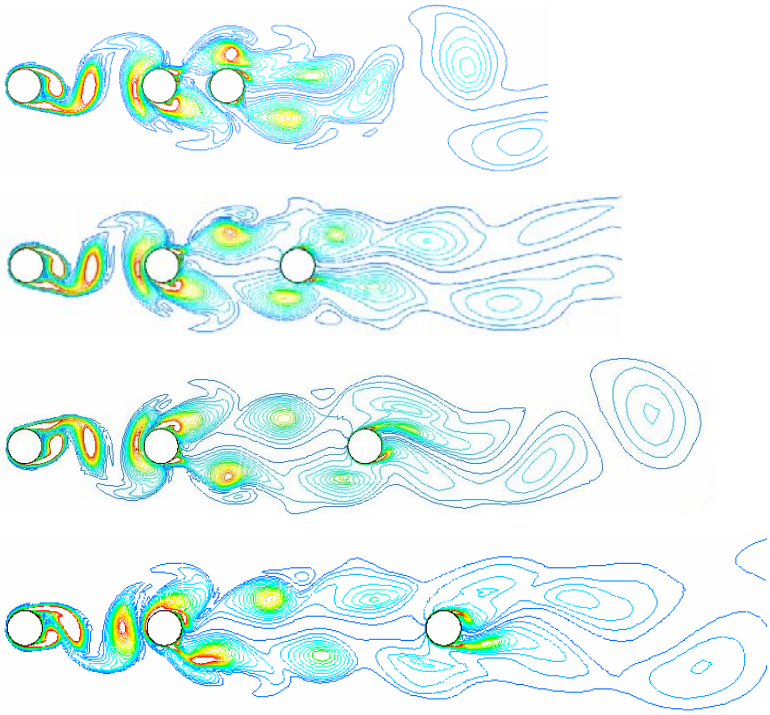

Figure 7-16 Contours of vorticity magnitude, L_1 = 4D, L_2 = 2D, 4D, 6D and 8D, respectively.

The drag coefficient of the cylinders varying with L_2 is shown in Figure 7-17. Again, those of the upstream cylinders are not affected, except that C_{D2} slightly increases when L_2 = 2D. Similar to the case L_1 = 2D, C_{D3} does not increase when L_2 increases from 2D to 4D as the shielding effect of the near wake of the second cylinder is still strong. What makes this case special is the abrupt jump of C_{D3} when L_2 is increased from 4D to 6D. Such a jump in the fluid loading is often associated with a characteristic change in the flow pattern. But on the other hand, puzzlingly, for L_2 = 2D to 8D the flow pattern shows no marked difference, all of which are vortex impingement flow patterns, according to the results in Figure 7-18.

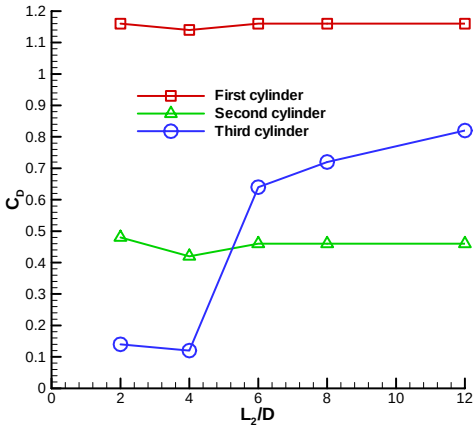

Figure 7-17 Drag coefficient of the third cylinder versus L_2 while L_1 = 8D.

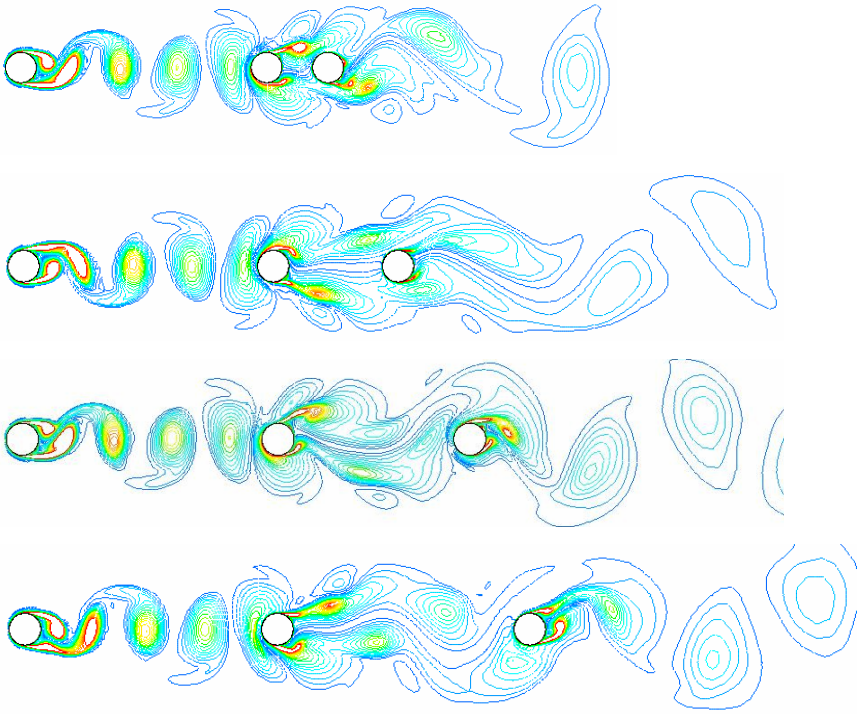

Figure 7-18 Contours of vorticity magnitude, L_1 = 8D, L_2 = 2D, 4D, 6D and 8D, respectively.

Strouhal numbers for these cases are shown in Figure 7-19. Surprisingly all the case have a reduced frequency, with a Strouhal number of around 0.12. This again indicates the special influence of the second cylinder situated in the far wake of the

first one on the flow around the third cylinder. It can be observed from the vorticity contours that the frequency of the vortices shedding from the third cylinder is much lower than that from the upstream two for all the cases here, as shown in Figure 7-18.

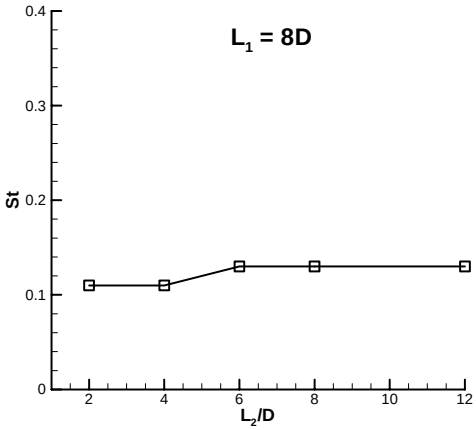

Figure 7-19 Strouhal number for flow around three in-line cylinders versus L_2 while $L_1 = 8D$.

7.3 The influence of L_1 on the third cylinder

From the results above it can be seen that the spacing between the first two cylinders L_1 also has an influence on the flow around the third cylinder, though one can expect that the main factor is still L_2. In this part the influence of L_1 on the third cylinder is examined, by fixing the last two cylinders at certain distance, while moving the first cylinder along the wake centre line.

Shown in Figure 7-20 are the drag coefficients of all three cylinders varying with L_1 while $L_2 = 2D$. The flow around the upstream two cylinder is actually a tandem cylinders flow, for it is only slightly influenced by the third cylinder when $L_2 = 2D$, as described in the above part. Thus the drag coefficients of the upstream two cylinders resemble those in the tandem case.

$C_{D3} = 0.4$ when $L_1 = 2D$ and the flow around the first two cylinders is in

reattachment pattern. As long as two vortex streets happen behind the first cylinder the drag coefficient of the third cylinder is very small and slightly increases with increasing L_1. This indicates the third cylinder under proximity interference with the second one is hardly affected by the position of the first cylinder once $L_1 > 4D$.

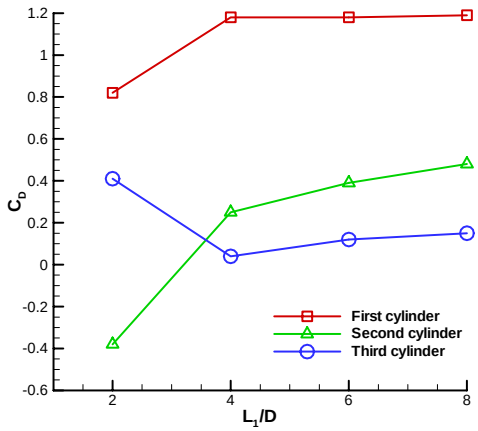

Figure 7-20 Drag coefficient of the third cylinder versus L_1 while $L_2 = 2D$.

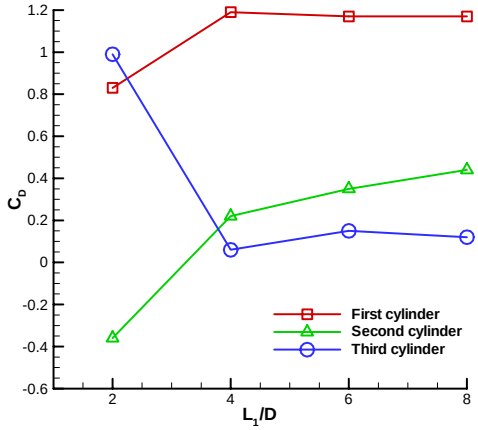

Figure 7-21 Drag coefficient of the third cylinder versus L_1 while $L_2 = 4D$.

Shown in Figure 7-21 are the drag coefficients of all three cylinders varying with L_1 while $L_2 = 4D$. Similar with the above case $L_2 = 2D$, the drag coefficient of the third cylinder is significant when the upstream two cylinders are in reattachment regime, while near zero when two vortex streets regime happens. There is no tendency of

increasing in C_{D3} with increasing L_1. This indicates when the two downstream cylinders are moderately spaced at the distance of 4D, the drag coefficient of the last cylinder is very small and does not depend on the position of the first cylinder, unless the upstream two cylinders are too close, or of course, too far that the wake effect on the second cylinder weakens.

For L_2 = 8D, when the downstream two cylinders are widely spaced, the position of the first cylinder has significant influence on the drag coefficient of the third cylinder, as shown in Figure 7-22. Again, C_{D3} is remarkable when the first cylinder is very close to the second one. The tendency of increasing in C_{D3} can be observed when moving the first cylinder upstream. This phenomenon may be the result of wakes superposition.

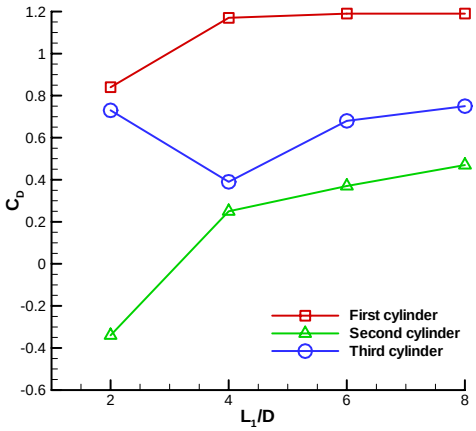

Figure 7-22 Drag coefficient of the third cylinder versus L_1 while L_2 = 8D.

Shown in Figure 7-23 are Strouhal numbers varying with L_1 while L_2 = 2D, 4D and 8D, respectively. It is obvious that vortex shedding frequency from the third cylinder is around 0.2 when L_1 = 2D and 4D, except for the case $L_1 = L_2$ = 2D, while near 0.1 when L_1 = 6D and 8D. The decrease of Strouhal number from 0.2 to 0.1 happens between L_1 = 4D and 6D, for arbitrary distance between the downstream two cylinders shown here. This indicates that the vortex shedding frequency of the third cylinder depends on the spacing of the upstream two cylinders to a large extent.

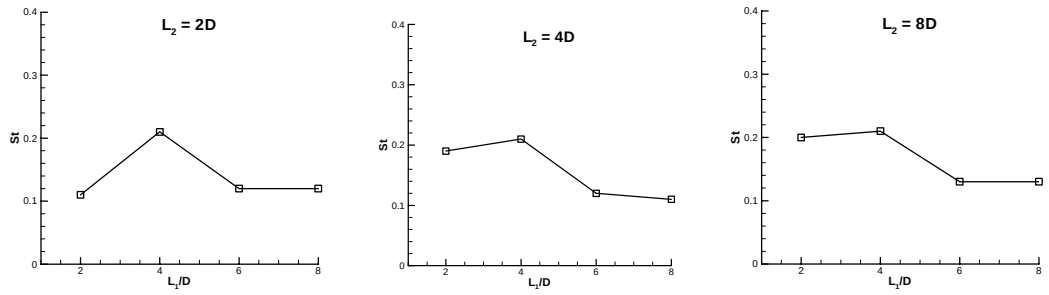

Figure 7-23 Strouhal number for flow around three in-line cylinders versus L_1 while $L_2 = 2D$.

7.4 Discussion

Figure 7-24 summarises the influence of the spacing between the first and second cylinder, L_1, and the spacing between the second and third cylinders, L_2, on drag coefficients of three in-line cylinders. For the cases investigated here, it can be seen that C_{D1} is independent of L_1 and L_2, C_{D2} is dependent on L_1 only, and C_{D3} is dependent on both L_1 and L_2. Generally the downstream cylinder(s) have insignificant influences on the upstream cylinder(s).

For L_1 = 4D, 6D and 8D, C_{D3} is very small when $L_2 \le 4D$, and there is a jump between L_2 = 4D and 6D. When $L_2 \ge 6D$, C_{D3} slowly increases with L_2. The reason can be explained by the averaged wake behind two tandem cylinders shown in Figure 5-17. For L = 4D, 6D and 8D, the increase in the wake velocity along the wake centreline behind the second cylinder is slow. Therefore, for the third cylinder, the oncoming flow velocity u is only about $0.2U_0$ when $L_2 \le 4D$. With the increasing distance behind the second cylinder, the wake velocity increases. As a result, increase in C_{D3} can be expected.

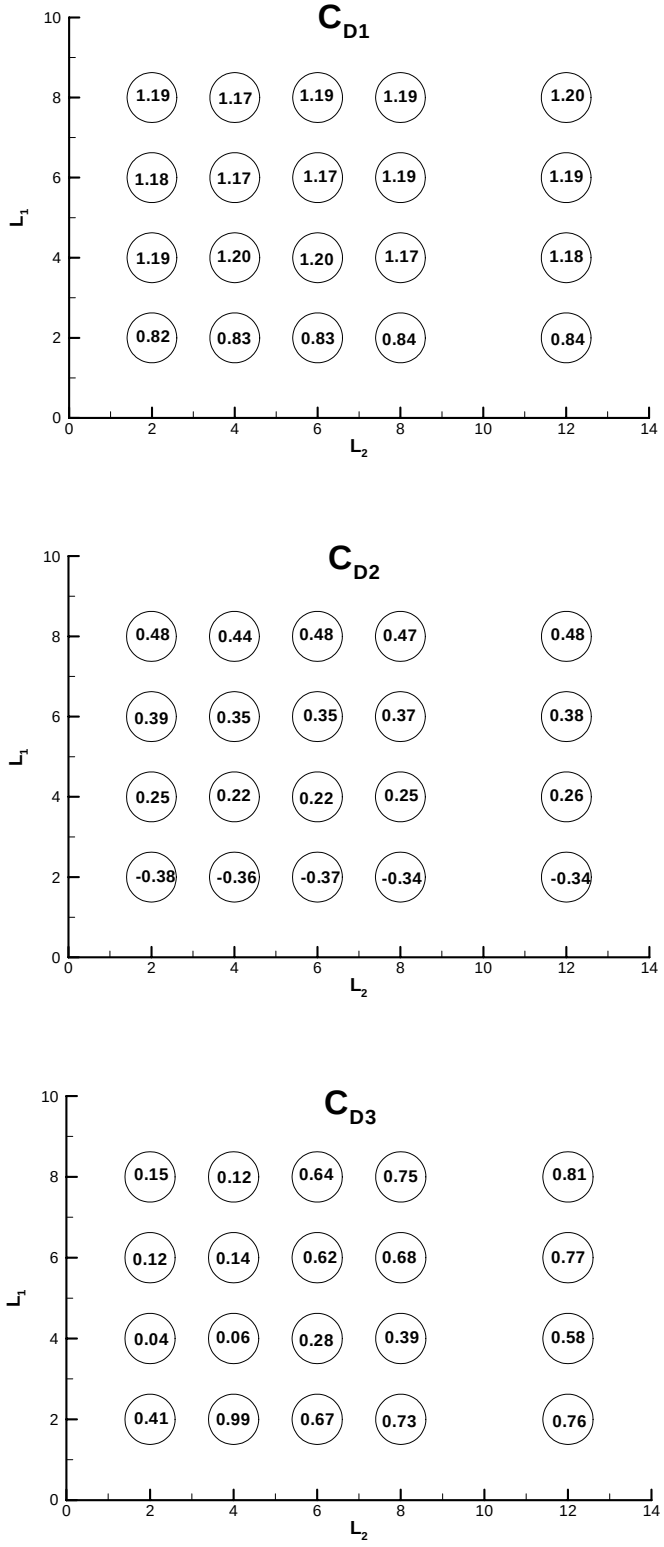

Figure 7-24 Drag coefficients of three in-line cylinders versus spacings L_1 and L_2.

For L_1 = 2D, the flow around first two cylinders is in reattachment pattern. The averaged velocity behind the second cylinder increase very fast and the vortices are very weak compared to those behind an isolated cylinder. So the drag coefficient of the third cylinder is significant for any L_2.

Figure 7-25 summarises the Strouhal numbers of the third cylinder with different L_1 and L_2. It is interesting to note that there are two distinct regions in Figure 7-25. The region over the dash line all have a reduced vortex shedding frequencies for the third cylinder, with the exception for L_1 = 4D and L_2 = 8D for which the lift force of the third cylinder has a significant component at a lower frequency, i.e. Figure 7-15.

Power spectra analysis of the wake of two tandem cylinders with spacing L = 6D (Figure 5-21) and 8D (Figure 5-22) suggests the velocity in the wake has a reduced frequency of around 0.13, so the reduced vortex shedding frequency for the third cylinder can be expected for L_1 = 6D and 8D.

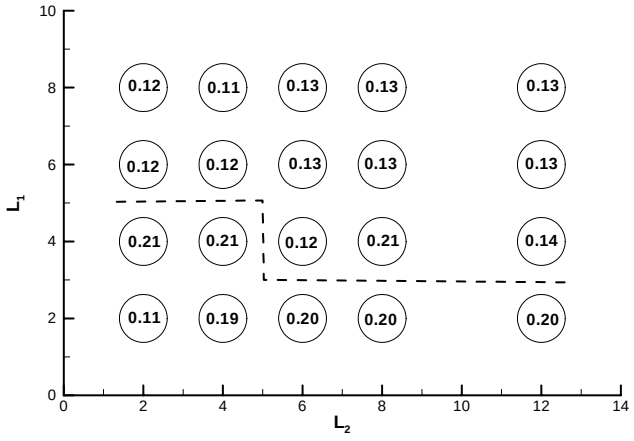

Figure 7-25 Strouhal number of the third cylinder varying with the spacing between three in-line cylinders.

For L_1 = 4D, the vortex shedding frequency of the third cylinder has a tendency to decrease when it is situated in the far wake of the second cylinder, though the wake itself has a normal frequency of 0.22. The reason is not clear. This is possibly

because the wake at this frequency is not stable, especially when interacting with a third cylinder.

7.5 Concluding remarks

This chapter investigated uniform flow past three in-line circular cylinders of a same diameter at a subcritical Reynolds number Re = 10^4. The centre to centre spacing between the first two cylinders varies from 1.5D to 8D, and that between the second and third cylinders is from 1.5D to 12D. The drag coefficients and vortex shedding frequencies are the main focus in this chapter. Three aspects were studied, i.e. the influence of the third cylinder on the flow around first two; the spacing between the first and second cylinders, L_1, on the third cylinder; and the spacing between the second and third cylinder, L_2, on the third cylinder.

For the case of three cylinders with equal distances, it is found that the varaiation of drag coefficients of the first two cylinders with the spacing basically coincides with those in two cylinders flow, except that the critical spacing, where the flow pattern changes from shear layer reattachment to two vortex streets, decreases about 0.5D. Therefore the third cylinder only influences the drag of the upstream two when they are at such a distance apart that the flow pattern can change, i.e. the configuration is near the critical spacing.

The variation of the drag coefficient of the third cylinder with spacing is quite different from that for both upstream cylinders. When the flow around the first two cylinders is in reattachment pattern, the drag coefficient of the third cylinder $C_{D3} \approx 0.4$ is much higher than that of the second one. When the reattachment pattern is broken, but the third cylinder is still in the near wake behind the second one, i.e. L = 2.5D to 5D, C_{D3} drops rapidly to nearly zero, and is less than C_{D2} in this range. As the third cylinder locates in far wake, the drag coefficient again is greater than C_{D2}, as result of lower base pressure in comparison to that of the second cylinder.

The Strouhal number shows the opposite trend with increasing spacing. A reduced vortex shedding frequency is observed when the flow around the first two cylinders is in reattachment pattern or the spacing is more than 5D.

The influence of spacing between the second and third cylinder, L_2, on the third cylinder is significant. For L_1 = 4D, 6D and 8D, C_{D3} is very small when $L_2 \le 4D$, and there is a jump between L_2 = 4D and 6D. When $L_2 \ge 6D$, C_{D3} slowly increases with L_2. This is possibly due to the double shielding effects of the two upstream cylinders, behind which the flow velocity is greatly reduced in the near wake.

The influence of spacing between the first and second cylinder, L_1, on the third cylinder is also significant. For L_1 = 6D and 8D, the third cylinder experiences a reduced vortex shedding frequency. When the third cylinder situates in the near wake of the second cylinder, C_{D3} is not influenced by L_1; when L_2 = 8D, the tendency of increasing in C_{D3} can be observed when moving the first cylinder upstream.

8 Stability analysis of two elastically supported cylinders with wake interference

After investigating flow around multiple stationary cylinders, it is time to study the stability of real marine risers. A natural way is to dynamically simulate cross-flow around elastically mounted cylinders. But this will demand huge computational resources, as simulations of both VIVs and wake-induced motions are very time-consuming.

Based on the research work by Wu et al.(2001; 2002), a stability analysis model for two closely arranged marine risers is established in this chapter. The risers are simplified as elastically mounted cylinders in a two dimensional flow field, and the problem is formulated by taking account of the wake shielding effect. To trace the multiple solutions of the non-linear static problem, a continuation analysis methodology is adopted. For each equilibrium position its stability is further examined by finding the eigenvalues of linearised dynamic equations.

The position-related fluid forces used here are based on the numerical results of stationary cylinders and the experimental data by DHI Water & Environment in 2002.

Different nomenclature is used in this section, and this is noted when the variable is firstly employed.

8.1 Theoretical formulation

In the previous investigation into the wake-induced riser clashing by Wu et al. (2001;

2002; 2003), two identical risers with identical top tensions, or, in the two-dimensional case, two identical cylinders with identical supporting springs, were always assumed. The first task is therefore to extend the formulation as well as the computer code to the more general situation where the cylinder diameter and spring stiffness are not necessarily the same for the upstream and downstream cylinders.

8.1.1 Fluid forces on the elastically mounted downstream cylinder

Consider a pair of cylinders, with diameters D_1 and D_2, respectively, each supported on elastic springs, as shown in Figure 8-1. As only the drag force is considered on the upstream cylinder, its displacement is one-dimensional along the incoming flow direction. The downstream cylinder is allowed to move in both streamwise and cross flow direction. The co-ordinate system has its origin at the centre of the upstream cylinder's location when the fluid is stationary, with its x axis parallel to the flow direction and pointing towards downstream. The initial position of the downstream cylinder is (x_s, y_s). It is assumed here that the springs are ideal, i.e. the direction of the two springs supporting the downstream cylinder will not change with the displacement of the downstream cylinder.

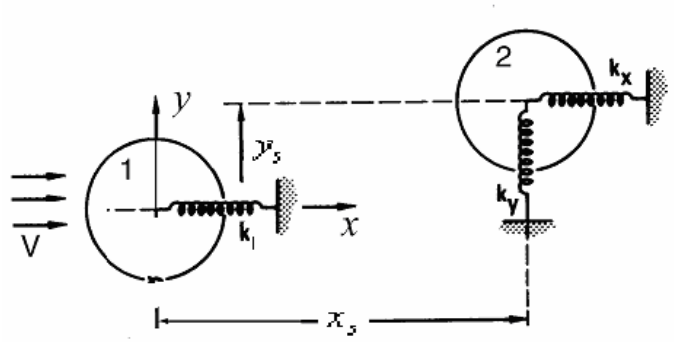

Figure 8-1 Schematic diagram of two elastically supported cylinders.

When the downstream circular cylinder with a velocity $(\dot{x}, \dot{y})$ is in the wake of another one, it is subjected to a wake velocity U (Figure 8-2). Based on the quasi-steady model (Price 1995), the time averaged fluid forces are

$$F_x = F_D \cos\beta - F_L \sin\beta = \frac{1}{2}\rho D_2 U_r^2 (\bar{C}_{D2}\cos\beta - \bar{C}_{L2}\sin\beta) \tag{8.1}$$

$$F_y = F_D \sin\beta + F_L \cos\beta = \frac{1}{2}\rho D_2 U_r^2 (\bar{C}_{D2}\sin\beta + \bar{C}_{L2}\cos\beta) \tag{8.2}$$

where F_D, F_L are drag and lift force; respectively; ρ is the fluid density; U_r is the relative velocity to the downstream cylinder; $\bar{C}_{D2}, \bar{C}_{L2}$ are drag and lift coefficients defined by the local wake velocity; and

$$U_r = \sqrt{(U - \dot{x}^2) + \dot{y}^2} \tag{8.3}$$

$$\cos\beta = \frac{U - \dot{x}}{U_r} \tag{8.4}$$

$$\sin\beta = \frac{-\dot{y}}{U_r} \tag{8.5}$$

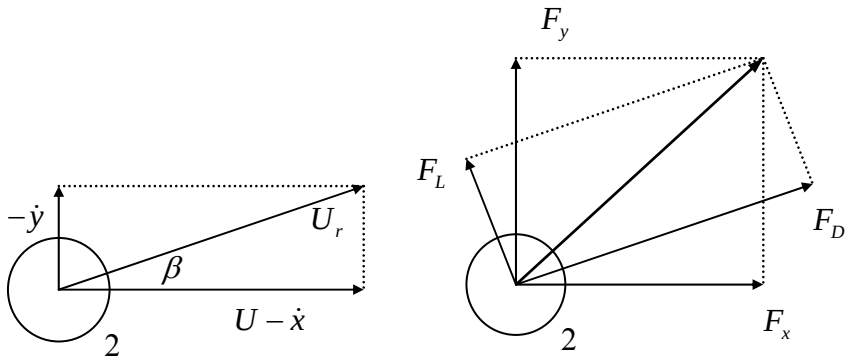

Figure 8-2 Force and velocity diagram.

Substituting equations (8.3)-(8.5) into equations (8.1) and (8.2) we have

$$F_x = \frac{1}{2}\rho D_2 U_r \left[\bar{C}_{D2}(U - \dot{x}) + \bar{C}_{L2}\dot{y}\right] \tag{8.6}$$

$$F_y = \frac{1}{2}\rho D_2 U_r \left[\bar{C}_{L2}(U - \dot{x}) - \bar{C}_{D2}\dot{y}\right] \tag{8.7}$$

8.1.2 Equations of motion

For the upstream cylinder only drag force is considered, which is calculated by Morison's equation. The motion equations of this system are

$$\left(m_1 + C_{m1}\frac{\pi}{4}\rho D_1^2\right)\ddot{x}_1 = \frac{1}{2}\rho D_1 C_{D1}\left|V - \dot{x}_1\right|\left(V - \dot{x}_1\right) - k_1 x_1 \tag{8.8}$$

$$\left(m_2 + C_{m2}\frac{\pi}{4}\rho D_2^2\right)\ddot{x}_2 = \frac{1}{2}\rho D_2 U_r\left[\bar{C}_{D2}(U - \dot{x}_2) + \bar{C}_{L2}\dot{y}_2\right] - k_x x_2 \tag{8.9}$$

$$\left(m_2 + C_{m2}\frac{\pi}{4}\rho D_2^2\right)\ddot{y}_2 = \frac{1}{2}\rho D_2 U_r\left[\bar{C}_{L2}(U - \dot{x}_2) - \bar{C}_{D2}\dot{y}_2\right] - k_y y_2 \tag{8.10}$$

Where x_1 is the in-line displacement of the upstream cylinder from its initial position at the origin, $(x_2,\ y_2)$ are the in-line and transverse displacements of the downstream cylinder from its initial position at $(x_s,\ y_s)$, and their upper dot and upper dot dot represent first and second order derivatives with respect to time *t*, respectively; k_1 is stiffness of the upstream cylinder, and k_x, k_y are stiffness of the downstream cylinder in *x*-direction and *y*-direction, respectively; *V* is the free stream velocity; m_1, m_2 are masses of unit cylinders and C_{m1}, C_{m2} are added mass coefficients, respectively.

By non-dimensionalising *x*, *y* with the D_1 and introducing $\tau = \omega_1 t$ with $\omega_1 = \sqrt{\dfrac{k_1}{m_1 + C_{m1}\dfrac{\pi}{4}\rho D_1^2}}$, the above equations can be given as

$$\ddot{X}_1 = \frac{U_R^2 C_{D1}}{2\pi^3(a + C_{m1})}\left|1 - \frac{2\pi\dot{X}_1}{U_R}\right|\left(1 - \frac{2\pi\dot{X}_1}{U_R}\right) - X_1 \tag{8.11}$$

$$\ddot{X}_2 = \frac{R_D U_R^2}{2\pi^3(R_m a + R_{C_m} C_{m1} R_D^2)}\sqrt{\left(1 - \frac{2\pi V\dot{X}_2}{UU_R}\right)^2 + \left(\frac{2\pi V\dot{Y}_2}{UU_R}\right)^2}\left[C_{D2}\left(1 - \frac{2\pi V\dot{X}_2}{UU_R}\right) + C_{L2}\frac{2\pi V\dot{Y}_2}{UU_R}\right] - \frac{R_{kx}(a + C_{m1})}{R_m a + R_{C_m} C_{m1} R_D^2} X_2 \tag{8.12}$$

$$\ddot{Y}_2 = \frac{R_D U_R^2}{2\pi^3 (R_m a + R_{C_m} C_{m1} R_D^2)} \sqrt{\left(1 - \frac{2\pi V \dot{X}_2}{U U_R}\right)^2 + \left(\frac{2\pi V \dot{Y}_2}{U U_R}\right)^2} \left[C_{L2} \left(1 - \frac{2\pi V \dot{X}_2}{U U_R}\right) - C_{D2} \frac{2\pi V \dot{Y}_2}{U U_R} \right] - \frac{R_{ky}(a + C_{m1})}{R_m a + R_{C_m} C_{m1} R_D^2} Y_2 \tag{8.13}$$

where $X_1 = x_1 / D_1$ and $X_2 = x_2 / D_1$; $a = \dfrac{m_1}{\frac{\pi}{4}\rho D_1^2}$ is mass parameter of the upstream cylinder; $U_R = \dfrac{V}{f_1 D_1}$ is the reduced velocity, where $f_1 = \omega_1 / 2\pi$; The ratios R_D, R_{kx}, R_{ky}, R_m, R_{C_m} are defined as $R_D = D_2 / D_1$, $R_{kx} = \dfrac{k_x}{k_1}$, $R_{ky} = \dfrac{k_y}{k_1}$, $R_m = \dfrac{m_2}{m_1}$, $R_{C_m} = \dfrac{C_{m2}}{C_{m1}}$, respectively. As the force coefficients are usually based on free stream velocity, the reference velocity for $\overline{C}_{D2}$ and $\overline{C}_{L2}$ is transformed from the local wake velocity U to the free stream velocity V by the relations $C_{D2} = \overline{C}_{D2} \dfrac{U^2}{V^2}$, $C_{L2} = \overline{C}_{L2} \dfrac{U^2}{V^2}$.

For simplicity, let

$$M_1 = a + C_{m1} \tag{8.14}$$

$$M_2 = R_m a + R_{C_m} C_{m1} R_D^2 \tag{8.15}$$

$$b = \frac{U}{V} \tag{8.16}$$

$$U_f = \sqrt{\left(1 - \frac{2\pi V \dot{X}_2}{U U_R}\right)^2 + \left(\frac{2\pi V \dot{Y}_2}{U U_R}\right)^2} \tag{8.17}$$

Then we have

$$\ddot{X}_1 = \frac{U_R^2 C_{D1}}{2\pi^3 M_1} \left|1 - \frac{2\pi \dot{X}_1}{U_R}\right| (1 - \frac{2\pi \dot{X}_1}{U_R}) - X_1 \tag{8.18}$$

$$\ddot{X}_2 = \frac{R_D U_R^2 U_f}{2\pi^3 M_2} \left[C_{D2} \left(1 - \frac{2\pi \dot{X}_2}{b U_R}\right) + C_{L2} \frac{2\pi \dot{Y}_2}{b U_R} \right] - \frac{R_{kx} M_1}{M_2} X_2 \tag{8.19}$$

$$\ddot{Y}_2 = \frac{R_D U_R^2 U_f}{2\pi^3 M_2}\left[C_{L2}\left(1-\frac{2\pi\dot{X}_2}{bU_R}\right)-C_{D2}\frac{2\pi\dot{Y}_2}{bU_R}\right]-\frac{R_{ky}M_1}{M_2}Y_2 \tag{8.20}$$

In the above equations, X_1 is the dimensionless in-line displacement of the upstream cylinder from its initial position at the origin. X_2, Y_2 are the dimensionless in-line and transverse displacements of the downstream cylinder from its initial position at $(X_s,\ Y_s)$.

Compared with the formula by Wu (2003), current ones count in the influence of added mass, redefine the reduced velocity U_R, and introduce the ratios of diameter and stiffness, therefore the results based on current formula should be more accurate and can be used to study the effects of diameter and stiffness ratios.

8.1.3 Equilibrium positions

While finding the equilibrium positions of the upstream cylinder is straightforward, the equilibrium positions of the downstream cylinders are identified by applying a continuation analysis methodology (Seydel 1994) as there exist multiple solutions with branch points.

Let the vector

$$H = \begin{bmatrix} h_1 \\ h_2 \\ h_3 \\ h_4 \\ h_5 \\ h_6 \end{bmatrix} = \begin{bmatrix} X_1 \\ \dot{X}_1 \\ X_2 \\ \dot{X}_2 \\ Y_2 \\ \dot{Y}_2 \end{bmatrix} \tag{8.21}$$

then we have

$$\dot{H} = F(H,\lambda) = \begin{cases} h_2 \\ \dfrac{U_R^2 C_{D1}}{2\pi^3 M_1}\left|1-\dfrac{2\pi h_2}{U_R}\right|(1-\dfrac{2\pi h_2}{U_R}) - h_1 \\ h_4 \\ \dfrac{R_D U_R^2 U_f}{2\pi^3 M_2}\left[C_{D2}\left(1-\dfrac{2\pi h_4}{bU_R}\right)+C_{L2}\dfrac{2\pi h_6}{bU_R}\right]-\dfrac{R_{kx}M_1}{M_2}h_3 \\ h_6 \\ \dfrac{R_D U_R^2 U_f}{2\pi^3 M_2}\left[C_{L2}\left(1-\dfrac{2\pi h_4}{bU_R}\right)-C_{D2}\dfrac{2\pi h_6}{bU_R}\right]-\dfrac{R_{ky}M_1}{M_2}h_5 \end{cases} \tag{8.22}$$

where λ can be any of the parameters, typically, the reduced velocity U_R. Mathematically, the equilibrium positions are obtained by solving

$$\dot{H} = F(H,\lambda) = 0 \tag{8.23}$$

Together with a complementary equation

$$p(h,\lambda,s) = \sum_{i=1}^{6}(h-h_i)^2 + \left[\lambda-\lambda(s_j)\right]^2 - (s-s_j)^2 = 0 \tag{8.24}$$

Here s is the arc length along the continuation solution curve. Equation (8.24) together with (8.23) constitutes self-contained non-linear equations, among which the continuation step length $\Delta s = s - s_j$ is prescribed beforehand. Such a system is solvable by predictor and corrector two steps method (Wu 2003).

Predictor step

Predictor is a procedure to provide an initial guess for equilibrium based on the already known equilibrium. The procedure starts from a known solution (h^j, λ_j), which can be sought at a small reduced flow velocity for system (8.23). In fact, the specified position of $(X_s,\ Y_s)$ itself is an equilibrium position at zero flow velocity. By taking prescribed arc length $\Delta s = s - s_j$, the predictor is made by the AKIMA

extrapolation in present investigation (Akima 1970).

Corrector step

The objective of corrector step is to find the exact equilibrium based on the guess provided by predictor step. In this chapter, it is made via the modified version of M. J. D. Powell's hybrid algorithm contained in the package of ISML library (ISML user manual), which is a variation of Newton's method. The algorithm uses a finite-difference approximation to the Jacobian and takes precautions to avoid large step sizes or increasing residuals. For further description, see (More et al. 1980).

8.1.4 Stability analysis of the downstream cylinder

Each equilibrium position along the solution curve is further examined on its dynamic stability. A conventional approach is adopted here by linearsing the equations of motion in the vicinity of the equilibrium position and finding eigenvalues of the Jacobian matrix of $F(H,\lambda)$. The stability is determined by the signs of the real parts of the eigenvalues.

The Jacobian matrix of vector $F(H,\lambda)$

$$\frac{\partial F(H,\lambda)}{\partial H} = A \tag{8.25}$$

where

$a_{11}=0$, $a_{12}=1, a_{13}=0, a_{14}=0, a_{15}=0, a_{16}=0,$

$a_{21}=-1$, $a_{22}=-\frac{2U_R C_{D1}}{\pi^2 M_1}\left|1-\frac{2\pi h_2}{U_R}\right|$, $a_{23}=0, a_{24}=0, a_{25}=0, a_{26}=0,$

$a_{31}=0$, $a_{32}=0$, $a_{33}=0$, $a_{34}=1$, $a_{35}=0$, $a_{36}=0$,

$$a_{41}=-\frac{R_D U_R^2 U_f}{2\pi^3 M_2}\left[C_{DX}\left(1-\frac{2\pi h_4}{bU_R}\right)+C_{LX}\frac{2\pi h_6}{bU_R}\right], a_{42}=0,$$

$$a_{43}=\frac{R_D U_R^2 U_f}{2\pi^3 M_2}\left[C_{DX}\left(1-\frac{2\pi h_4}{bU_R}\right)+C_{LX}\frac{2\pi h_6}{bU_R}\right]-\frac{R_{kx}M_1}{M_2},$$

$$a_{44}=-\frac{R_D U_R}{\pi^2 b M_2}\left[\frac{\left(1-\frac{2\pi h_4}{bU_R}\right)\left[C_{D2}\left(1-\frac{2\pi h_4}{bU_R}\right)+C_{L2}\frac{2\pi h_6}{bU_R}\right]}{U_f}+U_f C_{D2}\right],$$

$$a_{45}=\frac{R_D U_R^2 U_f}{2\pi^3 M_2}\left[C_{DY}\left(1-\frac{2\pi h_4}{bU_R}\right)+C_{LY}\frac{2\pi h_6}{bU_R}\right],$$

$$a_{46}=\frac{R_D U_R}{\pi^2 b M_2}\left[\frac{\frac{2\pi h_6}{bU_R}\left[C_{D2}\left(1-\frac{2\pi h_4}{bU_R}\right)+C_{L2}\frac{2\pi h_6}{bU_R}\right]}{U_f}+U_f C_{L2}\right],$$

$a_{51}=0$, $a_{52}=0$, $a_{53}=0$, $a_{54}=0$, $a_{55}=0$, $a_{56}=1$,

$$a_{61}=-\frac{R_D U_R^2 U_f}{2\pi^3 M_2}\left[C_{LX}\left(1-\frac{2\pi h_4}{bU_R}\right)-C_{DX}\frac{2\pi h_6}{bU_R}\right],\ a_{62}=0,$$

$$a_{63}=\frac{R_D U_R^2 U_f}{2\pi^3 M_2}\left[C_{LX}\left(1-\frac{2\pi h_4}{bU_R}\right)-C_{DX}\frac{2\pi h_6}{bU_R}\right],$$

$$a_{64}=-\frac{R_D U_R}{\pi^2 b M_2}\left[\frac{\left(1-\frac{2\pi h_4}{bU_R}\right)\left[C_{L2}\left(1-\frac{2\pi h_4}{bU_R}\right)-C_{D2}\frac{2\pi h_6}{bU_R}\right]}{U_f}+U_f C_{L2}\right],$$

$$a_{65}=\frac{R_D U_R^2 U_f}{2\pi^3 M_2}\left[C_{LY}\left(1-\frac{2\pi h_4}{bU_R}\right)-C_{DY}\frac{2\pi h_6}{bU_R}\right]-\frac{R_{ky}M_1}{M_2},$$

$$a_{66}=\frac{R_D U_R}{\pi^2 b M_2}\left[\frac{\frac{2\pi h_6}{bU_R}\left[C_{L2}\left(1-\frac{2\pi h_4}{bU_R}\right)-C_{D2}\frac{2\pi h_6}{bU_R}\right]}{U_f}-U_f C_{D2}\right],$$

where C_{D1} is assumed keeping constant, and $C_{D2}=C_{D2}(X_2-X_1,Y_2)$, $C_{L2}=C_{L2}(X_2-X_1,Y_2)$. C_{DX}, C_{DY}, C_{LX}, C_{LY} are defined as $C_{DX}=\frac{\partial C_{D2}}{\partial(X_2-X_1)}$, $C_{DY}=\frac{\partial C_{D2}}{\partial Y_2}$, $C_{LX}=\frac{\partial C_{L2}}{\partial(X_2-X_1)}$, $C_{LY}=\frac{\partial C_{L2}}{\partial Y_2}$, respectively.

If H_0 denotes an equilibrium position and

$$A=\left.\frac{\partial F(H,\lambda)}{\partial H}\right|_{H=H_0} \tag{8.26}$$

then

$a_{11}=0$, $a_{12}=1$, $a_{13}=0$, $a_{14}=0$, $a_{15}=0$, $a_{16}=0$,

$a_{21}=-1$, $a_{22}=-\frac{2U_R C_{D1}}{\pi^2 M_1}$, $a_{23}=0$, $a_{24}=0$, $a_{25}=0$, $a_{26}=0$,

$a_{31}=0$, $a_{32}=0$, $a_{33}=0$, $a_{34}=1$, $a_{35}=0$, $a_{36}=0$,

$a_{41}=-\frac{R_D U_R^2 C_{DX}}{2\pi^3 M_2}$, $a_{42}=0$, $a_{43}=\frac{R_D U_R^2 C_{DX}}{2\pi^3 M_2}-\frac{R_{kx} M_1}{M_2}$, $a_{44}=-\frac{2R_D U_R C_{D2}}{\pi^2 b M_2}$,

$a_{45}=\frac{R_D U_R^2 C_{DY}}{2\pi^3 M_2}$, $a_{46}=\frac{R_D U_R C_{L2}}{\pi^2 b M_2}$,

$a_{51}=0$, $a_{52}=0$, $a_{53}=0$, $a_{54}=0$, $a_{55}=0$, $a_{56}=1$,

$$a_{61} = -\frac{R_D U_R^2 C_{LX}}{2\pi^3 M_2} \quad , \quad a_{62} = 0 \quad , \quad a_{63} = \frac{R_D U_R^2 C_{LX}}{2\pi^3 M_2} \quad , \quad a_{64} = -\frac{2R_D U_R C_{L2}}{\pi^2 b M_2} \quad ,$$

$$a_{65} = \frac{R_D U_R^2 C_{LY}}{2\pi^3 M_2} - \frac{R_{ky} M_1}{M_2} \, , \quad a_{66} = -\frac{R_D U_R C_{D2}}{\pi^2 b M_2} \, ,$$

8.2 Some applications

In order to obtain the static solution of equation (8.23) and examine its eigenvalues, the fluid force coefficients have to be given beforehand. In the present study, they are mapped out by considering the numerical results from two cylinders flow and the experimental data from Zdravkovich (1997), the 2D model test data of two equal/unequal cylinders carried out by DHI Water & Environment (2002) and Huang and Sworn (2006).

8.2.1 Multiple stable/unstable equilibrium positions of the downstream cylinder

Some typical numerical results are presented in the following examples for two identical circular cylinders, with one cylinder located in the wake of another one. Identical supporting springs are also assumed for both cylinders. So we have $R_D = 1$ and $R_k = 1$. The mass parameter a = 2.183, which is a typical value for marine risers.

Shown in Figure 8-3 is an example of the continuation and stability analysis. Only the streamwise equilibrium positions of the downstream cylinder are shown here. The two cylinders are in a tandem arrangement with the initial spacing L = 10D. The upstream cylinder is initially at X = 0 with zero flow velocity and downstream cylinder X_s = 10, Y_s = 0. As the flow velocity increases from zero, the upstream cylinder is pushed downstream along the flow direction. The downstream cylinder also moves along the flow direction, but due to the wake shielding effect its displacement is not as great as that of the upstream cylinder. As the reduced velocity

increases further, two equilibrium positions emerge with one close to the upstream cylinder and another further downstream. Further increasing the reduced flow velocity, a critical state is then reached where the two equilibrium positions converge into a single equilibrium position (A in Figure 8-3) and above this critical reduced flow velocity no equilibrium positions exists.

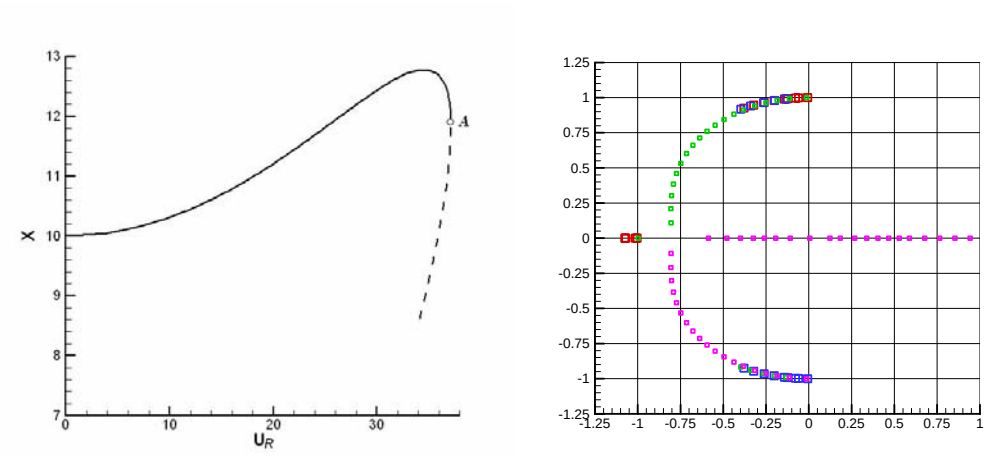

Figure 8-3 Equilibrium positions and relative eigenvalues of the downstream cylinder ($X_s = 10, Y_s = 0$). Left: equilibrium positions versus the reduced velocity; Right: relative eigenvalues.

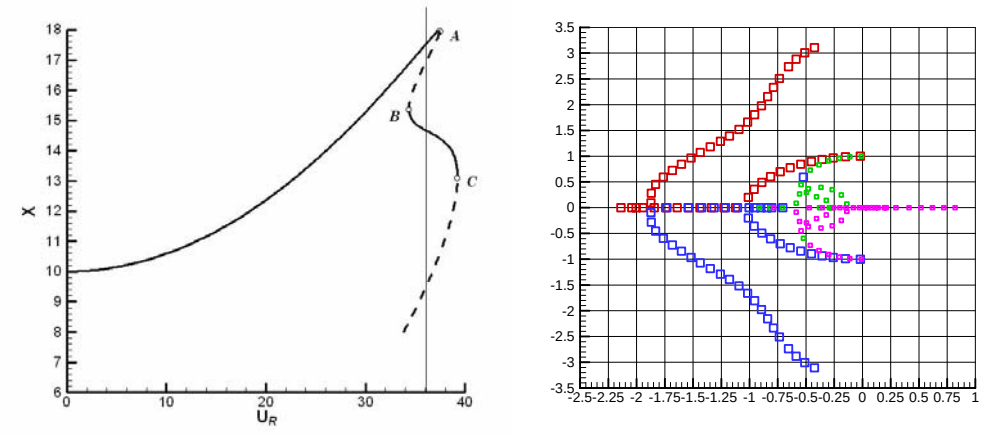

Figure 8-4 Equilibrium positions and relative eigenvalues of the downstream cylinder ($X_s = 10, Y_s = 2.5$). Left: equilibrium positions versus the reduced velocity; Right: relative eigenvalues.

The variation of the two pairs of eigenvalues of the Jacobian matrix (8.26) with the reduced velocity for the downstream cylinder is depicted in Figure 8-3. They all start from (0, *i*) or (0, -*i*) on the imaginary axis at zero flow velocity. As the velocity increases, they vary within the left half plane with negative real parts. At certain velocity, eigenvalues with positive real parts emerge, indicating unstable equilibrium positions. The unstable equilibrium positions are depicted by dash line in Figure 8-3.

Figure 8-4 shows a case when the two cylinders are in staggered arrangement, X_s = 10, Y_s = 2.5. As the reduced velocity increases, the downstream cylinder is pushed downstream and also moves towards the wake centreline. The streamwise displacement of the downstream cylinder is similar to that in Figure 8-3, except that more equilibrium positions can be identified here. Along the solution curve in Figure 8-4, stability changes at every turning point (A, B and C in Figure 8-4). Therefore at a reduced velocity U_R = 36, the downstream cylinder has two stable equilibrium positions and two unstable ones.

Along each solution curve of above equilibrium positions, there is a critical reduced velocity beyond which no equilibrium positions can be identified. At this critical velocity, the downstream cylinder is about to leave its equilibrium position, i.e. a loss of stability. Above the critical velocity the movement of the downstream cylinder will not converge to another stable equilibrium as there are no equilibrium positions. Instead the cylinder will move about in the wake. In this scenario, clashing with the upstream cylinder is very likely. This is demonstrated in experiments where clashing largely happens in case of loss of the stability. The critical velocity is therefore regarded as the onset condition of clashing.

8.2.2 Wake shielding effect on clashing onset – the worst scenario

In the model described in 8.1, the downstream cylinder can be situated anywhere in the wake (if outside the wake, wake-induced clashing will not occur). As far as the riser clashing onset condition is concerned, the tandem arrangement, i.e. the downstream cylinder is on the wake centreline of the upstream cylinder, possibly represents the worst scenario. That is to say that, for two given elastically supported

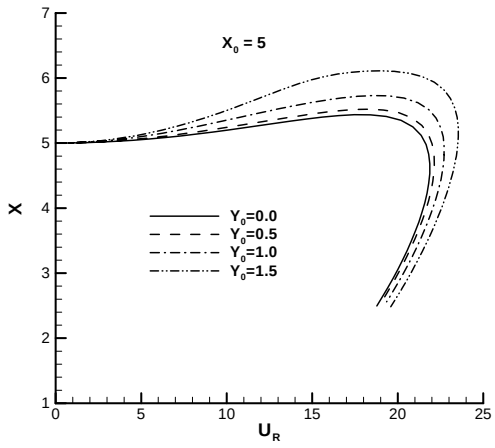

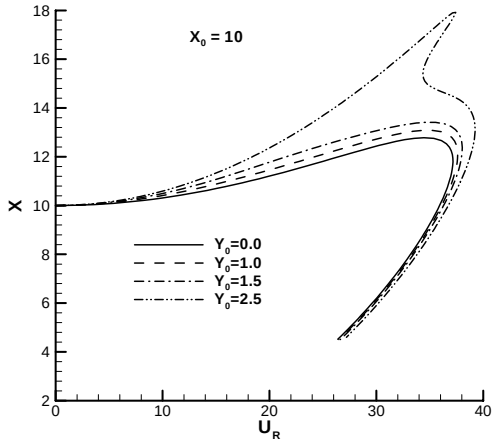

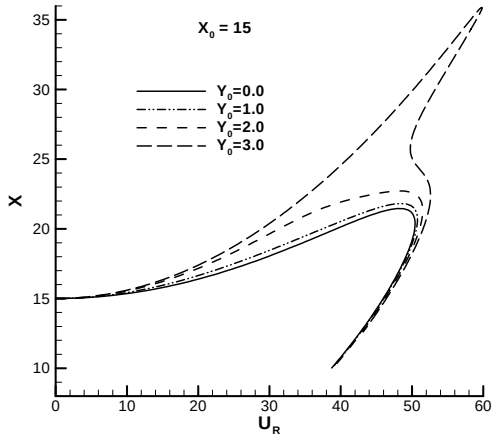

Figure 8-5 Traces of static solution of the downstream cylinder's in-line displacement as the in-flow velocity increases.

rigid cylinders in a current, they are most susceptible to the loss of stability as the in-flow velocity increases (i.e. onset condition of clashing) if these two cylinders are arranged in tandem.

To verify the conjecture, a detailed parametric study is carried out for two cylinders of an equal diameter with the downstream cylinder placed at various positions in the wake. The initial streamwise spacing varies from 5D to 15D, while the transverse spacing varies from 0 to 3D. The results are given in Figure 8-5 in terms of the streamwise solution curve as a function of the current velocity. The critical current speed, i.e. the clashing onset condition, corresponds to the maximum U_R of each curve. U_R is further defined by the current speed.

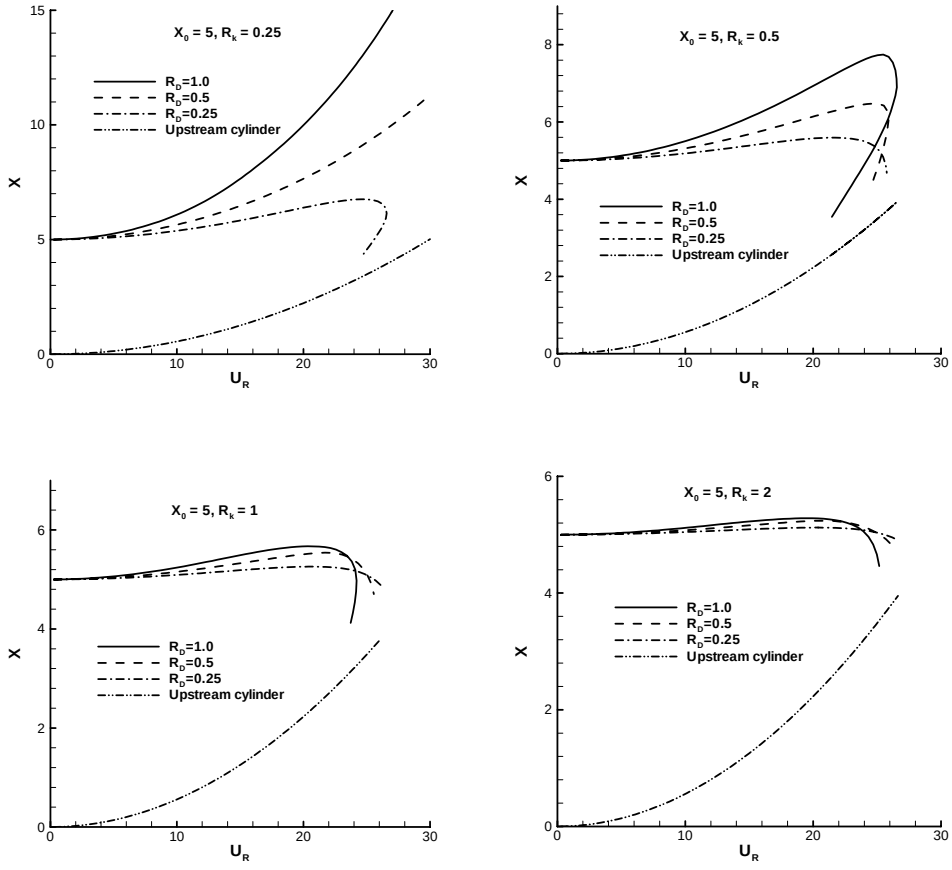

Figure 8-6 Trace of static solution versus reduced velocity (initial streamwise spacing $L = 5D_1$).

It can be seen that the tandem arrangement gives the smallest critical current velocity. It is therefore concluded that the tandem arrangement represents the worst wake shielding scenario in so far as the riser clashing onset condition is concerned. Based upon the conclusion of this investigation, it is decided that in the subsequent analysis, we consider the tandem arrangement only.

8.2.3 Effects of diameter and stiffness ratios

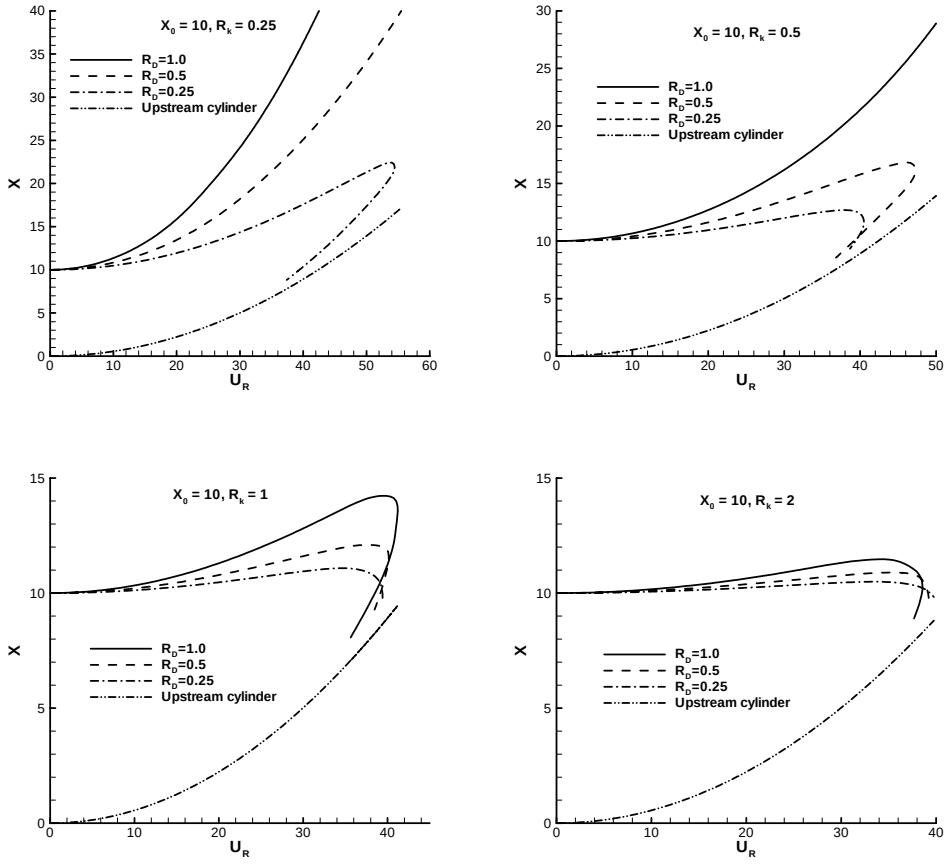

Figure 8-7 Trace of static solution versus reduced velocity (initial streamwise spacing $L = 10D_1$).

The effects of diameter and stiffness ratios between two cylinders on clashing onset are investigated here. As we consider the tandem arrangement only, the downstream cylinder is supported on a single spring aligned in the flow direction. The spring

stiffness is denoted as k_2. In this case, there are two varying parameters given below

$R_D = D_2 / D_1$ and $R_k = k_2 / k_1$

A systematic computation is carried out to trace the static solutions, as the current speed increases, of the two cylinders of different diameters and spring stiffness. From these results, the critical current speed can then be obtained and the effects of the diameter and stiffness ratios can be ascertained.

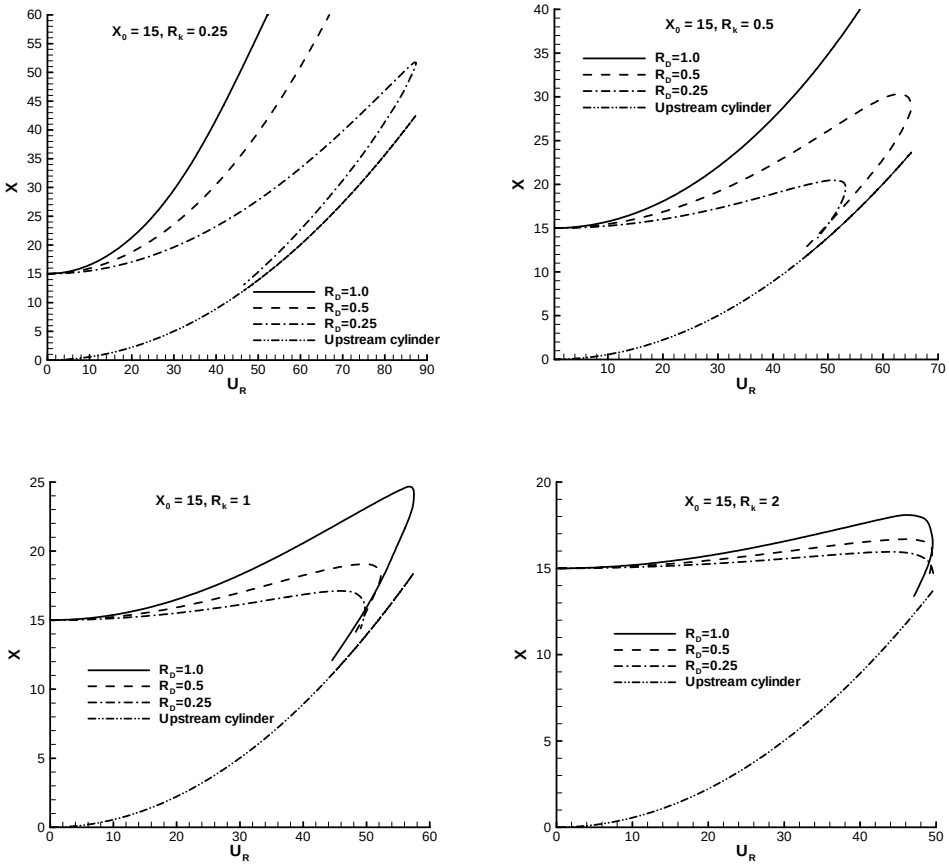

Figure 8-8 Trace of static solution versus reduced velocity (initial streamwise spacing $L = 15D_1$).

Figure 8-6 to Figure 8-8 give the traces of the non-linear static solutions of the cylinder's displacement as the in-flow velocity increases, based upon the continuation method. The critical current speed, i.e. the clashing onset condition,

corresponds to the maximum reduced velocity U_R of each curve. The results are given for a variety of diameter ratio, stiffness ratio and initial spacing between the two cylinders.

The results of the parametric analysis, in terms of the critical in-flow velocity, are summarised in Figure 8-9 and Figure 8-10. It can be seen that both the diameter and the stiffness ratios have significant impact on the riser clashing onset condition. Although the results presented here are for the two-dimensional case, these charts are potentially useful for riser design.

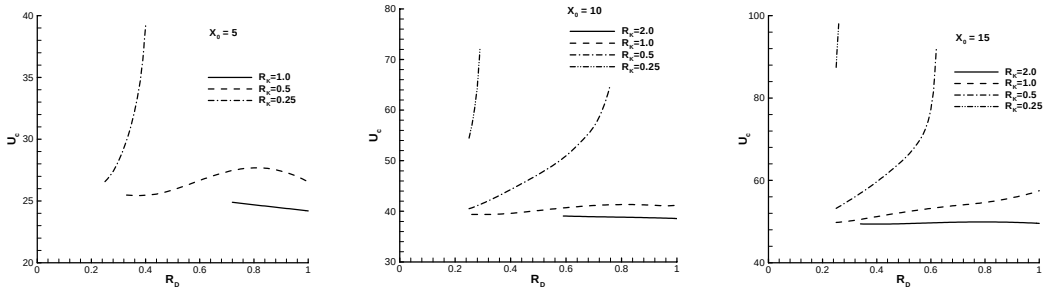

Figure 8-9 Critical inflow velocity *vs* diameter ratio.

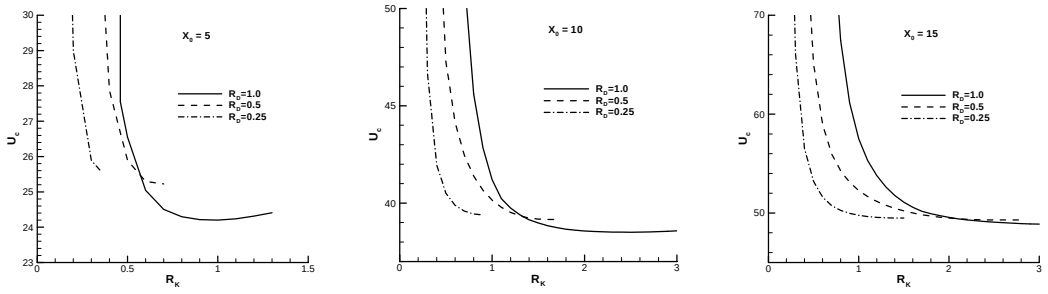

Figure 8-10 Critical inflow velocity *vs* stiffness ratio.

8.2.4 Effects of VIV

It should be noted that previous investigations are based on the fluid forces of stationary cylinders, which ignore the influence of VIV. For elastically supported

cylinders in cross-flow, VIV motions can significantly increase the mean drag coefficients of both the upstream and downstream cylinders. The effects of the drag increase upon the clashing onset condition are investigated in the present section.

Figure 8-11 gives the amplified drag coefficients of the downstream cylinder at various reduced velocities, which are reproduced from Huang and Sworn (2006). Note that $V_r = 0$ is used here to denote the case of fixed cylinders. The corresponding drag coefficients of the upstream cylinder are 1.1 ($V_r = 0$), 1.563 ($V_r = 4$) and 2.019 ($V_r = 5$).

It is important to understand that the analysis in the present section assumes that the cylinder has multiple natural frequencies and it is possible to undergo a combined VIV and low-frequency large-amplitude motion. The definition of the reduced velocity for VIV (V_r) is based upon a higher natural frequency, whilst the definition of the reduced velocity for the clashing onset condition (U_R) is based upon the fundamental natural frequency.

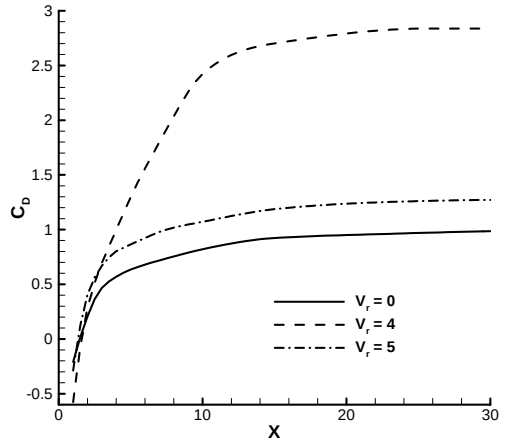

Figure 8-11 Amplified drag coefficient of the downstream cylinder versus the spacing ($D_1/D_2 = 2$). Reproduced from Huang and Sworn (2006).

Figure 8-12 shows the effect of the drag amplification on the clashing onset

condition. With the drag amplification, the critical inflow velocity, at which the clashing is about to occur, is significantly reduced in this particularly case ($L = 15D_1$, $R_D = D_2 / D_1 = 0.5$, $R_k = k_2 / k_1 = 0.5$, and the drag coefficient of the upstream cylinder 2.019, the drag coefficient of the downstream cylinder given by the middle curve of Figure 8-11).

The drag amplification does not always reduce the critical inflow velocity of the clashing onset. Its effect is more dependent upon to what extent the drag is increased for the upstream and downstream cylinders, respectively. In Figure 8-11, at $V_r = 4$ the drag coefficient of the downstream cylinder is increased significantly with the maximum value approaching 3.0, while the drag coefficient of the upstream cylinder is only increased moderately to 1.563 at the reduced velocity. In this case, the drag amplification helps to separate the two cylinders and completely prevents the occurrence of the clashing (hence the result of continuation analysis is not given here).

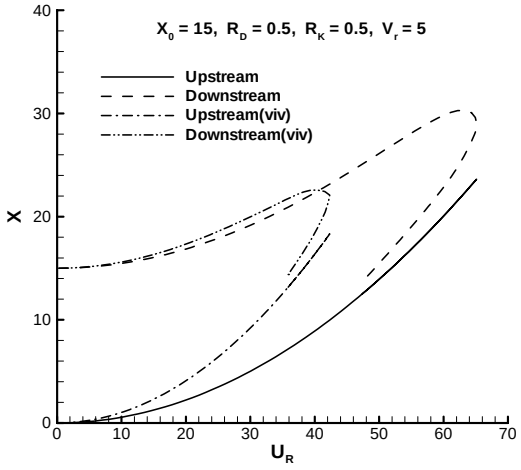

Figure 8-12 Trace of static solutions, with and without VIV drag amplification.

8.2.5 Huse's wake model

The above calculations are based on the force coefficients from numerical

simulations and experiments. By using Huse's wake model equations (2.6) - (2.11) (Huse 1993), it is possible to estimate the drag on the downstream cylinder simply from the empirical formula. A typical result for two cylinders of an equal diameter in tandem is given in Figure 8-13.

The drag prediction based upon the Huse's wake model has at least two problems, i.e. (i) the prediction does not agree well with the test data in all cases, and (ii) for the tandem arrangement, the drag-versus-spacing curve is rather flat. The experimental data and numerical results, on the other hand, show a negative drag region in the near wake as well as a sharp rise of the drag as the spacing increases.

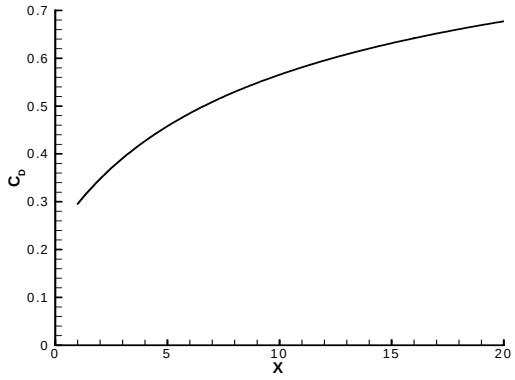

Figure 8-13 Drag coefficient of the downstream cylinder based upon Huse's model (Tandem arrangement, Upstream cylinder C_{D1} = 1.1).

The effect of the "mis-prediction" of Huse's wake model upon the clashing onset condition is examined here. The clashing onset condition is computed based upon two drag curves with one given by the experimental data and the other by Huse's wake model. The drag coefficient of the upstream cylinder is 1.1 for both cases. The results are given in comparison in Figure 8-14 for $R_D = 1$ and $R_k = 1$. Note that, unlike the solid line (result based upon the experimental data), the dashed line (based upon Huse's wake model) does not have a turning point. At the top end of U_R, it meets up with the line of the upstream cylinder, i.e. the two cylinders become in touch with each other.

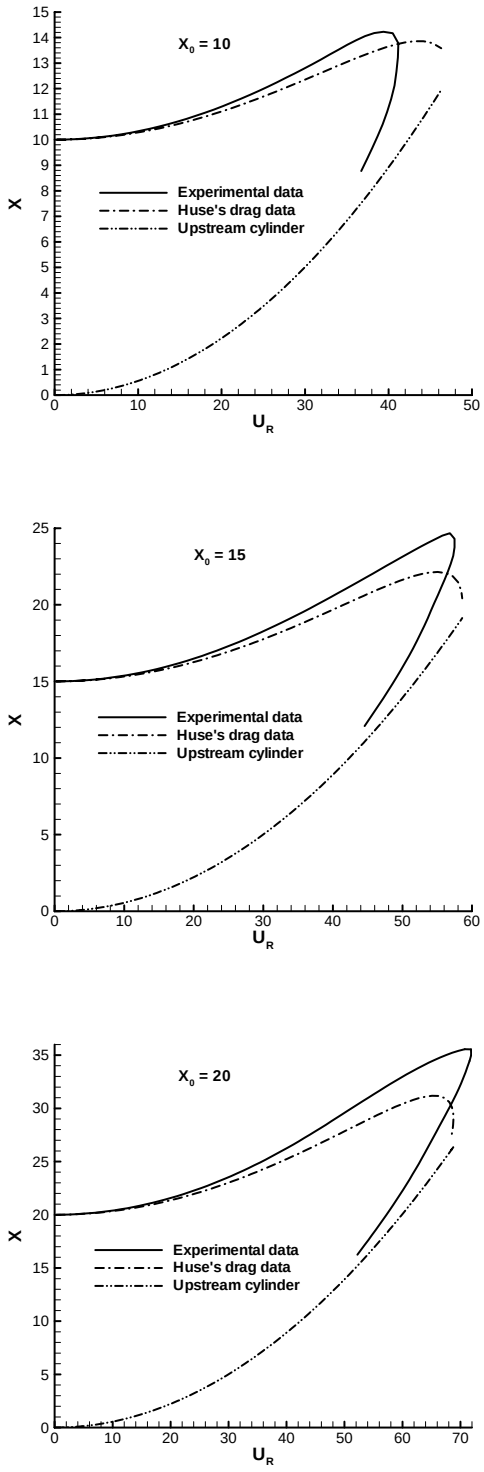

Figure 8-14 Trace of static solutions based upon experimental data and Huse's wake model, respectively.

As far as the clashing onset condition is concerned, the greatest discrepancy among the cases investigated here is about 15%. However, the fundamental difference between Huse's wake model and the experimental data lies in the interpretation of the physical phenomenon. If the experimental data are used, then a critical instability condition can be identified. The clashing follows once the instability sets in as the downstream cylinder moves upstream, gathers its momentum and ultimately collides with the upstream cylinder. Based upon Huse's wake model, on the other hand, the two cylinders would ultimately touch each other as the in-flow velocity increases, i.e. there is no instability issue. From the investigations in literature (Price 1995; Wu et. al 2002), it is clear that the riser clashing is an instability issue, not that the risers are pushed by the underwater current to touch each other.

8.3 Concluding remarks

In this chapter a stability analysis model for two marine risers is set up. Continuation analysis is used to find the equilibrium positions and the relative dynamic stability is identified by the eigenvalues of the relative Jacobian matrix.

It is found that for a cylinder located in the wake of an upstream one, there can be multiple stable/unstable equilibrium positions. There exists a critical reduced velocity, above which there will be no equilibrium positions. This indicates a likely clashing between the two cylinders once the critical velocity is exceeded.

The effects upon the clashing onset condition of various parameters, such as diameter ratio, stiffness ratio and VIV drag amplification are quantified. The validity of Huse's wake model, in the context of predicting clashing onset condition, is also investigated.

For two given elastically supported cylinders in cross flow, the tandem arrangement, i.e. the downstream cylinder situated on the wake centreline of the upstream cylinder, has the smallest critical inflow velocity for the occurrence of wake-induced clashing. The tandem arrangement is therefore identified as the worst situation for the clashing

onset.

Both the diameter and the stiffness ratios have significant impact on the riser clashing onset condition. Charts are produced to show their effects.

The drag amplification, caused by VIV, can significantly change the riser clashing onset condition. In some cases, the drag amplification can prevent riser clashing, for example, when the VIV amplifies the drag of the downstream riser a great deal more than it does to the upstream one. In other cases, the drag amplification can significantly reduce the critical inflow velocity for clashing to occur.

Huse's wake model, together with the drag prediction based on the model, does not explain the underlying mechanism of riser clashing. Nor does it predict the clashing onset condition accurately. Typically, the error of predicting the critical inflow velocity is about 15%.

9 Conclusion and future work

9.1 Conclusion

The turbulent cross flow past multiple identical circular cylinders at Reynolds number Re = 10^4 was simulated in this thesis by using a commercial CFD software FLUENT with a $k-\omega$ SST model. Flow patterns and fluid forces have been obtained. The effect of spacing on fluid forces has also been obtained and analysed. Based on numerical results and the experimental data by DHI Water & Environment in 2002, a stability analysis model is set up and applied for various aspects.

A computation model has been validated to simulate flow around circular cylinders in subcritical regime. Reasonable accuracy has been achieved considering the complexity of this bluff-body flow with unfixed separation points. It is optimised to allow a balance between computation efficiency and accuracy.

Five flow patterns for two cylinders in cross-flow, in tandem and staggered arrangements, are identified. The patterns 'shear layer reattachment', 'shear layer enveloping', 'vortex pairing and enveloping' and 'complete vortex shedding' emerge when the two cylinders are streamwise close and gradually moving out of the centreline of the upstream cylinder. The 'vortex impingement' flow pattern, or 'two vortex streets' pattern, happens when the downstream cylinder is situated in the wake of the upstream one and the streamwise spacing is more than 3D.

The bistable and hysteresis features of flow around two tandem cylinders are observed. The drag coefficients of the both cylinders experience a jump when the flow pattern changed.

Generally, the downstream cylinder experiences a significant drag reduction for tandem arrangement, and also a non-zero time-averaged lift force for staggered

arrangement. The drag reduction decreases when the streamwise or transverse clearance of the two cylinders is increased. The lift force of the downstream cylinder is always towards the wake centre. It is zero when it is situated out of the wake of the upstream one or on the wake centreline.

The nature of drag reduction and time-averaged lift was analysed in detail. It is found that the drag reduction is the result of fluctuation incident flow and the time-averaged lift is due to the asymmetry of fluctuating incident flow.

It is found for a tandem arrangement that the change of the stagnation point, as a result of the fluctuating incident velocity, is strongly associated with the large and periodical variations of the drag and lift forces, while the stagnation pressure is not. The cosine and minus sine of the stagnation angle are highly correlated with the drag and lift force, respectively. For a staggered arrangement, the change of the stagnation point is still strongly associated with the periodic variation of lift force, but not with the drag force. The reason lies in the asymmetry of separation points. The influences of stagnation point and separation point are synchronous on lift force but not on drag force.

The wake behind two tandem cylinders shows some different characteristics from those of an isolated cylinder. The velocity is greatly reduced due to the cascading shielding effects by both cylinders. It is observed that the increase in averaged velocity along the wake centreline for tandem arrangement is slower than that for an isolated cylinder flow. The wake power spectra analysis shows the oscillating flow in the wake behind the downstream cylinder is strongly influenced by its own vortex shedding when $L \geq 6D$.

Corresponding to the wake distribution behind two tandem cylinders, flow around three in-line cylinders display some interesting features. While the third cylinder only influences the drag of the upstream two when they are at such a distance apart that the flow pattern can change, i.e. the configuration is near the critical spacing, the first two cylinders' influence on the third one is remarkable. When the three cylinders are

equally spaced, $C_{D3} \approx 0.4$ is much higher than that of the second one for L < 2.5D, then drops rapidly to zero for L = 2.5D to 5D. At L = 5D, C_{D3} experiences a jump and again is greater than C_{D2}.

The influence of spacing between the second and third cylinder, L_2, on the third cylinder is significant. C_{D3} is very small when $L_2 \leq 4D$, and there is a jump between L_2 = 4D and 6D, as a result of the double shielding effects of the two upstream cylinders. It is also found that when the first two cylinders are widely spaced, the third cylinder experiences a reduced vortex shedding frequency.

A stability analysis model for two marine risers was set up. Continuation analysis was used to find the equilibrium positions and the relative dynamic stability was identified by the eigenvalues of the relative Jacobian matrix.

It was found that for a cylinder located in the wake of an upstream one, there can be multiple stable/unstable equilibrium positions. There exists a critical reduced velocity, above which there will be no equilibrium positions. This indicates a likely clashing between the two cylinders once the critical velocity is exceeded.

The effects upon the clashing onset condition of various parameters, such as diameter ratio, stiffness ratio and VIV drag amplification are quantified. The validity of Huse's wake model, in the context of predicting clashing onset condition, is also investigated.

The tandem arrangement is identified as the worst situation for the clashing onset. It is revealed both the diameter and the stiffness ratios have significant impact on the riser clashing onset condition. The drag amplification, caused by VIV, can significantly change the riser clashing onset condition. In some cases, the drag amplification can prevent riser clashing, while in other cases, the drag amplification can significantly reduce the critical inflow velocity for clashing to occur.

Huse's wake model, together with the drag prediction based on the model, does not explain the underlying mechanism of riser clashing. Nor does it predict the clashing

onset condition accurately.

9.2 Suggestions for future work

The following research areas are of interest of future work.

Strouhal number reduction

The reduced Strouhal number of the wake behind two tandem cylinders with large spacing (>5D) between them is numerically observed, and so is for the three in-line cylinders flow. This is a very interesting phenomenon and is not fully investigated in this thesis. The reasons could be the lower locally incident velocity to the second cylinder, the effect of the upstream vortices or both of them. Theoretical vortex structure research is needed to study this phenomenon.

Quantitative analysis of the cause of fluid forces on a cylinder in a wake

It is found in this thesis that the change of stagnation point is strongly associated with the periodic variation of the fluid forces on a cylinder in a wake. This qualitative conclusion can be the first step of investigating the analytical or empirical calculation of the fluid forces under wake effects, which will leads to simple and accurate stability analysis of multiple cylinders.

Dynamic simulation of two elastically mounted cylinders

In this thesis, the static fluid forces are used to study the stability of two elastic cylinders. The limitation of this approach is obvious as the influence of VIVs on fluid loading is remarkable. To eliminate this drawback, dynamic simulation of two elastically mounted cylinders in a cross flow can be performed, based on the dynamic mesh technique in FLUENT. This of course will demand much of the computer resources.

Flow around three cylinders in triangular arrangement

Only in-line arrangement of three cylinders is investigated in this thesis. Further work should be carried out of triangular configurations. The triangular arrangement represents the engineering practise and is a very complex fluid mechanics problem. There exist the drag reduction and mean lift force for both downstream cylinders under the wake shielding effect.

References

Akbari,M.H. & Price,S.J. 2005. Numerical investigation of flow patterns for staggered cylinder pairs in cross-flow. Journal of Fluids and Structures, 20**,** 533-554.

Akima,H. 1970. A New Method of Interpolation and Smooth Curve Fitting Based on Local Procedures. Journal of the Acm, 17**,** 589-602.

Alam,M.M. & Zhou,Y. 2007. Phase lag between vortex shedding from two tandem bluff bodies. Journal of Fluids and Structures, 23**,** 339-347.

Bai,Y. 2009. Pipelines and Risers. Amsterdam: Elsevier ocean engineeringbook series, V. 3.

Barltrop,N.D.P. 1998. Floating Structures: A guide for design and analysis. England: Oilfield Publications Limited.

Benard,H. C.R.Acad.Sci.Paris 147, 970-972. 1908.
Ref Type: Journal (Full)

Best,M.S. & Cook,N.J. 1967. The forces on a circular cylinder in a shear flow. University of Bristol, Aeronautical Engineering Department, Report 103.

Blevins,R.D. 1990. Flow-Induced Vibration (Second Edition). New York: Van Nostrand reinhold.

Blevins,R.D. 2005. Forces on and stability of a cylinder in a wake. Journal of Offshore Mechanics and Arctic Engineering-Transactions of the Asme, 127**,** 39-45.

Breuer,M. 1998. Numerical and modeling influences on large eddy simulations for the flow past a circular cylinder. International Journal of Heat and Fluid Flow, 19**,** 512-521.

Cantwell,B. & Coles,D. 1983. An Experimental-Study of Entrainment and Transport in the Turbulent Near Wake of A Circular-Cylinder. Journal of Fluid Mechanics, 136**,**

321-374.

Catalano,P., Wang,M., Iaccarino,G. & Moin,P. 2003. Numerical simulation of the flow around a circular cylinder at high Reynolds numbers. International Journal of Heat and Fluid Flow, 24**,** 463-469.

Dalton,C. & Szabo,J.M. 1977. Drag on A Group of Cylinders. Mechanical Engineering, 99**,** 103.

DHI Water & Environment 2002. Norwegian deepwater programme - Model test of dual risers. Final Report.

FLUENT Inc. 2003. FLUENT 6.1 User's Guide. Lebanon, USA.

Gu,Z.F. & Sun,T.F. 1999. On interference between two circular cylinders in staggered arrangement at high subcritical Reynolds numbers. Journal of Wind Engineering and Industrial Aerodynamics, 80**,** 287-309.

Gushchin,V.A., Kostomarov,A.V., Matyushin,P.V. & Pavlyukova,E.R. 2002. Direct numerical simulation of the transitional separated fluid flows around a sphere and a circular cylinder. Journal of Wind Engineering and Industrial Aerodynamics, 90**,** 341-358.

Halse,K.H. 1997. On vortex shedding and prediction of vortex induced vibrations of circular cylinder. Norwegian University of Science and Technology: Department of Marine Structures.

Holloway,D.S., Walters,D.K. & Leylek,J.H. 2004. Prediction of unsteady, separated boundary layer over a blunt body for laminar, turbulent, and transitional flow. International Journal for Numerical Methods in Fluids, 45**,** 1291-1315.

Huang,S. & Sworn,A. 2006. VIV motion and drag amplification of two cylinders in cross flow with one in the wake of the other. Marine Systems & Ocean Technology, Vol. 1, No. 3.

Huse,E. 1993. Interaction in Deep-Sea Riser Arrays. Proceedings of the 25th annual

offshore technology conference, OTC7237, Houston, TX, 313-322.

Igarashi,T. 1981. Characteristics of the flow around two circular cylinders arranged in tandem first report. Bulletin of the Jsme-Japan Society of Mechanical Engineers, 24**,** 323-331.

Igarashi,T. 1986. Characteristics of the Flow Around 4 Circular-Cylinders Arranged in Line. Bulletin of the Jsme-Japan Society of Mechanical Engineers, 29**,** 751-757.

Igarashi,T. & Suzuki,K. 1984. Characteristics of the Flow Around 3 Circular-Cylinders Arranged in Line. Bulletin of the Jsme-Japan Society of Mechanical Engineers, 27**,** 2397-2404.

Jester,W. & Kallinderis,Y. 2003. Numerical study of incompressible flow about fixed cylinder pairs. Journal of Fluids and Structures, 17**,** 561-577.

Kitagawa,T. & Ohta,H. 2008. Numerical investigation on flow around circular cylinders in tandem arrangement at a subcritical Reynolds number. Journal of Fluids and Structures, 24**,** 680-699.

Kiya,M., Arie,M., Tamura,H. & Mori,H. 1980. Vortex shedding from two circular-cylinders in staggered arrangement. Journal of Fluids Engineering-Transactions of the Asme, 102**,** 166-173.

Lam,K., Li,J.Y., Chan,K.T. & So,R.M.C. 2003. Flow pattern and velocity field distribution of cross-flow around four cylinders in a square configuration at a low Reynolds number. Journal of Fluids and Structures, 17**,** 665-679.

Launder,B.E. 1984. Numerical Computation of Convective Heat-Transfer in Complex Turbulent Flows - Time to Abandon Wall Functions. International Journal of Heat and Mass Transfer, 27**,** 1485-1491.

Li,J., Chambarel,A., Donneaud,M. & Martin,R. 1991. Numerical Study of Laminar-Flow Past One and Tow Circular-Cylinders. Computers & Fluids, 19**,** 155-&.

Liang,C.L., Papadakis,G. & Luo,X.Y. 2009. Effect of tube spacing on the vortex shedding characteristics of laminar flow past an inline tube array: A numerical study. Computers & Fluids, 38**,** 950-964.

Ljungkrona,L., Norberg,C. & Sunden,B. 1991. Free-stream turbulence and tube spacing effects on surface pressure-fluctuations for two tubes in an in-line arrangement. Journal of Fluids and Structures, 5**,** 701-727.

Lubcke,H., Schmidt,S., Rung,T. & Thiele,F. 2001. Comparison of LES and RANS in bluff-body flows. Journal of Wind Engineering and Industrial Aerodynamics, 89**,** 1471-1485.

Maekawa,T. 1964. Study on wind pressure against ACSR double conductor. Electrical Engineering in Japan, 84.

Mair,W.A. & Maull,D.J. 1971. Aerodynamic Behaviour of Bodies in Wakes of Other Bodies. Philosophical Transactions of the Royal Society of London Series A-Mathematical and Physical Sciences, 269**,** 425-&.

Meneghini,J.R., Saltara,F., Siqueira,C.L.R. & Ferrari,J.A. 2001. Numerical simulation of flow interference between two circular cylinders in tandem and side-by-side arrangements. Journal of Fluids and Structures, 15**,** 327-350.

Menter,F.R. 1994. Two-Equation Eddy-Viscosity Turbulence Models for Engineering Applications. Aiaa Journal, 32**,** 1598-1605.

Mittal,S. & Kumar,V. 2001. Flow-induced oscillations of two cylinders in tandem and staggered arrangements. Journal of Fluids and Structures, 15**,** 717-736.

Mittal,S., Kumar,V. & Raghuvanshi,A. 1997. Unsteady incompressible flows past two cylinders in tandem and staggered arrangements. International Journal for Numerical Methods in Fluids, 25**,** 1315-1344.

More,J., Garbow,B. & Hillstrom,K. 1980. Rep. No. Argonne National Labs Report ANL-80-74, Argonne, Illinois.

Newman,J.N. 1977. Marine Hydrodynamics. Massachusetts Institute ofTechnology: The MIT Press.

Norberg,C. 1998. LDV-measurements in the near wake of a circular cylinder. Advances in Understanding of Bluff Body Wakes and Vortex-induced Vibration, Washington, DC, 1-12.

Norberg,C. 2002. Pressure distributions around a circular cylinder in cross-flow. Proceedings of the Conference on Bluff Body Wakes and Vortex-Induced Vibrations, December, Port Gouglas, Australia, 237-240.

Norberg,C. 2003. Fluctuating lift on a circular cylinder: review and new measurements. Journal of Fluids and Structures, 17**,** 57-96.

Price,S.J. 1976. The Origin and Nature of Lift Force on Leeward of two Bluff Bodies. Aeronautical Quarterly, 27**,** 154-168.

Price,S.J. 1995. A Review of Theoretical-Models for Fluidelastic Instability of Cylinder Arrays in Cross-Flow. Journal of Fluids and Structures, 9**,** 463-518.

Price,S.J. & Paidoussis,M.P. 1984. The Aerodynamic Forces Acting on Groups of Two and Three Circular Cylinders When Subject to A Cross-Flow. Journal of Wind Engineering and Industrial Aerodynamics, 17**,** 329-347.

Rawlins,C.B. 1974. Discussion on 'on the use of damped and undamped quasi-static aerodynamic models in the study of wake-induced flutter'. IEEE Power Engineering Society Summer Meeting, Anaheim, California.

Richmond-Bryant,J. 2003. Verification testing in computational fluid dynamics: an example using Reynolds-averaged Navier-Stokes methods for two-dimensional flow in the near wake of a circular cylinder. International Journal for Numerical Methods in Fluids, 43**,** 1371-1389.

Rocchi,D. & Zasso,A. 2002. Vortex shedding from a circular cylinder in a smooth and wired configuration: comparison between 3D LES simulation and experimental analysis. Journal of Wind Engineering and Industrial Aerodynamics, 90**,** 475-489.

Rockwell,D. 1998. Vortex-body interactions. Annual Review of Fluid Mechanics, 30, 199-229.

Rodi,W. 1997. Comparison of LES and RANS calculations of the flow around bluff bodies. Journal of Wind Engineering and Industrial Aerodynamics, 71, 55-75.

Rubin,J. & Buchanan,P. 2006. The Time of Sands. Occasional Report #56, CIBC World Market Inc..

Schlichting,H. 1979. Boundary-Layer Theory. McGraw-Hill Book Company Inc., New York.

Seydel,R. 1994. From Equilibrium to Chaos - Practical Bifurcation and Stability Analysis. Elsevier Science Publishing Co.

Slaouti,A. & Stansby,P.K. 1992. Flow Around Two Circular-Cylinders by the Random-Vortex Method. Journal of Fluids and Structures, 6, 641-670.

Sumer,B.M. & Fredsoe,J. 1997. Hydrodynamics Around Cylindrical Structures. Singapore: World Scientific Publishing Co Pte Ltd.

Sumner,D., Price,S.J. & Paidoussis,M.P. 2000. Flow-pattern identification for two staggered circular cylinders in cross-flow. Journal of Fluid Mechanics, 411, 263-303.

Sumner,D., Richards,M.D. & Akosile,O.O. 2005. Two staggered circular cylinders of equal diameter in cross-flow. Journal of Fluids and Structures, 20, 255-276.

Szepessy,S. & Bearman,P.W. 1992. Aspect Ratio and End Plate Effects on Vortex Shedding from A Circular-Cylinder. Journal of Fluid Mechanics, 234, 191-217.

Ting,D.S.K., Wang,D.J., Price,S.J. & Paidoussis,M.P. 1998. An experimental study on the fluidelastic forces for two staggered circular cylinders in cross-flow. Journal of Fluids and Structures, 12, 259-294.

Tutar,M. & Holdo,A.E. 2001. Computational modelling of flow around a circular cylinder in sub-critical flow regime with various turbulence models. International Journal for Numerical Methods in Fluids, 35, 763-784.

Versteeg,H.K. & Malalasekera,W. 2007. An Introduction to Computational Fluid Dynamics : the Finite Volume Method. Pearson/Prentice Hall, USA.

West,G.S. & Apelt,C.J. 1993. Measurements of Fluctuating Pressures and Forces on A Circular-Cylinder in the Reynolds-Number Range 10(4) to 2.5 X 10(5). Journal of Fluids and Structures, 7**,** 227-244.

Williamson,C.H.K. 1985. Evolution of A Single Wake Behind A Pair of Bluff-Bodies. Journal of Fluid Mechanics, 159**,** 1-18.

Williamson,C.H.K. 1996. Vortex dynamics in the cylinder wake. Annual Review of Fluid Mechanics, 28**,** 477-539.

Wu,W.S. 2003. Interaction Between Two Marine Risers. PhD thesis, University of Glasgow.

Wu,W.S., Huang,S. & Barltrop,N. 2001. Multiple stable/unstable equilibria of a cylinder in the wake of an upstream cylinder. Journal of Offshore Mechanics and Arctic Engineering-Transactions of the Asme, 125**,** 103-107.

Wu,W.S., Huang,S. & Barltrop,N. 2002. Current induced instability of two circular cylinders. Applied Ocean Research, 24**,** 287-297.

Yokokawa,M., Itakura,K., Uno,A., Ishihara,T. & Kaneda,Y. 2002. 16.4-TFlops Direct Numerical Simulation of Turbulence by a Fourier Spectral Method on the Earth Simulator. Proceedings of the 2002 ACM/IEEE Conference on Supercomputing, Baltimore MD.

Yong,M.E. & Ooi,A. 2004. Turbulence Models and Boundary Conditions for Bluff Body Flow. 15th Australasian Fluid Mechanics Conference, The University of Sydney, Sydney, Australia.

Zdravkovich,M.M. 1977. Review of flow interference between two circular cylinders in various arrangements. ASME Journal of Fluids Engineering, 99**,** 618-633.

Zdravkovich,M.M. 1984. Classification of flow-induced oscillations of two parallel

circular cylinders in various arrangements. Symposium on Flow-induced Vibrations, 2, 1-18.

Zdravkovich,M.M. 1987. The effects of interference between circular cylinders in cross flow. Journal of Fluids and Structures, 1, 239-261.

Zdravkovich,M.M. 1997. Flow Around Circular Cylinders. Oxford University Press, Oxford.

Zdravkovich,M.M. & Pridden,D.L. 1977. Interference Between Two Circular Cylinders ; Series of Unexpected Discontinuities. Journal of Industrial Aerodynamics, 2, 255-270.

Zhang,H. & Melbourne,W.H. 1992. Interference Between 2 Circular-Cylinders in Tandem in Turbulent-Flow. Journal of Wind Engineering and Industrial Aerodynamics, 41, 589-600.